

# Theory for Hydrostatic Gas Journal Bearings for Micro-Electro-Mechanical Systems

by

Lixian Liu

Bachelor of Engineering in Mechanical Engineering, Tsinghua University, Beijing, 1997  
Master of Science in Physics, Tsinghua University, Beijing, 2000

Submitted to the Department of Mechanical Engineering  
in partial fulfillment of the requirements for the degree of

Doctor of Philosophy


at the

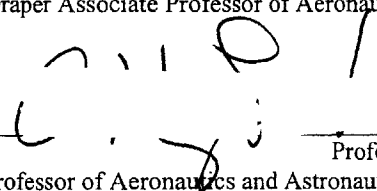
Massachusetts Institute of Technology

September 2005

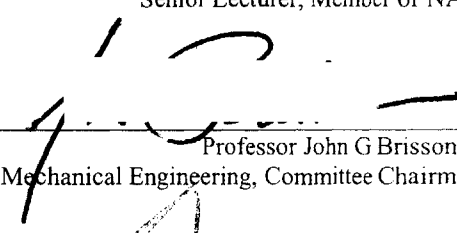
© Massachusetts Institute of Technology. All rights reserved.


Author  \_\_\_\_\_  
Department of Mechanical Engineering  
August 22, 2005

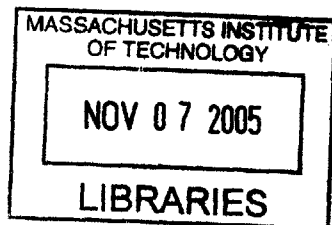
Certified by  \_\_\_\_\_  
Professor Zoltan S. Spakovszky  
C. S. Draper Associate Professor of Aeronautics and Astronautics

Certified by  \_\_\_\_\_  
Professor Alan H. Epstein  
R. C. Maclaurin Professor of Aeronautics and Astronautics, Member of NAE

Certified by  \_\_\_\_\_  
Dr. Fredric F. Ehrich  
Senior Lecturer, Member of NAE

Certified by  \_\_\_\_\_  
Professor John G. Brisson II  
Professor of Mechanical Engineering, Committee Chairman

Accepted by  \_\_\_\_\_  
Professor Lallit Anand  
Professor of Mechanical Engineering  
Chair, Committee on Graduate Students



ARCHIVES

# Theory for Hydrostatic Gas Journal Bearings for Micro-Electro-Mechanical Systems

by

Lixian Liu

Submitted to the Department of Mechanical Engineering  
on 8/22/05 in partial fulfillment of the requirements for the degree of  
Doctor of Philosophy

## Abstract

The goal of the MIT micro-engine project is to develop high-speed rotating Power MEMS (Micro-Electro-Mechanical Systems) using computer chip fabrication technologies. To produce high power (10-50 W) in a small volume (less than one cubic centimeter), the micro-turbo-machinery must be spun at a rotational speed on the order of million rpm. This ultra-high rotational speed, together with the small length-to-diameter ratio ( $L/D < 0.07$ ) limited by the chip manufacturing technology, entails many challenges in the design of the bearing system, such as an ultra-high whirl ratio of over 20 (compared with a whirl ratio of 2 for large-scale journal bearings) and a DN number of order 10 million mm-rpm. The thesis presents a newly developed theory for the hydrostatic gas journal-bearings for the micro-engine devices.

To investigate the underlying physical mechanisms, fluid models are established to analytically calculate the hydrostatic, hydrodynamic, and damping bearing forces. It is found from first principles that the hydrodynamic force due to viscous drag becomes dominant with an  $L/D \ll 1$  and acts in the opposite direction of the hydrodynamic force due to rotor pumping action. As a result, the net destabilizing hydrodynamic force can vanish for certain bearing geometries, causing singular behavior in the whirl instability limit. Thus, the ultra-short bearing is suggested to enable a large DN number and a high whirl ratio in the micro-journal-bearing system.

A novel variation of the axial-flow hydrostatic micro gas journal-bearing concept is introduced, which yields anisotropy in bearing stiffness. By departing from axial symmetry and introducing biaxial symmetry in hydrostatic stiffness, the bearing's top speed is increased and the fabrication tolerance requirements are substantially relieved.

The third-order nonlinear resonances in the micro-journal-bearing system are investigated by both analytical models and numerical simulations, and the predictions from these models agree well with the experimental observations. The model predicts a subharmonic resonance in the isotropic journal-bearing system, with a slow rotating noncircular orbit such that the symmetry of the system is broken by itself in the nonlinear resonance. Furthermore, the anisotropic journal-bearing system is found to be able to engage in multi-type nonlinear resonances: superharmonic resonances at one third of the natural frequencies, subharmonic resonances at three times the natural frequencies, and combinations (such as the average) of the two natural frequencies. The conditions under which these resonances can occur are derived analytically and are then verified by numerical simulation.

Thesis Supervisor: Zoltan S. Spakovszky

Title: Charles Stark Draper Associate Professor of Aeronautics and Astronautics



*I dedicate this thesis to my parents, FengZhen and ShuWen Liu.*

谨以此文献给我敬爱的父母亲：王凤珍，刘书文

# Acknowledgements

I consider this thesis to be the essence of the support, encouragement, good will, and friendship of a great many people, without whom it would have been impossible to complete. Since it is the conclusion of a long process, I offer my apologies in advance if I forget to mention someone who has helped me along the way.

First of all, I would like to thank my advisor, Prof. Zoltan Spakovszky, for being a good mentor and friend for the last four years. His door is always open to me, and over the past years, I have taken so many “seconds” from him for questions, both technical and not technical. The encouragement and inspiration I have received from him are the lubricants of my research work, for which I am indebted to him.

I would also like to thank the other members of my doctoral committee, Prof. Alan Epstein, Dr. Fredric Ehrich, and Prof. John Brisson, for their guidance and instructions. I am grateful to Prof. Alan Epstein for giving me the opportunity to join the micro-engine project and leading me to the fascinating micro-bearing research. I believe he should be proud of himself for having funded so many graduates with the micro-engine project, which wouldn't exist without his creativity and fundraising skills. I want to thank Dr. Fredric Ehrich for sharing his precious experiences with us and opening the gate to the rotordynamics field for me. And I also want to thank Prof. John Brisson for being the chair of my doctoral committee and supporting me through all five years.

On the non-faculty front, I am indebted to the other members of the micro-bearing group for broadening my horizons. In particular, I would like to thank Dr. Stuart Jacobson for inspiring discussions, Dr. Yifang Gong for teaching me how to use Fluent and verifying my fluid models, Dr. Hanqin Li and Dr. Li Wang for their hard work in fabricating the devices, and Chiang Juay Teo, Nicholas Savoulides, and Laurent Jamonet for sharing their experimental data. I have been working side by side with Chiang Juay Teo for five years, doing experiments, analyzing data, and establishing models; as a friend, he deserves heartfelt thanks for all our long conversations about things related and not related to bearings, in both English and Chinese.

Furthermore, I would like to thank Dr. Chia Ming Chen and Tahlia Day for proofreading my thesis. And because the thesis is based on the previous work of many people, I would like to thank them all for the wonderful jobs they have done, without which my thesis would be impossible.

Lastly, I would like to thank my family and my wife Bing for their unconditional love and support through the years!

This research was supported by DARPA and the Army Research Laboratory Collaborative Technology Alliance.



# Table of Contents

Abstract .....	I
Acknowledgements .....	III
Table of Contents .....	V
List of Figures .....	XI
Nomenclature .....	XXI
<i>Chapter 1</i> Introduction .....	1
1.1 The Micro-Engine Project .....	1
1.1.1 The Idea Behind Micro-Engines .....	1
1.1.2 Challenges Developing Micro-Engines.....	5
1.1.3 Micro-Devices Under Development .....	7
1.2 Micro-Bearing Systems .....	9
1.2.1 Micro-Bearing System Requirements .....	10
1.2.2 The Choice of Micro-Bearing Systems .....	11
1.2.3 Previous Work and Other Research .....	13
1.2.4 Nature of the Issues .....	16
1.3 Research Objectives .....	19
1.4 Structure of the Thesis.....	19
<i>Chapter 2</i> Basic Fluid and Rotordynamic Models.....	23
2.1 Fluid Dynamic Model of the Bearing Force .....	23
2.1.1 Assumptions and Approximations .....	24
2.1.2 Hydrostatic Forces.....	26
2.1.3 Hydrodynamic Force .....	31
2.1.4 Damping Force .....	36
2.2 Basic Rotordynamics.....	38
2.2.1 Rotordynamic Equations .....	39
2.2.2 Dynamic Response Curve of the Rotor-Bearing System .....	42
2.2.3 Distance to Contact .....	44
2.2.4 Nonlinear Response of the Rotor-Bearing System.....	46
2.2.5 Journal Bearing Operating Protocol .....	47
2.3 Summary and Conclusions .....	49

<i>Chapter 3</i> Dynamic Behavior and Whirl Instability Limit of Isotropic Hydrostatic Micro-Journal-Bearing Systems .....	51
3.1 Isotropic Journal-Bearing Systems .....	52
3.2 Singular Behavior of Whirl Instability Limit.....	52
3.3 Whirl Instability Limit of Micro-Journal-Bearing System with Zero Unbalance .....	55
3.3.1 Whirl Ratio $\mathfrak{R}$ and Whirl Number $W$ .....	55
3.3.2 Forward and Backward Whirl.....	58
3.3.3 Simple Criterion for Whirl Instability and Design Implications .....	60
3.4 Effect of Unbalance on Whirl Instability Limit.....	62
3.5 Summary and Conclusions .....	65
<i>Chapter 4</i> Dynamic Behavior and Whirl Instability of Anisotropic Hydrostatic Micro-Gas-Journal-Bearing Systems.....	67
4.1 Symmetry: Enemy of Stability.....	69
4.1.1 Anisotropic Bearing System Configuration: Part-Bearing System .....	69
4.1.2 Dynamic Response Curves of Anisotropic Bearing Systems.....	71
4.1.3 Whirl Instability Limit of Anisotropic Bearing Systems with Zero Unbalance .....	73
4.1.4 Stabilization Through Hydrostatic Stiffness Anisotropy .....	77
4.2 Numerical Simulation, Whirl Instability Limit for Systems with Unbalance and Sideload.....	79
4.2.1 Numerical Simulation of the Rotordynamics for Anisotropic Bearing Systems .....	80
4.2.2 Numerical Simulation of the Response Curve and the Stability Boundary for Anisotropic Bearing Systems.....	82
4.2.3 Effect of Sideload on Whirl Instability Boundary in Anisotropic Bearing Systems .....	85
4.3 Implementations of Anisotropy .....	87
4.3.1 Anisotropy in Axisymmetric Journal-Bearing with Sideload.....	88
4.3.2 Anisotropy in Part-Bearing Systems.....	89
4.3.3 Anisotropy in Micro-Turbo-Charger Devices .....	90
4.4 Summary and Conclusions .....	95
<i>Chapter 5</i> Experimental Assessment of Models.....	97
5.1 Static Flow Tests.....	97
5.2 Natural Frequencies .....	100
5.2.1 Natural Frequency Measurement.....	100

5.2.2 Natural Frequencies Measured for Isotropic Journal-Bearing System ..	103
5.2.3 Natural Frequencies Measured for Anisotropic Journal-Bearing System .....	103
5.3 Distance to Contact .....	104
5.3.1 Experimentally Determined Threshold in Distance to Contact.....	105
5.3.2 Application of the Threshold in Distance to Contact.....	107
5.4 Experimental Assessment of Stability Boundary Predictions.....	108
5.4.1 Stability Boundary in Isotropic Journal-Bearing Systems .....	109
5.4.2 Stability Boundary in Anisotropic Journal-Bearing Systems.....	113
5.5 Summary and Conclusions.....	113
<i>Chapter 6 Multi-Degree-of-Freedom Systems.....</i>	<i>115</i>
6.1 Experimental Evidence of Coupling Phenomena.....	116
6.2 Sources of Coupling Effect .....	119
6.2.1 Coupling Induced by Feed Plena.....	119
6.2.2 Coupling Induced by Thrust Bearings and Seals .....	122
6.3 Four-Degree-of-Freedom Model with Coupling Effect .....	125
6.3.1 Linearized Equations and Coupling Coefficients.....	125
6.3.2 Tilting stiffness and Damping from Thrust Bearings.....	128
6.3.3 Predictions Using the Four-Degree-of-Freedom Model and Comparisons with Experimental Observations .....	129
6.3.4 Effects of Axial Position and Seal Clearance on Coupling and Stability Boundary .....	137
6.4 Five-Degree-Of-Freedom Numerical Model.....	141
6.5 Summary and Conclusions.....	144
<i>Chapter 7 Centrally-Fed Micro-Hydrostatic Gas Journal Bearings.....</i>	<i>147</i>
7.1 Centrally-Fed Micro-Journal-Bearing Configuration .....	148
7.2 Fluid Models for Centrally-Fed Micro-Journal Bearings.....	149
7.2.1 Hydrostatic Flow and Forces.....	149
7.2.2 Hydrodynamic Force.....	153
7.2.3 Damping Force .....	157
7.3 Dynamic Behavior of Centrally-Fed Micro-Journal-Bearing Systems .....	158
7.3.1 Natural Frequencies.....	159
7.3.2 Distance to Contact .....	159
7.3.3 Stability Boundary.....	161
7.3.4 Design Guidelines for Centrally-Fed Micro-Journal-Bearing Systems Used in Micro-Bearing-Rig Devices.....	164

7.4 Summary and Conclusions .....	166
<i>Chapter 8</i> Rotordynamic Effect of Journal Bearing Profile Variations .....	169
8.1 Three Typical Journal Bearing Profiles .....	170
8.2 Fluid Model for Journal Bearings with Profile Variations .....	170
8.2.1 Flows in Journal Bearings of General Profile.....	171
8.2.2 Bearing Flow and Bearing Forces in Journal Bearings with Tapered Profiles .....	174
8.2.3 Bearing Flow and Bearing Forces in Journal Bearings with Bow-Shaped Profiles .....	179
8.3 Rotordynamic Behavior in Non-Straight-Wall Journal-Bearing Systems.....	183
8.3.1 Stability Boundary of Journal Bearings with Profile Variations .....	183
8.3.2 Nonlinear and Positive Hydrostatic Stiffness with Tapered Journal Bearings .....	186
8.3.3 Distance to Contact in Non-Straight-Wall Journal-Bearing Systems...	189
8.4 Summary and Conclusions .....	191
<i>Chapter 9</i> Nonlinear Dynamics of Micro-Journal-Bearing Systems.....	193
9.1 Nonlinearity in Hydrostatic Force .....	194
9.2 Nonlinear Resonance in Isotropic Systems.....	196
9.3 Nonlinear Resonance in Anisotropic Systems .....	203
9.3.1 Secondary Resonance near $\Omega_x/3$ or $\Omega_y/3$ .....	207
9.3.2 Secondary Resonance near $(\Omega_x - \Omega_y)/2$ .....	209
9.3.3 Secondary Resonance near $(\Omega_x + \Omega_y)/2$ .....	210
9.3.4 Secondary Resonance near $3\Omega_x$ or $3\Omega_y$ .....	213
9.3.5 Secondary Resonance near $2\Omega_x - \Omega_y$ and $2\Omega_y - \Omega_x$ .....	216
9.3.6 Secondary Resonance near $2\Omega_x + \Omega_y$ and $2\Omega_y + \Omega_x$ .....	217
9.3.7 Experimental Observations of Nonlinear Resonances.....	221
9.4 Summary and Conclusions .....	222
<i>Chapter 10</i> Hydrostatic Thrust-Bearing Systems .....	225
10.1 Circular Hydrostatic Thrust Bearings .....	226
10.1.1 Flow Field in Hydrostatic Thrust Bearings.....	226
10.1.2 Model Assessment .....	228
10.1.3 Effect of Rotor Rotation.....	233
10.2 Annular Hydrostatic Thrust Bearing.....	237
10.3 Tilting stiffness .....	239
10.4 Summary and Conclusions .....	242
<i>Chapter 11</i> Journal-Bearing System Design for Self-Sustained Micro-Engine .....	243

---

11.1 Design Requirements for Micro-Journal-Bearing Systems Used in Self-Sustained Micro-Engines .....	244
11.2 Dual-Bearing System without Wafer Misalignment .....	247
11.3 Dual Bearing System with Wafer Misalignment .....	251
11.3.1 Rotor Camming Motion Due to Wafer Misalignment .....	251
11.3.2 Parametric Description of Rotor Imperfection .....	252
11.3.3 Design Guidelines for Dual-Bearing Systems with Most-Likely Imperfection .....	254
11.3.4 Design Guidelines for Dual-Bearing Systems with Worst-Case Imperfection .....	256
11.4 Suggested Designs and Conclusions .....	260
<i>Chapter 12</i> Summary, Conclusions, and Suggestions for Future Work .....	263
12.1 Summary and Conclusions .....	263
12.1.1 Basic Fluid and Rotordynamic Models .....	263
12.1.2 Stability Boundary of the Micro-Hydrostatic Gas Journal-Bearing System .....	264
12.1.3 Barriers to High Speeds .....	266
12.1.4 Hydrostatic Gas Thrust Bearings: Axial and Tilting stiffness .....	269
12.1.5 Design Recommendations for the Journal-Bearing Systems Used in the Self-Sustained Micro-Engine .....	269
12.2 Suggested Future Research Work .....	270
12.3 Contributions of Thesis .....	271
Appendix A .....	273
Appendix B .....	275
Appendix C .....	279
Reference .....	281





# List of Figures

Figure 1-1: Specific Power vs. Specific Energy [5]; the strips show the micro-engine capacities with the top points representing zero fuel mass (courtesy of S. Jacobson).	3
Figure 1-2: Mass production of the micro-engine devices: Over 40 devices on one 6-inch wafer [31].	4
Figure 1-3: Cross section of MIT micro-engine [2].	5
Figure 1-4: DRIE etched 4mm-diameter turbine, with blade height of 150um (adopted from [2]).	6
Figure 1-5: Cross section of the MIT micro-turbo-charger (adopted from [6]).	8
Figure 1-6: Cross section of the MIT micro-bearing-rig or micro-electrostatic-motor/generator (adopted from [8]).	8
Figure 1-7: Sketch of micro-turbo-pump cross section (adopted from [13]).	9
Figure 1-8: Hydrodynamic and hydrostatic gas bearings (adopted from [8]).	13
Figure 1-9: Minimum eccentricity ratio contour for a bearing with $L/D=0.075$ (adopted from [19]).	14
Figure 1-10: Sample SEM picture of a journal bearing.	17
Figure 1-11: Micro-bearing yields an $L/D$ one order of magnitude smaller and a surface speed of one order magnitude larger than other bearing technologies (courtesy of Z. Spakovszky).	18
Figure 1-12: Rotordynamic and fluid models of the micro-bearing system are the core of the research.	19
Figure 2-1: Three-dimensional flow in journal bearings.	25
Figure 2-2: Axial flow in the journal bearing.	26
Figure 2-3: Cross section of the journal bearing and sketch of the pressure distribution along the bearing.	28
Figure 2-4: Velocity contours at the journal bearing entrance (left), and pressure along the journal bearing (right) calculated by 2-D Fluent.	29
Figure 2-5: Mass flow rate (left) and restoring forces (right) calculated by the incompressible model compared with 3-D compressible CFD results.	30
Figure 2-6: Journal bearing mass flow rate and hydrostatic force as functions of rotor eccentricity.	30
Figure 2-7: Hydrodynamic flow field.	31

Figure 2-8: Hydrodynamic pressure distribution in the circumferential direction. ....	33
Figure 2-9: Comparison between the analytical solution (incompressible, the dashed lines) and the numerical solution (compressible Reynolds equation, the solid lines) of hydrodynamic force in micro-bearing with $L/D=0.075$ (adopted from [19]). ....	33
Figure 2-10: Damping flow induced by the rotor translational motion. ....	36
Figure 2-11: Rotor translational velocity and appropriate coordinate system. ....	38
Figure 2-12: Coordinate system used to describe the rotor motion (sketch not to scale). ....	39
Figure 2-13: Geometric and mass centers, and definition of eccentricity and unbalance in the journal-bearing system. ....	39
Figure 2-14: Typical rotordynamic response curve of the rotor-bearing system. ....	43
Figure 2-15: Positions of geometric and mass centers of the rotor-bearing system at the natural frequency. ....	44
Figure 2-16: Peak function. ....	45
Figure 2-17: Calculated response curves of the rotor-bearing system for the micro Turbo-Charger device with $h=15\mu\text{m}$ , $L=300\mu\text{m}$ , $R=3\text{mm}$ , $m=70\text{mg}$ and $\Delta p=0.25\text{psig}$ . ....	46
Figure 2-18: Response curve with constant hydrostatic stiffness only (left); with constant damping and constant hydrodynamic stiffness (right). ....	47
Figure 2-19: Hysteresis phenomena in the rotor response curve. ....	47
Figure 2-20: Response curves at different bearing pressure difference $\Delta p$ : distance to contact decreases, while stability boundary increases with $\Delta p$ . ....	48
Figure 2-21: Operating protocol for micro-journal-bearing systems. ....	49
Figure 3-1: Sketch of isotropic journal bearing. ....	52
Figure 3-2: Singular behavior of the whirl instability limit of an isotropic micro-journal-bearing system. ....	53
Figure 3-3: Natural frequency vs. clearance. ....	53
Figure 3-4: Whirl ratio vs. clearance. ....	54
Figure 3-5: Hydrodynamic forces for micro-journal bearings with $W<1$ (left) and $W>1$ (right). ....	58
Figure 3-6: High whirl ratio and whirl instability limit for micro-journal bearings with whirl number $W$ of about 1. ....	61
Figure 3-7: Whirl ratio vs. whirl number for various levels of rotor unbalance. ....	65
Figure 4-1: Stability boundary as a function of bearing clearance for typical levels of rotor unbalance. ....	67
Figure 4-2: Elimination of singular behavior in stability boundary and relieved fabrication tolerance requirements due to hydrostatic stiffness anisotropy. ....	68
Figure 4-3: Sketch of the part-bearing system. ....	70

Figure 4-4: Hydrostatic stiffness of the part-bearing system compared with the isotropic case. ....	70
Figure 4-5: Amplitudes, phases, and the rotor precession orbits as functions of the rotational speed.....	72
Figure 4-6: Stability boundary for the anisotropic bearing system with zero unbalance, compared with the stability boundary in the isotropic bearing system. ....	77
Figure 4-7: Stable operating range extension using anisotropic bearing configuration....	77
Figure 4-8: Hydrostatic and hydrodynamic forces in the anisotropic journal-bearing system. ....	78
Figure 4-9: Flowchart of the numerical simulation.....	80
Figure 4-10: Interface of the numerical simulation program. ....	81
Figure 4-11: Sample orbits simulated for the bearing shown in Figure 4-10.....	82
Figure 4-12: Response curves for the micro-journal-bearing system in Figure 4-10, calculated using numerical simulations (left), compared with response curves calculated by linear analysis (right).....	83
Figure 4-13: Simulated rotor precession orbits in the anisotropic bearing system (9.2KRPM and 15.7KRPM are the natural frequencies in X and Y directions). ....	83
Figure 4-14: System stability boundary as a function of bearing clearance with different rotor unbalance levels.....	84
Figure 4-15: Spinning rotor shifted from its centered position due to sideload.....	85
Figure 4-16: Effect of rotor sideload on journal bearing stability boundary for the anisotropic bearing system. ....	86
Figure 4-17: Hydrodynamic stiffness and hydrostatic stiffness anisotropy as functions of rotor eccentricity.....	87
Figure 4-18: Hydrostatic stiffness anisotropy increases with rotor eccentricity due to sideload in axisymmetric journal-bearing systems. ....	88
Figure 4-19: Stability boundary of axisymmetric journal-bearing systems as a function of rotor eccentricity due to sideload. ....	88
Figure 4-20: Four-plenum configuration for the part-bearing system [7].....	90
Figure 4-21: Isotropic design of micro-turbo-charger journal bearings.....	91
Figure 4-22: Introduction of hydrostatic stiffness anisotropy by blocking four "coat hangers". ....	92
Figure 4-23: Pressure distribution in the plenum with four "coat hangers" blocked. ....	92
Figure 4-24: Natural frequencies of the micro-turbo-charger device with four "coat hangers" blocked. ....	93
Figure 4-25: New design of single journal bearing for micro-turbo-charger device [31]. 93	

Figure 4-26: Pressure distribution in the plenum for new design shown in Figure 4-25..	94
Figure 4-27: Natural frequencies of the four-plenum design (Figure 4-25) for micro-turbo-charger devices.....	94
Figure 5-1: SEM picture of a typical journal bearing trench.....	98
Figure 5-2: Flow rate calculated by the model compared with experimental measurement [32] for a micro-turbo-charger device.....	99
Figure 5-3: Experimental setup [30] to measure the natural frequencies of the journal-bearing systems.....	100
Figure 5-4: Rotor response curve measurement using an optical fiber (courtesy of C.J. Teo).....	101
Figure 5-5: Drop of pressure difference across the journal bearing at the natural frequency (experimental data [30]).....	102
Figure 5-6: Natural frequency prediction compared with experimental measurements [6] for a micro-turbo-charger device.....	103
Figure 5-7: Natural frequency predictions compared with the experimental measurements [7] for the micro-bearing-rig device.....	104
Figure 5-8: Required distance to contact to invert the rotor: larger than $1.2\mu\text{m}$ for micro-bearing rig #3-6 (experimental data [30]).....	106
Figure 5-9: Comparison of the damping ratios for the two devices: micro-bearing rig #3-6 (solid line) and micro-generator #1 (dashed line).....	107
Figure 5-10: Normalized distance to contact calculated for the micro-turbo-charger device #C8, compared with estimated threshold of 0.09.....	108
Figure 5-11: Experimental spin test: high whirl ratio achieved in micro-bearing device [30].....	110
Figure 5-12: Stability boundary predictions for the part-bearing system compared with the highest speeds achieved in micro-bearing rig builds 2 and 3.....	113
Figure 6-1: Multiple degrees of freedom of the rotor.....	115
Figure 6-2: Flow rates through both thrust bearings decreased with the pressure fed to the journal bearing, measured in the dual-bearing micro-turbo-charger device (experimental data from [31]).....	117
Figure 6-3: Frequency of the conical motions as a function of $\Delta p$ (experimental data from [31]), compared with the model prediction of the journal bearing natural frequency.....	118
Figure 6-4: Change in plenum clearance (height) due to rotor tilt.....	119
Figure 6-5: Pressure distribution in the plenum due to rotor tilt.....	119
Figure 6-6: Radial force induced by rotor tilt.....	120

Figure 6-7: Torques from the plenum induced by rotor tilt. ....	120
Figure 6-8: Plenum pressure distribution due to rotor radial displacement. ....	121
Figure 6-9: Torques induced by rotor radial displacement. ....	122
Figure 6-10: Sketch of the thrust bearings with a tilted rotor (not to scale).....	122
Figure 6-11: Single-compressor bearing configuration of micro-turbo-charger device (note seal in feed plenum). ....	124
Figure 6-12: Nondimensional Pressure distribution in the tilted thrust bearing due to rotor pumping action ( $\alpha_y=0.001$ rad, $\omega=50,000$ rad/s, $R=1$ mm). ....	128
Figure 6-13: Maximum real parts of the eigenvalues as functions of the rotational speed for the micro-turbo-charger device L4-2, using both two-degree-of-freedom and four-degree-of-freedom models. ....	130
Figure 6-14: Enlarged view of Figure 6-13.....	131
Figure 6-15: Maximum real parts of the eigenvalues as functions of rotor speed with larger seal clearance in the device L4-2. ....	132
Figure 6-16: Maximum real part of the eigenvalues as a function of the rotational speed for the dual-bearing systems of Table 6-6.....	134
Figure 6-17: Stability boundary of the coupled dual-bearing system decreases with $\Delta p$ , predicted by the four-degree-of-freedom model. ....	135
Figure 6-18: Stability boundary of the coupled dual-bearing system increases with the static tilting stiffness.....	135
Figure 6-19: Stability boundary of device L4-2 changes with the rotor axial position...	138
Figure 6-20: Enhanced stability boundary of micro-turbo-charger devices due to reduced coupling effects in the new journal-bearing system design. ....	139
Figure 6-21: Stability boundary in the micro-bearing-rig devices influenced by coupling with different rotor axial locations. ....	140
Figure 6-22: Part-bearing system becomes unstable with smaller seal clearance due to umbrella deformation of the rotor disk.....	140
Figure 6-23: Axial force $\delta F_z$ from the plenum as a function of rotor radial displacement and tilting angles. ....	141
Figure 6-24: Stability boundary of the micro-turbo-charger device L4-2 predicted by the nonlinear five-degree-of-freedom numerical simulation, compared with that predicted by the linear four-degree-of-freedom model. ....	142
Figure 6-25: Simulated rotor vibration in z direction with finite unbalances for micro- turbo-charger device L4-2, at rotor speed of 400KRPM.....	143
Figure 6-26: Simulated orbits of the rotor radial (left) and conical (right) motions in micro-turbo-charger device L4-2 at rotor speed of 400KRPM. ....	144

Figure 7-1: Centrally-fed micro-journal bearing with hydrostatic stiffness anisotropy.	148
Figure 7-2: Cross section of the centrally-fed micro-journal bearing with a sketch of the pressure distribution along the bearing.	149
Figure 7-3: Pressure distribution in the centrally-fed micro-journal-bearing system with $L_b=400\mu\text{m}$ , $h_b=15\mu\text{m}$ , $L_f=300\mu\text{m}$ , $h_f=30\mu\text{m}$ , $\Delta p=5\text{psig}$ , by 2D CFD (Fluent).	151
Figure 7-4: Calculations by the model compared with CFD: flow rate (left) and force (right) for the centrally-fed micro-journal bearings.	152
Figure 7-5: Flow rates (left) and natural frequencies (right) of the centrally-fed micro-journal-bearing system (CFJB) compared with those of the axially-fed micro-journal-bearing system (AFJB).	153
Figure 7-6: Decrease of bearing pressure due to the leakage flow.	154
Figure 7-7: Hydrodynamic forces due to rotor pumping action in the centrally-fed micro-journal-bearing system compared with the axially-fed micro-journal-bearing system.	155
Figure 7-8: Hydrodynamic stiffness due to rotor pumping action in the centrally-fed micro-journal bearing decreases with flow resistance ratio $\Phi$ .	157
Figure 7-9: Natural frequencies increase with flow resistance ratio $\Phi$ in the centrally-fed micro-journal-bearing system.	159
Figure 7-10: Normalized distance to contact calculated for the centrally-fed micro-journal bearing, compared with estimated threshold.	160
Figure 7-11: Normalized distance to contact for the centrally-fed micro-journal-bearing system with the bearing length $L_b=600\mu\text{m}$ .	161
Figure 7-12: Whirl ratio $\mathfrak{R}$ (left) and stability boundary (right) of the isotropic centrally-fed micro-journal-bearing system.	162
Figure 7-13: Stability boundary with bearing length of $600\mu\text{m}$ is much lower than that with bearing length of $300\mu\text{m}$ in the centrally-fed micro-journal-bearing system (CFJB).	163
Figure 7-14: Stability boundary of the anisotropic centrally-fed micro-journal-bearing system with bearing length of $600\mu\text{m}$ .	164
Figure 7-15: Design chart for the anisotropic centrally-fed micro-journal-bearing system with bearing length of $600\mu\text{m}$ .	165
Figure 8-1: SEM picture of a journal bearing fabricated to be straight and parallel with clearance of $15\mu\text{m}$ .	169
Figure 8-2: Three typical profiles of fabricated journal bearings.	170
Figure 8-3: Bearing clearance $h$ varies along $z$ in a non-straight-wall journal bearing (not to scale).	171

Figure 8-4: Bearing clearance varies with both $z$ and $\theta$ when rotor is off-centered with non-straight-wall bearing (not to scale).....	171
Figure 8-5: Sketch of a tapered journal bearing (not to scale). ....	175
Figure 8-6: Hydrostatic flow rate and force in tapered journal bearings with different levels of profile variation. ....	176
Figure 8-7: Ratios of hydrodynamic stiffness and damping coefficient in tapered bearings to those in straight-wall bearings. ....	178
Figure 8-8: Sketch of bow-shaped journal bearing (not to scale). ....	179
Figure 8-9: Hydrostatic flow rate and force in bow-shaped journal bearings.....	180
Figure 8-10: Ratios of hydrodynamic stiffness and damping coefficient in bow-shaped bearings to those in straight-wall bearings. ....	182
Figure 8-11: Whirl ratios for tapered journal bearings.....	184
Figure 8-12: Whirl ratio for the bow-shaped journal bearing. ....	184
Figure 8-13: Stability boundary in the anisotropic non-straight-wall journal-bearing system.....	185
Figure 8-14: Hydrostatic forces as functions of rotor eccentricity for journal bearings with different bearing profiles. ....	186
Figure 8-15: Hydrostatic stiffness as a function of rotor eccentricity for journal bearings with different bearing profiles.....	187
Figure 8-16: Pressure along the negatively tapered journal bearing, calculated by CFD. ....	188
Figure 8-17: Positive hydrostatic stiffness in the negatively tapered journal bearing changes with the pressure difference across the bearing $\Delta p$ , the bearing profile variation $\delta$ , and the rotor eccentricity $\epsilon$ . ....	189
Figure 8-18: Rotor response curves in journal bearings with various profiles. ....	190
Figure 9-1: Multiple resonances observed in the experiment for the micro-bearing-rig device with part-bearing configuration [30].....	193
Figure 9-2: Third-order subharmonic resonance with fixed orbit (sketch). ....	201
Figure 9-3: Rotating third-order subharmonic orbit (sketch). ....	202
Figure 9-4: Numerically simulated orbits for the nonlinear isotropic system (Equation (9-10)) at different rotational speeds: $\omega=3.3$ (left) and $\omega=3.4$ (right). ....	203
Figure 9-5: Third-order superharmonic resonance in $x$ direction (sketch). ....	208
Figure 9-6: Third-order superharmonic resonance in $y$ direction (sketch). ....	209
Figure 9-7: Simulated orbits for the anisotropic system at the rotor speed near the secondary resonance $(\Omega_x+\Omega_y)/2$ : $\omega=1.5$ and $1.8$ (left), $\omega=1.6$ (right).....	212
Figure 9-8: Third-order subharmonic resonance in $x$ direction (sketch).....	214



Figure 9-9: Third-order subharmonic resonance in y direction (sketch). .....	216
Figure 9-10: Simulated orbits for the anisotropic system at speeds near the secondary resonance $2\Omega_x + \Omega_y$ : $\omega=5.0$ (left) and $\omega=5.1$ (right). .....	219
Figure 9-11: Simulated orbits for the anisotropic system at speeds near the secondary resonance $\Omega_x + 2\Omega_y$ : $\omega=4.1$ (left) and $\omega=4.2$ (right). .....	220
Figure 9-12: Experimental data showing the secondary resonance at speed of $3\Omega_y$ [30]. .....	221
Figure 9-13: Experimental data showing the secondary resonances of $(\Omega_x + \Omega_y)/2$ and $\Omega_x/3$ [30]. .....	221
Figure 10-1: Sketch and dimensions of the structure of a typical thrust bearing used in a micro-bearing rig (not to scale). .....	226
Figure 10-2: Image Method for the electrostatic field. .....	228
Figure 10-3: The thrust bearing grids used in 3-D Fluent calculations. .....	228
Figure 10-4: Pressure distribution normalized by the inlet pressure in the thrust bearing with the mass flow rate of 0.02mg/s per nozzle, calculated by 3-D Fluent. ....	229
Figure 10-5: Temperatures in the thrust bearing gap with bearing wall temperature of 300K, by 3-D Fluent. ....	229
Figure 10-6: Pressure normalized by the inlet pressure along L1 and L2, calculated by the Image Method and 3-D Fluent. ....	230
Figure 10-7: Thrust force as a function of the mass flow rate per nozzle, calculated by the Image Method and 3-D Fluent. ....	230
Figure 10-8: Curve-fitting to find the loss coefficients at the corner. ....	231
Figure 10-9: Model predictions with different supply pressures and bearing clearances, compared with 3-D Fluent results: the mass flow rate (left) and the thrust force (right). .....	232
Figure 10-10: Static flow tests (experimental data from [6]) in the thrust bearings, compared with the model predictions. ....	232
Figure 10-11: Natural frequency prediction by the model for the hydrostatic thrust bearing used in the micro-bearing-rig devices. ....	233
Figure 10-12: Pressure distribution in the thrust bearing (left) and the thrust force (right) due to the centrifugal force, without flows through the nozzles, calculated by both the model and 3-D Fluent. ....	236
Figure 10-13: Pressure distribution in the thrust bearing with rotor speed of 1.9 MRPM and supply pressure of 87 psig, calculated by 3-D Fluent. ....	236
Figure 10-14: Structural sketch (left, not to scale) of the micro-hydrostatic annular thrust bearing and the pressure distribution in the bearing calculated by 3-D Fluent. ....	238

Figure 10-15: Pressure distributions normalized by the inlet pressure along symmetry lines L1 and L2 in the micro-hydrostatic annular thrust bearing with pump pressures 0 (left) and 29 psig (right), compared with the CFD results. ....	238
Figure 10-16: Mass flow rate per nozzle and thrust force calculated by the model for the annular thrust bearing, compared with the CFD results. ....	239
Figure 10-17: Tilting stiffness (left) and pressure field (right, 70 psig supply and $2 \times 10^{-4}$ rad tilting angle) in the thrust bearings of the micro-turbo-charger device by the Image Method. ....	241
Figure 11-1: Sketch of the self-sustained micro-engine rotor (thrust bearing pads are not shown and the sketch is not to scale). ....	244
Figure 11-2: Implementation of the anisotropic journal bearings in the self-sustained micro-engine devices (not to scale). ....	245
Figure 11-3: Distance to contact and stability boundary as functions of bearing clearances for perfectly aligned dual-bearing systems. ....	248
Figure 11-4: Rotor unbalance and bearing sideload $\delta p$ reduce the stability boundary. ...	250
Figure 11-5: Rotor camming motion due to misalignment between the two journal bearings in a dual-bearing system. ....	251
Figure 11-6: Four parameters required to describe the rotor imperfection in dual-bearing systems with wafer misalignment. ....	252
Figure 11-7: Mass center of the rotor lies in a circle located between the geometric centers of the turbine and compressor disks. ....	253
Figure 11-8: Mass center distribution in the rotor frame. ....	254
Figure 11-9: Distance to contact and stability boundary as functions of bearing clearances for dual-bearing systems with a wafer misalignment of $4 \mu\text{m}$ and $r=0.5 \mu\text{m}$ . ....	255
Figure 11-10: Distance to contact (at $\Delta p$ of 0.2 psig) and stability boundary as functions of bearing clearances for dual-bearing systems with a wafer misalignment of $4 \mu\text{m}$ and $r=1 \mu\text{m}$ . ....	256
Figure 11-11: Distance to contact (at $\Delta p$ of 0.1 psig) and stability boundary as functions of bearing clearances for dual-bearing systems with a wafer misalignment of $6 \mu\text{m}$ and $r=1 \mu\text{m}$ . ....	257
Figure 11-12: Inverting the rotor with the single-compressor bearing at a pressure difference across the journal bearings $\Delta p$ of 0.2 psig. ....	258
Figure 11-13: Distance to contact (at $\Delta p$ of 0.2 psig with the single-compressor-bearing, and at $\Delta p$ of 0.1 psig with the dual-bearing) and stability boundary as functions of bearing clearances for the dual-bearing systems with a wafer misalignment of $6 \mu\text{m}$ and $r=1 \mu\text{m}$ . ....	259

Figure 11-14: Mass flow rate through the bearing system under normal operating conditions, normalized by the mass flow rate through the turbine. .... 260

Figure B-1: Circular boundary condition can be simulated by an image point sink. .... 276

Figure C-1: Arrangement of the series of image points..... 279

# Nomenclature

$a$	rotor static unbalance
$\alpha$	circumferential extent of feed plena
$C$	damping
$D$	bearing diameter
$K$	stiffness
$k$	intrinsic hydrodynamic stiffness
$h$	bearing clearance
$L$	bearing length
$R$	rotor radius
$\mathfrak{R}$	whirl ratio
$p, P$	pressure in journal, thrust bearings
$F$	force
$T$	torque
$q$	flow rate in bearing
$\gamma$	loss coefficient
$\phi$	rotor dynamic unbalance
$\mu$	viscosity
$\omega$	rotational speed
$\varepsilon$	rotor eccentricity
$\xi$	normalized rotor eccentricity (by bearing clearance)
$\Psi(\xi)$	peak function
$\Delta p$	pressure difference across the journal bearing
$\delta p$	pressure difference between opposite plena (side-load)
$\rho$	density
$\Delta$	bearing profile variation
$\delta$	normalized bearing profile variation (by the entrance clearance)
$P_a$	atmospheric pressure
$\rho_a$	density at standard conditions
$W$	whirl number
$m$	rotor mass
$\{\}^{hs}$	hydrostatic

$\{\}^{hd}$	hydrodynamic
$\{\}_p$	hydrodynamic $\{\}$ due to the rotor pumping action
$\{\}_v$	hydrodynamic $\{\}$ due to the viscous drag
$F^{dp}$	damping force
$u$	flow velocity in bearing
$v$	rotor velocity
$\Omega$	whirl frequency
$\Omega_N$	natural frequency
$\Omega_x$	natural frequency in $x$ direction
$\Omega_y$	natural frequency in $y$ direction
$\Omega_W$	stability boundary (threshold speed at onset of whirl instability)
$\Phi$	ratio of flow resistance through bearing to that through feed
$\{\}^{AF}$	axial-feed journal bearing
$\{\}^{CF}$	central-feed journal bearing
$\{\}_b$	bearing
$\{\}_f$	feed
$\{\}^{taper}$	taper-shaped bearing
$\{\}^{bow}$	bow-shaped bearing
$\dot{m}$	mass flow rate through thrust bearing nozzles
$L1, L2$	symmetric lines in the thrust bearings

BGC	bearing geometric center
RGC	rotor geometric center
MC	rotor mass center
SB	stability boundary
D2C	distance to contact
NF	natural frequency
AFJB	axial-feed journal bearing
CFJB	central-feed journal bearing
SSE	self-sustained engine
ATB	after thrust bearing
FTB	forward thrust bearing
CFD	computational fluid dynamics
TGC	turbine disk geometric center
CGC	compressor disk geometric center

## *Chapter 1*

# **Introduction**

In this introductory chapter, the micro-engine project at MIT is briefly described as the background of the thesis. Then, based on a discussion of the requirements of micro-bearing systems for micro-engine devices and the challenges of developing them, the objectives of the thesis are stated. The structure and the contributions of this thesis are summarized at the end of the chapter.

### ***1.1 The Micro-Engine Project***

In 1994, Epstein et al. [1] proposed the concept of Power MEMS (Micro-Electro-Mechanical Systems) and shirt-button-sized engines. This concept opened the door to a new field in MEMS and prompted groups around the world to begin working in that field. Now, a decade has passed, and there have been many papers published on this topic.

Among other the efforts to develop this revolutionary technology, the Gas Turbine Laboratory (GTL) at MIT has spent around ten years on the micro-engine project [2], developing high-speed rotating Power MEMS devices using silicon chip fabrication technologies.

#### **1.1.1 The Idea Behind Micro-Engines**

In this information era, portable electronic devices are becoming more and more popular. People use laptops, PDAs, GPS, and other media devices for both work and entertainment, and these portable devices are mainly powered by chemical batteries. The current battery technologies are well developed and seem sufficient for most devices.

However, in some areas, these chemical battery technologies are not at all satisfying. For example, the most advanced lithium batteries of normal size can only supply power to a laptop for about three hours. Obviously, this is not enough for travelers and people working in the field. Since the energy stored in a battery is proportional to the volume/weight of the battery, larger and heavier batteries are needed for longer battery life—yet a laptop battery already contributes around one third of the total weight and occupies a big portion of the total volume of the device.

With continuing advances in micro-electronics, the electric parts of a laptop can be made smaller, and thus laptops have the potential to be more portable. However, the large and heavy batteries have been the biggest obstacle to the development of smaller laptops, due to their low specific energy.

Power supplies used on the battlefield provide another example of the limitation of current battery technologies. Nowadays, soldiers in battle need to carry many electronic devices with them, such as GPS, night-vision goggles, a radio, and even a laptop. Since there are no electric outlets in the field, these devices have to be powered by chemical batteries. As mentioned above, the energy stored in the battery of unit weight (specific energy) is limited. Supplying power for these devices for several days requires a lot of batteries, which can be very heavy.

The fuel cells currently under development, which have a relatively high specific energy, could be another option to power these devices. But their power generated by unit weight is also limited; only about 10W/kg to 20W/kg, according to Figure 1-1. To generate 75 W for the laptop, about 4kg to 7.5kg of fuel cells are needed. This is obviously too heavy for a laptop, which normally weighs only about 2kg.

So far, therefore, there are two critical requirements for a future power supply for compact electric devices: high specific power (how much power the power supply can generate per unit weight), and high specific energy (how much energy the power supply can store per unit weight). The continuing advances in micro-electronics are making electronic devices for personal or commercial applications smaller and smaller, and these small devices demand power supplies whose specific energy and power exceed those of the best batteries available today.

The question is, what technology can solve this problem? The well-developed combustion engines used in aircraft and power plants can achieve a large specific power (700 to 900 W/kg) and specific energy (up to 2000 Wh/kg), despite their large volume (Figure 1-1). For comparison, the specific powers of chemical batteries are normally 10 to 600 W/kg, and some can be lower than 1 W/kg. As stated above, the most critical problem with chemical batteries is that the highest specific energy they can store is about 400 Wh/kg ( $\text{LiCl}_2$ ), much lower than that of combustion engines. On the other hand, although the specific energy stored by fuel cells can possibly be as high as that of combustion engines, their specific power is only about 10 to 20 W/kg, one order of magnitude lower than that of combustion engines. Therefore, the specific power and specific energy of combustion engines are unbeatable by either the most advanced chemical batteries or

the fuel cells under development. Another important point to be noted is that chemical batteries trade off specific power and specific energy to output high power, so the efficiency of batteries will rapidly drop due to their internal resistance. For the combustion engine, this trade-off is not as strong for a given engine type, because the efficiency of the combustion engine doesn't decrease as much with the power output.

When we consider all the merits of the combustion engine, another question arises: how can we use combustion engines in small electronic devices?

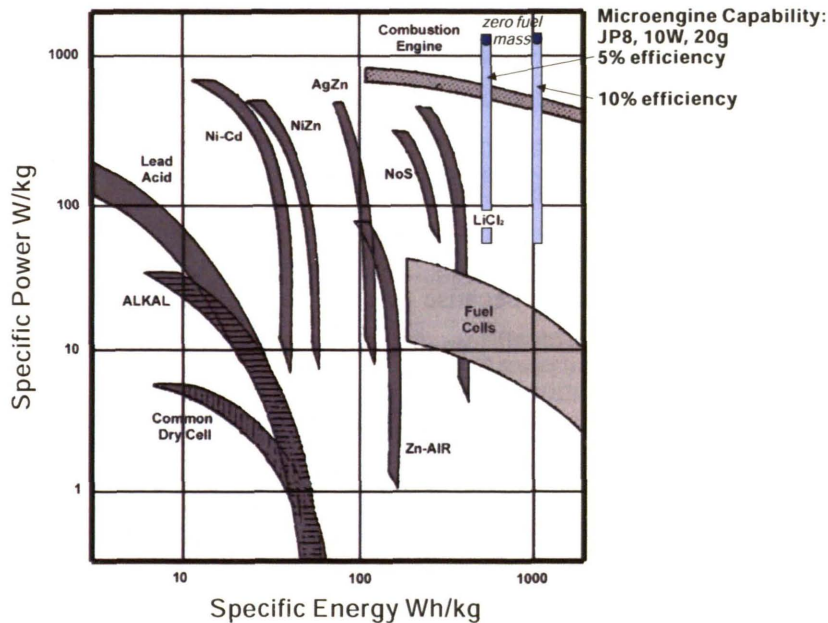


**Figure 1-1: Specific Power vs. Specific Energy [5]; the strips show the micro-engine capacities with the top points representing zero fuel mass (courtesy of S. Jacobson).**

A possible solution for the portable power source requirements is to develop micro-engines by scaling down combustion engines to millimeter size while keeping the specific power and energy. This is possible because of the well-known “cube-square law,” which implies that as the characteristic length of a device scales down, its volume (which is proportional to the cubic length) decreases much faster than its surface area (which is proportional to the square length). A large-scale engine with a 1-m-diameter air intake generates power on the order of 100 MW. Thus, when such a device is scaled to millimeter size, with airfoil spans measured in hundreds of microns rather than meters, this micro-engine would have about 1 millionth the airflow of its large counterpart and should produce about 1 millionth the power, 10-100 W. At the same time, the volume/weight of the micro-engine will be one billionth of those of the large engine. Therefore, in the ideal



case, the specific power of a micro-engine can be hundreds of times larger than that of a macro-engine, and even with only modest efficiency, it can still compete well with the most advanced batteries.

Another project undertaken at GTL, MIT that benefited from this cube-square law was the micro-rocket project, which was to develop a millimeter-size rocket engine. The weight of the rocket engine is proportional to its volume, while the thrust it produces is proportional to its throat area with the same chamber pressure, if everything else is kept equal. Therefore, in the ideal case, as the rocket engine system scales down by three orders of magnitude, the thrust-to-weight ratio of the engine will increase by the same orders of magnitude, making the rocket engine much more effective and reducing the launch cost significantly. Furthermore, the engine's small size and high thrust-to-weight ratio could enable very small launch vehicles.

Of course, the reality cannot be so optimistic (orders of magnitude better) and the actual scaling is not so dramatic because there are some side effects of scaling, such as relative larger viscous loss and heat transfer. However, even with these side effects taken into account, detailed calculations show that a millimeter-size engine would still have a thrust-to-weight ratio of about 100:1, compared to 10:1 for the best modern aircraft engines. The key point is that, with these Power MEMS technologies, macro-power (tens of watts) can be generated from micro-devices (millimeter-size) [3].

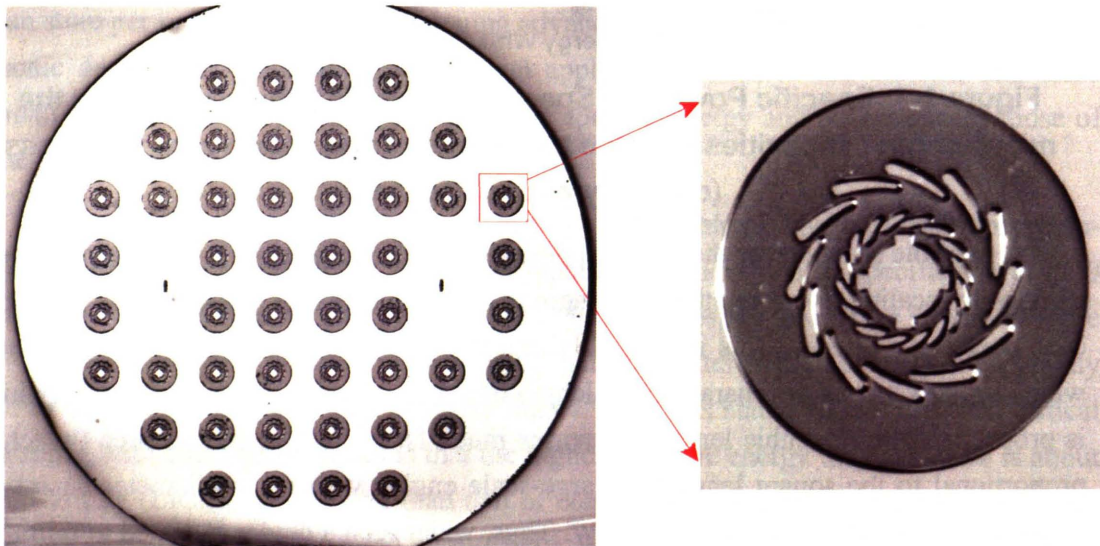


**Figure 1-2: Mass production of the micro-engine devices: Over 40 devices on one 6-inch wafer [31].**

Besides its high specific energy and power, another advantage of the micro-engine is the low cost due to mass production. Because these micro-engines are small in size and made of silicon, they can be built using fabrication technology similar to that of computer chips to achieve high accuracy and large quantity. A batch of devices can be manufactured in the same wafer at the same time as shown in Figure 1-2. Thus, the costs of fabrication can be significantly reduced.

As a summary, the micro-engine distinguishes itself from chemical batteries and large engines by its high specific power/energy and low fabrication cost. Just imagine a revolutionary future power sources that can power a laptop for much longer, is much smaller and lighter, and never needs to be recharged.

### 1.1.2 Challenges Developing Micro-Engines

The following sketch of a cross section of the micro-engine illustrates the basic components and concepts of the future micro-engine under development at MIT GTL:

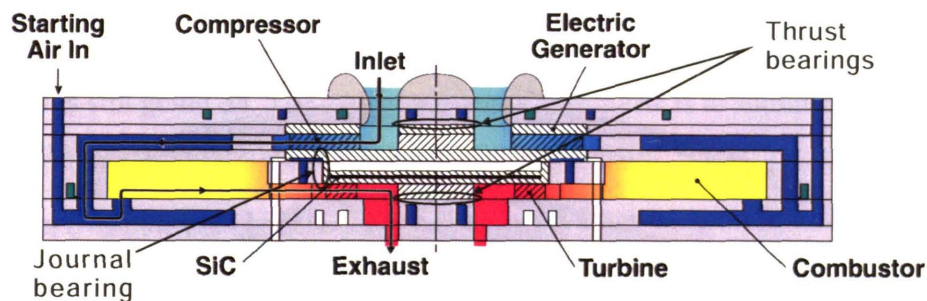


**Figure 1-3: Cross section of MIT micro-engine [2].**

The light shaded area in the center is the rotor, which is supported by a journal bearing and thrust bearings. The journal bearing is located on the circumferential periphery of the rotor, confining the rotor's radial movement. The thrust bearings are located up and down the sides of the rotor, confining the rotor's axial and conical movement. The rotor consists of a compressor and a turbine. The air is sucked in from an inlet, pressurized by the compressor. After it mixes with fuel in the flow path, it enters the combustor where the fuel is ignited. The hot pressurized exhaust of the combustor then goes through the turbine, driving the whole rotor to spin. The electric generator coated on the compressor shroud spins with the rotor and converts the mechanical energy into electric energy.

It can be seen that in order to sustain itself and then produce power, the micro-engine needs to have almost all the components of a large engine, such as compressor, turbine, generator, combustor and bearings, but in much smaller sizes. However, smaller

size doesn't necessarily mean easier. Although the thermodynamics of the micro-engine are the same as those of its large counterparts, the mechanics are much different due to fabrication constraints and scaling considerations.

Most of the components in this micro-system are several hundred microns high with vertical wall. The most suitable fabrication method is deep reactive ion etching (DRIE). Due to its intrinsic limits, DRIE can only produce planar structures (Figure 1-4), compared with the 3-D manufacture used for the macro-engines. This fabrication limitation can affect the performance of the micro-engine, especially for the blade flow path design. Another problem associated with this etch technology for the fabrication of the micro-engine devices is the quality control. Due to the imperfections of the etch machine, the variation of the etched dimensions can be from sub-microns to several microns [4]. Normally, this variation of several microns is almost negligible in the large-size engines and doesn't affect their performance much. However, because the typical dimensions of the micro-engine's critical features can be as small as several microns, this variation is too much for them.

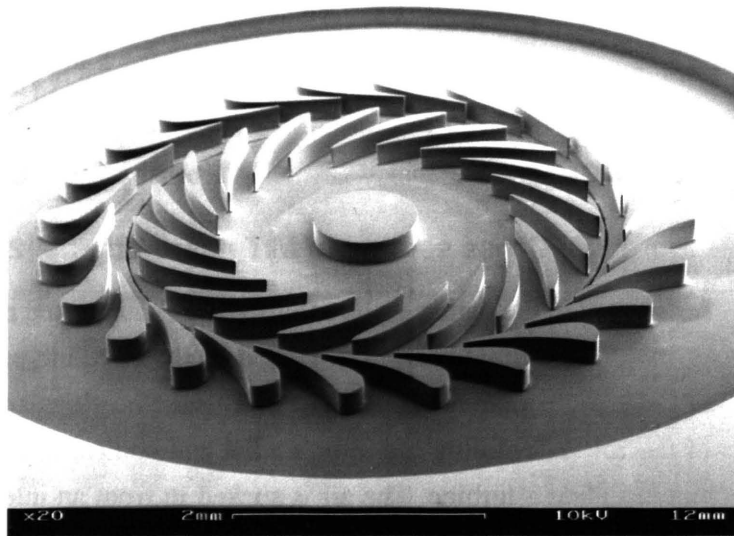


**Figure 1-4: DRIE etched 4mm-diameter turbine, with blade height of 150µm (adopted from [2]).**

As the size of the engine is scaled down by three orders of magnitude, the surface-force-to-body-force ratio increases by the same orders of magnitude due to the cube-square law. Therefore, the surface forces (such as viscous drag), which are normally negligible in the large-scale engines compared with the body forces (such as inertia), play an equally an important role in micro-engines. Furthermore, as the surface-to-volume ratio



dramatically increases, preventing heat transfer from the turbine to compressor (for higher efficiency) becomes much more difficult. The “cube-square law” makes the micro-engine totally different from its large counterparts. Thus, the knowledge and experiences obtained from the macro-engines for the last several decades cannot be directly applied to this millimeter-sized engine, and new theories need to be developed for the micro-engine systems. Both experimental and theoretical researches are needed to validate the concepts and search for feasible designs for this revolutionary micro-engine.

Since this complicated micro-system has just as many engineering challenges as large-scale conventional engine, about forty students, staff, and faculty from different disciplines have been involved in the research at MIT GTL over the past decade. One of these challenges is the micro-bearing system used in the micro-engine devices. In the micro-engine devices, the rotor also needs to be supported so that it can spin freely at the design speed without consuming too much power otherwise, the micro-engine cannot succeed. In the research, the micro-bearing systems are found to behave differently from their large-scale counterparts, and developing them also presents many challenges. The research on the bearing system at GTL started at the beginning of the MIT micro-engine project and is still going on. The major purpose of this thesis is to summarize the last five years research on this important and challenging component.

### **1.1.3 Micro-Devices Under Development**

To simplify the research process, the components of the engine, such as the combustor, compressor, turbine, bearing, and generator, are investigated individually at first and then combined. Since this thesis focuses on the bearing/rotor-dynamics of the micro-engine system, only the devices that have rotational part are described here. Through the following descriptions, one can see that these devices have essentially similar structures; hence, they share the same bearing technologies.

The micro-turbo-charger [6] has almost all the components of the micro-engine, except for the electric generator. The flow paths of the turbine and the compressor are separated as shown in Figure 1-5. With such a configuration, the rotor is driven by the external pressurized air going through the turbine, and thus the compressor can be tested without any combustion. Meanwhile, this design retains the capability to run the device as an engine by externally connecting the flow paths of the compressor and the turbine. In this device, the compressor’s outer radius is 4.1 mm and the turbine’s outer radius is 3 mm.

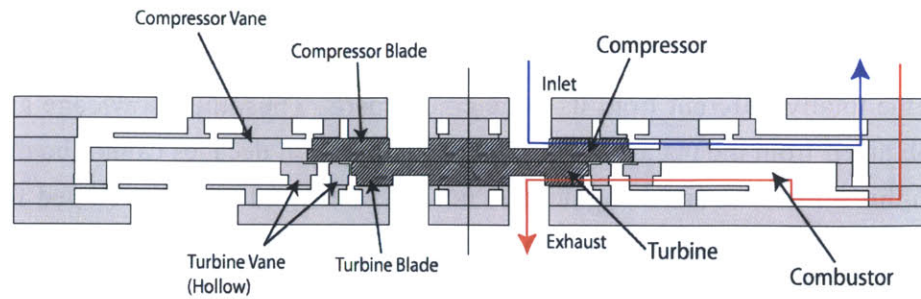


**Figure 1-5: Cross section of the MIT micro-turbo-charger (adopted from [6]).**

Micro-bearing-rig devices [8] and micro-electrostatic motor/generator devices [12] have similar structures as shown in Figure 1-6, except that the former do not have electrodes fabricated on the back of the rotor. As the external pressurized air goes through the turbine, the enthalpy of the air is transferred into the kinetic energy of the rotor. In the micro-electrostatic motor/generator, the electrodes integrated on the rotor run in either motor or generator mode, depending on the phase difference between the motions of rotor and the electrostatic field. The micro-bearing rig is designed and used purely to test the bearing technologies. The radius of its rotor is 2.1 mm.

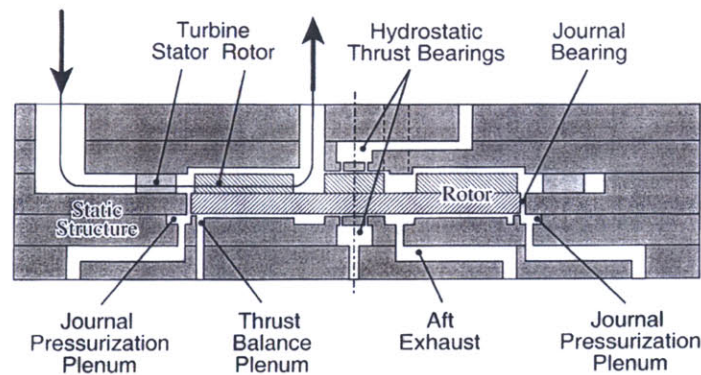


**Figure 1-6: Cross section of the MIT micro-bearing-rig or micro-electrostatic-motor/generator (adopted from [8]).**

Another device of interest is the micro-turbo-pump [13], which was developed for the micro-rocket project. As shown in Figure 1-7, the rotor is driven by the hot pressurized gas (which has collected energy from the exhaust of the micro-rocket) going through the turbine, and thus the liquid (oxidizer or fuel) is pressurized by the pump, which is located in the center area of the rotor. Since both the pump and the turbine are located on the same side of the rotor to simplify the fabrication process, annular thrust bearings are used in this device, which is located between the turbine blade row and the pump blade row. Meanwhile, due to its small clearance (about  $2\text{ }\mu\text{m}$ ), the forward thrust bearing also

acts as a seal to prevent the liquid from leaking from the pump to the turbine. The outer radius of the rotor in the micro-turbo-pump device was 3.1 mm.

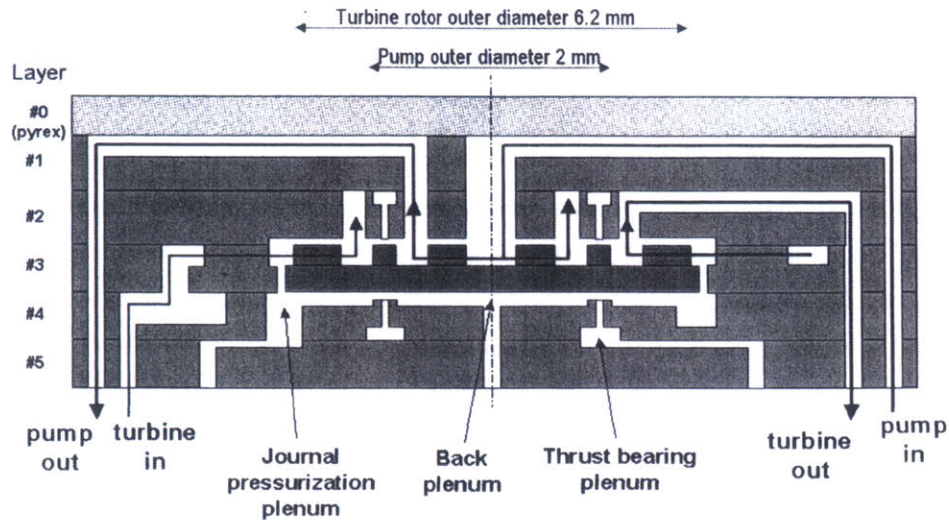


**Figure 1-7: Sketch of micro-turbo-pump cross section (adopted from [13]).**

Although all these devices were designed and fabricated to test different components/concepts of the micro-engine project, they all have rotational parts – the rotors. Thus the micro-bearing systems (both journal bearing and thrust bearings) must be used to support the rotors in the cavities of the devices, and they can share the same bearing technologies.

## 1.2 Micro-Bearing Systems

When the whole engine is scaled down by three orders of magnitude, the bearing systems used in the micro-engine system shrink by the same orders of magnitude. However, the challenges presented by the micro-bearing system are no less.

Looking at the cross sections of the devices (Figure 1-5-Figure 1-7) again, one can see that the micro-bearing systems are located on the outer peripheries of the rotors. In large-scale engines, the journal bearings are normally on the shaft. However, adding a shaft to the small rotor (2 to 3 mm radius) means another layer needs to be fabricated and bonded, making this complicated device even more difficult to fabricate because of the limitations of the fabrication technology. Therefore, at this stage, all the micro-devices are designed without shafts, and the journal bearings are located on the circumferential periphery of the rotor in each device.

### 1.2.1 Micro-Bearing System Requirements

As one can see from the above discussion, many stringent requirements need to be satisfied to design a micro-bearing system:

**High DN number.** As described in the last section, one of the advantages of the micro-engine is the high specific power it can produce, which is 20-30 times greater than those of most advanced batteries. Research [3] has shown that the key to achieving high specific power in both fluid and electrical rotating machinery is the high peripheral speed, which is found to be around 500 m/s, comparable to that of large conventional turbomachinery. As stated in the last section, the rotors of micro-engines normally have radii of around 2-4 mm. Therefore, that high peripheral speed translates into a rotational speed of 1-2 million rpm (rounds per minute), much higher than the rotational speeds of the conventional turbomachinery, which are usually in the tens of thousands of rpm. The greatest challenge is that the DN number—the diameter (in mm) multiplied by the rotating speed (in rpm) — is about 10 million mm-rpm for the micro-bearing system, which is one order of magnitude larger than the DN number of a large conventional bearing systems.

**Low power dissipation.** In large-scale engines, the power dissipation is almost negligible compared with the power output of the engine. However, due to the cube-square law, the power dissipation of the bearing system, which is proportional to the surface area, becomes comparable to the power output of the micro-engine system if the specific power of the engine stays the same at the small scale. Since the micro-engine is designed to produce power, the power dissipation in any component should be as low as possible. As discussed above, the peripheral speed is extremely high, so high drag force on the rotor surface should be avoided; otherwise the bearings may consume more power than the turbine can produce.

**Compatible with the fabrication.** As mentioned in the last section, the micro-engine is fabricated by DRIE technology, which can only create planar features. 3-D features, like grooves on the journal bearing wall cannot be fabricated. Furthermore, the etch depth is limited for a given opening, implying that the aspect ratio of features is also quite limited. For example, with a 15-micron opening (which is the typical clearance of the micro-journal-bearing), DRIE can only etch about 300 microns deep with acceptable bearing wall (straight and smooth) [3].

**Capable of working well at high temperatures.** Under normal operating conditions, the exhaust temperature of the micro-engine combustor can reach 1600K. Due to heat

transfer in the engine and the fact that the journal bearing is located at the outer periphery of the turbine rotor, the temperature of the bearing can be over 1000K, so the bearing system must be able to work well at this high temperature.

Compatible with the whole engine system. Normally, each component of the engine system is designed separately. Therefore, adding the micro-bearing system should not negatively affect the performance of other components. Furthermore, since the engine will operate as a stand-alone system, there will be no external pressure/power source to be used to supply the bearing system under normal operating conditions; the only pressure source it can use is the pressurized air produced by the compressor in the engine.

Sufficient load capacity. Because the micro-engine will be used in various conditions, the bearing system must be designed with enough load capacity for the engine to withstand reasonable shocks: no one wants to use a micro-engine that can only work on an air-table.

Long life. The life of a conventional bearing system is normally measured in hundreds of millions of cycles. This number of cycles may be large enough for conventional engines, because the typical rotational speeds of these engines are several thousand rpm. However, since the rotational speed of a micro-engine is 1-2 million rpm, a hundred million cycles translates into only several hours for the micro-engine, which is not at all sufficient. Micro-bearings with longer cycle life must be designed.

Last but not least, the resonances of the bearing system must be outside the steady operation envelope. When the rotor spins at the speed of resonance (or natural frequency), the amplitude of vibration of the rotor increases dramatically. With such a large amplitude of vibration, the rotor may touch the bearing wall, which in turn may cause it to rub and even crash. So, the critical speed of the bearing system needs to be either well above or well below the steady operation speed region. This is also true for large-scale engines.

With so many requirements to be satisfied, yet another question arises: what bearing technology can enable such a micro-high-speed turbine system?

### **1.2.2 The Choice of Micro-Bearing Systems**

According to the requirements listed above, the roller contacting bearing, widely used in industry, is not suitable for the micro-engine for two major reasons: it is difficult to fabricate and it has high power dissipation. The roller elements in a conventional bearing system are normally the size of a micro-engine's rotor. Even if the roller bearing can be made small enough, it is still difficult to be integrated into micro-engine because it is



not compatible with the semiconductor fabrication technology (recall that this technology cannot fabricate 3-D features). Finally, its large frictional power dissipation at high speed cannot be tolerated in the micro-engine system.

The magnetic bearing system seems like a good choice because of its low power dissipation. However, because the bearing temperature can be as high as 1,000 Kelvin in operating conditions—higher than the Curie points of most ferromagnetic materials—the magnetic materials will be demagnetized. Thus, the magnetic bearing system cannot be used in the micro-engine system.

Therefore, only fluid bearings can be used here. The great advantage of these kinds of bearings is that they have simple structures and thus are easy to fabricate. The fluid bearings are divided into two major subgroups according to the lubricant used in the bearing: one is the liquid/oil bearing, and the other is the gas/air bearing. Note that the viscosity of oil/liquid is orders of magnitude larger than that of gas: for example, liquid water has a viscosity two orders of magnitude higher than steam. As a result, the power dissipation of an oil/liquid bearing is orders of magnitude larger than that of a gas bearing. Thus, gas bearings are obviously the better choice here. Gas/air as the lubricant is much more compatible with the whole system, because it is gas/air that runs through the turbine and the compressor. Actually, gas bearing systems have already appeared in large devices where contamination of working fluid by lubricants is unacceptable, low drag is essential, and/or long life at high rotational speed is required. Examples of such applications include dental drills, navigational gyros [14], cryogenic expansion turbines [15], and air cycle machines [16].

Furthermore, gas bearings can be divided into two subcategories according to the different mechanisms they use to generate stiffness: hydrodynamic gas bearings and hydrostatic gas bearings, as shown in Figure 1-8.

Hydrodynamic gas bearings (Figure 1-8-a) use the hydrodynamic pumping effect to generate direct stiffness. A static load is applied to push the rotor toward the bearing wall, causing the non-uniform bearing gap around the rotor. Then pressure builds up in the bearing due to the pumping action of the rotor rotation, and the hydrodynamic bearing force is generated.

Unlike the hydrodynamic gas bearings, the hydrostatic ones (Figure 1-8-b and Figure 1-8-c) use external pressure sources to generate direct stiffness and keep the rotor centered. There are basically two kinds of hydrostatic gas journal bearings: radial-flow (Figure 1-8-b) and axial-flow (Figure 1-8-c).

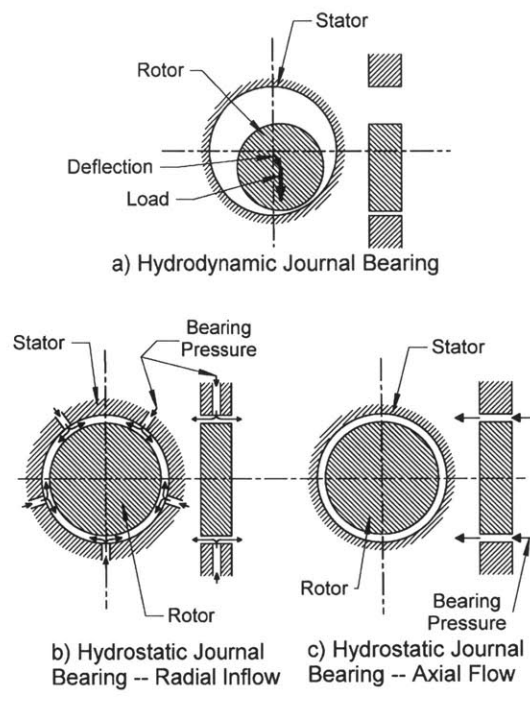


**Figure 1-8: Hydrodynamic and hydrostatic gas bearings (adopted from [8]).**

Based on the research by Piekos [17] and the discussion presented below, one can see that the hydrodynamic gas journal bearing is not a good choice for the micro-engine system due to the small  $L/D$ . Therefore, the only choice left is the hydrostatic gas journal bearing. It is difficult to fabricate the micro-radial-flow journal bearing (Figure 1-8-b), because the fabrication of the feed in the bearing wall requires an additional layer to be fabricated and bonded; thus, the axial-flow hydrostatic bearing (Figure 1-8-c) is the best choice of all.

### 1.2.3 Previous Work and Other Research

Comparing the structures of the two bearing systems, one can find that hydrodynamic gas bearings are simpler and easier to fabricate than hydrostatic ones, because no feed system is needed in the former. Piekos has done thorough modeling and simulations to investigate and design the micro-hydrodynamic gas journal bearing for the micro-engine. The results were reported in [17] [18] and [19]. The results of his research showed that the micro-hydrodynamic gas journal bearings can only spin stably at high speed and at large rotor eccentricities (the distance between the geometric centers of bearing and rotor), because the supporting bearing force generated by the hydrodynamic force relies on the rotor speed and eccentricity.

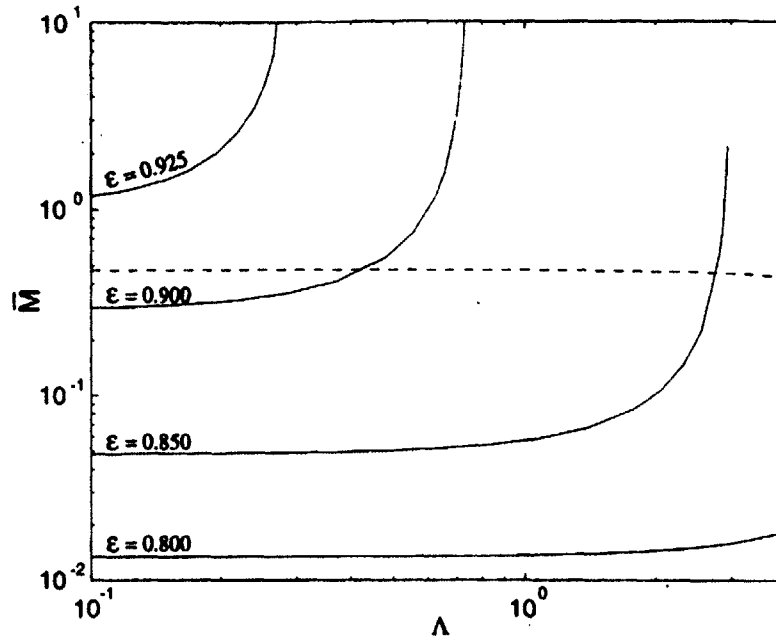


**Figure 1-9: Minimum eccentricity ratio contour for a bearing with  $L/D=0.075$  (adopted from [19]).**

Figure 1-9 is adopted from [19], where bearing number  $\Lambda=6\mu\omega R^2/(h^2P_a)$ , which expresses air compressibility in the bearing, is proportional to rotational speed  $\omega$  ( $\Lambda\approx 3$  at design speed); dimensionless mass  $\bar{M}=mP_a h^5/(72L\mu^2R^5)$ , which captures the bearing geometry and the rotor mass, is determined by the bearing length  $L$ , radius  $R$ , clearance  $h$ , gas viscosity  $\mu$  and atmospheric pressure  $P_a$ . The dashed line represents the operating line of the micro-bearing with the bearing clearance of  $10\ \mu\text{m}$ . Due to the fabrication constraints, the typical length-to-diameter ratio ( $L/D$ ) is about 0.075 for the micro-journal-bearing system. With this  $L/D$  and according to Figure 1-9, the minimum eccentricity ratio (the rotor eccentricity divided by the bearing clearance) must be larger than 90% at low speed, and it still should be about 85% at design speed. This result has raised several critical questions about operating the micro-hydrodynamic gas journal bearings:

First, it is difficult to apply the load to the micro-rotor to get the desired eccentricity. In conventional large hydrodynamic gas journal bearings, the load comes from the weight of the rotor itself. When the journal bearing system is placed horizontal or tilted, the weight of the heavy rotor itself is sufficient to push the rotor significantly off-center. However, for the micro-engine, the weight of the rotor is negligible compared with the restoring force from the journal bearing due to the cube-square law, and thus the weight of the micro-rotor itself is not sufficient at all.

Second, it is difficult to control the load precisely to achieve the correct rotor eccentricity ratio during the operation. The rotor eccentricity is critical to the stability of the micro-bearing system: its ratio needs to fall within the range of 85% to 1 at design speed, and even narrower at low speed. The problem is that there is no equipment/sensor on-site yet that can measure the eccentricity ratio in this millimeter-sized device. Therefore, even if a sufficient load can be applied to the rotor, there so far is no guarantee that the correct load can be obtained such that the eccentricity falls within the correct range (otherwise, the rotor may touch the bearing wall with larger loads or may not spin stably with smaller loads).

Last but not least, the rotor may touch the rough bearing wall with the minimum required eccentricity, which leads to crashes. Measurements show that the roughness of the journal bearing walls can be half microns, due to the fabrication imperfections [3]. Thus, the rotor should be at least one micron away from the bearing wall; otherwise, there will be a destructive contact. However, the eccentricity ratio should be larger than 90%, according to Figure 1-9, which means that the rotor needs be spun less than one micron from the journal bearing wall. With current fabrication technology, operating of this kind of hydrodynamic gas journal bearing is impossible.

Although multiple-lobed hydrodynamic journal bearings can offer slightly more stable behavior than plain cylindrical/plain journal bearings for large devices, as reported in [20] and [21], numerical simulations of multi-lobed gas journal bearings for the micro-engine showed that a lobed configuration deteriorates the stability of the short micro-bearings [19].

Gas bearing systems have already attracted the attention of many researchers, and their speed has become higher and higher. For example, the latest-developed hydrostatic gas journal bearings used in Nuclear Magnetic Resonance (NMR) have reached a rotational speed of around 3 million rpm [22], with a DN number of 6 million rpm-mm. However, this bearing technology still cannot be used in the micro-engine devices, due to the following two facts: (1) The pressure supply to this NMR bearing is high, such that the flow is supersonic. High pressure means high power dissipation. Furthermore, the pressure is higher than the highest pressure the micro-engine can produce by itself. Thus, it conflicts with the requirements listed above. (2) The length of this NMR bearing is comparable to the diameter of the rotor, and it is fabricated by conventional machining. Thus, it is not compliant with the fabrication technology used for the micro-engine. It is also important to note that this bearing is operated in the subcritical regime (speed lower than the resonance frequency) due to the high stiffness caused by the high pressure. This

subcritical operation also makes it distinct from the micro-bearing being developed for the micro-engine, because the micro-engine devices need to be operated in the supercritical region. This will be discussed later in the thesis.

### 1.2.4 Nature of the Issues

So far, it can be seen that the requirements for the micro-hydrostatic gas bearing systems create numerous challenges which include (but are not limited to) the following:

1. High DN number. The DN number for this micro-gas bearing is around 10 million mm-rpm. Compared with the DN number for large conventional bearings (below 1 million mm-rpm), the one for the micro-gas bearing is one order of magnitude higher. Due to the small diameter (4 to 8 mm) of the micro-rotor, the rotational speed needs to be as high as 2 million rpm.
2. Low bearing supply pressure. According to the highest pressure produced in the micro-engine, the pressure difference across the micro-journal bearing can only be about 5 psig, which is much lower than those used in other bearing systems. This low bearing pressure is also necessary due to the low power dissipation requirement. Furthermore, the low pressure difference is compatible with the design of the turbomachinery in the system because it can be bled at the compressor exit.
3. Low Reynolds number. Low pressure and small bearing gaps result in low velocity and flow rate through the bearing. Thus, the Reynolds number of the flow in the micro-bearing is around 300, which is much lower than that of other gas journal bearing systems, typically 30,000 to 300,000. As a result, the flows in the micro-gas bearing are laminar, while the flows in its large counterparts are turbulent. The laminar flow regime sets new challenges in establishing sufficient damping and improving whirl instability. A significant amount of work has been done on short seals for turbulent flows (see [29] for a summary). Unfortunately, the concepts that hold for large-scale annular seals do not apply to the ultra-short hydrostatic gas journal bearings used in the MIT micro-devices because of the laminar flow regime.
4. High whirl ratio  $\mathfrak{R}$ . The whirl ratio  $\mathfrak{R}$  is defined as the ratio of the highest stable speed at which the journal bearing system can spin to its natural frequency. Due to the low pressure supply, the natural frequency of the micro-journal bearing is relatively low. Thus  $\mathfrak{R}$  needs to be larger than 20 in order

to reach that high design speed. In large conventional gas journal bearing systems,  $\mathfrak{R}$  is normally around 2 [24], one order of magnitude lower than in the micro-systems. Another issue with high whirl ratio is that the micro-gas bearing system needs to be operated in the supercritical region, while many other bearing systems can only operate subcritically. To accelerate the rotor to the supercritical region is not a trivial task, because the large amplitude resonance needs to be crossed. This will be discussed in detail in the thesis.

5. Relatively large fabrication uncertainties. Due to the imperfection of the fabrication technology [3], the uncertainty of the micro-journal-bearing clearance is of order  $2\ \mu\text{m}$ , which is about 15% of the bearing clearance itself. Moreover, the walls of the micro-bearings cannot be guaranteed to be fabricated straight and parallel. In fact, research [3] shows that it is impossible to fabricate perfectly straight journal bearings, and the profile variations could be as large as several microns (Figure 1-10). For most other bearing systems, quality control is critical and this large an error is not acceptable. However, the design of the micro-bearing system must be compatible with these fabrication uncertainties.

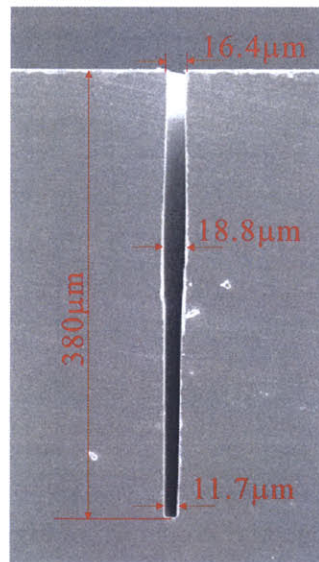


**Figure 1-10: Sample SEM picture of a journal bearing.**

6. Small  $L/D$  (length to diameter ratio). The current fabrication technology that is used to fabricate the micro-engine can only etch journal bearings with length up to around  $300\ \mu\text{m}$ . Thus the  $L/D$  for most micro-journal bearings is  $0.04\sim 0.075$ , while this number is normally about 1 for other large-scale gas



journal bearings (Figure 1-11). Therefore, the  $L/D$  in micro-bearing systems is more than one order of magnitude smaller than that of conventional ones. As a result, the damping of the micro-bearing is reduced significantly, making it difficult to invert the rotor.

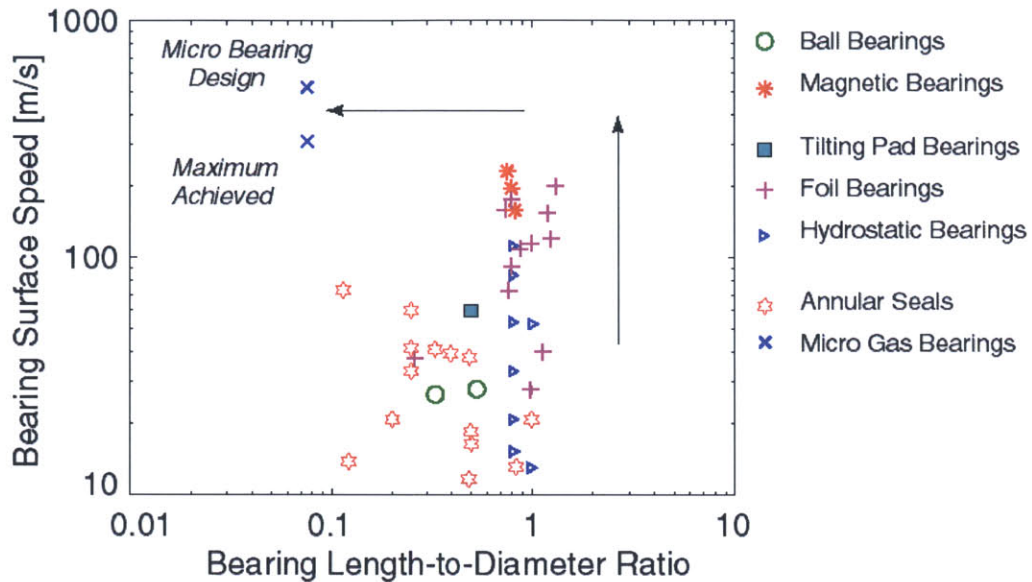


**Figure 1-11: Micro-bearing yields an  $L/D$  one order of magnitude smaller and a surface speed of one order magnitude larger than other bearing technologies (courtesy of Z. Spakovszky).**

7. The operability. As stated above, the micro-bearing system needs to be accelerated through natural frequencies to reach the high whirl ratio. Since the damping of the system is limited by the small  $L/D$ , the resonance amplitude at the natural frequency is large. This large amplitude may lead the rotor to touch the bearing wall and crash, which should be avoided. To overcome this difficulty, an operating protocol has been developed that will be presented later in the thesis.

Although some of these challenges may be easy to overcome individually, it is much more difficult to tackle them together. As shown in Figure 1-11, the micro-bearing yields an  $L/D$  one order of magnitude smaller and a surface speed one order of magnitude larger than other bearing technologies. The research presented in this thesis presents a first-of-a-kind criterion of the whirl instability for such micro-gas-bearing system configurations. A theory for hydrostatic gas journal bearings for micro-turbomachinery application is established, and the rotordynamic behavior of the micro-bearing systems, such as the natural frequency and the stability boundary, is investigated.

### 1.3 Research Objectives

Based on the bearing requirements and challenges discussed above, the objectives of this thesis are:

1. To establish a theory for the rotordynamic behavior of ultra-short hydrostatic gas journal bearings. Analytical expressions are found for hydrostatic stiffness, hydrodynamic stiffness, and damping. These are used to derive the rotor response curve, the natural frequency, and the distance to contact.
2. To derive bearing design guidelines. The onset of whirl instability is investigated for isotropic hydrostatic gas journal bearings and an analytical expression is given for the whirl ratio. This description is used to explain the physical mechanism underlying whirl instability in ultra-short gas journal bearings and a simple criterion for whirl instability is established.
3. To set up numerical models that can verify and complement the analytical models. These models are then assessed by experimental data.
4. To develop novel bearing configurations to enable high-speed operation.
5. To investigate non-linear behavior of micro-journal-bearing systems.

### 1.4 Structure of the Thesis

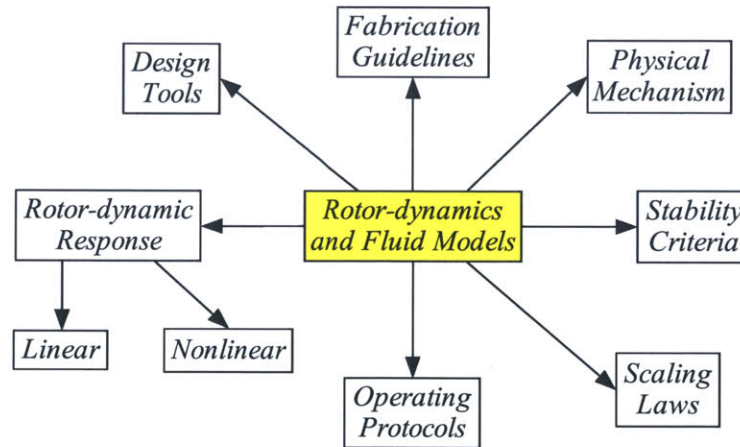


**Figure 1-12: Rotordynamic and fluid models of the micro-bearing system are the core of the research.**

Since there was little physical understanding of the bearings' dynamic behavior and no full modeling for the system, the thesis aims to establish the models step by step and achieve all the objectives stated above. First, the fluid models are derived analytically to calculate the bearing forces acting on the rotor according to its rotational speed, position,



and velocity. Then, using these bearing forces, the rotordynamic models are established. Based on the fluid and rotordynamic models, the physical mechanism is then investigated through analytical linear analysis. Meanwhile, the rotordynamic response is calculated, and the operating protocols and stability criteria can be established. Furthermore, with the analyses and calculations, the design tools and fabrication guidelines can ultimately be obtained. Thus, as shown in Figure 1-12, one can see that the rotor-dynamics and fluid models are the core of the research.

In Chapter 2, the fluid models and the fundamental rotordynamic model are established based on first principles. One of the key features of these models is that the bearing force components are solved analytically and individually. Most importantly, the two components of the hydrodynamic force—the hydrodynamic force due to the viscous drag effect and the one due to the rotor pumping action—are found to be of comparable amplitude and acting in the opposite directions. Normally the former is small compared to the latter in the large conventional bearing systems, and is negligible. However, since in the micro-ultra-short bearing system the two components are capable of canceling each other and have significant impact on the whirl instability of the system, with these bearing forces, the rotor response curve can be obtained analytically. Then the natural frequency and distance to contact are calculated, and the operating protocol is established in this chapter.

In Chapter 3, the isotropic/axisymmetric journal bearing system is investigated analytically. Using the linear eigenvalue analysis, the stability boundary of the system is derived. Then the singularity in stability boundary is discovered. The profound reason for this unique phenomenon is that the destabilizing force—hydrodynamic force—can vanish in the micro-bearing system due to the opposite directions of its two components, as stated above, and the small  $L/D$ . With the physical understanding, a simple criterion for the bearing whirl instability is obtained, and the design implications for the micro-hydrostatic isotropic journal bearing system are derived.

In Chapter 4, both analytical and numerical models are established for the anisotropic journal bearing system. Result shows that anisotropy (the hydrostatic stiffness difference in the two principal directions) is the key to relaxing the fabrication tolerance for high fabrication yield and designing a system with a higher stability boundary where it is easier to cross the natural frequency. Thus, the micro-bearing system with ultra-high speed becomes practically feasible in the fabrication sense. Also in this chapter, the effects of bearing side-load and rotor unbalance on the system's dynamic behavior are investigated through numerical simulations. The side-load is found to greatly reduce the sta-

bility boundary in the anisotropic system, while increasing the stability boundary in the isotropic system. Therefore, it should be avoided in the operation of the former.

The models established in the above chapters are assessed by the experimental data in Chapter 5. The static flow rates, the natural frequencies, and the distance to contact predicted by the models match the experimental measurements well, and thus the corresponding models are validated. The essential mechanisms of whirl instability are also assessed by experimental observations in both large conventional bearings and micro-bearings. Meanwhile, an accurate and nondestructive way to measure the bearing clearance is introduced in this chapter, which utilizes the fluid models to calculate the bearing clearance according to the static flow tests.

Since the coupling between the rotor's radial and conical motions is found to be severe in the micro-turbo-charger devices and can destabilize the system at a speed much lower than the radial whirl instability limit of the journal bearing system, it is investigated in Chapter 6. Furthermore, investigations by both linear analysis and numerical simulations of multi-degree-of-freedom models in Chapter 6 match the observations in the experiments. As a possible way to eliminate the coupling from the journal bearing system, the centrally-fed journal bearing is proposed and investigated in Chapter 7. The results show that although it can eliminate the coupling, this kind of bearing can produce much lower damping than the axially-fed journal bearing system, making it difficult to invert the system.

The influence of the journal bearing profile on system performance is investigated in Chapter 8, because the etched journal bearings are found not to be straight and parallel in most cases, due to the imperfection of the fabrication processes. Results show that the deviation from straight-wall bearings can make it even more difficult to cross the natural frequencies. Furthermore, the negatively-tapered journal bearing can cause the system to be statically unstable when the pressure difference across the journal bearing is low.

Because the rotors were found to engage in nonlinear resonance in the experiments, and in some cases these nonlinear resonances caused the system to crash, a preliminary investigation on the nonlinear dynamics of the journal bearing system using the multi-scale method is presented in Chapter 9. The result shows that the micro-bearing system can only engage in odd-order nonlinear resonances, which is verified by the numerical simulations and is consistent with the observations in experiments.

For the rotordynamics of the micro-engine, the thrust bearing systems are equally important. Models by Teo [9][10] are capable of calculating the natural frequency as well

as the unstable operating conditions of the thrust bearing system. To complement this, Chapter 10 presents a new way to compute the thrust force from the thrust bearing using the image method, which is simpler and faster than the Green's Function method. The results compare well with the 3-D CFD (Fluent) calculations. Also in this chapter, the rotor rotation effect on the thrust force due to the centrifugal forces is investigated, which was not covered by any models before.

As the last chapter of the thesis, Chapter 11 presents a design example of micro-hydrostatic gas journal bearings. In this example, the micro-bearing is designed for the self-sustained micro-engine (SSME), essentially the prototype micro-engine that can self-sustain and is currently under development at GTL. Based on this system, dual-bearing systems (two journal bearings in parallel) are investigated, and the misalignment between the two bearings is found to reduce the system stability boundary and make it difficult to cross the natural frequencies. Finally, several journal bearing system designs are suggested for this self-sustained micro-engine.

Using the modeling and analysis presented in the thesis, one can: 1) calculate the bearing forces analytically and individually, and then understand how the bearing geometry affects the system rotordynamics, such as the natural frequency, the damping ratio, and the distance to contact; 2) design a micro-journal bearing that can spin stably at a high rotational speed/whirl ratio; 3) know what mechanisms in the system can limit the top speed, and avoid them in both design and fabrication; 4) understand the system's nonlinear resonance behavior, such as the cause of the nonlinear resonance and the speeds at which resonance can occur; and 5) establish an operating protocol to avoid large amplitude resonance and operating conditions that may make the system unstable, such as sideload.

## *Chapter 2*

# **Basic Fluid and Rotordynamic Models**

In this chapter, a new analytical approach is developed to model axial-flow gas journal bearings. The model is capable of dealing with all the elements of (1) micro-devices, (2) dynamic response characteristics of axial-flow hydrostatic bearings, (3) evaluation of stiffness, natural frequency and damping, and (4) evaluation of stability boundary. Some of these aspects have been investigated in depth by a number of researchers (for example [29] and [19]). The key feature of this new model is that it is able to deal with all of these aspects together analytically.

In order to capture the underlying physics of the micro-bearing system, both the fluid and rotordynamic models will be established based on first principles. With this approach, the hydrodynamic force induced by the viscous drag effect, which is normally negligible in the large conventional bearings, turns out to be of comparable magnitude to the hydrodynamic force due to the rotor pumping action in the micro-bearing system because of its small  $L/D$  ( $<0.075$ ). This has a strong impact on the system's whirl instability limit which can be greatly increased by balancing the two force components. The details will be discussed in the next chapter.

This chapter starts with the fluid models to calculate the journal bearing forces acting on the rotor. The fluid forces will be analytically derived component by component. As a result, the influence of bearing parameters on each force component and then on the rotordynamics can be quantified.

Next, the basic rotordynamics of the system are described. With the forces calculated by the fluid models, the rotordynamic equations that have been established analytically based on first principles can be used to compute the natural frequency, the limit speed of whirl instability, and the distance to contact.

### ***2.1 Fluid Dynamic Model of the Bearing Force***

To determine the hydrodynamic fluid field in gas bearings, the Reynolds equation [29] is generally solved. With the Reynolds equation, the three-dimensional flow in the bearing can be simplified into a two-dimensional compressible flow, based on the as-

assumptions that the flow is fully developed and isothermal. And it can only be solved numerically.

Piekos [19] has developed numerical codes (SPECTRES) to solve the Reynolds equation for the micro-engine project. However, the numerical codes will not be used in this thesis for the following reasons:

1. The ultra-short hydrostatic bearings essentially act like short annular seals where the hydrostatic direct coupled stiffness is induced by the Lomakin effect [25], which was not accounted for, and hence the natural frequency of the system was not calculated correctly in the previous research.
2. Since the Reynolds equation couples hydrodynamic force and damping force together, it is difficult to gain insight into how each component affects the rotordynamics. Thus, in this chapter all the components will be calculated individually, based on the assumptions/approximations stated below.
3. The numerical approach is expensive, and it is difficult to understand from the results how the parameters in the bearing system influence the forces.
4. The viscous stress on the rotor surface, which was not captured by the Reynolds equation or the research by Piekos, is found to play a much more important role in the micro-system than in the macro-system because of the bearing's small  $L/D$ . This will be further discussed in this chapter.

Therefore, in this section, the force components—hydrostatic force, hydrodynamic force and damping force—will instead be calculated individually and analytically. Thus, these bearing force components as functions of the bearing geometry can be obtained. Most importantly, the viscous stress on the rotor surface that is negligible in the research on conventional bearings will be accounted for in the new models because of its comparable magnitude.

### **2.1.1 Assumptions and Approximations**

The flow in the journal bearing is a three-dimensional flow in which axial flow (due to the pressure difference across the bearing  $\Delta p$ ) and tangential flow (due to the rotor's rotation  $\omega$ ) combined (Figure 2-1). In order to solve the problem analytically, several approximations or assumptions can be made.

First, since the pressure supply to the bearing is below 5 psig (pressure ratio is smaller than 1.3) according to the requirements of the micro-bearing system in Chapter 1,

the flow can be approximated as incompressible flow. To assess this assumption, the comparison between incompressible and compressible models is presented later in the thesis.

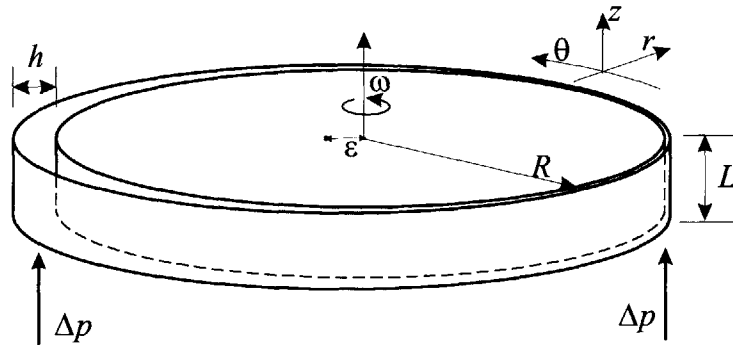


**Figure 2-1: Three-dimensional flow in journal bearings.**

Second, since the time it takes a fluid particle to go through the bearing ( $L/u_z \sim 3\mu\text{s}$ ) is much smaller than the period of the rotor rotation ( $1/\omega \sim 60\mu\text{s}$  at  $\omega = 1$  million rpm), the flow can be approximated as steady flow. When the flow axial speed is low (at low pressure difference across the journal bearing) and the rotor speed is high, the unsteady effects will be at play. In this case, numerical simulation may be needed to investigate the bearing flow coupled with the rotor movement. In the thesis, however, the research uses the quasi-steady flow approximation for simplicity.

Third, since the velocity ( $u_z$ ) is around 100 m/s and the clearance of the bearing ( $h$ ) is around 15  $\mu\text{m}$ , the Reynolds Number  $Re = \rho u_z h / \mu$  is of order 100. Thus, the flow is a laminar flow. Furthermore, the flow can be approximated to be fully developed, in both tangential and axial directions. This approximation for the axial flow is verified by the CFD calculations, which will be further discussed later in this chapter. For the tangential flow, however, this approximation is not accurate when the axial flow rate and rotor speed are high [30]. The effect of a tangential flow that is not fully developed on the rotor dynamic behavior is still under investigation and will be briefly discussed later in the chapter. In the research, however, this effect is neglected for simplicity.

Last, when the flow is fully developed under the assumptions and approximations above, the inertial terms in the Navier-Stokes equations can be dropped and then the equations become linear. As a result, the flow field can be decomposed into the three components in the corresponding three principal directions and then solved separately. In other words, the flow induced by the rotor motion can be separated from the flow induced by the static pressure drop across the journal; then, the fluid forces exerted on the rotor

can be split into a direct-coupled (aligns with the displacement of the rotor) hydrostatic force, a cross-coupled (perpendicular to the rotor displacement) hydrodynamic force, and a damping force. The modeling of these three main force components constitutes the fluid dynamic model.

### 2.1.2 Hydrostatic Forces

As stated before, the hydrostatic stiffness or the direct coupled stiffness is induced by the Lomakin effect. Assuming the rotor is stationary and is displaced from the center of the bearing by  $\varepsilon$  to the right, the bearing clearance becomes smaller on the right-hand side than on the opposite side, as depicted in Figure 2-2. The imposed total pressure drop  $\Delta p$  is the same all around the bearing. However, the flow rate through the right half of the bearing becomes lower due to the increased flow resistance (reduced clearance). As a consequence, the static pressure loss at the entrance decreases and an increased bearing pressure prevails in the right half of the bearing. In the left half of the bearings, the pressure decreases based on the same reasoning. Therefore, a hydrostatic force  $F^{hs}$  against  $\varepsilon$  is induced, as depicted. This effect is further discussed quantitatively as follows:

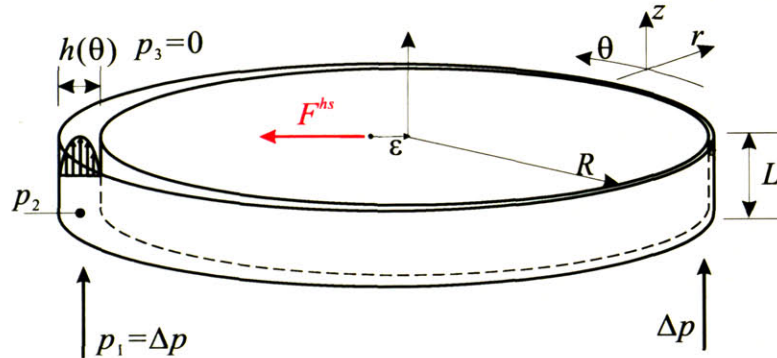


**Figure 2-2: Axial flow in the journal bearing.**

Figure 2-2 illustrates the axial flow in the bearing. The pressurized air is fed from the bottom. If the pressure at the exit (point 3) of the journal bearing is the atmospheric pressure ( $p_3=0$ ), the pressure difference through the journal bearing  $\Delta p$  equals the supply pressure at point 1  $p_1$ .

In the bearing gap, the axial flow is described by the steady Navier-Stokes equation in the axial direction ( $z$ ,  $r$ , and  $\theta$  are local coordinates):

$$\rho \left( u_z \frac{\partial u_z}{\partial z} + u_r \frac{\partial u_z}{\partial r} + u_\theta \frac{\partial u_z}{R \partial \theta} \right) = - \frac{\partial p}{\partial z} + \mu \left( \frac{\partial^2 u_z}{\partial z^2} + \frac{\partial^2 u_z}{\partial r^2} + \frac{\partial^2 u_z}{R^2 \partial \theta^2} \right). \quad (2-1)$$

Since the flow is assumed to be fully developed, the inertial terms on the left-hand side can be dropped. And because  $\partial^2/\partial z^2$ ,  $\partial^2/\partial r^2$  and  $\partial^2/R^2\partial\theta^2$  are of order  $1/L^2$ ,  $1/h^2$ , and  $1/R^2$  respectively, the second term is orders of magnitude larger than the other two due to small  $h/R$  ( $\sim 15/2100$ ) and  $h/L$  ( $\sim 15/300$ ). Thus Equation (2-1) can be simplified to

$$\frac{dp}{dz} = \mu \frac{\partial^2 u_z}{\partial r^2}. \quad (2-2)$$

With the no-slip boundary conditions at the walls ( $u_z=0$  at  $r=0$  and  $r=h$ ), the velocity profile yields

$$u_z = -\frac{1}{2\mu} \frac{dp}{dz} r(h-r). \quad (2-3)$$

Then the axial flow rate ( $q_z$ ) through the journal bearing (per unit length in the circumferential direction) becomes

$$q_z = \int_0^h u_z dr = -\frac{h^3}{12\mu} \frac{dp}{dz}. \quad (2-4)$$

Applying conservation of mass,  $q_z$  and hence  $dp/dz$  are constant along the bearing. Thus

$$\bar{u}_z = \frac{q_z}{h} = -\frac{h^2}{12\mu} \frac{dp}{dz} = \frac{h^2}{12\mu} \frac{p_2}{L}, \quad (2-5)$$

where  $\bar{u}_z$  is the average axial velocity. As the air enters the journal bearing, the static pressure will decrease from  $\Delta p$  at point 1 to a smaller pressure at point 2, due to the contraction and the entrance loss. According to Bernoulli's Equation, the pressure at the entrance of the journal bearing  $p_2$  is

$$p_2 = p_1 - \frac{\gamma}{2} \rho \bar{u}_z^2 = \Delta p - \frac{\gamma}{2} \rho \bar{u}_z^2, \quad (2-6)$$

where  $\gamma$  is the entrance loss coefficient. According to hydraulic handbooks, the entrance loss coefficient for the static pressure drop is 1.5 for this sharp-edge inlet. This value has been verified by both 2-D and 3-D steady CFD calculations for the micro-bearing system geometry, which is shown next.

Combining Equations (2-5) and (2-6), one can write

$$\frac{\gamma}{2} \rho \bar{u}_z^2 + \frac{12\mu}{h^2} L \bar{u}_z = \Delta p. \quad (2-7)$$

The 1<sup>st</sup>-order Taylor expansion of the above equation in  $d\bar{u}_z$  and in  $dh$  yields:



$$\gamma \rho \bar{u}_z d\bar{u}_z + \frac{12\mu}{h^2} L d\bar{u}_z - \frac{24\mu}{h^3} L \bar{u}_z dh = 0. \quad (2-8)$$

Thus, the sensitivity of the average axial velocity to a change in bearing clearance  $d\bar{u}_z/dh$  becomes:

$$\frac{d\bar{u}_z}{dh} = \frac{24\mu L \bar{u}_z}{\gamma \rho \bar{u}_z h^3 + 12\mu h L} > 0. \quad (2-9)$$

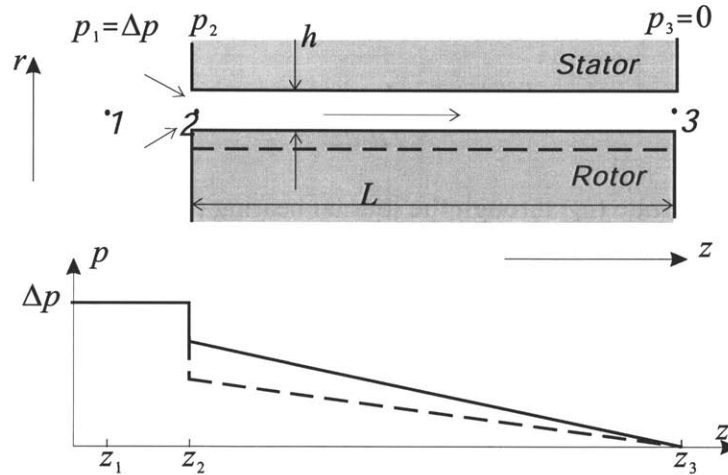


**Figure 2-3: Cross section of the journal bearing and sketch of the pressure distribution along the bearing.**

Note that the sensitivity is positive, implying that when the clearance decreases (from dashed line to solid line as shown in Figure 2-3), the average velocity  $\bar{u}_z$  becomes smaller according to Equation (2-9) and so does the entrance loss according to Equation (2-6). As a result, the pressure at the entrance  $p_2$  as well as in the bearing will increase (as shown in the bottom plot of Figure 2-3). Conversely, the pressure in the bearing will become smaller with larger clearance.

Thus, for the situation depicted in Figure 2-2 where the rotor moves right, the integration of the pressure field in the bearing will generate a net restoring force acting on the rotor in the opposite direction of the rotor displacement (direct coupled). This effect is known as the Lomakin effect.

In fact, both  $p_2$  and  $q_x$  can be solved explicitly by combining Equation (2-5) and (2-6):

$$q(\theta) = \frac{-b(\theta) + \sqrt{b^2(\theta) + 4a(\theta) \cdot \Delta p}}{2a(\theta)}, \quad (2-10)$$

$$p_2(\theta) = b(\theta) \cdot q(\theta), \quad (2-11)$$

where,  $a(\theta) \equiv \frac{\gamma}{2} \frac{\rho}{h^2(\theta)}$ ,  $b(\theta) \equiv \frac{12\mu L}{h^3(\theta)}$  and  $h(\theta) = h_0 - \varepsilon \cos(\theta)$ .  $h_0$  is the clearance when the rotor is centered and  $\varepsilon$  is the rotor displacement/eccentricity. Integration of Equations (2-10) and (2-11) yields the total mass flow rate  $\dot{m}$  and the net hydrostatic force  $F^{hs}$ :

$$\dot{m} = \rho \int_0^{2\pi} q(\theta) R d\theta, \quad (2-12)$$

$$F^{hs} = \int_0^{2\pi} -R \cos(\theta) d\theta \int_0^L dz \cdot p_2(\theta) \cdot \frac{(L-z)}{L} = -\frac{LR}{2} \int_0^{2\pi} p_2(\theta) \cos(\theta) d\theta. \quad (2-13)$$

It is important to note that the above analysis is based on the assumption that flow in the journal bearing is fully developed. CFD calculations using Fluent were run to verify this assumption. The results are shown in Figure 2-4.

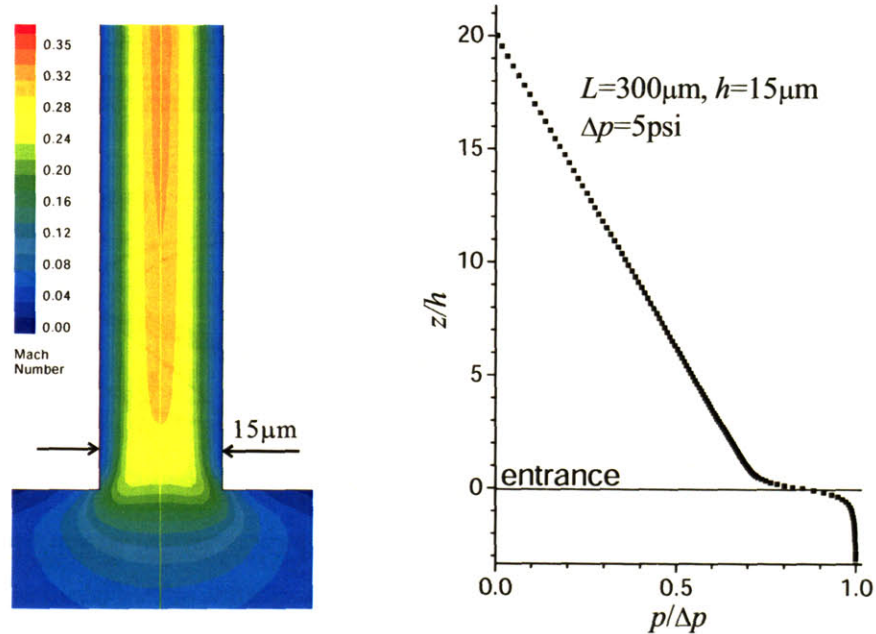


**Figure 2-4: Velocity contours at the journal bearing entrance (left), and pressure along the journal bearing (right) calculated by 2-D Fluent.**

It can be seen that the distance from the entrance to where the flow can be treated as fully developed is short, just on the order of the clearance of the journal bearing. Therefore, the assumption of fully developed flow is reasonable.

In addition, the modeling results compare well with the 3-D compressible CFD calculations calculated by Gong [26] using Fluent for both the journal bearing flow rate and

the hydrostatic force (Figure 2-5). This means that the fluid model based on incompressible flow with the entrance static pressure loss coefficient of 1.5 is accurate.

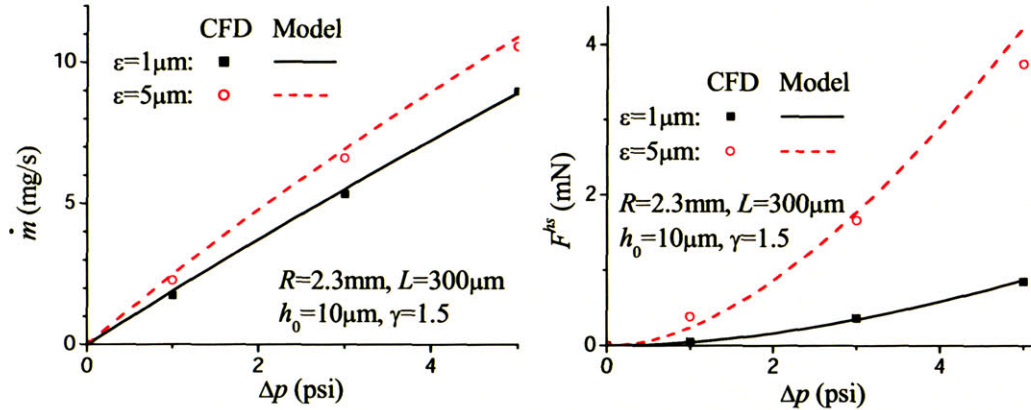


**Figure 2-5: Mass flow rate (left) and restoring forces (right) calculated by the incompressible model compared with 3-D compressible CFD results.**

Since the flow rate and pressure in the bearing gap are nonlinear functions of bearing clearance (Equation (2-10) and (2-11)),  $\dot{m}$  and  $F^{hs}$  vary with eccentricity  $\epsilon$  as shown in Figure 2-6.

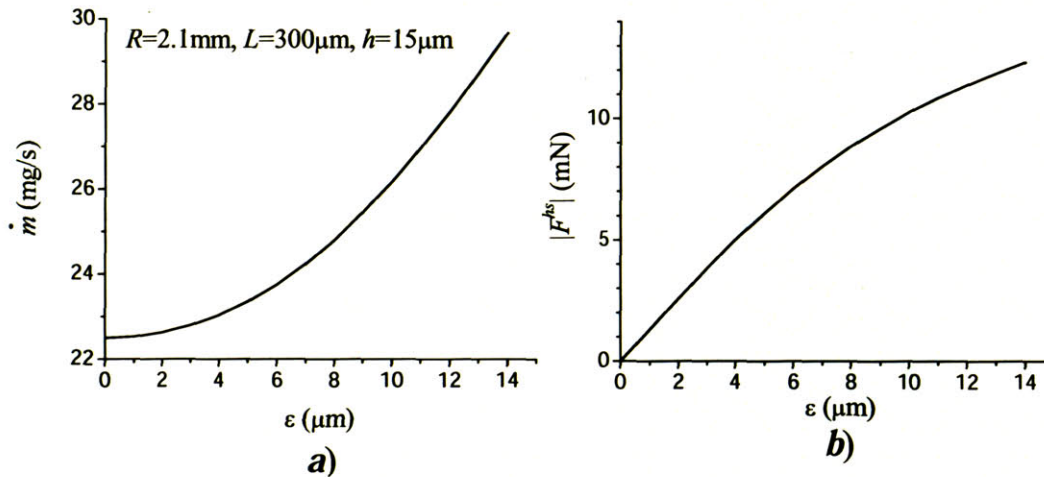


**Figure 2-6: Journal bearing mass flow rate and hydrostatic force as functions of rotor eccentricity.**

It can be seen that  $\dot{m}$  increases with rotor eccentricity due to the decrease in flow resistance. As the rotor moves from the centered position to a position near the bearing wall, the flow rate will increase by about 35%. This is a significant change in flow rate, and this effect can be used to determine the eccentricity of the rotor, as will be further dis-



cussed in the next chapter. Figure 2-6-*b* also shows that the amplitude of  $F^{hs}$  increases with eccentricity due to the Lomakin effect. Note that the hydrostatic force acts in the opposite direction of the rotor displacement, which means that the force tends to decrease the rotor eccentricity (negative stiffness). Differentiating  $F^{hs}$  with respect to  $\varepsilon$  yields the hydrostatic direct-coupled stiffness of the system.

It is worth noting that the hydrostatic force  $F^{hs}$  is nonlinear in eccentricity  $\varepsilon$  due to the nonlinear dependence between the bearing pressure and the clearance. In this case, the stiffness decreases (softens) as the rotor approaches the bearing wall. The nonlinearity affects the rotordynamic behavior of the system and even prevents the rotor from accelerating to high speed, leading the rotor to crash at the secondary resonances that occur at speeds other than the system's natural frequency. These will be discussed later in the chapter and will be revisited in a fully nonlinear analysis in Chapter 9.

### 2.1.3 Hydrodynamic Force

The surface movement of the displaced rotor generates a hydrodynamic force in the journal bearing. This hydrodynamic force is function of rotational speed  $\omega$ , instead of the pressure difference across the journal bearing  $\Delta p$ .

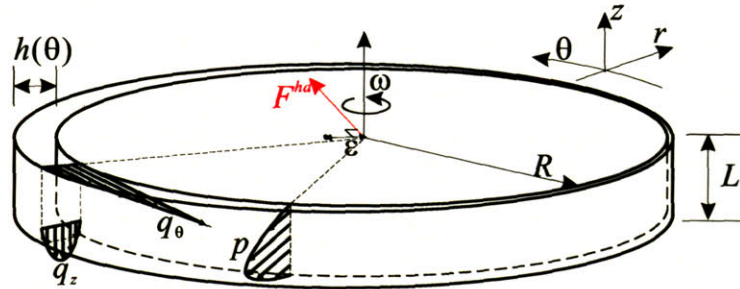


**Figure 2-7: Hydrodynamic flow field.**

As discussed earlier, the flow induced by the rotor motion can be decoupled from the flow induced by the static pressure drop across the journal bearing under the assumptions/approximations of quasi-steady, fully developed flow. The rotating motion of the rotor drags the flow along the circumference, and the combination of a Couette-type flow and a Poiseuille-type flow is locally set up as shown in Figure 2-7. For this type of flow, the local tangential flow rate is

$$q_{\theta} = \frac{\omega R h}{2} - \frac{h^3}{12\mu} \frac{\partial p}{R \partial \theta}. \quad (2-14)$$

The first term is due to the Couette flow and proportional to the local journal clearance.  $\omega R$  is the rotor surface speed. When the rotor moves closer to the wall, the fluid will be forced to flow in the axial direction, and this builds up pressure  $p$  as depicted in Figure 2-7. Then the flow rate of the Poiseuille flow in the axial direction becomes

$$q_z = -\frac{h^3}{12\mu} \frac{\partial p}{\partial z}. \quad (2-15)$$

Applying conservation of mass in the bearing gap and assuming the flow is incompressible, one can obtain

$$\frac{\partial q_z}{\partial z} + \frac{\partial q_\theta}{R \partial \theta} = 0. \quad (2-16)$$

Substituting Equations (2-14) and (2-15) into (2-16) yields

$$\frac{\omega}{2} \frac{\partial h}{\partial \theta} - \frac{1}{12\mu} \frac{1}{R^2} \frac{\partial}{\partial \theta} \left( h^3 \frac{\partial p}{\partial \theta} \right) - \frac{h^3}{12\mu} \frac{\partial^2 p}{\partial z^2} = 0. \quad (2-17)$$

Since  $R$  is much larger than  $L$  of the bearing ( $L/D < 0.075$ ), and  $\partial^2/\partial z^2$  is of order  $1/L^2$ , the second term in the above equation is negligible compared with the third term. Then Equation (2-17) can be simplified to

$$\omega \frac{\partial h}{\partial \theta} = \frac{h^3}{6\mu} \frac{\partial^2 p}{\partial z^2}. \quad (2-18)$$

Integrating the equation with respect to  $z$ , and considering the boundary condition  $p(L, \theta) = p(0, \theta) = 0$ , the static pressure in the bearing land  $p(z, \theta)$  becomes

$$p(z, \theta) = \frac{3\mu\omega}{h^3} \frac{\partial h}{\partial \theta} z(z-L) \equiv p^*(\theta) \frac{z(z-L)}{L^2}, \quad (2-19)$$

where  $p^*(\theta) \equiv \frac{3\mu\omega}{h^3} \frac{\partial h}{\partial \theta} L^2$  is a function of  $\theta$ . This bearing land pressure distribution in the circumferential direction is depicted in Figure 2-8.

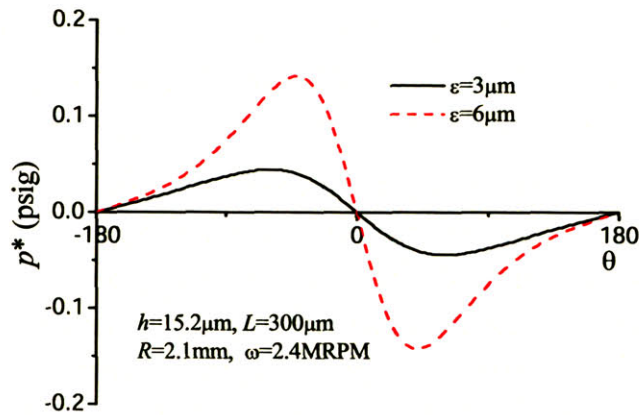


**Figure 2-8: Hydrodynamic pressure distribution in the circumferential direction.**

Note that the pressure distribution in the  $\theta$  direction is skew-symmetric. Therefore, the integration of the pressure over the bearing generates a net hydrodynamic force that acts in the direction perpendicular to the rotor displacement  $\varepsilon$  as depicted in Figure 2-7. Thus the hydrodynamic force is a cross-coupled force of magnitude

$$F_p^{hd} = \frac{\pi}{2} \mu \frac{RL^3}{h_0^2} \omega \frac{\xi}{(1-\xi^2)^{1.5}}, \quad (2-20)$$

where  $\xi = \varepsilon/h_0$  is the eccentricity normalized by the bearing clearance. This hydrodynamic force can drive the rotor into a whirling motion and destabilize the system. This whirl instability induced by the hydrodynamic force is further discussed in Chapter 3.

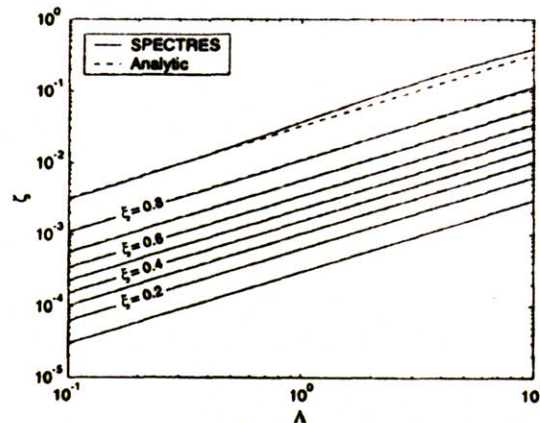


**Figure 2-9: Comparison between the analytical solution (incompressible, the dashed lines) and the numerical solution (compressible Reynolds equation, the solid lines) of hydrodynamic force in micro-bearing with  $L/D=0.075$  (adopted from [19]).**

In the above analysis, the flow in the bearing has been assumed incompressible. However, the widely used Reynolds equation treats the gas as compressible. The assumption of incompressibility in the micro-bearing system is assessed next.

In Figure 2-9 above, the bearing number  $\Lambda = 6\mu\omega R^2 / (h^2 P_a)$  is the nondimensionalized rotational speed  $\omega$  ( $\Lambda \approx 3$  at design speed), while the load parameter  $\zeta = F^{hd} / 2RLP_a$  is the nondimensionalized hydrodynamic force  $F^{hd}$ . The dashed lines represent the analytical incompressible solution given by Equation (2-20), while the numerical solution of the compressible Reynolds equation by SPECTRES developed by Pikeos is marked by the solid lines. The calculations were done for the micro-bearing system with an  $L/D$  of 0.075. Due to the small  $L/D$ , the pressure in the bearing due to the rotor pumping action is small according to Equation (2-20), and hence the incompressible flow assumption is valid, which is also verified by the comparison in Figure 2-9.

In addition to the pressure field, there is a viscous stress on the rotor surface due to the Couette flow:

$$\tau = \mu \frac{\omega R}{h}. \quad (2-21)$$

As a result, in addition to the hydrodynamic force due to the rotor pumping action, the integration of the viscous stress of the above equation over the bearing also generates a net hydrodynamic force in the direction perpendicular to the rotor displacement with an amplitude of

$$F_v^{hd} = -2\pi\mu \frac{R^2 L}{h_0} \omega \frac{1 - \sqrt{1 - \xi^2}}{\xi \sqrt{1 - \xi^2}}. \quad (2-22)$$

Thus, this cross-coupled force component can contribute to the destabilizing force driving the system into whirl instability. In summary, the total cross-coupled hydrodynamic force becomes

$$F^{hd} = \frac{\pi}{2} \mu \frac{RL^3}{h_0^2} \omega \frac{\xi}{(1 - \xi^2)^{1.5}} - 2\pi\mu \frac{R^2 L}{h_0} \omega \frac{1 - \sqrt{1 - \xi^2}}{\xi \sqrt{1 - \xi^2}}. \quad (2-23)$$

The first term is  $F_p^{hd}$ , the hydrodynamic force due to the pumping action of rotor rotation (Equation (2-20)), while the second term is  $F_v^{hd}$ , the hydrodynamic force due to the viscous drag effect (Equation (2-22)). Note that they are of opposite signs. This indicates that the total cross-coupled hydrodynamic force can be reduced or even eliminated by balancing the two components, if they are of the same order of magnitude.

Dividing Equation (2-22) by (2-20) yields the ratio of the hydrodynamic force due to viscous drag effect to the hydrodynamic force due to rotor pumping action, which is  $2Rh_0/L^2$  when the rotor is centered.

For large-scale conventional journal bearings, such as the ones investigated by Larson and Richardson [24], this ratio is much smaller than 1, since the bearings have an  $L/D$  of order 1 and  $h_0/L \ll 1$ . More specifically, the bearings investigated by Larson and Richardson had geometry of  $L=25.4\text{mm}$ ,  $R=15.9\text{mm}$ , and  $h_0$  varied from  $15\mu\text{m}$  to  $81\mu\text{m}$ . Thus, the ratios of the hydrodynamic force due to viscous drag effect to the hydrodynamic force due to rotor pumping action are estimated to be between 0.00075 and 0.004. Therefore, for large-scale conventional journal bearings, the hydrodynamic force due to viscous drag is negligible compared with the hydrodynamic force due to rotor pumping action.

On the other hand, for the micro-journal-bearing system, due to the small  $L/D$  (of order 0.04~0.075), the ratio of the hydrodynamic force due to viscous drag effect to the one due to rotor pumping action is of order 1 with  $L$  near  $300\mu\text{m}$  and  $h$  around  $15\mu\text{m}$ . Thus, for such low  $L/D$ , the hydrodynamic force due to viscous drag effect is comparable in magnitude to the one due to rotor pumping action. Therefore, this effect is not negligible, and it is found to have a significant impact on the whirl instability limit of the micro-journal-bearing system, which will be discussed in Chapter 3.

As mentioned earlier, the above analyses and the Reynolds equations are based on the approximation that the tangential flow is the fully developed Couette-type flow. However, according to [30], if the flow doesn't have any pre-swirl before entering the journal bearing and has a high axial velocity, due to the small length, the flow through time can be comparable to the time scale of the tangential boundary layer development when the rotor speed is high. In this case, the tangential flow is not strictly Couette flow in the vicinity of the bearing entrance, and the hydrodynamic force predicted by the models based on that approximation will be not accurate. The extent of the effect of a flow that is not fully developed on the hydrodynamic force is still under investigation at GTL. However, in most cases when either the rotor speed or the axial flow rate is not high, the approximation is still valid.

It is important to note that the essential physics has been captured in the first-order models based on first principle analysis; the two components of the cross-coupled hydrodynamic force, which act in opposite directions, are of the same magnitude due to the small  $L/D$ . In Chapter 3 on whirl instability, it will be shown that this physical mecha-



nism is the key to improving the stability boundary of the micro-bearing system and that rotordynamic behavior is captured well in the above models.

### 2.1.4 Damping Force

In addition to the hydrostatic force induced by the pressure difference across the journal bearing and the hydrodynamic force induced by the rotation of the rotor, the translational movement of the rotor will generate a damping force. From the following analysis, one can find that this damping force is proportional to the rotor velocity and in the opposite direction of the rotor motion.

As shown in the cross-section sketch in Figure 2-10, when the rotor is moving radially toward the bearing wall, gas in the bearing gap is squeezed out axially. Pressure builds up, and then a force is generated that acts on the rotor in the opposite direction of the rotor velocity. This is the damping force, which is derived next.

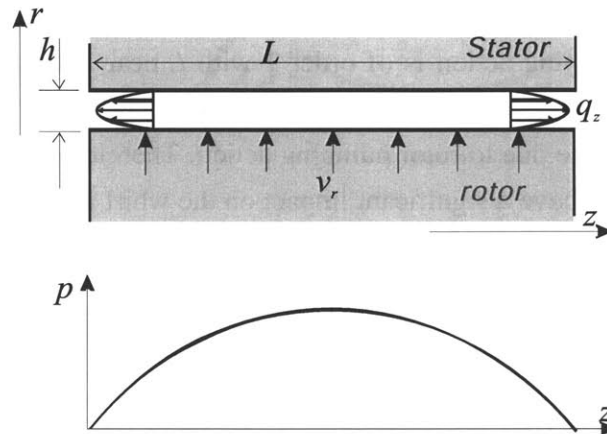


**Figure 2-10: Damping flow induced by the rotor translational motion.**

Similar to the hydrodynamic flow, the flow rates induced by the rotor motion in the circumferential and axial direction respectively are

$$q_{\theta} = -\frac{h^3}{12\mu} \frac{\partial p}{R\partial\theta}, \quad (2-24)$$

$$q_z = -\frac{h^3}{12\mu} \frac{\partial p}{\partial z}. \quad (2-25)$$

And according to the conservation of mass,

$$\frac{\partial q_z}{\partial z} + \frac{\partial q_{\theta}}{R\partial\theta} = v_r, \quad (2-26)$$

where  $v_r$  is the radial component of the rotor translational velocity. The above equation then becomes

$$v_r + \frac{1}{12\mu} \frac{1}{R^2} \frac{\partial}{\partial \theta} \left( h^3 \frac{\partial p}{\partial \theta} \right) + \frac{h^3}{12\mu} \frac{\partial^2 p}{\partial z^2} = 0. \quad (2-27)$$

Due to the small  $L/D$  ( $<0.075$ ), the second term in the above equation (of order  $1/R^2$ ) is much smaller than the third term (of order  $1/L^2$ ), and hence is negligible. Thus, Equation (2-27) can be simplified to

$$v_r = -\frac{h^3}{12\mu} \frac{\partial^2 p}{\partial z^2}. \quad (2-28)$$

Integrating the equation with respect to  $x$ , and considering the boundary condition  $p(L, \theta) = p(0, \theta) = 0$ , the pressure in the bearing induced by the rotor radial motion  $p(z, \theta)$  becomes

$$p(z, \theta) = \frac{6\mu}{h^3(\theta)} v_r(\theta) z(z-L). \quad (2-29)$$

Note that both  $h$  and  $v_r$  are functions of  $\theta$ .

The translational velocity of the rotor  $v$  can be decomposed into two directions, in the direction along the displacement of the rotor  $\varepsilon$  and in the perpendicular direction  $\beta$ , as sketched in Figure 2-11. Then  $v_r$  can be expressed as

$$v_r = v_\varepsilon \cos(\theta) + v_\beta \sin(\theta). \quad (2-30)$$

The final expression of  $p(z, \theta)$  can be rewritten accordingly:

$$p(z, \theta) = \frac{6\mu}{h^3} (v_\varepsilon \cos(\theta) + v_\beta \sin(\theta)) z(z-L). \quad (2-31)$$

Through the integration of Equation (2-31) with respect to  $z$  and  $\theta$ , one can obtain

$$\vec{F}^{dp} = C_\varepsilon v_\varepsilon \hat{\varepsilon} + C_\beta v_\beta \hat{\beta}, \quad (2-32)$$

where  $C_\varepsilon$  and  $C_\beta$  are the damping coefficients in  $\varepsilon$  and  $\beta$  direction respectively:

$$\begin{cases} C_\varepsilon \equiv -\pi\mu R \frac{L^3}{h_0^3} \frac{1+2\xi^2}{(1-\xi^2)^{2.5}} \\ C_\beta \equiv -\pi\mu R \frac{L^3}{h_0^3} \frac{1}{(1-\xi^2)^{1.5}} \end{cases} \quad (2-33)$$

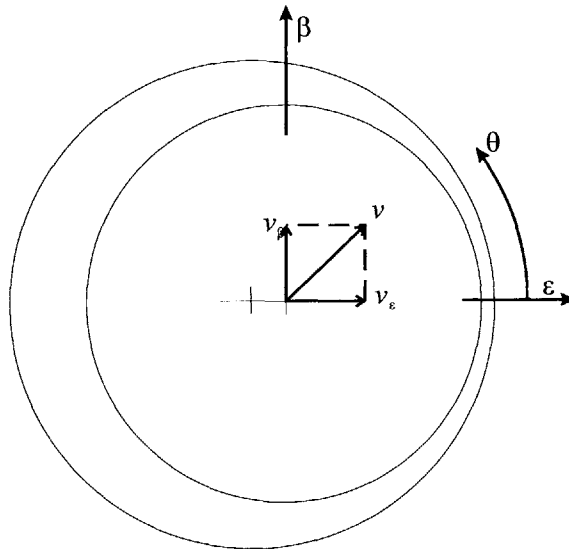


**Figure 2-11: Rotor translational velocity and appropriate coordinate system.**

Note that the damping force is proportional to  $(L/h_0)^3$ , a strong function of length over clearance. The implication is that in order to increase damping, the length must be increased and the clearance must be reduced.

Besides the damping due to the squeezing effect, the damping force can also be induced by viscous stress on the rotor surface. Due to the translational motion of the rotor, the viscous stress on the rotor surface will be  $\tau = \mu v_\theta / h \sim \mu v / h$ , where  $v_\theta$  is the tangential velocity of the rotor surface. After integration with respect to  $\theta$  and  $x$ , the damping force due to viscous drag is found to be of order  $\mu v R L / h$ . Thus, the ratio of the damping force due to the squeezing effect (Equation (2-32)) to the one due to viscous drag is of order  $(L/h)^2 = 400$ , much greater than 1. As a result, the squeezing effect dominates over the damping force.

## 2.2 Basic Rotordynamics

Using the force models and description developed in the last section, the rotordynamic behavior of the micro-journal-bearing system can now be investigated.

First, to describe the motions of the rotor, different coordinates will be used from now on. In the coordinate system adopted,  $z$  is along the axis of the rotor, while  $x$  and  $y$  define the plane in which the rotor has translational motions, as shown in Figure 2-12.

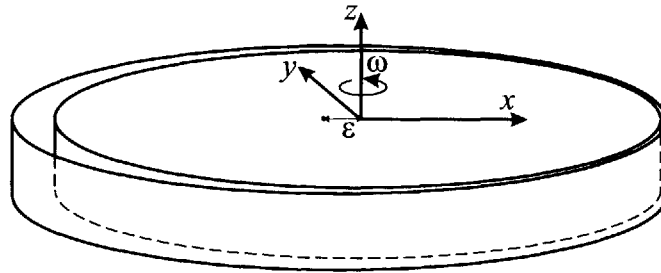


**Figure 2-12: Coordinate system used to describe the rotor motion (sketch not to scale).**

### 2.2.1 Rotordynamic Equations

Due to imperfections in fabrication, such as etch non-uniformities and pattern misalignment, the rotor's mass center is not necessarily at its geometric center. Considering this circular rotor displaced in a circular bearing, one can find that there are 3 centers in the system as shown in Figure 2-13: the bearing geometric center (BGC), the rotor geometric center (RGC), and the mass center (MC) of the rotor.

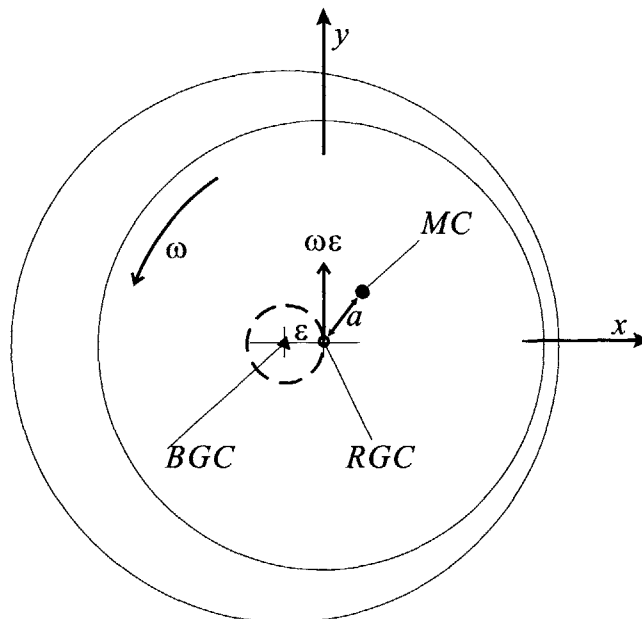


**Figure 2-13: Geometric and mass centers, and definition of eccentricity and unbalance in the journal-bearing system.**

As mentioned in the last section, the eccentricity of the rotor  $\epsilon$  is the distance between the bearing geometric center and the rotor geometric center, and the distance between the rotor geometric center and mass center is denoted by the unbalance of the rotor  $a$ .

Thus if the coordinates are fixed in the stator frame, the rotordynamic equations can be written based on Newton's Second Law:

$$\begin{cases} m\ddot{X} = F_x^{hs} + F_x^{hd} + F_x^{dp} + m\omega^2 a \cos(\omega t) \\ m\ddot{Y} = F_y^{hs} + F_y^{hd} + F_y^{dp} + m\omega^2 a \sin(\omega t) \end{cases} \quad (2-34)$$

where  $m$  is the mass of the rotor:  $X$  and  $Y$  are the displacement of the rotor along  $x$  and  $y$  directions respectively:  $F^{hs}$ ,  $F^{hd}$  and  $F^{dp}$  are the hydrostatic force, hydrodynamic force, and damping force respectively: and  $\omega$  is the rotational speed. The last terms on the right-hand side are the centrifugal forces introduced by the unbalance and rotation, and they are the excitations.

For the simple journal bearing, as shown in Figure 2-13, the geometry is axisymmetric around the BGC. In this case, the rotor will engage in a translational motion--precessing as it spins due to the unbalance. Due to the symmetry of the system, the orbit of the precessing rotor geometric center (the dashed circle in Figure 2-13) is a circle with its center superposed on the bearing geometric center. At the same time, the frequency of the precession is the rotor rotational speed  $\omega$ , because the frequency of excitation (the centrifugal force due to unbalance and rotation) is  $\omega$ . Therefore, this motion is called a synchronous precession [29].

Thus, for this geometrically axisymmetric system, in the rotor frame, the rotor is static while the stator rotates around the rotor without precession. Then, the forces in this frame can be viewed as steady. As a result, it is simpler to investigate the rotordynamics in the coordinates fixed in the rotor frame, and the rotordynamic equations in this frame become

$$\begin{cases} m(\ddot{X} - 2\omega\dot{Y} - \omega^2 X) = F_x^{hs} + F_x^{hd} + F_x^{dp} + m\omega^2 a_x \\ m(\ddot{Y} + 2\omega\dot{X} - \omega^2 Y) = F_y^{hs} + F_y^{hd} + F_y^{dp} + m\omega^2 a_y \end{cases} \quad (2-35)$$

In these equations,  $X$  and  $Y$  are the displacement of the rotor along the  $x$  and  $y$  directions in the rotor frame respectively.

Without loss of generality, it can be assumed that the dynamic eccentricity  $\varepsilon$  (the radius of the precession orbit) is in the  $x$  direction in the rotor frame. Perturbing the motion in the rotor frame about the dynamic eccentricity  $\varepsilon$ ,  $X$  and  $Y$  can be written as  $X = \varepsilon + x$  and  $Y = y$ , where  $x$  and  $y$  are the unsteady perturbations much smaller than  $\varepsilon$ . Then through linearization, the equation above can be divided into two equations: one describes the steady motion of the rotor, while the other describes its unsteady motion due to the perturbation. From the first equation, the steady rotor response due to the unbalance can be derived.

Using the equation describing the unsteady motion, the stability of the system can be obtained through an eigenvalue analysis in the frequency domain.

In order to utilize the results obtained from the last section, the forces are calculated in the stator frame. This approach is valid because the pressure distributions in the bearing remain the same no matter what coordinate system they are looked at from. Thus, the rotor velocity of  $\dot{\bar{R}} + \bar{\omega} \times \bar{R}$  in the stator frame is used to calculate the damping force  $F^{dp}$ , where  $\bar{R} = X\hat{x} + Y\hat{y}$ . Hydrostatic, hydrodynamic, and damping forces then become

$$F_x^{hs} = F^{hs}\Big|_{\varepsilon} + \frac{\partial F^{hs}}{\partial x}\Big|_{\varepsilon} x + O(x^2) = F^{hs}\Big|_{\varepsilon} + \frac{\partial F^{hs}}{\partial \varepsilon}\Big|_{\varepsilon} x + O(x^2) \equiv F^{hs}\Big|_{\varepsilon} + K_{xx}\Big|_{\varepsilon} x + O(x^2),$$

$$F_y^{hs} = 0 + \frac{\partial F^{hs}}{\partial y}\Big|_{\varepsilon} y + O(y^2) = \frac{F^{hs}}{\varepsilon}\Big|_{\varepsilon} y + O(y^2) \equiv K_{yy}\Big|_{\varepsilon} y + O(y^2),$$

$$F_y^{hd} = F^{hd}\Big|_{\varepsilon} + \frac{\partial F^{hd}}{\partial x}\Big|_{\varepsilon} x + O(x^2) = F^{hd}\Big|_{\varepsilon} + \frac{\partial F^{hd}}{\partial \varepsilon}\Big|_{\varepsilon} x + O(x^2) \equiv F^{hd}\Big|_{\varepsilon} + K_{yx}\Big|_{\varepsilon} x + O(x^2),$$

$$F_x^{hd} = 0 + \frac{\partial F^{hd}}{\partial y}\Big|_{\varepsilon} y + O(y^2) = \frac{F^{hd}}{\varepsilon}\Big|_{\varepsilon} y + O(y^2) \equiv K_{xy}\Big|_{\varepsilon} y + O(y^2)$$

$$F_x^{dp} = 0 + C_x\Big|_{\varepsilon} (\dot{x} - \omega y) + O(\dot{x}^2, y^2) \equiv C_x\Big|_{\varepsilon} (\dot{x} - \omega y) + O(\dot{x}^2, y^2),$$

$$F_y^{dp} = C_y\Big|_{\varepsilon} \omega \varepsilon + C_y\Big|_{\varepsilon} (\dot{y} + \omega x) + O(\dot{y}^2, x^2) \equiv C_y\Big|_{\varepsilon} \omega \varepsilon + C_y\Big|_{\varepsilon} (\dot{y} + \omega x) + O(\dot{y}^2, x^2),$$

where  $K$  denotes the stiffness and is a function of  $\varepsilon$ .  $K_{xx}$  and  $K_{yy}$  are the direct-coupled stiffness induced by the hydrostatic force, while  $K_{xy}$  and  $K_{yx}$  are the cross-coupled stiffness induced by the hydrodynamic force.  $C_x \equiv C_\varepsilon$  and  $C_y \equiv C_\beta$  are the damping coefficients in the  $x$  and  $y$  directions respectively. Note that  $F^{hs}$  has a zero steady component in  $y$  direction under the assumption that the steady displacement  $\varepsilon$  is in  $x$  direction, while  $F^{hd}$  has a zero steady component in  $x$  direction due to the fact that the hydrodynamic force is perpendicular to the displacement of the rotor.  $F^{dp}$  has a steady component only in the  $y$  direction because the steady velocity of the rotor is along the  $y$  direction due to the precession.

Substituting the above forces into Equation (2-35) and omitting higher-order terms in  $x$  and in  $y$ , the unsteady rotor motion yields

$$\begin{cases} m(\ddot{x} - 2\omega\dot{y} - \omega^2 x) = K_{xx}x + K_{xy}y + C_x(\dot{x} - \omega y) \\ m(\ddot{y} + 2\omega\dot{x} - \omega^2 y) = K_{yx}x + K_{yy}y + C_y(\dot{y} + \omega x) \end{cases} \quad (2-36)$$

At low rotational speed, the real parts of all eigenvalues of the above equations are negative, indicating that the system is stable. However, as the speed increases, some of the eigenvalues approach the imaginary axis in the complex plane, making the system less stable. At one rotor speed, the eigenvalues cross the imaginary axis and their real parts become positive. At this point, the system becomes unstable and the rotor engages in a whirling motion with exponentially growing amplitude, eventually crashing into the bearing wall. Thus, using an eigenvalue analysis, the dynamic stability of the bearing system can be assessed and the highest rotational speed at onset of instability can be calculated. From now on, this threshold speed will be referred to as the stability boundary (SB).

On the other hand, the dynamic eccentricity  $\varepsilon$  of the rotor can be calculated from the equation describing the rotor's steady motion, which can be derived from the steady parts of Equation (2-35):

$$\begin{cases} -m\omega^2(\varepsilon + a_x) = F^{hs}|_{\varepsilon} \\ -ma_y = F^{hd}|_{\varepsilon} + C_y\omega\varepsilon \end{cases} \quad (2-37)$$

Since  $a^2 = a_x^2 + a_y^2$ , the sum of the squares of the above equations yields

$$(m\omega^2 a)^2 = (F^{hs}|_{\varepsilon} + m\omega^2 \varepsilon)^2 + (F^{hd}|_{\varepsilon} + C_y\omega\varepsilon)^2. \quad (2-38)$$

It can be seen that the eccentricity  $\varepsilon$  is a function of the unbalance  $a$  and the rotational speed  $\omega$ , and can be calculated from the above equation. During high-speed operation, the eccentricity  $\varepsilon$  should be much smaller than the bearing clearance to keep the rotor from crashing into the bearing wall.

### 2.2.2 Dynamic Response Curve of the Rotor-Bearing System

In order to understand the dynamic and vibratory behavior of the rotor-bearing system and to quantify the stable operational range above the critical speed and below the stability boundary, the rotordynamic response of the system is sketched vs. the rotational speed according to Equation (2-38) in Figure 1-17. The stability boundary obtained from Equation (2-36) is also shown in Figure 2-14.

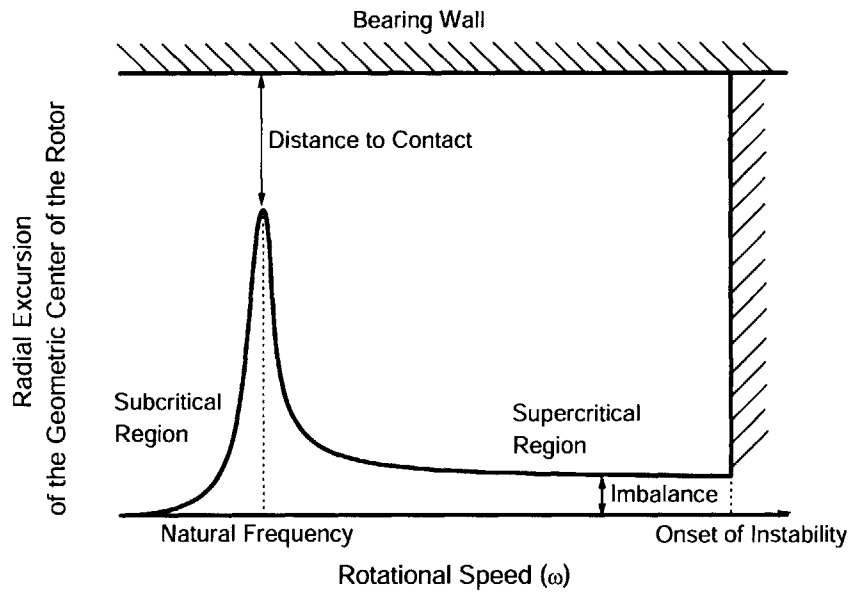


**Figure 2-14: Typical rotordynamic response curve of the rotor-bearing system.**

The response has a peak at the resonance frequency, which is called the natural frequency, denoted  $NF$  ( $\Omega_N$ ). Thus, to avoid the large-amplitude vibrations which may cause the rotor to crash, the system should be operated at speeds above and below the natural frequency.

The speed range below the natural frequency is denoted as the subcritical region, and the range above the natural frequency is denoted as the supercritical region. In the subcritical region, the response has relatively small amplitude and the rotor basically rotates around its geometric center. In the supercritical region, the amplitude asymptotically approaches a constant value. It can be shown that this constant value is the unbalance of the rotor according to Equation (2-38). Therefore, in the supercritical region, the rotor essentially self-centers and rotates around its center of mass (MC).

As discussed in Chapter 1, one of the major challenges in designing and operating the micro journal-bearing-system is the high-speed operation. Since the design speed of about 2.4 million rpm is well above the natural frequency, the rotor will be accelerated to eventually spin stably in the supercritical region. And because the natural frequency of the micro-journal-bearing system is limited by the low pressure difference across the journal bearing ( $\Delta p < 5$ psig), to reach the high design speed, the whirl ratio (defined as the ratio of the stability boundary to the natural frequency) should be as large as possible.



### 2.2.3 Distance to Contact

The distance to contact (D2C) is defined as the difference between bearing clearance and the peak amplitude of the response curve as depicted in Figure 2-14.

Because the rotor design speed is much higher than the natural frequency, the rotor always needs to cross the natural frequency to get into the supercritical region (inverted). And whether or not the rotor can be inverted depends on the distance to contact: only with sufficient distance to contact can the rotor be inverted.

In the linear bearing system with the rotor mass  $m$ , system damping  $C$  and natural frequency of  $\Omega_N$ , the damping ratio is defined as  $\zeta \equiv C/(2m\Omega_N)$ , which is essentially the ratio of unbalance to the peak amplitude of the rotor response curve. Due to the small  $L/D$  limited by the fabrication, the damping of the micro-bearing system is low according to Equation (2-33), resulting in a small damping ratio and hence a small distance to contact. This presents great challenges in both design and operation for the micro-bearing system.

Since the distance to contact is critical for stable high-speed operation, the following section discusses how to calculate the distance to contact and how the various bearing parameters affect it.

As the rotor speed  $\omega$  increases, according to Equation (2-38), the rotor eccentricity  $\varepsilon$  is largest when the first term on the right-hand side of the equation  $(F^{hs}|_{\varepsilon} + m\omega^2\varepsilon)^2$  is zero, because the second term  $(F^{hd} + C_y\omega\varepsilon)^2$  is proportional to  $\omega^2$ . In this case, the rotor geometric and mass centers are located relative to the bearing center, as sketched in Figure 2-15.

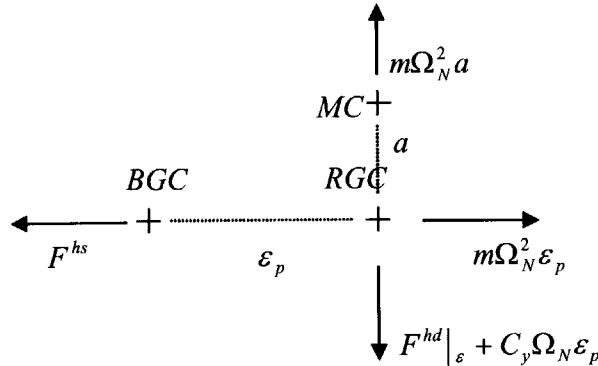


**Figure 2-15: Positions of geometric and mass centers of the rotor-bearing system at the natural frequency.**

Thus, when the rotor spins at the natural frequency  $\Omega_N$ , the direction of unbalance  $a$  is perpendicular to that of the peak eccentricity  $\varepsilon_p$ . The centrifugal force due to the rotor eccentricity  $\varepsilon_p$  is  $m\Omega_N^2 \varepsilon_p$ , balanced by the hydrostatic force  $F^{hs}$ . In the perpendicular di-

rection ( $a$ ), the centrifugal force due to the unbalance  $a$  is  $m\Omega_N^2 a$ , and is balanced by the hydrodynamic force  $F^{hd}$  and the damping force  $C_y\Omega_N\varepsilon_p$  together. Thus the natural frequency  $\Omega_N$  and peak amplitude  $\varepsilon_p$  are determined by

$$F^{hs}\Big|_{\varepsilon_p} + m\Omega_N^2\varepsilon_p = 0 \quad (2-39)$$

and

$$m\omega_N^2 a = \left| F^{hd}\Big|_{\varepsilon_0} + C_y\omega_N\varepsilon_p \right|. \quad (2-40)$$

Then the natural frequency of the system  $\Omega_N$  can be derived from the first equation and yields

$$\Omega_N = \sqrt{\frac{-F^{hs}}{m\varepsilon}} = \sqrt{\frac{-K_{yy}}{m}}. \quad (2-41)$$

Substituting Equations (2-23) and (2-32) into Equation (2-40) gives

$$\frac{a}{h_0} = \frac{\pi}{2} \frac{\mu}{m\Omega_N} \frac{RL^3}{h_0^3} \left( \frac{\xi_p}{(1-\xi_p^2)^{1.5}} + 4 \frac{Rh_0}{L^2} \frac{1-\sqrt{1-\xi_p^2}}{\xi_p^2 \sqrt{1-\xi_p^2}} \right) \equiv \Psi(\xi_p). \quad (2-42)$$

$\Psi(\xi_N)$  is denoted as the peak function, which determines the peak amplitude  $\xi_p$  of the rotor response for a given rotor unbalance level  $a/h_0$ , and  $\xi = \varepsilon/h_0$  is the rotor eccentricity normalized by the bearing clearance. Then the distance to contact can be calculated by subtracting the peak amplitude  $\varepsilon_p$  from the bearing clearance  $h_0$ .

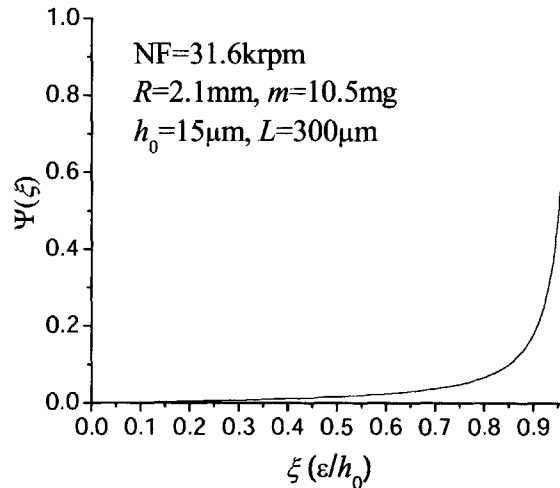


**Figure 2-16: Peak function.**

Figure 2-16 shows that the peak function monotonously increases with the rotor eccentricity. Thus, for a larger unbalance, the peak amplitude of the rotor response  $\xi_p$  is larger according to Equation (2-42). And for a constant unbalance level  $a/h_0$ ,  $\xi_p$  increases with the bearing length  $L$  and the radius  $R$ , while it decreases with the rotor mass  $m$ , the bearing clearance  $h_0$ , and the natural frequency  $\Omega_N$ .

## 2.2.4 Nonlinear Response of the Rotor-Bearing System

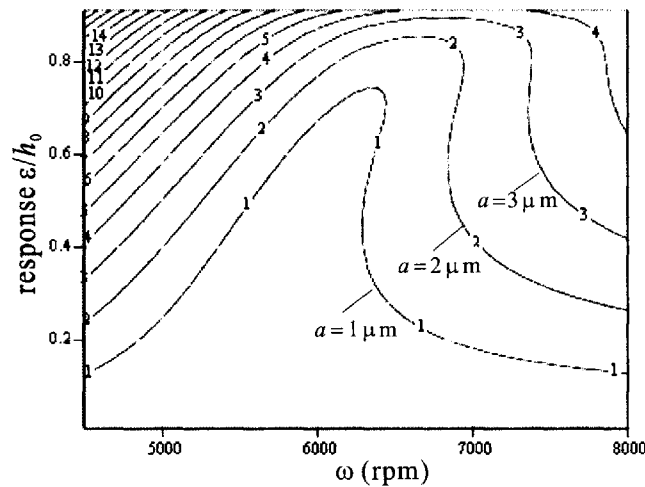


**Figure 2-17: Calculated response curves of the rotor-bearing system for the micro Turbo-Charger device with  $h=15\mu\text{m}$ ,  $L=300\mu\text{m}$ ,  $R=3\text{mm}$ ,  $m=70\text{mg}$  and  $\Delta p=0.25\text{psig}$ .**

The response curves plotted in Figure 2-17 are calculated for the rotor-bearing system in micro-turbo-charger devices with a pressure difference across the journal bearing  $\Delta p$  of 0.25psig and bearing geometry of clearance  $h=15\mu\text{m}$ , length  $L=300\mu\text{m}$ , and radius  $R=3\text{mm}$ . The horizontal axis is the rotating speed in rpm, while the vertical axis is the radial response normalized by the clearance. The numbers on the curves represent the unbalance  $a$  in  $\mu\text{m}$ . As expected, the response amplitude increases with unbalance.

It is important to note that the response curves for these devices are skewed and flat, and the skew and flatness of the response curves result from the nonlinearity of the forces. If the nonlinearity of the hydrostatic stiffness is neglected, the response curve becomes un-skewed, as shown in the left-hand-side plot of Figure 2-18.

In essence, it is the nonlinearity of forces that causes the response curve to skew and flatten: as the rotor approaches the bearing wall, the hydrostatic stiffness increases nonlinearly, and the response curve leans right. Meanwhile, the damping and hydrodynamic forces also increase (as manifested by the peak function), and the peak becomes

wide and flat. If the hydrostatic stiffness decreases with eccentricity as shown in Figure 2-6-*b*, the response curve will skew left.

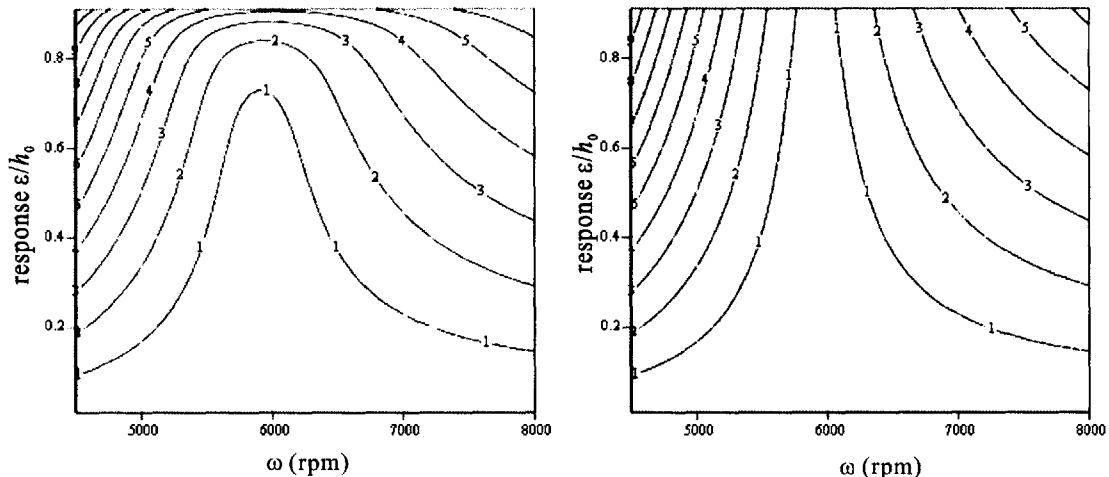


**Figure 2-18: Response curve with constant hydrostatic stiffness only (left); with constant damping and constant hydrodynamic stiffness (right).**

Due to the skew of the response curve, there will be a hysteresis phenomenon in the rotor response. As shown in Figure 2-19, the rotor will follow different paths on the response curve depending on whether it is accelerating (speed is increasing and response is following A-B-C-E-F) or decelerating (speed is decreasing and response is following F-E-D-B-A). The branch of D-C in the response curve can be found unstable using eigenvalue analysis (see textbooks on nonlinear oscillations for details). Thus, there is a jump from C to E in the acceleration path, and from D to B in the deceleration path. This hysteresis phenomenon is also observed in the experiments [30].

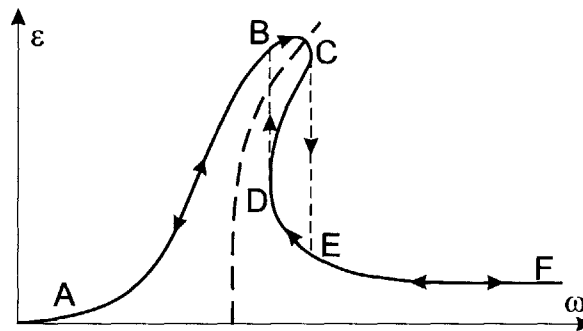


**Figure 2-19: Hysteresis phenomena in the rotor response curve.**

### 2.2.5 Journal Bearing Operating Protocol

Since the rotor design speed is on the order of a million rpm, which is much higher than the natural frequency of the system, the rotor must be accelerated through the reso-

nance to the supercritical region to achieve the design speed. Therefore, one of the major challenges encountered in the experiments was the ability to smoothly transition from subcritical to supercritical operation when accelerating to high speed.

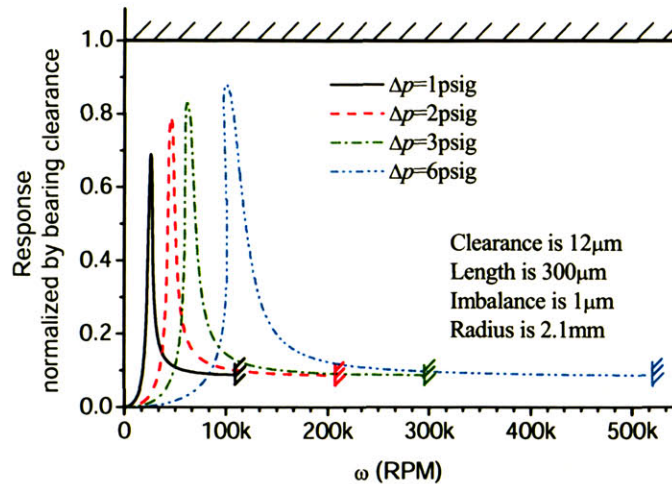


**Figure 2-20: Response curves at different bearing pressure difference  $\Delta p$ : distance to contact decreases, while stability boundary increases with  $\Delta p$ .**

As discussed in the hydrostatic models, the hydrostatic force increases with bearing pressure difference  $\Delta p$  (Figure 2-5). According to Equation (2-41), the natural frequency also increases with  $\Delta p$ . At the same time, Equation (2-40) indicates that the peak amplitude of the response increases with natural frequency and hence  $\Delta p$ , which makes the distance to contact decrease with  $\Delta p$  as shown in Figure 2-20. Thus, the rotor should be inverted at low  $\Delta p$  to avoid possible contact with the bearing wall.

On the other hand, note that whirl ratio (the ratio of stability boundary to natural frequency) is around 5. The whirl ratio is independent of  $\Delta p$ , since it is only a function of the bearing geometry. This is reflected in the shift of stability boundary to the right as shown in Figure 2-20, similar to the natural frequency, which is also shown in Figure 2-21. There is a detailed discussion of this topic in Chapter 3: and the whirl ratio can be higher than 20 for a given bearing geometry.

For stable high-speed operation, the bearing pressure difference  $\Delta p$  needs to be set to a high value so that the stability boundary is high enough for the system to reach the design speed. The system needs to be able to both cross the natural frequency and have a high stability boundary, but there is a conflict in that a low  $\Delta p$  is desired for a large distance to contact, while a high  $\Delta p$  is desired for a high stability boundary. To solve this problem, an operating protocol can be developed based on the model results. This operat-

ing protocol is shown in Figure 2-21 and consists of two major steps: (1) the natural frequencies are crossed at a low, fixed bearing pressure difference  $\Delta p$  and low speed, and (2) the rotor is accelerated to high speed by increasing  $\Delta p$  and staying within the corridor bounded by the stability boundary and the natural frequency as illustrated by the shaded area in Figure 2-21.

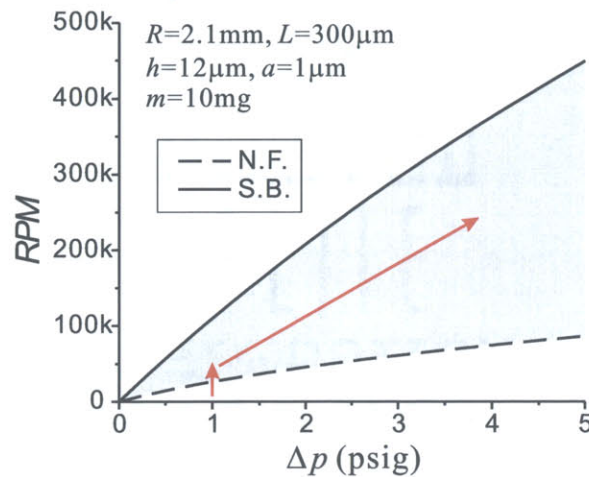


**Figure 2-21: Operating protocol for micro-journal-bearing systems.**

This type of operating protocol has been successfully implemented in other MIT micro-devices (the micro-turbo-charger devices and micro-turbo-pump devices) [32]. Attempts have also been made to automate the bearing operation by scheduling the journal bearing supply flow and the turbine main flow using a single pressure source and metering valves. The “single knob” automated operation of the micro-bearing rig has been experimentally demonstrated at low speeds and is under further investigation for high-speed operation.

### 2.3 Summary and Conclusions

In this chapter, both the rotordynamic and fluid models have been analytically established based on first principles. They are capable of dealing with all the elements of, (1) micro-devices, (2) dynamic response characteristics of axial-flow hydrostatic bearings, (3) evaluation of stiffness, natural frequency and damping, and (4) evaluation of stability boundary.

The fluid forces are analytically modeled component by component. The hydrostatic direct-coupled force is induced by the Lomakin effect. The hydrostatic force is found to increase with the pressure difference across the bearing  $\Delta p$ , and hence the natural frequency of the system also increases with  $\Delta p$ . Furthermore, the hydrostatic force is a nonlinear function of the rotor eccentricity, making the rotor response curve either lean



right with stiffening hydrostatic stiffness or lean left with softening hydrostatic stiffness. This skewing of the rotor response curve is accompanied by a hysteresis phenomenon.

The hydrodynamic cross-coupled force has two components: one is due to the rotor pumping action and the other is due to the viscous drag effect. In the micro-bearing system, the hydrodynamic force due to viscous drag is comparable in magnitude to the hydrodynamic force due to rotor pumping action because of the small  $L/D$ . And since they act in opposite directions, these two hydrodynamic force components can cancel each other, making the net hydrodynamic force vanish. In Chapter 3, it is shown that this has a significant impact on the system stability boundary.

The damping force is generated by the squeezing effect caused by the rotor translational motion, and is found to be strongly dependent on the length over clearance of the bearing. Both the hydrodynamic stiffness and the damping coefficient are strong nonlinear functions of the rotor eccentricity--they increase rapidly as the rotor approaches the bearing wall. As a result, the rotor response curve becomes wide and flat.

According to the model results, either decreasing the bearing clearance, the rotor mass, the rotor unbalance, and/or the system's natural frequency to invert the rotor (or pressure difference across the journal bearing), or increasing the bearing length and/or the radius can enlarge the distance to contact and help the rotor to cross the natural frequency.

Based on the models obtained in this chapter, the distance to contact and stability boundary of the micro-bearing system can be calculated. Since the distance to contact should be large for the rotor to be inverted, which requires a low pressure difference across the journal bearing  $\Delta p$ , and the stability boundary should be high for the system to reach the high design speed, which requires high  $\Delta p$ , an operating protocol has been developed to achieve controlled acceleration to high speed.

In the following chapters, the micro-bearing system is further investigated with the models to be established based on these rotordynamic and fluid models. The experimental evaluations of these models can be found in Chapter 5.

## *Chapter 3*

# **Dynamic Behavior and Whirl Instability Limit of Isotropic Hydrostatic Micro- Journal-Bearing Systems**

In the last chapter, both fluid and basic rotordynamic models were established based on first principles. With these models, the stability boundary of the system can be calculated by an eigenvalue analysis of the linearized rotordynamic equations (Equations (2-36)). In this chapter, analysis shows that due to the small  $L/D$  (one order of magnitude smaller than that of conventional large-scale bearings) and the low Reynolds number flow (on the order of 100), the ultra-short micro-bearings exhibit different dynamic behavior and whirl instability limit than their large-scale counterparts.

More specifically, as discussed in Chapter 2, the two components of the cross-coupled hydrodynamic force, which act in opposite directions, are of comparable magnitude due to the low bearing  $L/D$ . The consequence is that for a certain range and combination of geometric bearing parameters the onset of whirl instability resembles singular behavior with a potentially infinitely high limit speed. This singular behavior of the stability boundary is unique to the ultra-short micro-bearing system and has not been observed in the conventional large-scale systems. As a result, it turns out to be theoretically possible to utilize the singularity in stability boundary and design ultra-high-speed/whirl-ratio micro-bearing systems with a small  $L/D$ .

The goals of this chapter are to (1) quantify the dynamic behavior and whirl instability limit of the hydrostatic micro-journal-bearing systems, (2) investigate the physical mechanism at play and establish a theoretical understanding of the observed dynamic behavior, (3) derive a simple criterion for the whirl instability limit, and (4) develop design guidelines for stable high-speed operation.



### 3.1 Isotropic Journal-Bearing Systems

In the last chapter, a simple axisymmetric journal-bearing system was introduced. This axisymmetric journal bearing system has a unique characteristic, which is that the bearing forces are independent of the rotor displacement direction when the rotor is centered because of the symmetry. Thus, this simple axisymmetric journal-bearing system is called the isotropic journal-bearing system

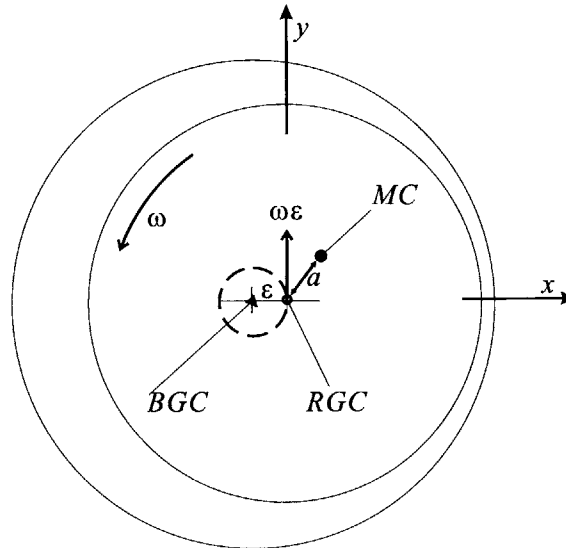


Figure 3-1: Sketch of isotropic journal bearing.

As discussed in the last chapter, when the rotor is rotating, it precesses synchronously because of the rotor unbalance. Due to the symmetry in the isotropic journal bearing system, the orbit of the precessing rotor geometric center is a circle with its center located at the bearing geometric center (BGC, the axisymmetric axis, Figure 3-1).

### 3.2 Singular Behavior of Whirl Instability Limit

Analysis in the last chapter also shows that the rotor eccentricity (or the radius of the recessing orbit) is essentially the rotor unbalance when it is spinning well above the system natural frequency (the supercritical region). On the other hand, since the stability boundary of the system is normally much higher than the natural frequency (equivalently whirl ratio  $\mathfrak{R}$  is large), as shown in Figure 2-20 and Figure 2-21, it is reasonable to set the eccentricity to the unbalance  $\varepsilon=a$  in the rotor frame to calculate the stability boundary, because the normal operating speed is several times higher than the natural frequency.

Thus, during the eigenvalue analysis of Equation (2-36) used to find the stability boundary, the stiffness and damping are calculated at the eccentricity  $\varepsilon=a$ .

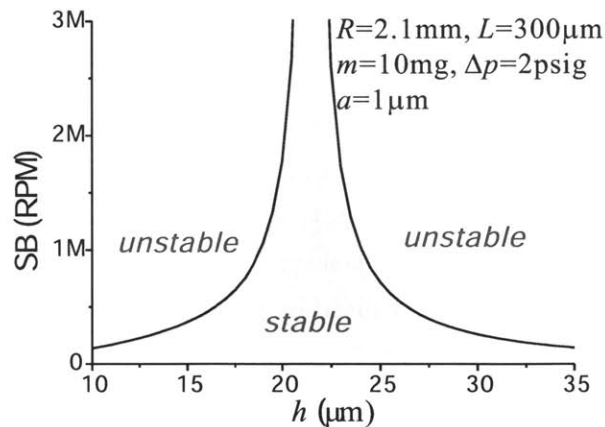


**Figure 3-2: Singular behavior of the whirl instability limit of an isotropic micro-journal-bearing system.**

Shown in Figure 3-2, the stability boundary as a function of the bearing clearance is calculated for a micro-bearing rig, with radius  $R=2.1\text{mm}$ , length of the bearing  $L=300\mu\text{m}$ , mass of the rotor  $m=10\text{mg}$ , rotor unbalance  $a=1\mu\text{m}$ , and pressure difference across the journal bearing  $\Delta p=2\text{psig}$ . On the plot, the region below the stability boundary curve is the stable operating region (the shaded area), while the region above the curve is the unstable region. There clearly is a singularity in the stability boundary curve at the clearance  $h$  of around  $21\mu\text{m}$ , which means that the stability boundary can be much higher than the design speed of  $2.4\text{Mrpm}$  for micro-bearing rig with this clearance. But with the narrow singularity, the bearing clearance fabrication tolerance requirement is beyond the fabrication capability. This will be discussed in detail in Chapter 4.

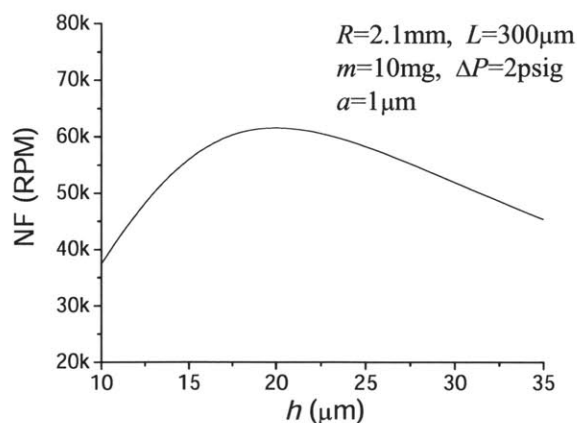


**Figure 3-3: Natural frequency vs. clearance.**

Since in the conventional large-scale bearings, the whirl ratio  $\mathfrak{R}$  (stability boundary to natural frequency ratio) is about 2, the high stability boundary means there is a high

natural frequency. The question then arises: does the singularity in the micro-isotropic-journal-bearing system have anything to do with the system's natural frequency?

The system natural frequency shown in Figure 3-3 is found to have a maximum around the same clearance. However, careful analysis will indicate that the increase is only about 50% for the natural frequency, while it approaches infinite for the stability boundary. Thus, the singularity of the stability boundary cannot be explained by the peak of the natural frequency; it must be caused by some singular behavior of the whirl ratio  $\mathfrak{R}$  instead.

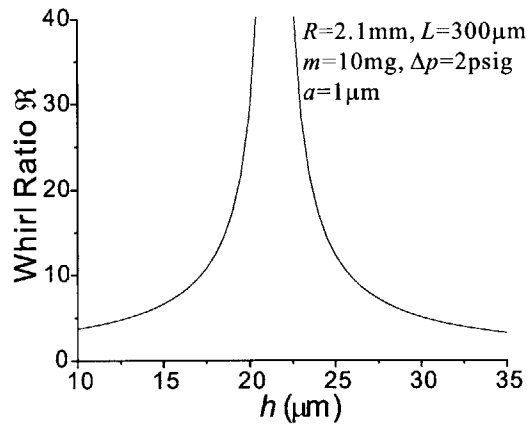


**Figure 3-4: Whirl ratio vs. clearance.**

The whirl ratio  $\mathfrak{R}$  shown in Figure 3-4 is derived by dividing the stability boundary in Figure 3-2 by the natural frequency in Figure 3-3. Thus the cause of the singularity of the stability boundary is the singularity of the whirl ratio.

It should be noted that, according to literature [24], the whirl ratios are always near 2 for large-scale conventional bearings, and this kind of singular behavior has never been observed in them. Thus, there must be some physical mechanism unique to the micro-bearing system that causes the whirl ratio to be singular with certain bearing geometry and can be an order of magnitude higher than that of a conventional large-scale system.

From the following analysis based on first principles, this mechanism is found to be that the two components of the cross-coupled hydrodynamic force in ultra-short micro-bearing systems, which act in opposite directions and are of the same magnitude due to the small  $L/D$ , cancel each other and hence the net force vanishes with certain bearing geometry, making the system always stable.

### 3.3 Whirl Instability Limit of Micro-Journal-Bearing System with Zero Unbalance

To understand the underlying physics of the singularity in whirl ratio, it is useful to start the analysis with an isotropic journal-bearing system with even simpler dynamics—that is, a system with negligible rotor unbalance. Journal-bearing systems with finite rotor unbalance will be further investigated in the next section.

When the rotor unbalance is zero, the mass center of the rotor is located at the geometric center of the rotor. Then the radius of rotor precession orbit is zero according to Equation (2-38) and the three centers (mass center of rotor, rotor geometric center, and bearing geometric center) coincide. It is convenient to analyze the system in the stator frame.

#### 3.3.1 Whirl Ratio $\mathfrak{R}$ and Whirl Number $W$

First, the whirl ratio of the system will be derived by the following analytical approach through the eigenvalue analysis.

Based on the analysis above and according to Equation (2-34), the rotordynamic equations for the isotropic journal-bearing system with zero unbalance in the stator frame become

$$\begin{cases} m\ddot{x} = K_{xx}x + K_{xy}y + C_x\dot{x} \\ m\ddot{y} = K_{yx}x + K_{yy}y + C_y\dot{y} \end{cases} \quad (3-1)$$

As in the last chapter,  $K$  denotes the stiffness and  $C$  denotes the damping coefficient. The rotational speed  $\omega$  consists in  $K_{xy}$  and  $K_{yx}$  (the cross coupled stiffness from hydrodynamic force) —  $K_{xy}=k_{xy}\omega$  and  $K_{yx}=k_{yx}\omega$  according to Equation (2-23), where  $k_{xy}$  and  $k_{yx}$  denote the intrinsic hydrodynamic stiffness, which is independent of  $\omega$ . Since the system is isotropic and  $\varepsilon=0$ , due to the symmetry, the stiffness and damping coefficient can be rewritten as

$$\begin{cases} K_{xx} = K_{yy} \equiv K^{hs} \\ -K_{xy} = K_{yx} \equiv K^{hd} \\ C_x = C_y \equiv C \end{cases} \quad (3-2)$$

where  $K^{hs}$  is the hydrostatic stiffness (direct-coupled stiffness),  $K^{hd}$  is the hydrodynamic stiffness (cross-coupled stiffness), and  $C$  is the isotropic damping coefficient. They are all calculated at the centered position ( $\varepsilon=0$ ). Equations (3-1) can then be simplified to

$$\begin{cases} m\ddot{x} = K^{hs}x - K^{hd}y + C\dot{x} \\ m\ddot{y} = K^{hd}x + K^{hs}y + C\dot{y} \end{cases} \quad (3-3)$$

Using the Laplace transform ( $\dot{x} \rightarrow sx$ ,  $\ddot{x} \rightarrow s^2x$ ), the characteristic polynomial of Equation (3-3) yields

$$m^2s^4 - 2mCs^3 - (2mK^{hs} - C^2)s^2 + 2K^{hs}Cs + (K^{hs})^2 + (K^{hd})^2 = 0, \quad (3-4)$$

where  $s$  is the Laplace variable.

The system described by Equations (3-3) will be unstable if one or more of the roots of the characteristic Equation (3-4) have positive real parts. Therefore, at the onset of instability, some roots will be purely imaginary, and hence the Laplace variable  $s$  can be replaced by  $i\Omega$ . Equation (3-4) then becomes

$$m^2\Omega^4 + 2imC\Omega^3 + (2mK^{hs} - C^2)\Omega^2 + 2iK^{hs}C\Omega + (K^{hs})^2 + (K^{hd})^2 = 0. \quad (3-5)$$

Separating the real parts from the imaginary parts of this equation, and noticing that  $m$ ,  $K^{hs}$ ,  $K^{hd}$ , and  $C$  are all real, one can obtain

$$\begin{cases} m^2\Omega^4 + (2mK^{hs} - C^2)\Omega^2 + (K^{hs})^2 + (K^{hd})^2 = 0 \\ 2mC\Omega^3 + 2K^{hs}C\Omega = 0 \end{cases} \quad (3-6)$$

From the second equation of Equations (3-6),  $\Omega$  is found to be

$$\Omega^2 = -K^{hs}/m. \quad (3-7)$$

Thus, at the onset of whirl instability, the rotor is whirling at the natural frequency of the rotor-bearing system.

To determine the threshold rotor speed at the onset of the instability, one can obtain the following equation by substituting Equation (3-7) into the first equation of Equations (3-6):

$$C^2\Omega^2 = (K^{hd})^2. \quad (3-8)$$

Meanwhile, differentiating Equation (2-23) with respect to  $\varepsilon$  at  $\varepsilon=0$  gives the expression for  $K^{hd}$ :

$$K^{hd} = \pi\mu \frac{RL}{h_0^2} \left( \frac{1}{2} \frac{L^2}{h_0} - R \right) \omega, \quad (3-9)$$

where  $\omega$  is the rotor rotating speed. As discussed in the last chapter, the first term on the right hand side of Equation (3-9) is due to the rotor pumping action, while the second

term is due to the viscous drag effect. It can be seen that  $K^{hd}$  is linearly proportional to the rotating speed  $\omega$ ,  $K^{hd}=k^{hd}\omega$ , and  $k^{hd}$  is the intrinsic hydrodynamic stiffness, which is composed of two parts:

$$k^{hd} \equiv k_p - k_v, \text{ where, } k_p \equiv \frac{\pi}{2} \mu \frac{RL^3}{h_0^3}, \quad k_v \equiv \pi \mu \frac{R^2 L}{h_0^2}. \quad (3-10)$$

In the above equation (3-10),  $k_p$  and  $k_v$  are the intrinsic hydrodynamic stiffness due to rotor pumping action and the intrinsic hydrodynamic stiffness due to viscous drag effect respectively. It is important to note that  $k^{hd}$  is only a function of bearing geometry. Substituting Equation (3-10) into Equation (3-8), the threshold rotating speed at the onset of instability ( $\Omega_w$ ) can be obtained:

$$\Omega_w^2 = \Omega^2 \left( \frac{C}{k^{hd}} \right)^2 = \Omega_N^2 \left( \frac{C}{k^{hd}} \right)^2. \quad (3-11)$$

The above equation can also be rewritten in terms of whirl ratio  $\mathfrak{R}$ :

$$\mathfrak{R}^2 = \left( \frac{\Omega_w}{\Omega_N} \right)^2 = \left( \frac{C}{k^{hd}} \right)^2. \quad (3-12)$$

At the same time, according to Equation (2-32), with  $\varepsilon=0$ , the damping  $C$  coefficient is

$$C = -\pi \mu R \frac{L^3}{h_0^3}. \quad (3-13)$$

Comparing Equation (3-13) with (3-10), one can find that  $C=-2k_p$ . Substituting Equation (3-13) and (3-10) into (3-12) yields

$$\mathfrak{R} = \left| \frac{C}{k^{hd}} \right| = \left| \frac{C}{k_p - k_v} \right| = \left| \frac{2}{1 - k_v/k_p} \right| = \left| \frac{2}{1 - 2Rh_0/L^2} \right|. \quad (3-14)$$

It is useful to define a non-dimensional parameter denoted as whirl number  $W$ , which only depends on the bearing geometry:

$$W \equiv \frac{k_v}{k_p} = \frac{2Rh_0}{L^2}. \quad (3-15)$$

The whirl number indicates the ratio of the intrinsic hydrodynamic stiffness due to viscous drag effect to the intrinsic hydrodynamic stiffness due to rotor pumping action. With this definition, the whirl ratio becomes

$$\mathfrak{R} = \left| \frac{2}{1-W} \right|. \quad (3-16)$$

It is important to note that the expression for the whirl ratio  $\mathfrak{R}$  is singular when the whirl number  $W=1$ . With  $R=2.1\text{mm}$  and  $L=300\mu\text{m}$ ,  $h_0$  of around  $21\mu\text{m}$  produces a whirl number  $W\approx 1$  and hence yields an infinite whirl ratio. This explains why it has singular behavior around  $h_0=21\mu\text{m}$  in Figure 3-4.

### 3.3.2 Forward and Backward Whirl

It is important to note that in Equation (3-14), the intrinsic hydrodynamic stiffness  $k^{hd}$  is the denominator, which means that the hydrodynamic force is the driving factor of the unstable rotor whirling motion. On the other hand, as discussed in the last chapter, the hydrodynamic force acts in the direction perpendicular to the rotor displacement ( $\delta\epsilon$ ), and has two components: the one due to rotor pumping action and the one due to viscous drag effect, which act in opposite directions and are of comparable magnitude (Figure 3-5). The ratio of the hydrodynamic force due to viscous drag effect to the hydrodynamic force due to rotor pumping action is denoted as whirl number  $W$  (Equation (3-15)).

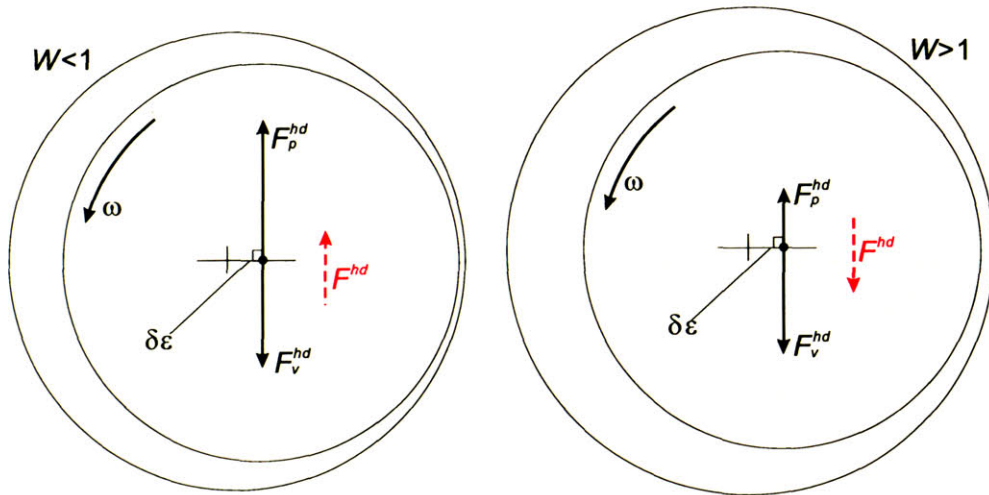


**Figure 3-5: Hydrodynamic forces for micro-journal bearings with  $W < 1$  (left) and  $W > 1$  (right).**

In the journal-bearing system with  $W < 1$ , the hydrodynamic force due to rotor pumping action is larger than that due to viscous drag effect, resulting in a net hydrodynamic force acting in the direction of the rotor rotation (the left sketch of Figure 3-5). Then, the whirling tendency induced by this net destabilizing hydrodynamic force is in the direction of the rotor rotation. This whirl motion is referred to as forward whirl.

Contrarily, in a journal bearing with  $W > 1$ , the hydrodynamic force due to rotor pumping action is smaller than that due to viscous drag effect, resulting in a net hydrodynamic force acting in the direction opposite to the rotor rotation (the right sketch of Figure 3-5). In this case, the whirling tendency induced by this net destabilizing hydrodynamic force is against the rotor rotation. This whirl motion is then referred to as backward whirl.

The above discussion on the underlying physics of the whirl motion is supported by the following simple analysis. To obtain the direction of the whirl motion, it is useful to introduce the complex eccentricity  $\varepsilon = x + y \cdot i$ , where  $i^2 = -1$ , and then Equations (3-3) can be combined into one,

$$m\ddot{\varepsilon} = K^{hs} \varepsilon + iK^{hd} \dot{\varepsilon} + C\dot{\varepsilon}. \quad (3-17)$$

Again, at the threshold of instability, the system is neutrally stable. Thus some eigenvalues will be purely imaginary, which can be written as  $i\Omega$ , implying that  $\varepsilon$  has the solution of form:

$$\varepsilon = \varepsilon_0 \exp(i\Omega t), \quad (3-18)$$

where,  $\varepsilon_0$  is the amplitude of the whirl. Substituting this into Equation (3-17) and separating the real parts from the imaginary parts yields

$$\begin{cases} m\Omega^2 + K^{hs} = 0 \\ C\Omega + K^{hd} = 0 \end{cases} \quad (3-19)$$

The first equation indicates that the frequency of the whirl is the natural frequency of the journal bearing, similar to Equation (3-7). Although the second equation is also similar to Equation (3-12), it contains the information of the whirling direction as well as the threshold speed ( $\Omega_w$ ),

$$\frac{\Omega_w}{\Omega} = -\frac{C}{k^{hd}} = \frac{2}{1-W}. \quad (3-20)$$

The above equation is positive when  $W$  is smaller than 1, which means the frequency of the whirl  $\Omega$  has the same sign as the threshold rotating speed  $\Omega_w$  at the onset of whirl instability. This whirling motion, which is in the same direction as the rotor rotation, is the forward whirl. On the other hand, the above equation is negative when  $W$  is larger than 1, resulting in a whirling motion in the direction opposite to the rotor rotation: the backward whirl.



In addition, if the hydrodynamic force due to rotor pumping action is equal in magnitude to the hydrodynamic force due to viscous drag effect, the net hydrodynamic force can vanish. As a result,  $W$  is 1 and the stability boundary becomes infinite according to Equation (3-20); this means that the system is stable independent of rotor speed.

More specifically, since the hydrodynamic stiffness  $K^{hd}$  is always zero in this case ( $W=1$ ), the rotordynamic equations (3-3) then degenerate into two uncoupled equations, which effectively describe the well-know simple mass-spring-damper systems in  $x$  and  $y$  directions respectively:

$$\begin{cases} m\ddot{x} = K^{hs} x + C\dot{x} \\ m\ddot{y} = K^{hs} y + C\dot{y} \end{cases} \quad (3-21)$$

These simple mass-spring-damper systems are always stable no matter what the oscillation frequency is, given negative stiffness  $K$  and damping coefficient  $C$ .

Thus, it can be seen from the above analysis that the hydrodynamic force is the destabilizing factor in the journal-bearing system. At the speed of onset of whirl instability, the rotor is driven into forward or backward whirl depending on the direction of the net hydrodynamic force. However, if the net hydrodynamic force is zero, the system becomes stable independent of the rotor speed, resulting in the singular behavior of the stability boundary.

### 3.3.3 Simple Criterion for Whirl Instability and Design Implications

The above analysis results in a simple criterion of the rotor whirling motion: the rotor is driven into a forward whirl with whirl number  $W < 1$  at the onset of instability or driven into a backward whirl with  $W > 1$  at the onset of instability. More importantly, with  $W=1$ , the micro-bearing system becomes stable independent of the rotor speed, and the whirl instability limit of the system can be potentially infinite.

Furthermore, a design implication can be obtained from this simple criterion of the rotor whirling motion: that is, the micro-bearing system should be designed to have whirl number  $W$  of near 1. As a result of this, the two components of the hydrodynamic force will balance each other and the net destabilizing hydrodynamic force will be minimized, resulting in a high whirl ratio (Figure 3-6).

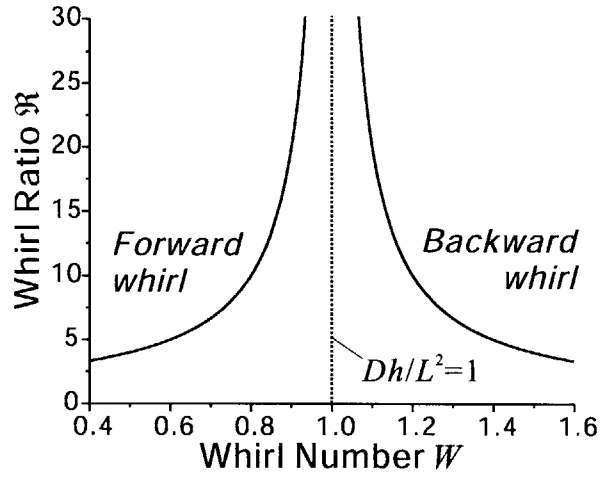


**Figure 3-6: High whirl ratio and whirl instability limit for micro-journal bearings with whirl number  $W$  of about 1.**

However, a high whirl ratio alone is not sufficient, and there are still more requirements to be met in the design. For instance, the natural frequency  $\Omega_N$  of the system needs to be high so that 1) the load capacity of the system can be sufficient and 2) the stability boundary, which is the product of the whirl ratio and the natural frequency, can be high. Furthermore, the peak amplitude of the rotor response should be small so that the system can be accelerated through the resonance. In Chapter 2, a dimensionless parameter, the damping ratio  $\zeta \equiv C/(2m\Omega_N)$ , was introduced. This damping ratio is widely used in the linear system, because it determines the peak amplitude of the response for a given rotor unbalance.

With the fluid model developed in Chapter 2, the scaling laws for the natural frequency and the damping ratio can be derived based on the linear analysis (see [37] for details):

$$\Lambda_N \propto \left(\frac{h}{R}\right)^{-1} \left(\frac{\Delta p}{p_a}\right)^{\frac{1}{2}}, \quad (3-22)$$

$$\zeta \propto \left(\frac{L}{D}\right)^2 \left(\frac{h}{R}\right)^{-1} \left(\frac{\Delta p}{p_a}\right)^{-\frac{1}{2}}. \quad (3-23)$$

One of the most critical issues, apart from the high whirl instability limit, is the requirement for a damping ratio large enough to safely invert the rotor from subcritical to supercritical speeds. Since the damping ratio  $\zeta$  scales with  $(L/D)^2$ ,  $(h/R)^{-1}$  and  $(\Delta p/p_a)^{-1/2}$ , a high  $\zeta$  requires a low bearing pressure setting  $\Delta p/p_a$ , a large  $L/D$  and a small  $h/R$ . Although the natural frequency increases when decreasing  $h/R$ , both decrease when reduc-

ing  $\Delta p/p_a$ . The catch is that for a fixed bearing geometry with a small  $h/R$  and a large  $L/D$ , the damping ratio and the natural frequency change in opposite directions when increasing the bearing pressure setting  $\Delta p/p_a$ :  $\zeta$  decreases and  $\Lambda_N$  increases, which makes crossing critical frequencies difficult.

The highest possible whirl ratio  $\mathfrak{R}$  is desired (typically over 20), which means that the whirl number  $W=Dh/L^2$  should be close to 1 according to Equation (3-15), or the length-over-diameter ratio  $L/D$  needs to be equal to the clearance-over-length ratio  $h/L$ . And in the journal-bearing system,  $h/L$  is small—about 0.05 in the micro-bearing system and 0.0006–0.0032 in the large-scale conventional bearings investigated in [24], which is also required for the damping ratio. Thus the high whirl instability limit requirement demands a small  $L/D$  ( $<0.075$  in the micro-journal-bearing system): an ultra-short hydrostatic gas bearing with an  $L/D$  one order of magnitude smaller than that of a conventional hydrostatic gas bearing yields a whirl ratio  $\mathfrak{R}$  one order of magnitude larger than that of a conventional gas bearing. Or, to put it another way, ultra-high-speed devices that require high whirl ratios demand ultra-short (small  $L/D$ ) bearings.

Therefore, according to the scaling laws and the simple criterion, one can roughly find out what the bearing geometry should be if the rotor size changes. For example, if  $R$  increases by a factor of 2, both the bearing clearance  $h$  and the bearing length  $L$  should increase by a factor of 2 so that the natural frequency  $\Lambda_N$ , the damping ratio  $\zeta$ , and the whirl ratio  $\mathfrak{R}$  (or the whirl number  $W$ ) can be kept roughly unchanged. Starting from here, one can further utilize the models established in this chapter and the last chapter, which account for the nonlinearity of the bearing forces, to make a more accurate design.

### **3.4 Effect of Unbalance on Whirl Instability Limit**

The above analysis has focused on systems with zero or negligible unbalance. In the real micro-devices, due to imperfections in the fabrication process like etch non-uniformities and pattern misalignments, the blade height is not uniform and the center of the blade row circle is not located at the center of the bearing. As a result of this, the devices normally have a rotor unbalance of several microns. How this unbalance affects the stability boundary of the system is investigated in the following analyses. One can find that the singular behavior of the stability boundary still exists with the rotor unbalance and that singularity point shifts with the unbalance.

The unsteady equations of the unbalanced rotor motions in the rotor frame are linearized first about the circular rotor precession orbit. The equations are then analyzed in

the frequency domain to determine the eigenvalues of the rotor-bearing system so that the stability boundary can be obtained.

As discussed previously, the isotropic journal-bearing system has a unique and important feature during high-speed operation: that is, the rotor spins around its mass center, or the radius of its precessing orbit equals its unbalance. With this feature, the rotordynamics can be modeled more simply in the rotor frame as Equation (2-36), which is copied below:

$$\begin{cases} m(\ddot{x} - 2\omega\dot{y} - \omega^2 x) = K_{xx}x + K_{xy}y + C_x(\dot{x} - \omega y) \\ m(\ddot{y} + 2\omega\dot{x} - \omega^2 y) = K_{yx}x + K_{yy}y + C_y(\dot{y} + \omega x) \end{cases} \quad (2-36)$$

The stiffness  $K$  and damping coefficient  $C$  in the above equation are calculated at rotor eccentricity  $\varepsilon=a$  (the unbalance). It is useful to introduce the following variables:  $S_{xx} \equiv K_{xx}/m + \omega^2$ ,  $S_{yy} \equiv K_{yy}/m + \omega^2$ ,  $S_{xy} \equiv (K_{xy} - C_x\omega)/m$ ,  $S_{yx} \equiv (K_{yx} + C_y\omega)/m$ ,  $D_{xx} \equiv C_x/m$ ,  $D_{yy} \equiv C_y/m$ ,  $D_{xy} \equiv 2\omega$ , and  $D_{yx} \equiv -2\omega$ . With these variables, Equation (2-36) can be rewritten as

$$\begin{cases} \ddot{x} = S_{xx}x + S_{xy}y + D_{xx}\dot{x} + D_{xy}\dot{y} \\ \ddot{y} = S_{yx}x + S_{yy}y + D_{yx}\dot{x} + D_{yy}\dot{y} \end{cases} \quad (3-24)$$

Using the Laplace transformation, the characteristic polynomial of the above equation is found to be

$$\begin{aligned} s^4 - (D_{xx} + D_{yy})s^3 + (D_{xx}D_{yy} - D_{xy}D_{yx} - (S_{xx} + S_{yy}))s^2 \\ + (S_{xy}D_{yx} + S_{yx}D_{xy} - S_{xx}D_{yy} - S_{yy}D_{xx})s + S_{xx}S_{yy} - S_{xy}S_{yx} = 0, \end{aligned} \quad (3-25)$$

where  $s$  is the Laplace variable. Similarly, at the onset of instability the Laplace variable  $s$  is purely imaginary, and can be written as  $i\Omega$ . Substituting this into Equation (3-25) and separating real parts and imaginary parts, one can obtain

$$\Omega^4 + (D_{xy}D_{yx} + (S_{xx} + S_{yy}) - D_{xx}D_{yy})\Omega^2 + S_{xx}S_{yy} - S_{xy}S_{yx} = 0, \quad (3-26)$$

and

$$(D_{xx} + D_{yy})\Omega^2 + S_{xy}D_{yx} + S_{yx}D_{xy} - S_{xx}D_{yy} - S_{yy}D_{xx} = 0. \quad (3-27)$$

Equation (3-27) shows that the whirl frequency is the system natural frequency as previously determined for the bearing systems with zero rotor unbalance. Substituting Equation (3-27) into Equation (3-26) yields the following equation. The stability boundary can then be calculated.

$$\begin{aligned} & \frac{(S_{xy}D_{yx} + S_{yx}D_{xy} - S_{xx}D_{yy} - S_{yy}D_{xx})^2}{(D_{xx} + D_{yy})^2} + S_{xx}S_{yy} - S_{xy}S_{yx} \\ & - (D_{xy}D_{yx} + m(S_{xx} + S_{yy}) - D_{xx}D_{yy}) \frac{S_{xy}D_{yx} + S_{yx}D_{xy} - S_{xx}D_{yy} - S_{yy}D_{xx}}{(D_{xx} + D_{yy})} = 0. \end{aligned} \quad (3-28)$$

Note that  $K_{xy}=k_{xy}\omega$  and  $K_{yx}=k_{yx}\omega$ , implying that  $S_{xy}\equiv\omega(k_{xy}-C_x)/m$ ,  $S_{yx}\equiv\omega(k_{yx}+C_y)/m$ , and then Equation (3-28) can be rewritten as

$$A\omega^4 + B\omega^2 + E = 0; \quad (3-29)$$

where

$$A = 4(k_{xy} - k_{yx})^2,$$

$$\begin{aligned} B = 2 & \frac{(k_{xy} - k_{yx})(K_{xx} - K_{yy})(C_y - C_x) + (C_x + C_y)^2(K_{xx} + K_{yy})}{m} \\ & + \frac{(k_{yx}C_x + k_{xy}C_y)(C_x^2 - C_y^2) - k_{xy}k_{yx}(C_x + C_y)^2}{m^2}, \end{aligned}$$

$$E = -\frac{C_x C_y (K_{xx} - K_{yy})^2}{m^2} + \frac{C_x C_y (C_x + C_y) (K_{xx} C_y + K_{yy} C_x)}{m^3}.$$

Thus the stability boundary can be calculated by solving Equation (3-29). Since the equation is singular for  $A=0$ , the stability boundary of the system with non-zero unbalance will also have singular behavior with  $A=0$ . It is important to note that  $A$ ,  $B$ , and  $E$  are calculated at the eccentricity  $\varepsilon$  of the rotor unbalance  $a$ .

Furthermore,  $A=4(k_{xy}-k_{yx})^2=0$  if and only if  $k_{xy}=k_{yx}$ . As discussed in the last chapter,  $k_{xy}=K_{xy}/\omega = -F^{hd}/\omega\varepsilon$  and  $k_{yx}=K_{yx}/\omega = \partial F^{hd}/\omega\partial\varepsilon$ , and  $F^{hd}=F_p-F_v$ , where  $F_p$  is the hydrodynamic force due to the rotor pumping action and  $F_v$  is the hydrodynamic force due to the viscous drag effect. Thus  $k_{xy}=k_{yx}$  gives

$$F_p + \frac{\partial F_p}{\partial \varepsilon} \varepsilon = F_v + \frac{\partial F_v}{\partial \varepsilon} \varepsilon \quad (3-30)$$

$F^* \equiv F + \varepsilon \partial F / \partial \varepsilon$  is denoted as effective force. Then with  $F_p^* = F_v^*$ , the system with non-zero unbalance is stable independent of rotor speed, which is consistent with the result obtained for the system with zero unbalance (Equation (3-21)). Note that these effective forces are also calculated with  $\varepsilon=a$ .

Therefore, hydrodynamic force is also the destabilizing factor in systems with non-zero unbalance. The unbalanced rotor can also evolve into either the forward or backward whirl at the onset of whirl instability, depending on the direction of net effective hydrodynamic force. Furthermore, since the two components of the hydrodynamic force are different functions of the rotor eccentricity (Equation (2-20) and (2-22) respectively), one can expect that the singularity point (or the balance point of the hydrodynamic force) shifts with the rotor unbalance (which determines the eccentricity at the operating conditions). This effect of unbalance on stability boundary is clearly captured in Figure 3-7.

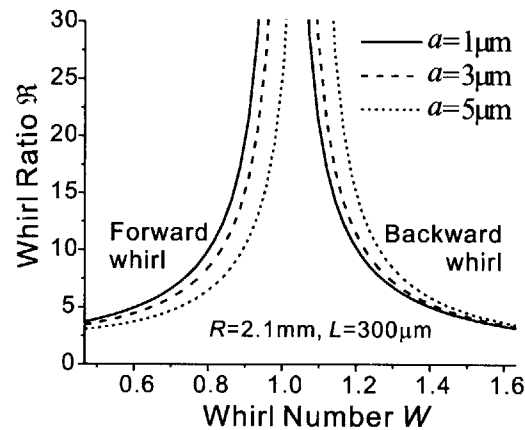


**Figure 3-7: Whirl ratio vs. whirl number for various levels of rotor unbalance.**

It has been mentioned several times that when the rotor is spinning, it also precesses due to the unbalance. At the onset of instability, the rotor also engages in another motion: whirl about the bearing center. Thus, the rotor will engage in 3 modes of motion superimposed on one another at the onset of whirl instability: rotation at rotational speed  $\omega$ , precession with the frequency of  $\omega$  (synchronous precessing), and whirl at the natural frequency of the system.

### **3.5 Summary and Conclusions**

The ultra-short isotropic micro-journal-bearing system has been investigated in this chapter. Based on first-principle analysis, a singular behavior of the stability boundary was discovered in this bearing system that has not been observed in large conventional gas journal bearings. The profound physical mechanism of this unique singularity is that, due to the small  $L/D$  in the ultra-short micro-bearing system, the two components of the cross-coupled hydrodynamic force—hydrodynamic force due to rotor pumping action

and hydrodynamic force due to viscous drag effect, which act in opposite directions—are of comparable magnitude and are capable of canceling each other.

Furthermore, the analysis shows that it is the hydrodynamic force that destabilizes the system and drives the rotor into a whirling motion, which is the same as in the large-scale gas bearings. A simple criterion of the whirl instability was established based on first-principle analysis: that is, at the onset of whirl instability, the rotor will be driven into forward whirl if the hydrodynamic force due to the rotor pumping effect is larger than the hydrodynamic force due to the viscous drag effect, and otherwise it will be driven into a backward whirl. Furthermore, a system with a net zero hydrodynamic force will always be stable, resulting in the singular behavior of the stability boundary. As discussed in Chapter 2, the approximation of the flow in the bearing as a fully developed Couette-type flow in the tangential direction may not be accurate with high axial velocity and rotor speed. As a result, the singularity point may shift from the model prediction. The whirl ratio may also be higher than the prediction, because the hydrodynamic force is smaller with an undeveloped flow. These effects are still under investigation.

The highest possible whirl ratio  $\mathfrak{R}$  (over 20) is desired so that the high design speed can be reached with the natural frequency of the micro-bearing system. This means that the whirl number  $W$  should be close to 1, so that the destabilizing hydrodynamic force is small and the singularity of the stability boundary can be utilized. In other words, the length-to-diameter ratio should be equal to the clearance-to-length ratio,  $L/D=h/L$ , in order to obtain a high whirl ratio. This means that for a small  $h/L$ , governed by the damping coefficient (Equation (2-33)) and damping ratio ( $\zeta \propto (h/R)^{-1}(L/D)^2$ ) requirements, the bearing length-to-diameter ratio  $L/D$  should be small and of order  $h/L$ . Thus, the high whirl instability limit requirement demands a small  $L/D$ : an ultra-short hydrostatic gas bearing with an  $L/D$  one order of magnitude smaller than that of a conventional hydrostatic gas bearing yields a whirl ratio  $\mathfrak{R}$  one order of magnitude larger than that of a conventional gas bearing. Or put another way, ultra-high-speed devices that require high whirl ratios demand ultra-short (small  $L/D$ ) bearings.

## Chapter 4

# Dynamic Behavior and Whirl Instability of Anisotropic Hydrostatic Micro-Gas-Journal-Bearing Systems

In the previous chapter, the ultra-short isotropic hydrostatic micro-journal-bearing system was investigated. In that system, the two components of hydrodynamic force are found to be able to balance each other with certain bearing geometry, causing a singularity in the system stability boundary. Because of this, ultra-high-speed devices which require high whirl ratios demand ultra-short (small  $L/D$ ) bearings.

Furthermore, a design of the journal bearing for a micro-bearing rig can be obtained from Figure 3-7, which is plotted below using the stability boundary (SB) and clearance  $h$  of the bearing in Figure 4-1:

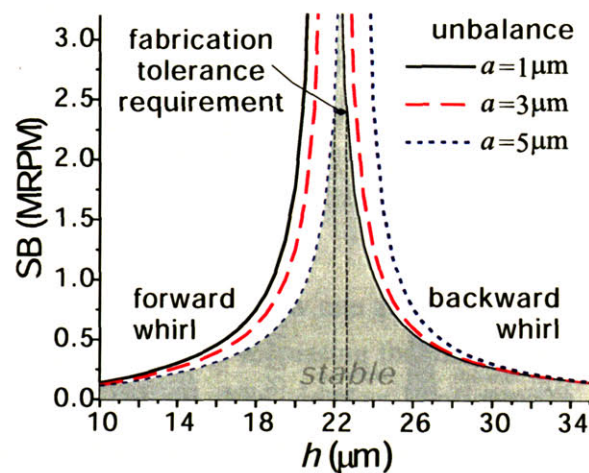


**Figure 4-1: Stability boundary as a function of bearing clearance for typical levels of rotor unbalance.**

According to [4] and [30], the rotor unbalances are normally from  $1 \mu\text{m}$  to  $5 \mu\text{m}$  due to the varying height of the blades caused by etch non-uniformity and misalignment between the blade ring center and the rotor geometric center. Moreover, control of the fabrication process is limited. Therefore, to stably operate the micro-devices at high design



speed (2.4 million rpm at  $\Delta p$  of 5 psig) with any possible rotor unbalance from 1 to 5  $\mu\text{m}$ , the journal bearings should be designed and fabricated with a bearing clearance of  $22.2 \pm 0.8 \mu\text{m}$ .

Unfortunately, journal bearing clearances with such tight tolerance ( $\pm 0.8 \mu\text{m}$ ) can hardly be fabricated according to [4]. As mentioned in the introductory chapter, the MIT micro-devices are fabricated on silicon wafers using Deep Reactive Ion Etching (DRIE). Due to the limitations of this manufacturing technology, when etching a journal bearing trench that is 300  $\mu\text{m}$  deep and 22.5  $\mu\text{m}$  wide at a radius of 2.1 mm, the fabrication uncertainty can be as much as 2  $\mu\text{m}$  in bearing clearance and 20  $\mu\text{m}$  in bearing length. Thus, the fabricated bearing clearance can be easily off target, resulting in a reduction of the maximum achievable rotor speed to roughly half the design speed.

Furthermore, when designing a bearing to reach a specific speed, a safety margin is normally needed, and thus the designed micro-journal bearing should have an even higher stability boundary. This makes the fabrication tolerance requirement even tighter. For example, a stability boundary of 3 million rpm, with only a modest safety margin (25%), requires a tighter tolerance of  $\pm 0.6 \mu\text{m}$ , which is impossible to achieve using the current fabrication technologies.

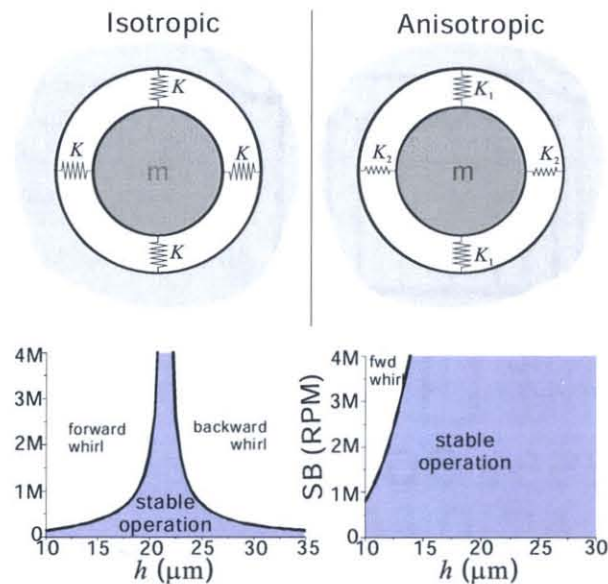


**Figure 4-2: Elimination of singular behavior in stability boundary and relieved fabrication tolerance requirements due to hydrostatic stiffness anisotropy.**

The novel micro-gas-journal bearing configuration presented in this chapter to solve the problem above is based on the idea of bearing support stiffness anisotropy. The concept is to break symmetry in hydrostatic direct stiffness and thus eliminate the narrow singularity of the stability boundary. This relieves the fabrication tolerance requirements and further increases the whirl instability limit of the system. These effects are conceptually shown in Figure 4-2, with a comparison to an isotropic journal-bearing system.

### ***4.1 Symmetry: Enemy of Stability***

It was suggested by Smith (1933) [27] that when there is considerable lack of symmetry in the bearing support stiffness, the transition speed from stable to unstable operation is high compared with critical speeds even if there is no stationary damping. And Ehrich (1989) [28] analyzed the stability boundary of a Jeffcott rotor model for a representative range of values of support stiffness anisotropy and system damping ratio. The results showed that anisotropy is effective in suppressing of instability for lightly damped systems, but less so for systems with higher damping.

It will be shown through both analytical modeling and numerical simulations that, the hydrostatic anisotropy introduced to the micro-journal-bearing system can greatly improve the stability boundary of the system and eliminate the narrow singularity.

#### **4.1.1 Anisotropic Bearing System Configuration: Part-Bearing System**

In anisotropic journal-bearing systems, the hydrostatic stiffness is different in the two perpendicular directions (principal directions). One of the implementations of this kind of journal-bearing system is the part-bearing system that is used in micro-bearing-rig devices. There are many other ways to realize the anisotropy in the micro-bearing system that will be introduced later in this chapter.

Since the bearing feed pressure and flow rate govern the hydrostatic stiffness, anisotropy can be introduced by reducing or increasing the amount of flow through a circumferential sector of the bearing gap. The simplest configuration is to block the flow through two circumferential sectors, as depicted in Figure 4-3.

The two remaining circumferential sectors are fed with pressurized air from plena located on the aft side of the rotor. Since the axial clearance gap between the rotor and the static structure in the blocked region is small and yields high flow resistance, the hydrostatic pressure buildup is limited, and thus the hydrostatic force is reduced in these locations. As a consequence, the hydrostatic stiffness in the  $X$  and  $Y$  directions will be different, introducing anisotropy in the journal bearing stiffness. Note that the journal and

rotor geometries are still circular and axisymmetric, and that asymmetry is introduced only in the hydrostatic feed air system (without the blocked feed regions, the journal bearing is axisymmetric and the hydrostatic stiffness is isotropic).

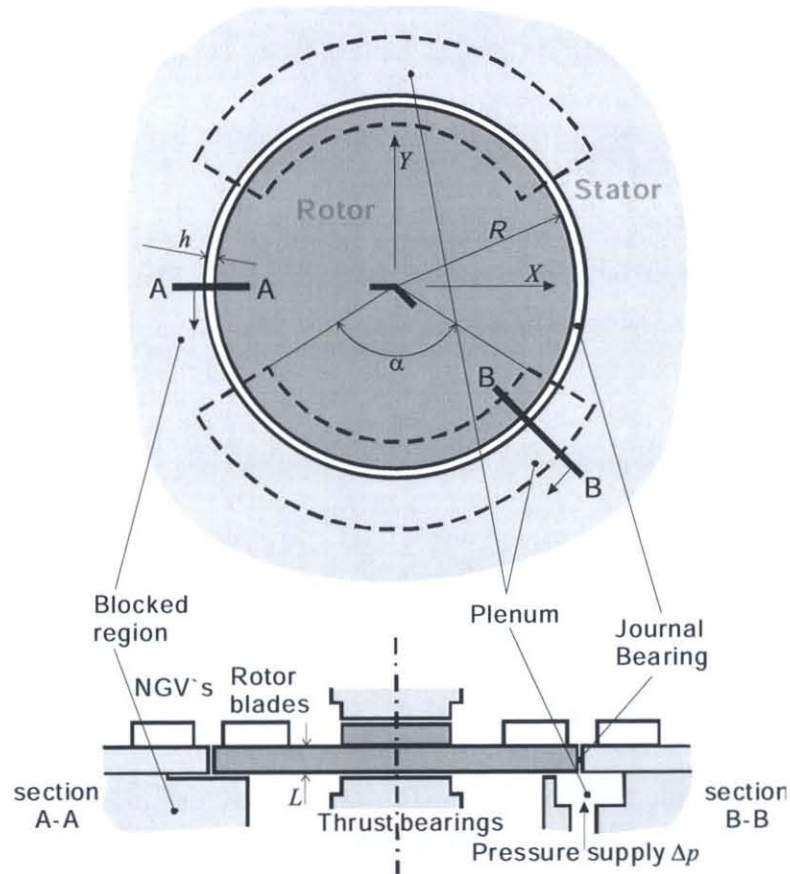


Figure 4-3: Sketch of the part-bearing system.

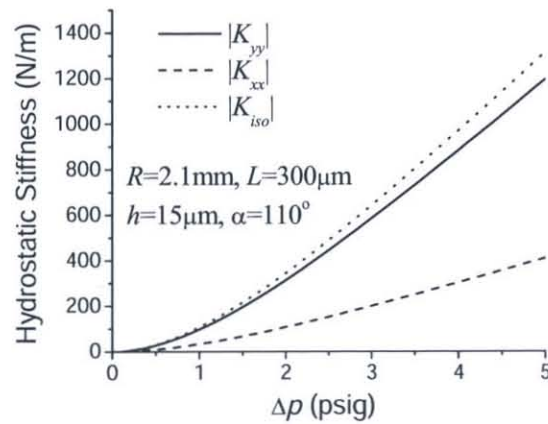


Figure 4-4: Hydrostatic stiffness of the part-bearing system compared with the isotropic case.

The models for the hydrostatic force and stiffness are similar to the ones for the isotropic journal-bearing system derived in Chapter 2, except that the circumferential integration ranges are limited to the two plena ( $2\alpha$ ) instead of the whole circumference ( $2\pi$ ). The stiffness calculated for the part-bearing system is shown in the plot Figure 4-4, compared with the one calculated for the isotropic system which, has the same bearing geometry otherwise.

It is worth noting that the hydrostatic stiffness in  $Y$  direction ( $K_{yy}$ ) doesn't decrease much, while the one in  $X$  direction ( $K_{xx}$ ) is reduced by a factor of 3. Thus, using this part-bearing configuration, the anisotropy of hydrostatic stiffness is introduced to the micro journal-bearing system. The following analysis on the anisotropic bearing system is based on this part-bearing configuration without losing generality.

#### 4.1.2 Dynamic Response Curves of Anisotropic Bearing Systems

Due to the anisotropy of the system, which breaks the axisymmetry in the isotropic system, the rotor precession orbit in the anisotropic bearing system will not necessarily be circular. The following linear analysis shows that both the response curve and the orbits in the anisotropic system are different from those in the isotropic journal-bearing system. The results show that the anisotropic journal-bearing system has two natural frequencies due to the direct coupled hydrostatic stiffness anisotropy.

First, to get a rough picture of the rotor precession orbits and response curves in the anisotropic bearing system, the rotordynamic equations in the stator frame (Equations (2-34)) are linearized around the centered position, which yield

$$\begin{cases} m\ddot{x} = K_{xx}x + K_{xy}y + C_x\dot{x} + m\omega^2 a \cos(\omega t) \\ m\ddot{y} = K_{yx}x + K_{yy}y + C_y\dot{y} + m\omega^2 a \sin(\omega t) \end{cases} \quad (4-1)$$

Since the stiffnesses in  $X$  and  $Y$  directions are different in the anisotropic bearing system, there are two natural frequencies in the system. Like the natural frequency of the isotropic bearing system, the ones in the anisotropic bearing system can be calculated from the hydrostatic stiffness:

$$\Omega_x = \sqrt{\frac{-K_{xx}}{m}}, \quad \Omega_y = \sqrt{\frac{-K_{yy}}{m}}. \quad (4-2)$$

Equations (4-1) describe forced oscillations. The solutions of the oscillations are in the form  $x=x_s\sin(\omega t)+x_c\cos(\omega t)$  and  $y=y_s\sin(\omega t)+y_c\cos(\omega t)$ . Substituting these into the above equation, equations of  $x_s$ ,  $x_c$ ,  $y_s$  and  $y_c$  can be derived:

$$\begin{bmatrix} K_{xx} + m\omega^2 & -C_x\omega & K_{xy} & 0 \\ C_x\omega & K_{xx} + m\omega^2 & 0 & K_{xy} \\ K_{yx} & 0 & K_{yy} + m\omega^2 & -C_y\omega \\ 0 & K_{yx} & C_y\omega & K_{yy} + m\omega^2 \end{bmatrix} \begin{pmatrix} x_s \\ x_c \\ y_s \\ y_c \end{pmatrix} = \begin{pmatrix} 0 \\ m\omega^2 a \\ m\omega^2 a \\ 0 \end{pmatrix}. \quad (4-3)$$

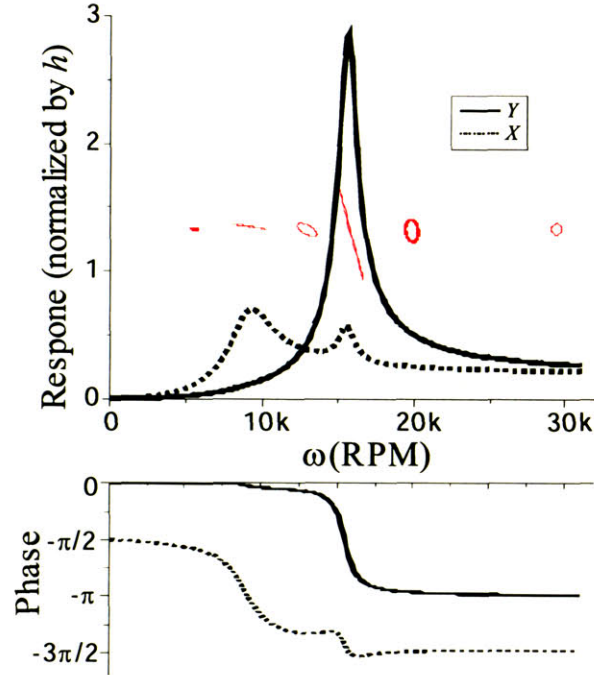


**Figure 4-5: Amplitudes, phases, and the rotor precession orbits as functions of the rotational speed.**

Thus the amplitude and the phase of the rotor response can be calculated using Equations (4-3). The results shown in Figure 4-5 are calculated for the part-bearing system with unbalance  $3 \mu\text{m}$ ,  $\Delta p$  0.5 psig, and  $\alpha$  of  $110^\circ$ . The amplitudes of the responses are normalized by the bearing clearance, which is  $15 \mu\text{m}$ . Amplitude larger than 1 at the higher resonance in the plot means that the rotor cannot cross the natural frequency, according to the linear model.

Judging from the amplitude and the phase change of the rotor response plotted in Figure 4-5, as expected, one can find that there are two resonances (natural frequencies) in the anisotropic bearing system, which is different from the isotropic system. At the lower natural frequency, the amplitude of the rotor response curve in  $X$  direction has a peak, and the corresponding phase is shifted by  $180^\circ$ . Thus this natural frequency is denoted as the natural frequency in  $X$  direction,  $\Omega_x$ . Similarly, at the higher natural frequency, the rotor response curve in  $Y$  direction has a peak with the corresponding phase



shift of  $180^\circ$ , and this natural frequency is denoted as the natural frequency in  $Y$  direction ( $\Omega_y$ ).

Similar to the curve for the isotropic system, the response curve in each direction increases with speed in the subcritical region, while it approaches the unbalance of the rotor in the supercritical region. Thus the rotor in the anisotropic bearing system also spins around its mass center when the rotational speed is far above the natural frequencies.

It is important to note that the rotor precession orbit in the anisotropic bearing system is not circular as plotted in Figure 4-5 (red ones) when the rotational speed is not high. Moreover, when the rotor speed is near one of the natural frequencies, the orbit almost shrinks to a line. This feature of the anisotropic bearing system also distinguishes it from the isotropic system.

Also note that the calculations shown in Figure 4-5 are based on the linearized Equation (4-1), and thus the nonlinear behavior of the rotor response curve, including the skew and flatness that were observed for the isotropic system with nonlinear bearing forces in Chapter 2, is omitted. If the nonlinearities of bearing forces are accounted for, there will be skewness and flatness in the response curves for the anisotropic bearing system. Most importantly, the nonlinearities of the bearing forces can greatly reduce the peak amplitudes, and hence the rotor can cross the natural frequencies in the above system. This nonlinear effect will be further investigated later using numerical simulations.

### 4.1.3 Whirl Instability Limit of Anisotropic Bearing Systems with Zero Unbalance

When the rotor is precessing induced by the rotor unbalance, the bearing force varies with time due to the anisotropy of the hydrostatic stiffness, and it is difficult to solve this time-dependent system through analytical approaches. To simplify analysis and enable an analytical approach, the rotor unbalance is assumed to be negligible in the following analysis, and the eigenvalue analysis can then be used for the linearized equation of the unsteady rotor motion to derive the stability boundary of the anisotropic bearing system. Furthermore, it can be shown that the equation of the stability boundary for the anisotropic journal-bearing system is the generalized form of that for the isotropic journal-bearing system.

As discussed in the last chapter, when the rotor has negligible unbalance, the radius of the rotor precession orbit is zero, or the rotor is fixed at the bearing center when spin-

ning. Then the rotordynamics can be investigated in the stator frame with Equation (3-1), which is repeated below:

$$\begin{cases} m\ddot{x} = K_{xx}x + K_{xy}y + C_x\dot{x} \\ m\ddot{y} = K_{yx}x + K_{yy}y + C_y\dot{y} \end{cases} \quad (3-1)$$

Note that the stiffness  $K$  and damping coefficient  $C$  in the anisotropic bearing system are different from those of the isotropic journal-bearing system in Chapter 3, due to the partial blockage of the journal-bearing flow. Still,  $K_{xx}$  and  $K_{yy}$  denote the direct-coupled hydrostatic stiffness,  $K_{xy}$  and  $K_{yx}$  denote the cross-coupled hydrodynamic stiffness, and  $C_x$  and  $C_y$  denote the damping coefficients in  $X$  and  $Y$  direction respectively. Using the Laplace transformation, the characteristic polynomial of the above equations can be obtained:

$$\begin{aligned} m^2s^4 - m(C_x + C_y)s^3 - [m(K_{xx} + K_{yy}) - C_xC_y]s^2 \\ + (K_{xx}C_y + K_{yy}C_x)s + K_{xx}K_{yy} - K_{xy}K_{yx} = 0. \end{aligned} \quad (4-4)$$

where  $s$  is the Laplace variable.

Then the system described by Equations (3-1) will be unstable if one or more of the roots of the characteristic Equation (4-4) have positive real parts. At the onset of instability, the system is neutrally stable, and some of the roots are purely imaginary. With this situation, the Laplace variable can be replaced by  $i\Omega$ , and Equation (4-4) becomes

$$\begin{aligned} m^2\Omega^4 + im(C_x + C_y)\Omega^3 + [m(K_{xx} + K_{yy}) - C_xC_y]\Omega^2 \\ + i(K_{xx}C_y + K_{yy}C_x)\Omega + K_{xx}K_{yy} - K_{xy}K_{yx} = 0. \end{aligned} \quad (4-5)$$

Decoupling the real parts and the imaginary parts of the above equation and noticing that  $m$ ,  $K$ s, and  $C$ s are all real yields

$$\begin{cases} m^2\Omega^4 + [m(K_{xx} + K_{yy}) - C_xC_y]\Omega^2 + K_{xx}K_{yy} - K_{xy}K_{yx} = 0 \\ m(C_x + C_y)\Omega^3 + (K_{xx}C_y + K_{yy}C_x)\Omega = 0 \end{cases} \quad (4-6)$$

The whirl frequency at the onset of instability can be derived from the second of the above equations:

$$\Omega^2 = -\frac{K_{xx}C_y + K_{yy}C_x}{m(C_x + C_y)}. \quad (4-7)$$

As a result, whirl frequency  $\Omega$  is the damping weighted average of the natural frequencies in  $X$  and  $Y$  directions.

In order to get the threshold speed at the onset of whirl instability, substituting equation (4-7) into the first equation of (4-6) yields

$$K_{xy}K_{yx} = -C_x C_y \left[ -\frac{K_{xx}C_y + K_{yy}C_x}{m(C_x + C_y)} + \frac{(K_{xx} - K_{yy})^2}{(C_x + C_y)^2} \right]. \quad (4-8)$$

As discussed in Chapter 2, the hydrodynamic stiffness  $K_{xy}$  and  $K_{yx}$  are linearly proportional to the rotational speed  $\omega$ :  $K_{xy} = k_{xy}\omega$  and  $K_{yx} = k_{yx}\omega$ , where  $k_{xy}$  and  $k_{yx}$  are the intrinsic hydrodynamic stiffness independent of the rotational speed. Note that the rotational speed  $\omega = \Omega_w$ , the threshold speed at the onset of instability, and the above equation then becomes

$$\Omega_w^2 = -\frac{C_x C_y}{k_{xy}k_{yx}} \left[ \Omega^2 + \frac{(K_{xx} - K_{yy})^2}{(C_x + C_y)^2} \right]. \quad (4-9)$$

Equation (4-9) shows that the stability boundary of the anisotropic journal-bearing system depends on the ratio of the damping coefficient and the intrinsic hydrodynamic stiffness, similar to that of isotropic journal-bearing system (refer to Equation (3-20)). Furthermore, in the isotropic limit as described by Equations (3-2) (repeated below),

$$\begin{cases} K_{xx} = K_{yy} \equiv K^{hs} \\ -K_{xy} = K_{yx} \equiv K^{hd} \\ C_x = C_y \equiv C \end{cases}, \quad (3-2)$$

Equation (4-9) degenerates exactly into Equation (3-11), the equation of the stability boundary for the isotropic journal-bearing system with zero rotor unbalance. Therefore, Equation (4-9) is the generalized form of Equation (3-11).

Note that the hydrodynamic stiffness is in the denominator of Equation (4-9), which means that it is also the destabilizing factor in the anisotropic system. A large hydrodynamic stiffness also results in a lower stability boundary in the anisotropic system. Therefore, one of the design guidelines of the anisotropic system is to reduce the hydrodynamic stiffness as much as possible.

In addition to the above similarities, Equation (4-9) is different from Equation (3-11) in the following two aspects:

First, due to the anisotropy in hydrodynamic and damping forces, the ratio of the damping coefficient to the intrinsic hydrodynamic stiffness in the anisotropy journal-bearing system is of form  $C_x C_y / k_{xy} k_{yx}$ , instead of  $(C/k^{hd})^2$  in the isotropic system.



Normally<sup>1</sup>, the hydrodynamic force due to the rotor pumping action  $F_p^{hd}$  is larger or smaller than the one due to the viscous drag effect  $F_v^{hd}$ , and hence the net hydrodynamic force acts in either a clockwise or counterclockwise direction. As a result,  $k_{xy}$  and  $k_{yx}$  are of different signs, which makes  $C_x C_y / k_{xy} k_{yx}$  positive and makes a real root of  $\Omega_W$  exist in Equation (4-9).

Another difference between Equation (4-9) and (3-11) is that Equation (4-9) has an additional term:  $(K_{xx} - K_{yy})^2 / (C_x + C_y)^2$ . This means anisotropic hydrostatic stiffness helps stabilize the system. Furthermore, the ratio of this additional term to the first term  $\Omega^2$  in the square brackets is

$$\frac{\frac{(K_{xx} - K_{yy})^2}{(C_x + C_y)^2}}{\frac{K_{xx} C_y + K_{yy} C_x}{m(C_x + C_y)}} \sim O\left(\frac{-mK^{hs}}{C^2}\right), \quad (4-10)$$

where  $K^{hs}$  is the hydrostatic stiffness and  $K_{xx}$ ,  $K_{yy}$  and  $K^{hs}$  are of the same order of magnitude. The ratio of Equation (4-10) is on the order of 500 with a pressure difference across the journal bearing  $\Delta p$  of 0.5psig, and is much larger with a higher  $\Delta p$ . Therefore, the additional term  $(K_{xx} - K_{yy})^2 / (C_x + C_y)^2$  dominates in Equation (4-9) for the system stability boundary.

The stability boundary plotted in Figure 4-6 (red dashed line) is calculated for the anisotropic bearing system based on the analytical model above, with a comparison to the stability boundary in the isotropic journal-bearing system (black solid lines). One can find that the anisotropy introduced by the anisotropic bearing configuration is an effective way to increase the system stability boundary, and it opens the window of stable operation so that the tolerance constraints can be greatly released.

Furthermore, the stability boundary in the anisotropic journal-bearing system as a function of pressure difference across the journal bearings  $\Delta p$  is plotted in Figure 4-7 (the red dashed line), compared with the one in the isotropic journal-bearing system (the black solid line). Both bearing systems have the same bearing dimensions:  $R=2.1$  mm,  $h=15$   $\mu$ m, and  $L=300$   $\mu$ m. The comparison shows that the hydrostatic stiffness anisotropy greatly enhances the stable operating range: i.e. at a bearing supply pressure of  $\Delta p=5$  psig, the bearing top speed of 700KRPM in the isotropic case is increased to a maximum stable

<sup>1</sup> There are rare cases where  $k_{xy}$  and  $k_{yx}$  have the same signs with certain bearing geometry, and the right hand side of Equation (4-9) is negative. In these cases, the unstable motion of the rotor is not the whirling motion, and the system stability boundary is not governed by Equation (4-9), which is discussed in Appendix A.

speed of over 3 million rpm using the anisotropic bearing configuration sketched in Figure 4-3.

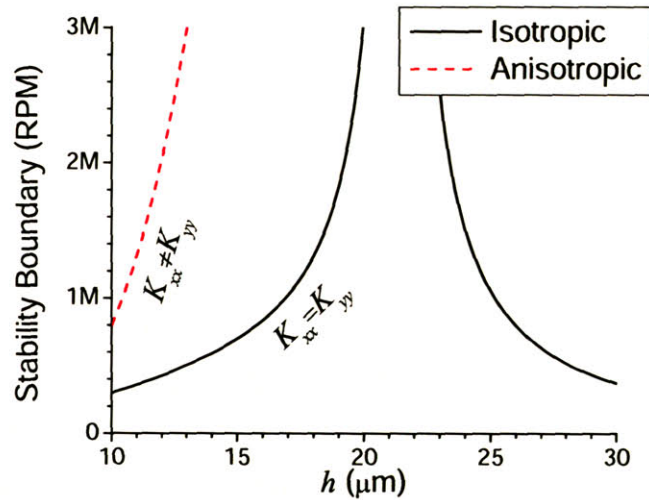


**Figure 4-6: Stability boundary for the anisotropic bearing system with zero unbalance, compared with the stability boundary in the isotropic bearing system.**

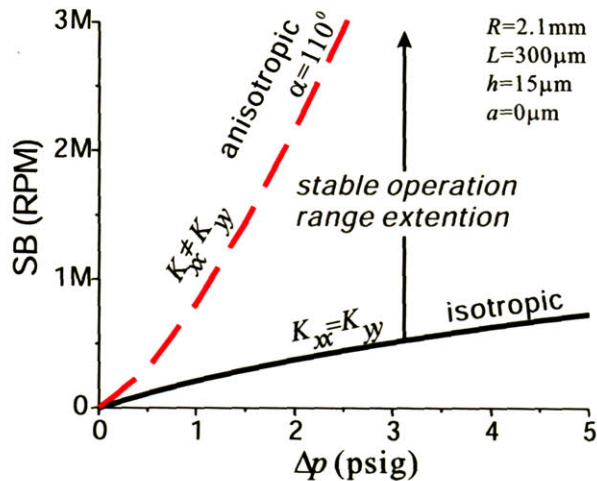


**Figure 4-7: Stable operating range extension using anisotropic bearing configuration.**

#### 4.1.4 Stabilization Through Hydrostatic Stiffness Anisotropy

To investigate the underlying mechanisms of why the hydrostatic stiffness anisotropy can greatly improve the system stability boundary, the following simplifications can be made. Since the second term on the right-hand side of Equation (4-9) is much larger than the first, the latter is negligible. Furthermore, the anisotropic bearing system can be

simplified by considering anisotropy only in the hydrostatic stiffness while keeping the hydrodynamic stiffness and damping isotropic, as in Equation (3-2). Equation (4-9) then reduces to

$$\Omega_w = \frac{|K_{xx} - K_{yy}|}{2k^{hd}}, \quad (4-11)$$

where  $k^{hd}$  is the intrinsic hydrodynamic stiffness. Then, in addition to keeping the cross-coupled hydrodynamic stiffness  $k^{hd}$  as low as possible, the anisotropic journal-bearing design can also use as large a difference in hydrostatic stiffness between the two orthogonal directions  $|K_{xx} - K_{yy}|$  as possible to further increase the stability boundary.

The physical mechanism behind the enhanced stability margin and increased rotor speed at whirl instability onset is demonstrated as follows. The hydrostatic and hydrodynamic forces acting on the rotor for an anisotropic bearing configuration are depicted in Figure 4-8. Due to anisotropy in hydrostatic stiffness,  $K_{xx} \neq K_{yy}$  as shown above, the hydrostatic force  $F^{hs}$  has a non-zero component in the tangential direction  $\theta$ :

$$F_\theta^{hs} = F_y^{hs} \cos(\theta) - F_x^{hs} \sin(\theta) = (K_{yy} - K_{xx})\varepsilon \sin(\theta)\cos(\theta). \quad (4-12)$$

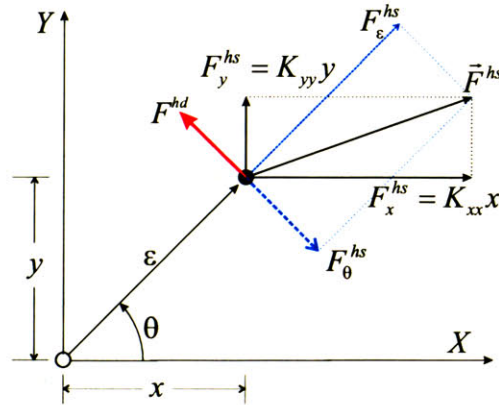


**Figure 4-8: Hydrostatic and hydrodynamic forces in the anisotropic journal-bearing system.**

The hydrodynamic force  $F^{hd} = k^{hd} \omega \varepsilon$  acts in the direction perpendicular to the rotor deflection, and the net force in the  $\theta$  direction then becomes:

$$F_\theta = \left( k^{hd} \omega - \frac{1}{2} (K_{xx} - K_{yy}) \sin(2\theta) \right) \varepsilon. \quad (4-13)$$

Thus the net tangential force is sinusoidal in the circumferential angle  $\theta$ , with an average value of  $k^{hd} \omega \varepsilon$  and a variation of  $|K_{xx} - K_{yy}| \varepsilon / 2$ .

When the rotational speed  $\omega$  is higher than  $\Omega_W$  given by equation (4-11) and hence  $|k^{hd}\omega| > |K_{xx} - K_{yy}|$ , the tangential force  $F_\theta$  will be positive (when  $k^{hd} > 0$ ) or negative ( $k^{hd} < 0$ ) independent of the rotor circumferential location  $\theta$ . This means that with this speed, the direction of  $F_\theta$  stays the same (either counterclockwise or clockwise) no matter where the rotor is in the bearing. Take the case where  $k^{hd} > 0$ , for instance: when the rotor is displaced from its centered position due to perturbations, the tangential force  $F_\theta$  will accelerate the rotor in the counterclockwise direction. Since  $F_\theta$  is always in the counterclockwise direction (though its amplitude varies), it keeps accelerating the rotor in that direction and inputting energy into this tangential motion. Therefore, the rotor tangential velocity keeps increasing and the radius of the corresponding orbit will grow. As a result, this tangential counterclockwise motion driven by the hydrodynamic force becomes unstable, and the rotor engages in a forward whirl.

Conversely, when the rotational speed  $\omega$  is lower than  $\Omega_W$  given by Equation (4-11) and hence  $|k^{hd}\omega| < |K_{xx} - K_{yy}|$ , the tangential force  $F_\theta$  is positive when the rotor is located in some circumferential sectors of the bearing and negative when the rotor is located in other sectors. In this situation, as the rotor moves around the bearing counterclockwise or clockwise, it is accelerated by  $F_\theta$  in some portions of its trajectory, while it is decelerated by  $F_\theta$  in other portions. Thus,  $F_\theta$  pumps the energy into the tangential rotor motion as well as takes the energy out. Therefore, the energy of the rotor tangential motion will not grow as in the above case, and the system is stable.

It is the anisotropy of hydrostatic force that acts against the destabilizing hydrodynamic force, stabilizing the system. To make the micro-bearing system stable, the hydrodynamic force, as the destabilizing factor, should be made as small as possible, while the anisotropy of hydrostatic force, as the stabilizing factor, should be made as large as possible.

#### ***4.2 Numerical Simulation, Whirl Instability Limit for Systems with Unbalance and Sideload***

The above analysis has assumed negligible unbalance on the rotor and thus allowed the linearization of the rotordynamic equations around the centered position as shown in Equations (3-1). However, as mentioned at the beginning of this chapter, since the rotor unbalances are normally 1~3  $\mu\text{m}$  or even larger, they are not negligible in comparison to the bearing clearance and inevitably drive the rotor into a precessing motion. Although the rotor precession orbit is almost a circle with its center located at the rotor mass center at high rotational speed, the amplitude of the bearing forces acting on the rotor varies



with the rotor position due to the anisotropy of the system. Thus, the dynamics of the system are time-dependent, which is nonlinear and cannot be solved analytically.

Furthermore, to accurately calculate the peak amplitude of the rotor response and hence the distance to contact, the rotor dynamics need to be investigated at the natural frequencies of the system with the nonlinearity of the bearing forces. As shown by the linear analysis in the last section, the rotor precession orbit in the anisotropic system is not circular at natural frequencies (Figure 4-5). Therefore, the analytical approach to calculating the peak amplitude of the rotor response curve used for the isotropic system in Chapter 2 becomes inappropriate for the anisotropic system. Because of this, a numerical simulation is the only suitable way to calculate the peak amplitude of the rotor response.

In addition, if the journal bearing supply pressures of the two feed plena are different, the rotor will experience a side-load and the journal bearing clearance will decrease on one side, introducing nonlinear behavior of the bearing fluid forces at larger eccentricities, which also requires a nonlinear numerical simulation.

#### 4.2.1 Numerical Simulation of the Rotordynamics for Anisotropic Bearing Systems

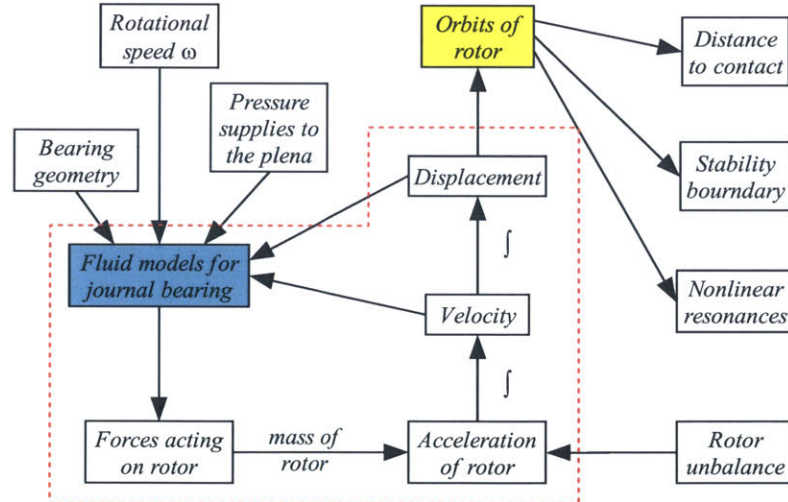


**Figure 4-9: Flowchart of the numerical simulation.**

The rotordynamics Equations (2-34) can be simulated by using the numerical ordinary differential equations (ODE) solver, with the structure of the numerical simulation program sketched in Figure 4-9.

In every time step of the simulation, the bearing forces are computed with the given rotational speed, pressure supplies, and geometry of the bearing as well as the velocities and displacements of the rotor, using the fluid models developed in Chapter 2. Then, with the mass and the rotor unbalance, the acceleration of the rotor can be calculated according to Equations (2-34). The ODE solver integrates the acceleration into the rotor velocity and displacement afterward. All these calculations are repeated in every time step and enclosed by the red dashed line box in Figure 4-9.

After all the iterations, with the rotor displacements computed from each time step, the rotor precession orbit can then be plotted. From the orbit, one can obtain the amplitude of the rotor response and determine whether the system is stable at that particular speed.

Furthermore, by altering the rotational speed and repeating the above process of simulation, the distance to contact can be obtained by searching the peak of the rotor response, and the stability boundary can also be derived by searching the threshold speed at the onset of instability.

The characteristics of the micro journal bearing

Radius (mm)	Length (um)	Clearance (um)	Imbalance (um)	Mass of the Rotor (mg)
2.1	300	15	3	10.5

Angle of the plenum (degree) 110

Gas properties		Operation Condition	
Density (Kg/m <sup>3</sup> )	Viscosity (uPa*s)	Dp in up plenum (Psig)	Dp in lower plenum (Psig)
1.25	17.8	0.5	0.5

Rotational speed (KRPM) 5

Calculate the Natural Frequency and the Stability Boundary by linear model >>>

Natural Frequency (KRPM) X direction: 9.19896 Y direction: 15.7147

Stability Boundary by linear model (MRPM) 0.123752

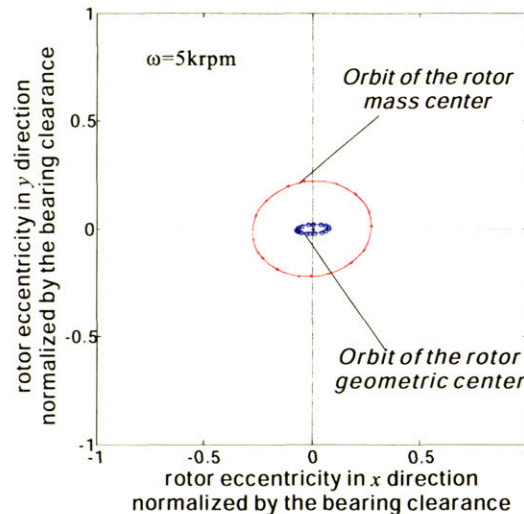
Close Simulate (mass center) >>> Simulate (geometric center) >>>

Figure 4-10: Interface of the numerical simulation program.

Figure 4-10 shows the interface of the developed simulation program. In this interface, the bearing geometry ( $R$ ,  $L$ ,  $h$ ,  $a$ ,  $m$  and  $\alpha$ ) and gas properties (density and viscosity) are inputted into the program. Then, according to the operating conditions (the pressures in two plena), the natural frequencies (in both  $X$  and  $Y$  directions) can be calculated and



displayed in the program interface. Finally, with the inputted rotational speed, the rotor precession orbit can be simulated and then plotted as in Figure 4-11.



**Figure 4-11: Sample orbits simulated for the bearing shown in Figure 4-10.**

In Figure 4-11, the red line with crosses is the orbit of the rotor mass center, while the blue line with circles is the orbit of the rotor geometric center. The orbits are normalized by the bearing clearance ( $h=15\mu\text{m}$ ). It can be seen that at this rotational speed (5 KRPM), the orbit radius of the mass center is larger than that of the geometric center, which means this speed is subcritical.

#### 4.2.2 Numerical Simulation of the Response Curve and the Stability Boundary for Anisotropic Bearing Systems

Using the numerical simulations described above, with orbits calculated for various rotating speeds, the rotor response curve can be plotted and the system stability boundary can be found.

The response curves in Figure 4-12 are calculated by the numerical simulations for the anisotropic bearing system with parameters shown in Figure 4-10, and then normalized by the bearing clearance. Compared with the response curves calculated by the linear model, they have much flatter/broader peaks due to the nonlinearities of the bearing forces. And since the distance to contact is positive and large (more than 20% of the clearance, or  $3\mu\text{m}$ ), this system can cross the natural frequency with the corresponding bearing settings.

The corresponding orbits of the rotor mass center (red crossings) and geometric center (blue circles) with increasing speeds are plotted in Figure 4-13. It can be seen that the

orbits of the rotor geometric center are similar to the ones obtained from the linear analysis shown in Figure 4-5 – the rotor spins around the geometric center in the subcritical region, while it spins around the mass center in the supercritical region.

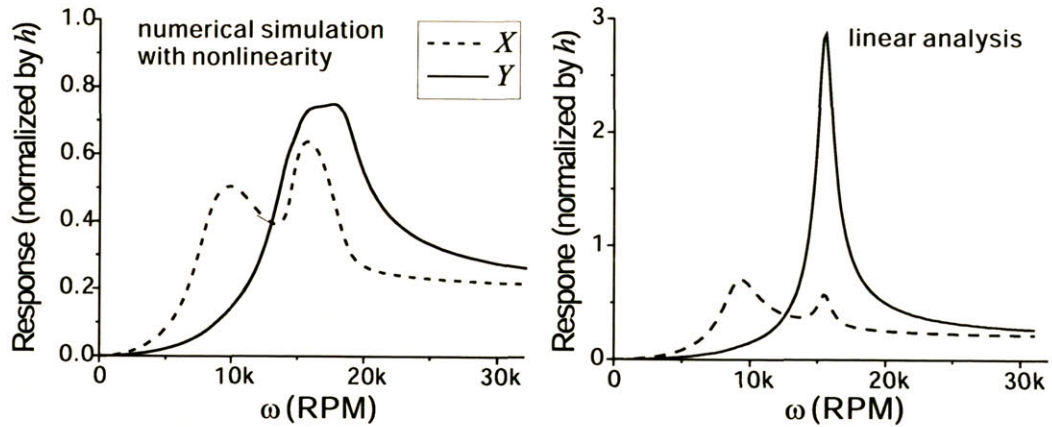


**Figure 4-12: Response curves for the micro-journal-bearing system in Figure 4-10, calculated using numerical simulations (left), compared with response curves calculated by linear analysis (right).**

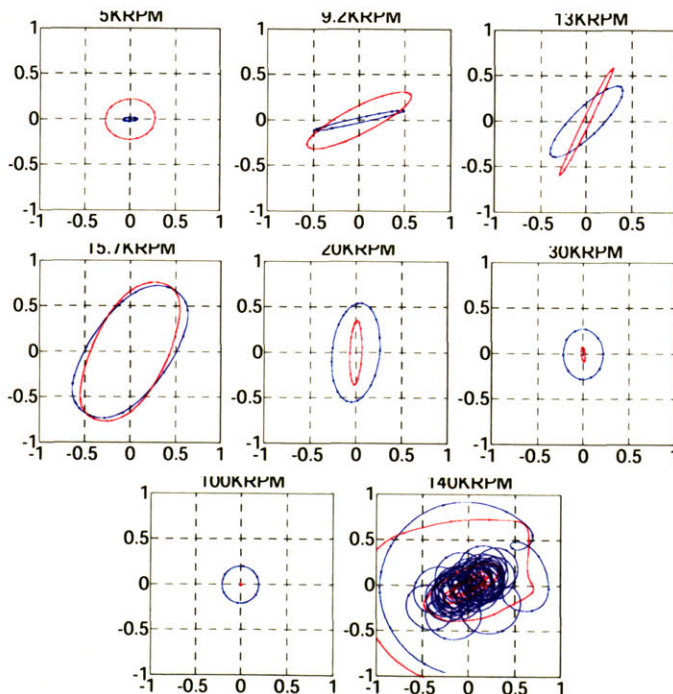


**Figure 4-13: Simulated rotor precession orbits in the anisotropic bearing system (9.2KRPM and 15.7KRPM are the natural frequencies in X and Y directions).**



It is important to note that, due to the fast increase of damping as the rotor approaches the wall, large oscillations at the natural frequencies (especially at the one in  $Y$  direction) are damped dramatically and thus the orbits tend to be flat when they are near the bearing wall. This nonlinear effect cannot be captured by the linear analytical model, and it makes the distance to contact larger so that the rotor can cross the natural frequencies. Thus, when establishing operating protocols for the anisotropic bearing system, the numerical simulation with the nonlinearity of the bearing forces must be used to predict the distance to contact, instead of the linear analysis.

In addition, since the orbits at the natural frequencies are not circular due to the anisotropy, the rotor is not near the bearing wall all the time when it is crossing the natural frequencies. This is different from the case in the isotropic system where the orbit is always circular and thus the rotor is near the bearing wall all the time when it is crossing the natural frequency. Because the bearing wall is not smooth due to the imperfections of the DRIE etching process, the rotor has less chance to touch the bearing wall in the anisotropic bearing system than in the isotropic one. Therefore, it is more possible for the rotor to cross the natural frequencies in the former, which has been observed in experiments [30].

Judging from the orbits shown in Figure 4-13, the system is stable at 100KRPM, while unstable at 140KRPM. Thus the stability boundary is between these two speeds. Repeating the calculations of orbits with smaller speed steps, a more accurate stability boundary can be found.

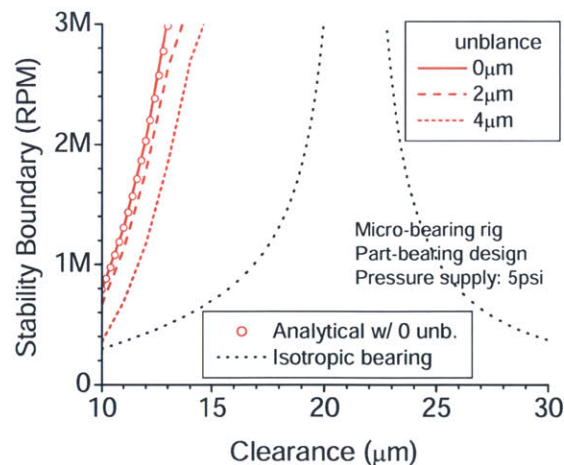


**Figure 4-14: System stability boundary as a function of bearing clearance with different rotor unbalance levels.**

As shown in Figure 4-14, the rotor unbalance decreases the system stability boundary in the anisotropic bearing system, and the larger the unbalance is, the lower stability boundary. In addition to the numerical simulations, the stability boundary is also calculated by linearized analysis (Equation (4-9)) with the same bearing conditions and zero unbalance. The analytical result is plotted as circles in Figure 4-14, which fall upon the corresponding numerical ones, and thus the simple analytical approach of equation (4-9) is validated by numerical simulations for low rotor unbalance.

At the same time, results in Figure 4-14 indicate that the stability boundary of the anisotropic bearing system is much higher compared with the stability boundary of the isotropic bearing system (the black dotted lines), even with a significant amount of rotor unbalances. Furthermore, due to the stabilizing effect of the hydrostatic stiffness anisotropy, the singular behavior in the stability boundary vanishes in the anisotropic case (only the forward whirl tendency branch is left) such that the journal bearing top speed is increased and the stringent tolerance requirements are relieved.

#### 4.2.3 Effect of Sideload on Whirl Instability Boundary in Anisotropic Bearing Systems

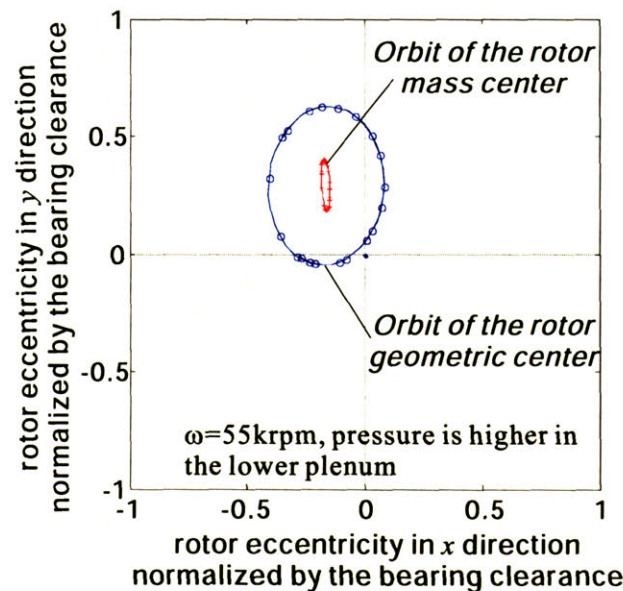


**Figure 4-15: Spinning rotor shifted from its centered position due to sideload.**

Since the two plena and the corresponding channels that supply air into the plena cannot be fabricated perfectly symmetrically due to the imperfection of the fabrication machines, there is always a certain difference between the two feeding systems that may



cause a pressure difference between the plena. This pressure difference in turn induces sideload exerting on the rotor, pushing it to the plenum with lower pressure, as shown in Figure 4-15. The numerical simulations in this section show that this sideload can significantly reduce the stability boundary of the system and should be avoided in operation.

Due to the hydrodynamic force, the equilibrium point is shifted left even though the direction of the sideload is up (the pressure is higher in the lower plenum in this case). Since the rotor is spinning near to the wall due to the sideload, it will experience different stiffness and anisotropy; hence, the system stability boundary will be affected.

In Figure 4-16, the system stability boundary is shown as a function of rotor sideload (the difference in supply pressures between the two opposite feed plena) for three levels of rotor unbalance marked by the solid, dashed and dotted lines. The results reveal that the effect of rotor sideload dramatically decreases the bearing top speed. This behavior and the underlying mechanisms are investigated next. At the same time, since the stability boundary is calculated with the bearing geometry of the devices that reached a speed of around 1.3 MRPM—the maximum experimental achieved speed range for those devices [8]—these top speeds are also indicated in the plot as a comparison. The sideloads during the experiments were high, up to 1 psig according to [8], and the fabrication research showed that the unbalances of those devices could be 1~3  $\mu\text{m}$ . Thus, the plot in Figure 4-16 indicates that they may have crashed due to the instability of the journal bearings.

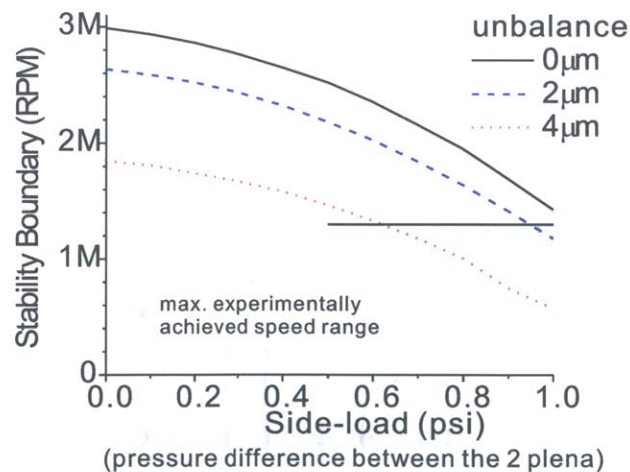


**Figure 4-16: Effect of rotor sideload on journal bearing stability boundary for the anisotropic bearing system.**

As mentioned earlier, the asymmetry in feed pressure between the two bearing air supply plena pushes the rotor toward the lower-supply-pressure side, and thus the equilibrium point of the rotor is no longer at the center of the bearing. For higher rotor sideloads, the eccentricity of the rotor relative to the bearing will increase and the hydrodynamic force  $F^{hd}$  will be larger and growing faster at large rotor eccentricity, according to Equation (2-23), which is shown in Figure 4-17. As a result, the intrinsic hydrodynamic stiffness  $k^{hd} = \partial F^{hd} / \omega \partial \varepsilon$  will increase with the rotor sideload.

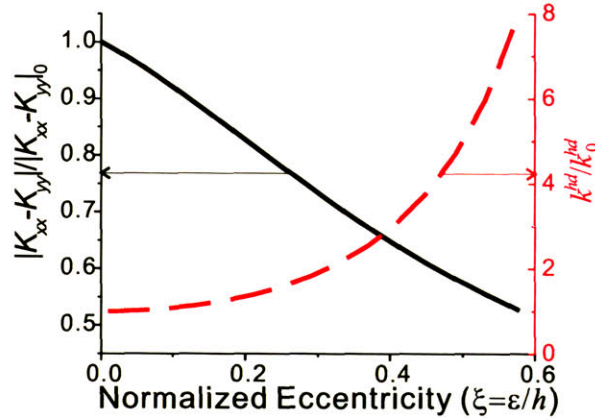


**Figure 4-17: Hydrodynamic stiffness and hydrostatic stiffness anisotropy as functions of rotor eccentricity.**

Also plotted in Figure 4-17 is the anisotropy of the hydrostatic stiffness  $|K_{xx} - K_{yy}|$ , which decreases with the rotor eccentricity and hence the sideload. Approximately, the stability boundary is the ratio of hydrostatic stiffness anisotropy to the intrinsic hydrodynamic stiffness as given in Equation (4-11), and therefore it will decrease with eccentricity. This behavior and the effect of sideload on stability boundary are clearly captured in Figure 4-16. It is important to note that the level of anisotropy in hydrostatic stiffness  $|K_{xx} - K_{yy}|$  and the magnitude of intrinsic hydrodynamic stiffness  $k^{hd}$  constitute two competing effects in the dynamic behavior of the micro-gas-bearing system: the former stabilizes the system, while the latter destabilizes it. Rotor sideload has a detrimental impacts on both effects in the light of whirl instability.

### 4.3 Implementations of Anisotropy

The above analyses have shown that the anisotropy of hydrostatic stiffness stabilize the system as well as helping the rotor to cross the natural frequency. In this section, several ways to introduce anisotropy into the micro-gas-journal-bearing system will be presented.

### 4.3.1 Anisotropy in Axisymmetric Journal-Bearing with Sideload

Conceptually, the axisymmetric journal-bearing system (or isotropic system in the previous analyses) can be transformed into an anisotropic system by applying a fixed side force/load to the rotor.

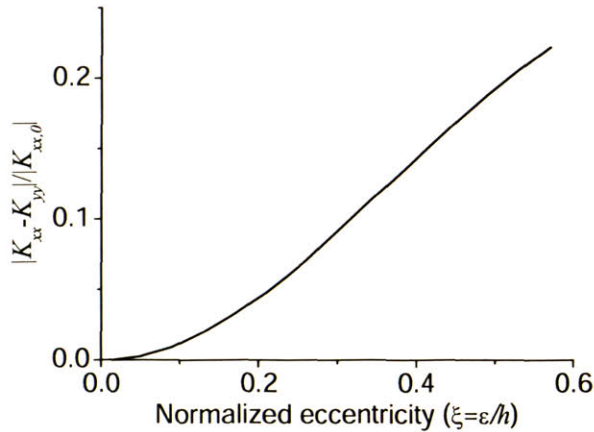


**Figure 4-18: Hydrostatic stiffness anisotropy increases with rotor eccentricity due to sideload in axisymmetric journal-bearing systems.**

When a sideload is applied to the rotor, it moves to a new equilibrium position accordingly, at which the symmetry of the system is broken and the rotor experiences anisotropic stiffness as shown in Figure 4-18.

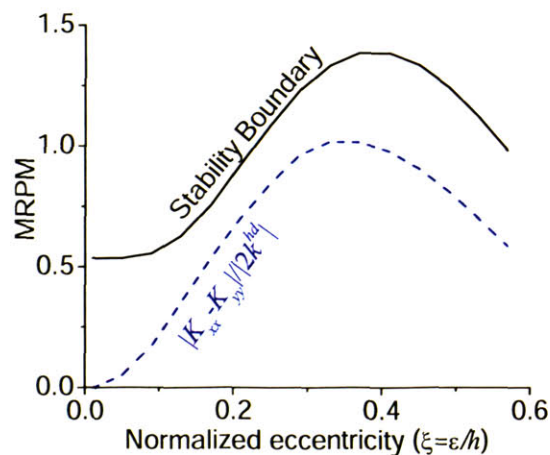


**Figure 4-19: Stability boundary of axisymmetric journal-bearing systems as a function of rotor eccentricity due to sideload.**

Meanwhile, as discussed earlier, the intrinsic hydrodynamic stiffness  $k^{hd}$  increases with the rotor eccentricity (Figure 4-17). Note that, at small eccentricities,  $k^{hd}$  increases

slower than the hydrostatic stiffness anisotropy  $|K_{xx}-K_{yy}|$ , while the former increases much faster at large eccentricities. Therefore, as the sideload increases, the stability boundary of the axisymmetric system increases with a small sideload, then decreases with a large sideload as depicted in Figure 4-19.

However, it is difficult to implement the sideload in the axisymmetric micro-gas-journal-bearing system. Normally, in the large-scale conventional journal-bearing system, the rotor weight can be used as a sideload by aligning the bearing horizontally. However, in the micro-bearing system, the rotor weight ( $\sim 0.1\text{mN}$ ) is much smaller than the hydrostatic restoring force ( $\sim 1\text{mN}$  at  $\xi=0.1$  according to Figure 2-6) due to the cube-square law, so the rotor weight is not sufficient to act as the sideload in the micro-bearing system because it can barely move the rotor.

Therefore, the axisymmetric journal bearing is not a suitable system in which to implement anisotropy.

### 4.3.2 Anisotropy in Part-Bearing Systems

The part-bearing configuration sketched in Figure 4-3 and investigated above as an implementation of anisotropy has been used for micro-bearing rigs.

However, with a more profound understanding of the system, this configuration is found to have negative side effects on the rotordynamic behavior of the system. For example, the viscous stress on the rotor in the blocked region can introduce serious coupling between the radial motion and conical (tilting) motion due to the tight clearance ( $\sim 2\ \mu\text{m}$ ) and lead the system to be unstable at a much lower speed. This is further discussed in Chapter 6 on multi-degree-of-freedom systems.

To eliminate these unwanted side effects, an alternate configuration is used: the four-plenum design, as sketched in Figure 4-20. In this four-plenum configuration, the blocked regions with tight clearance are replaced by two plena, so there are a total of four plena supplying air to the journal bearing. The four plena are divided by seals, and each of the plena has its own external pressure supply. During the normal operation, the up and down plena will be fed with high-pressure air, while the left and right ones are fed with low pressure or connected to the turbine inter-row (between the turbine blade row and the NGVs, so that the pressure drop across the journal bearing in that region is zero) to generate the hydrostatic stiffness anisotropy. It is important to note that the pressures supplied to each pair of opposite plena should be the same to eliminate unwanted sideload.



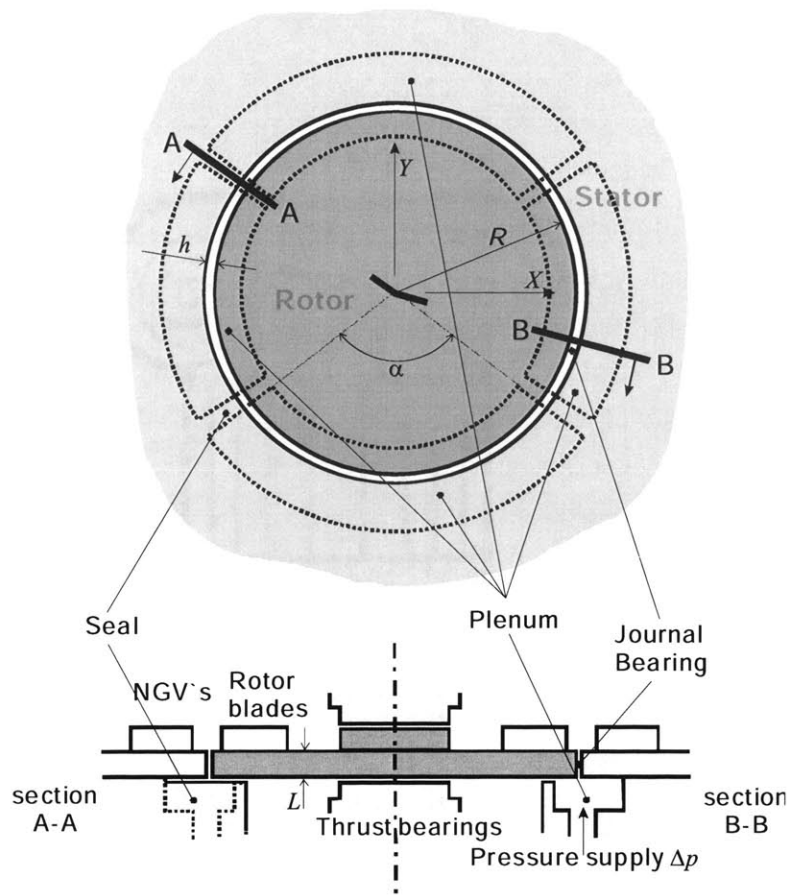


**Figure 4-20: Four-plenum configuration for the part-bearing system [7].**

Furthermore, the pressure difference between the up-down and left-right pairs of plena can be varied to adjust the level of hydrostatic stiffness anisotropy. If the supplied pressures are the same in all the plena, the system will become isotropic. Thus, the hydrostatic stiffness anisotropy of the device can be turned on and off at will. For more details of the design and experimental testing of this type of bearings see [7].

### 4.3.3 Anisotropy in Micro-Turbo-Charger Devices

Since the micro-turbo-charger has the turbine and compressor disks bonded together and the two disks (the compressor disk and the turbine disk) have different radii (Figure 1-5), the implementation of anisotropy here is different than in the micro-bearing rig discussed above.

The original journal-bearing system used in the micro-turbo-charger was isotropic, as sketched in Figure 4-21, with the blades and thrust bearing pads bonded to the two disks omitted in the figure. The pressure air is supplied through eight “coat hangers” (blue circles in the sketch that are holes through turbine NGVs with shapes like coat hang-

ers in the real devices), then flows circumferentially through the plenum between the aft-side of the compressor disk and the static structure, and finally enters the bearing(s) axially.

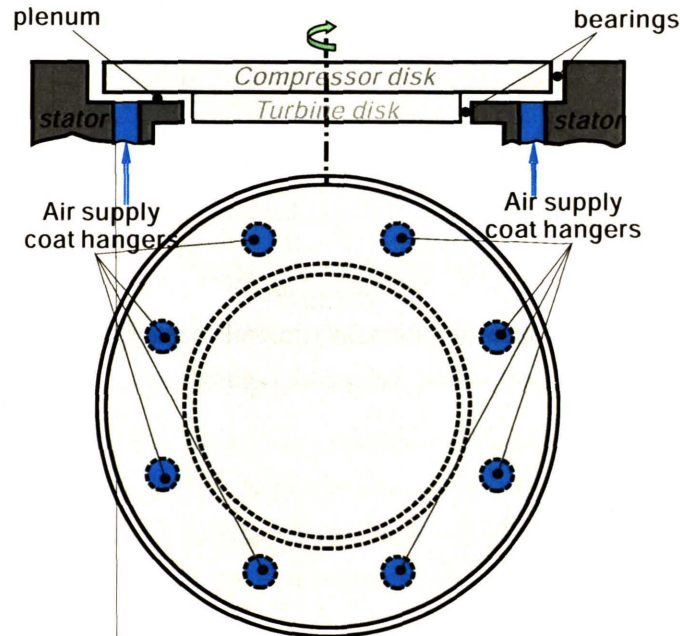


**Figure 4-21: Isotropic design of micro-turbo-charger journal bearings.**

Note that the bearing system shown in the sketch is actually a dual-bearing system (one journal bearing on each disk). A seal can be added in the plenum to block the flow to one of the bearings and thus a single-bearing system can be constructed. Since the eight coat hangers are evenly distributed along the circumferential direction in the plenum, the feed system to the bearing(s) is basically axisymmetric, and thus the journal bearings are isotropic.

The simplest way to introduce hydrostatic stiffness anisotropy to the micro-turbo-charger system, which makes the fewest changes to the structure, is to block four of the “coat hangers” as depicted in Figure 4-22.

Then, the air fed through the remaining four “coat hangers” goes circumferentially through the plenum, reaches the region where the other four “coat hangers” are blocked, and then enters the journal bearing(s) in that region. Due to the flow resistance of the plenum, the air pressure will decrease along its flow path through the plenum as plotted in Figure 4-23.



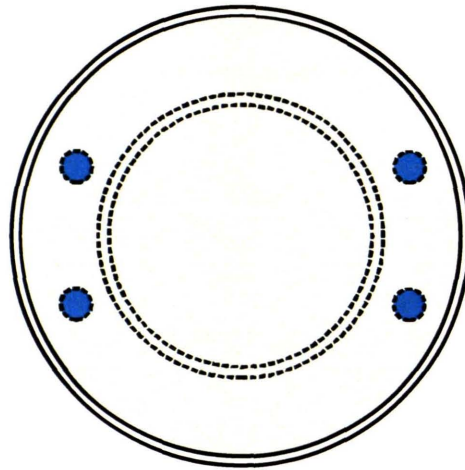


**Figure 4-22: Introduction of hydrostatic stiffness anisotropy by blocking four "coat hangers".**

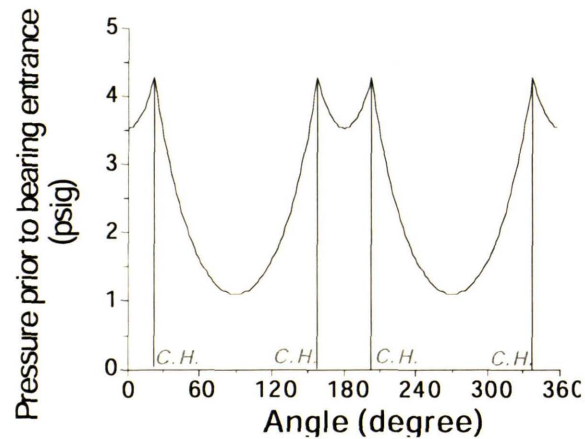


**Figure 4-23: Pressure distribution in the plenum with four "coat hangers" blocked.**

The pressure distribution shown in Figure 4-23 is calculated for a typical micro-turbo-charger device with a single bearing on the compressor side. In the calculation, the flows in both the plenum and the bearing are assumed to be one-dimensional Poiseuille flows: circumferential in the plenum, axial in the bearing. Then the pressure distribution in the plenum can be calculated by modeling the plenum and the bearing as a resistance network with mass conservation. However, modeling the flows as one-dimensional flows may not be accurate, and it can only give a rough estimation of the anisotropy in the bearing system. For accurate solutions, three-dimensional CFD calculation is needed.

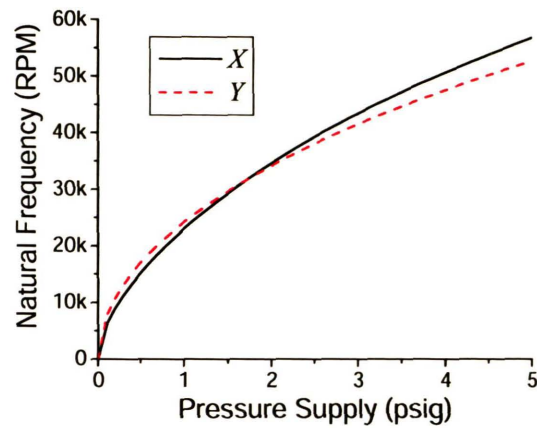


**Figure 4-24: Natural frequencies of the micro-turbo-charger device with four "coat hangers" blocked.**

The natural frequencies of the above system are then calculated and plotted in Figure 4-24. It can be seen that hydrostatic stiffness anisotropy is introduced to the system, indicated by the two different natural frequencies. However, these two natural frequencies are close to each other, implying that the hydrostatic stiffness anisotropy is small.

In order to improve the hydrostatic stiffness anisotropy, a new design is proposed as shown in Figure 4-25.

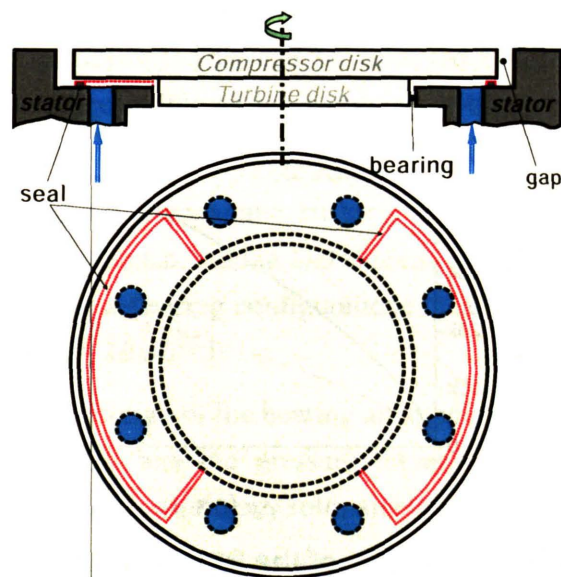


**Figure 4-25: New design of single journal bearing for micro-turbo-charger device [31].**

In the proposed new design of anisotropic journal-bearing systems for micro-turbo-charger devices, the plenum is divided into four sections as sketched in Figure 4-25, similar to the part-bearing system used in the micro-bearing rig. The two sets of plena in opposite directions are fed with the same pressure to avoid unwanted side-load. With pressure difference between the left-right and up-down pairs of plena, anisotropy is introduced to the system. Under normal operating conditions, the up-down plena are connected to the turbine inter-row so that the pressure drops across the bearing in these sections are zero and the hydrostatic stiffness anisotropy is maximized.

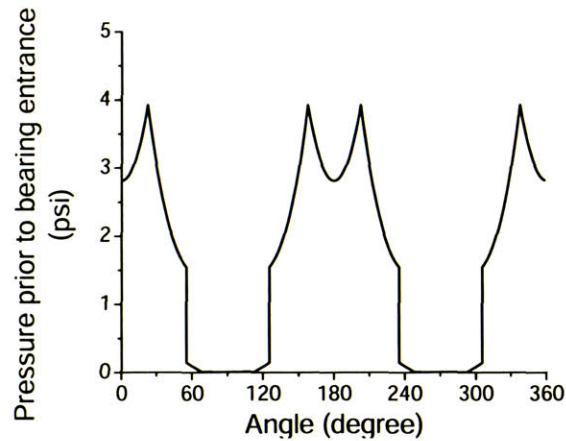


**Figure 4-26: Pressure distribution in the plenum for new design shown in Figure 4-25.**

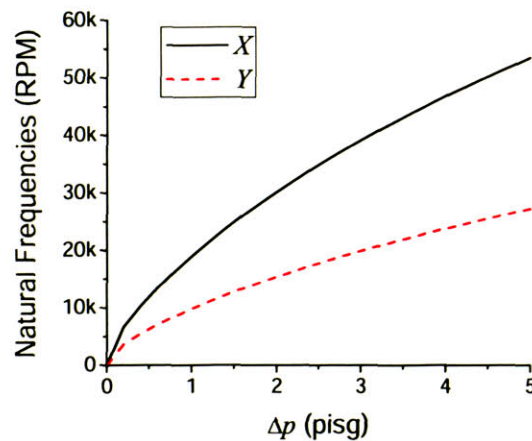


**Figure 4-27: Natural frequencies of the four-plenum design (Figure 4-25) for micro-turbo-charger devices.**

The pressure distribution along the plenum is calculated and depicted in Figure 4-26. In the plot, the peaks indicate the locations of the “coat hangers,” while the abrupt pres-

sure drops indicate the positions of radial seals. The natural frequencies of this system can then be calculated and plotted in Figure 4-27.

Thus, with more structure changes (addition of seals), greater hydrostatic stiffness anisotropy is introduced into the system. The micro turbo-charger devices using this bearing configuration are under fabrication.

#### **4.4 Summary and Conclusions**

The micro-journal-bearing system with hydrostatic stiffness anisotropy has been investigated using both an analytical linear approach and numerical full nonlinear simulations. It was shown that by breaking symmetry in hydrostatic stiffness, this novel bearing design increases bearing top speed and relieves fabrication tolerance requirements. This enables stable high-speed bearing operation and extends the bearing operating range. Furthermore, numerical simulations show that the nonlinearity of bearing forces increases the distance to contact and hence helps the rotor cross the natural frequencies. Finally, several implementations of anisotropy in the micro-bearing systems were discussed.

Given the insights gained from the anisotropic gas bearing theory and the experimental results, the following bearing design implications can be established:

1. In order to improve dynamic behavior and increase the whirl ratio, the difference in hydrostatic stiffness in the two orthogonal directions (anisotropy) should be maximized. This can be achieved (while maintaining adequate levels of average stiffness) by supplying hydrostatic feed air at different pressures over parts of the journal circumference.
2. In addition, the hydrodynamic stiffness of the journal bearing should be minimized. For a given bearing  $L/D$  this can be done using the criteria established for isotropic bearing configurations by adjusting the bearing geometry according to  $W = 2Rh/L^2 = 1$ .
3. The mechanical design of the bearing air supply system and piping should be kept bi-symmetric and the pressure losses in the opposite feed systems should be matched to avoid any rotor sideload.
4. The rotor unbalance should be kept low. However, anisotropic bearing designs enable a relief in fabrication tolerance requirements and a relaxation in rotor balancing constraints compared to their isotropic counterparts.



## Chapter 5

# Experimental Assessment of Models

In the previous chapters, both fluid and rotordynamic models were established analytically and numerically and used to calculate the rotordynamic behavior, such as the natural frequency, distance to contact, and stability boundary, of journal-bearing systems.

In this chapter, the model predictions are compared with experimental measurements of the journal bearing flow rate, the natural frequency, the distance to contact, and the stability boundary of the system, so that the aspects of the model are assessed by the experimental data.

### 5.1 Static Flow Tests

As mentioned earlier, due to the imperfection of the fabrication machines, the variation in the bearing clearance can be as large as several microns. According to the research in previous chapters, the bearing clearance is a critical dimension that affects the natural frequency, distance to contact, and stability boundary of the system. Thus, it needs to be measured accurately to characterize the fabricated journal bearing. Furthermore, precise measurement of the bearing clearance also helps develop the fabrication process, making the fabrication more accurate.

Before the establishment of the fluid models, there were two ways to measure the clearance. One was to measure the top opening of the etched bearing under an optical microscope during the fabrication process. However, because the microscope cannot zoom into the bearing due to its large aspect ratio ( $L/h$  is of order 20), the measurement cannot give any idea of the clearance in the bearing: SEM pictures show that the clearance in the bearing can be different from its top opening. As an example, in the SEM picture of a typical etched bearing shown in Figure 5-1, the measurement of the top opening under optical microscope is about  $12.8\mu\text{m}$ , more than  $3\mu\text{m}$  smaller than the clearance in the bearing ( $16.2\mu\text{m}$ ).

The other way is to cut the whole device by saw, with the cutting surface perpendicular to the journal bearing trench, and then measure the journal bearing under SEM. Figure 5-1 shows that the clearance in the bearing can be measured by this method. The



accuracy of the measurement is only 1-2 $\mu\text{m}$ , due to the blur of the bearing edge under SEM after the die-saw process. Of course, the disadvantage of this method is that it destroys the device. Another limitation of SEM measurement is that this destructive measurement is not comparable with the high-speed tests used to search for the system top speeds. This is because in these tests the rotors need to be accelerated until they crash, and they break into pieces in the high-speed crashes, making it impossible to measure the bearing clearances afterward. In other words, using SEM measurement, there is no way to know the bearing clearances of the devices that are going to be spun to high speed until they crash.

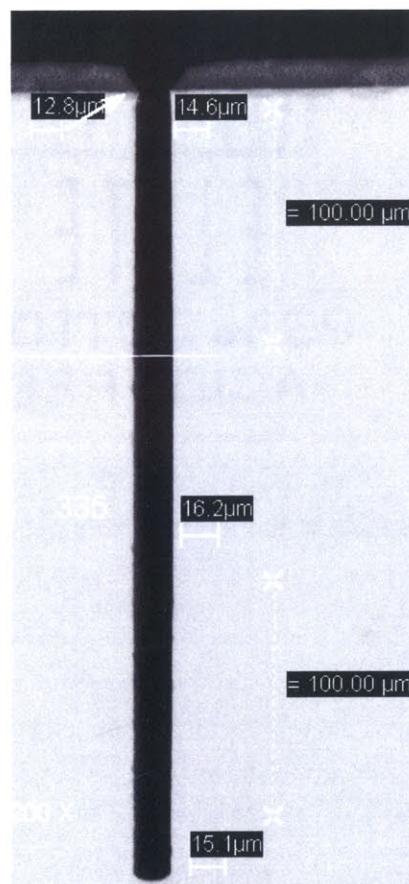


**Figure 5-1: SEM picture of a typical journal bearing trench.**

Because of the shortcomings of the methods above, another way to measure the bearing clearance was developed along with the bearing fluid modeling: using the model to reversely calculate the bearing clearance with the experimental measured flow rate. The measurement by this method is accurate, nondestructive, and compatible with the high-speed experiments, as will be shown next.

During the fabrication processes of the micro-engine devices, the millimeter-sized rotors are normally bonded to the static structures. After the whole fabrication process is finished, the rotor is then released and is free to move before the spin tests. Thus, before the release, the rotor is centered and a static flow test can be done experimentally by measuring the flow rate through the journal bearing with increasing pressure difference across the journal bearing, as shown in Figure 5-2.

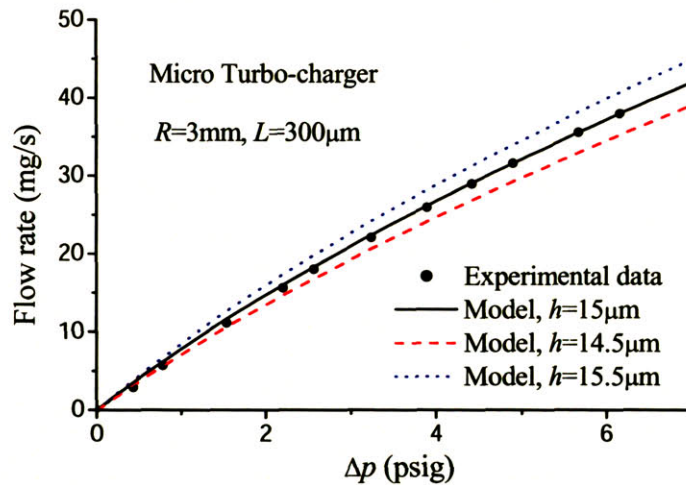


**Figure 5-2: Flow rate calculated by the model compared with experimental measurement [32] for a micro-turbo-charger device.**

The dots in the plot are the static flow measurements through the journal bearing of a micro-turbo-charger device with a rotor radius of 3mm and bearing length of 300 $\mu\text{m}$ . The destructive SEM measurement indicated that the bearing clearance was about 15 $\mu\text{m}$  [32].

The predictions of flow rate calculated by the fluid models were also plotted on the chart to compare against the experimental data. The solid line is the model prediction with the bearing clearance of 15 $\mu\text{m}$ , which matches the experimental data well. Thus, the fluid models are validated as tools to measure the bearing clearance.

At the same time, the dashed and dotted lines are the predictions using a bearing clearance of 0.5 $\mu\text{m}$  smaller and larger respectively. They both are noticeably divergent (~7%) from the experimental data. This shows that using the fluid model to reversely calculate the bearing clearance with the static flow test can have an accuracy of less than one micron. The high accuracy of this method is due to the fact that the flow rate is sensitive to the bearing clearance, because the bearing flow resistance is inversely proportional to  $h^3$  according to Equation (2-5).



Note that this method is nondestructive: after the static flow test, the rotor will be released, and then it is free to spin. Thus, the clearance of the journal bearing can be accurately measured before the high-speed test and the destructive crash.

## 5.2 Natural Frequencies

As discussed earlier, the pressure difference across the journal bearing  $\Delta p$  essentially sets the stiffness, and thus the natural frequency, of the gas journal bearing. In this section, it will be shown that the natural frequency can be measured vs.  $\Delta p$  experimentally by the methods briefly outlined below (detailed description can be found in [9] and [10]). Afterward, the model predictions are compared to the experimental measurements for both isotropic and anisotropic micro-journal-bearing systems.

### 5.2.1 Natural Frequency Measurement

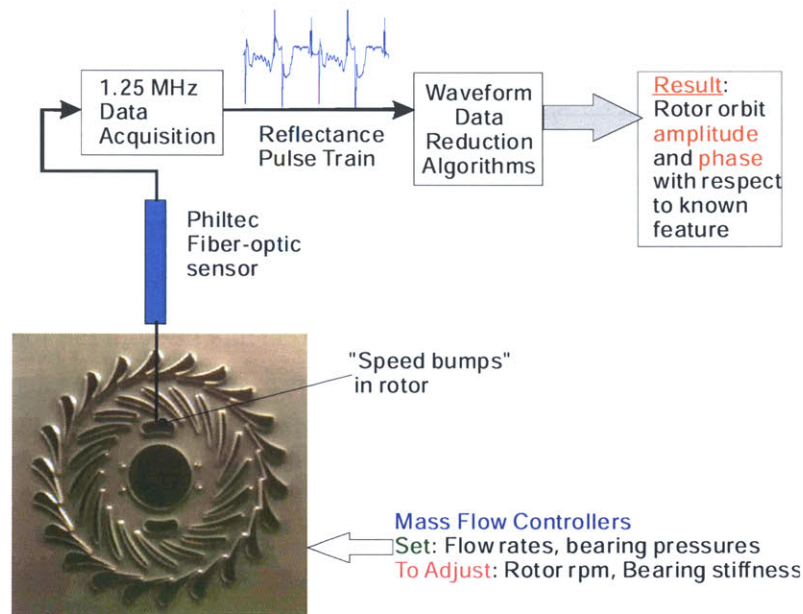


**Figure 5-3: Experimental setup [30] to measure the natural frequencies of the journal-bearing systems.**

With the experimental setup schematically shown in Figure 5-3, the turbine and bearing flow rates and pressures are regulated to achieve a particular set of rotational speed  $\omega$  and pressure difference across the journal bearing  $\Delta p$ . The rotational speed of the rotor is determined by tracking the passage of speed bumps on the surface of the rotor using a Philtec fiber-optic sensor that is inserted through an opening on top of the device. Then the bearing response is deduced using a waveform data reduction algorithm [11], which is briefly outlined below.

The imbalance of the rotor (i.e. the distance between the geometric center of the rotor and its mass center) induces a precessing motion superimposed on the rotational motion of the rotor. The precession frequency of precession-induced imbalance is known to be synchronous with the rotational frequency of the rotor, and the precession velocity yields an increase or decrease in the absolute velocity of the speed bumps. This is reflected in the fiber-optic signal, where the features of the speed bumps are cyclically compressed or dilated in time. The resulting sinusoidal waveform is essentially a pulse-width modulation of the reference waveform obtained in the absence of rotor precession. A leastsquares technique is used to deduce the optimum waveform dilation necessary to transform the whirl waveform to the reference waveform. The amplitude and the phase of this modulating function correspond to the size of the precession orbit and to the position or orientation of the orbit with respect to a particular feature on the rotor. The whirl-induced response curve is obtained by repeating this procedure for a range of rotational speeds at a fixed bearing pressure difference  $\Delta p$ .

Repeating the process for a range of rotational speeds at a fixed bearing pressure difference  $\Delta p$  will produce the corresponding response curve and thus reveal the natural frequency. The unbalance of the rotor can also be measured using this method because the amplitude of response is essentially the unbalance at high rotational speed.

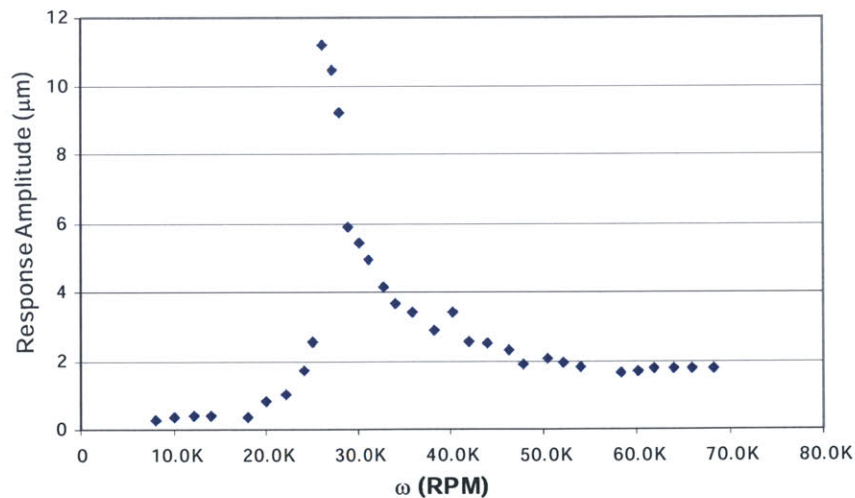


**Figure 5-4: Rotor response curve measurement using an optical fiber (courtesy of C.J. Teo).**

Figure 5-4 is the rotor response curve measured by the method mentioned above for a micro-bearing-rig device at a pressure difference across the journal bearing  $\Delta p$  of about 1psig. It can be clearly seen that the system underwent a resonance at a speed of about 30Krpm, indicating that the natural frequency of the system was 30Krpm. Furthermore,

when the rotor speed was far above the natural frequency, the rotor response amplitude was about  $2\ \mu\text{m}$ , which means that the unbalance of the rotor was approximately  $2\ \mu\text{m}$ .

Another way to measure the system's natural frequency is based on the discovery that the resistance of the journal bearing is a function of the rotor eccentricity. At the natural frequency, the eccentricity of the rotor is largest, and hence the flow resistance of the journal bearing is smallest according to Figure 2-6-a. Therefore, as the rotating speed increases with constant flow rate through the journal bearing, the pressure difference across the journal bearing  $\Delta p$  drops at the natural frequency as shown in Figure 5-5, which resembles the response curve shown in Figure 5-4.

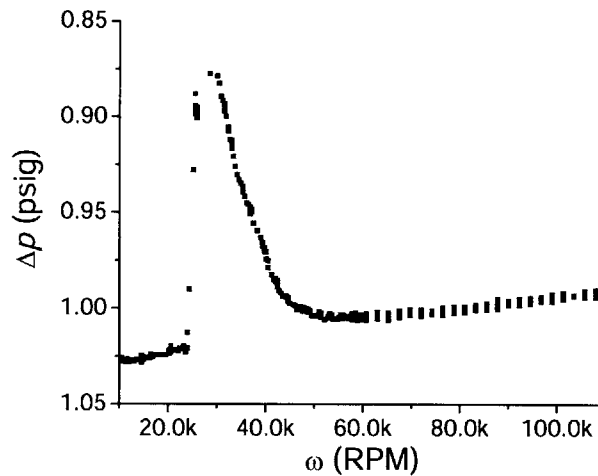


**Figure 5-5: Drop of pressure difference across the journal bearing at the natural frequency (experimental data [30]).**

It is important to note that the above two methods of measuring the natural frequency require one to invert the rotor, which can only be done at low  $\Delta p$  to get sufficient distance to contact according to the analyses in Chapter 2. Thus, only natural frequencies at low  $\Delta p$  can be measured with these methods.

The simple way to find out the natural frequency of the journal-bearing system at high  $\Delta p$  is to crash the rotor. As the rotor is accelerated to the natural frequency at high  $\Delta p$ , it crashes due to insufficient distance to contact, and hence the natural frequency can be obtained. Because the natural frequency is relatively low (below 100Krpm), the crash is normally not destructive according to the experimental results [30]. The rotor can still spin after crashing at the natural frequency, and the experiment can be repeated to find natural frequencies at other high  $\Delta p$  values.

All three of these methods have been successfully implemented in experiments, and these measurement techniques were applied to several micro-devices, such as the micro-bearing rig and micro-turbo-charger, with the results shown next.

### 5.2.2 Natural Frequencies Measured for Isotropic Journal-Bearing System

The natural frequencies of a micro-turbo-charger device were measured [6] using the methods described above, as shown in the plot of Figure 5-6.

In the plot, the data points at low  $\Delta p$  (0.1~0.2 psig) were obtained using the optical fiber data measurement process with the rotor was inverted, and the points at high  $\Delta p$  were the speeds at which the rotor crashed due to insufficient distance to contact at the natural frequencies.

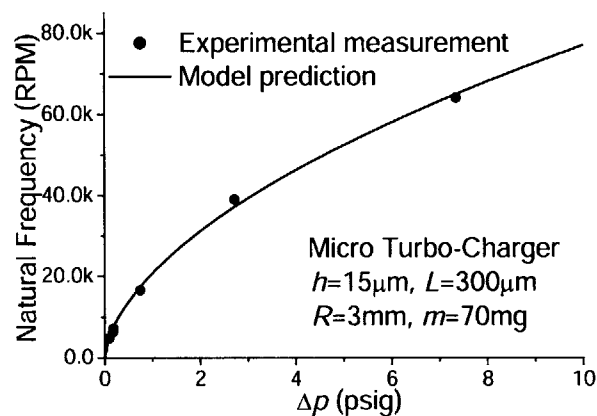


**Figure 5-6: Natural frequency prediction compared with experimental measurements [6] for a micro-turbo-charger device.**

Also in Figure 5-6, the model predictions of natural frequency according to the bearing geometry are plotted and compared with the experimental measurements. It can be seen that the model predictions match the experimental data well. Thus both the fluid model to calculate the hydrostatic stiffness and the rotordynamic model to calculate the natural frequency are accurate and validated by the experimental data.

### 5.2.3 Natural Frequencies Measured for Anisotropic Journal-Bearing System

In Chapter 4, it was shown through both linear analyses and numerical simulations that the anisotropic journal-bearing system has two natural frequencies in the two principal directions, due to the hydrostatic stiffness anisotropy introduced into the system.



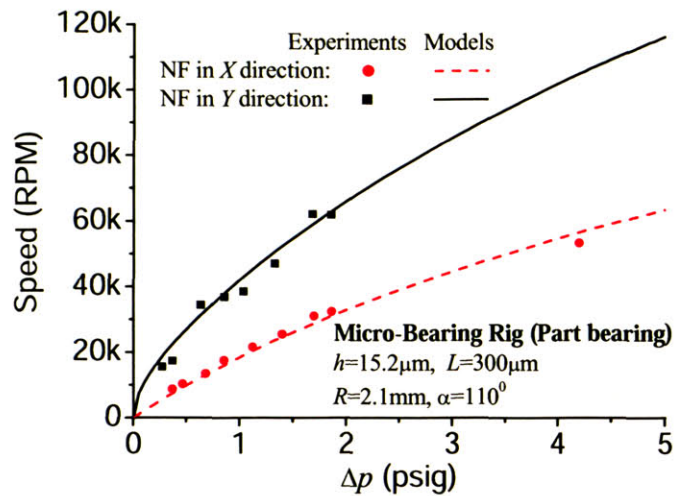


**Figure 5-7: Natural frequency predictions compared with the experimental measurements [7] for the micro-bearing-rig device.**

All the data points of the measured natural frequencies shown in Figure 5-7 were obtained by accelerating the rotor through the natural frequencies. Some are derived from the optical fiber data, while the others are derived from the drop in pressure difference across the journal bearing with constant flow rate. The data showed that the anisotropy had been successfully introduced into the micro-bearing-rig devices in practice, through the part-bearing configuration sketched in Figure 4-3.

According to the static flow test, the clearance of the journal bearing is calculated by the fluid model was  $15.2\mu\text{m}$ . With this clearance, a bearing length of  $300\mu\text{m}$ , and a rotor mass of  $10.5\text{mg}$ , the natural frequencies of the bearing were calculated using the models presented in Chapter 4 and plotted in Figure 5-7. The model predictions agree well with the experimental data; thus, the fluid and rotordynamic models are also validated by the experimental data in the anisotropic journal-bearing system.

Furthermore, it is worth noting that the clearance used in the above calculations of natural frequencies was obtained using the fluid model and static flow tests described in the first section. Thus, the agreement of the natural frequency predictions with the experimental measurements once again validates the fluid models as well as that bearing clearance measurement method.

### **5.3 Distance to Contact**

As was emphasized earlier, one of the major challenges encountered in the experiments was the ability to smoothly transition from subcritical to supercritical operation when accelerating to high speed. As described in Chapter 2, in the linear system, the peak

amplitude of the rotor response is determined by the system damping ratio, which is proportional to the damping coefficient  $C$ . However, in the micro-bearing system,  $C$  is a strong nonlinear function of the rotor eccentricity itself according to Equation (2-32), and the rotor eccentricity normalized by the bearing clearance can vary from 0 to almost 1. As a result, when the rotor crosses the natural frequency, the damping ratio can change by an order of magnitude. Therefore, although the damping ratio is a critical design parameter to look at as described in Chapter 3, it cannot tell whether the rotor can be inverted precisely.

The distance to contact can be used to judge whether the micro-bearing system can be inverted: with a small distance to contact, the rotor can hardly be inverted; but with sufficient distance to contact, it will be possible to invert the rotor. So, what is the minimum distance to contact required for the rotor to be safely inverted? To answer this question, experiments have been done that are briefly outlined below [30].

The key idea behind the experiments is that the distance to contact decreases with the pressure difference across the journal bearing  $\Delta p$ , according to the analysis in the previous chapters. Thus, with the highest  $\Delta p$  at which the rotor can be inverted, the minimum required distance to contact can be calculated by Equation (2-42) for an isotropic system (Chapter 2) or by numerical simulations for an anisotropic system (Chapter 4).

### 5.3.1 Experimentally Determined Threshold in Distance to Contact

One of the experiments done to find the minimum distance to contact was done on a micro-bearing-rig device, numbered 3-6 (device 6 in build 3). The part-bearing configuration was used in this device, with a radius of 2.1mm, a length of 300 $\mu$ m, and a clearance of 13.2 $\mu$ m (measured by the static flow test again). The rotor had a mass of 10.5mg and an unbalance of 3 $\mu$ m (measured by optical data).

During the experiment, the rotor was accelerated through the natural frequencies with a gradually increasing pressure difference across the journal bearing  $\Delta p$ . The highest  $\Delta p$  at which it could be inverted was found to be 2.4psig.

The distance to contact as a function of  $\Delta p$  was calculated using the numerical simulations and the above parameters and plotted in Figure 5-8 (the solid line). Since the natural frequency increases with  $\Delta p$ , the distance to contact will decrease with  $\Delta p$  according to Equation (2-42). This is clearly shown in the plot. Furthermore, corresponding to  $\Delta p=2.4$ psig, the highest pressure difference across the journal bearing at which the rotor

could be inverted, the distance to contact was  $1.2\ \mu\text{m}$ . This means that for this device, the minimum distance to contact required for the rotor to be inverted was about  $1.2\ \mu\text{m}$ .

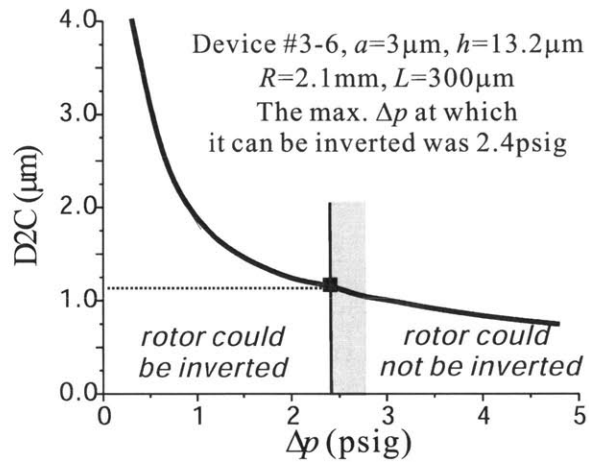


**Figure 5-8: Required distance to contact to invert the rotor: larger than  $1.2\ \mu\text{m}$  for micro-bearing rig #3-6 (experimental data [30]).**

The measurement showed that the surface roughness on each wall of the bearing was about  $0.5\ \mu\text{m}$  [4], so the  $1.2\ \mu\text{m}$  minimum distance to contact calculated by the model is quite reasonable.

Another experiment to identify the minimum distance to contact was done on a micro-motor-generator device, #1 (the first micro-motor-generator device). This device also used the part-bearing configuration, with the same radius and length as the micro-bearing-rig device #3-6 above, but with a clearance and unbalance of  $20\ \mu\text{m}$  and  $2\ \mu\text{m}$  respectively. The highest  $\Delta p$  at which it could be inverted was about  $0.7\ \text{psig}$ . Following the same procedure, the minimum distance to contact for this device to cross the natural frequency was calculated to be about  $1.66\ \mu\text{m}$ .

Furthermore, if both the minimum distances to contact are normalized by the corresponding bearing clearance, the normalized distances to contact (ND2C) were found to be around  $0.083$  and  $0.09$ , close to each other.

Meanwhile, the damping ratios for the above two cases were calculated to be  $0.011$  (for the micro-bearing rig at  $\Delta p$  of  $2.4\ \text{psig}$ ) and  $0.006$  (for the micro-generator at  $\Delta p$  of  $0.7\ \text{psig}$ ) at the center position (Figure 5-9). One can see that these two damping ratios are quite different, so it is impossible to use the damping ratio as the criterion for whether the rotor can be inverted.

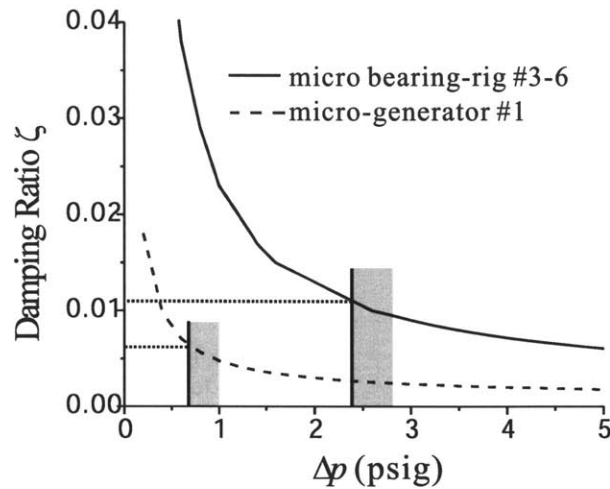


**Figure 5-9: Comparison of the damping ratios for the two devices: micro-bearing rig #3-6 (solid line) and micro-generator #1 (dashed line).**

Since the roughness of the bearing wall may have some dependence on the bearing clearance and the system damping decreases with clearance, a slightly larger distance to contact is needed for devices with larger clearance. Therefore, it is more reasonable to use the normalized distance to contact of 0.09 as the threshold: a device with a normalized distance to contact smaller than 0.09 may have difficulty crossing the natural frequency. Note that there were only two experimental data points of the minimum normalized distance to contact, so the threshold of 0.09 can only be a rough value. As more experiments are done to search for the minimum distance to contact, a more accurate threshold can be obtained.

### 5.3.2 Application of the Threshold in Distance to Contact

Furthermore, with this normalized distance-to-contact threshold of 0.09, the highest  $\Delta p$  at which the rotor can be inverted can be predicted by the models according to the bearing geometry and the rotor unbalance.

The distances to contact shown in Figure 5-10 were calculated for the micro-turbo-charger device #C8 and then normalized by the turbine bearing clearance. This device had a relatively massive rotor (70mg) and a large unbalance ( $5\mu\text{m}$ ) compared with the micro-bearing rig in Figure 5-8 above, resulting in a much lower distance to contact. Although this micro-turbo-charger device used an isotropic single-turbine bearing, the clearance of the compressor gap was comparable to that of the turbine bearing. Thus, the damping contributed by the compressor gap was about one eighth of the one contributed



by the turbine bearing according to Equation (2-33), and hence is not negligible in the calculations of distances to contact.

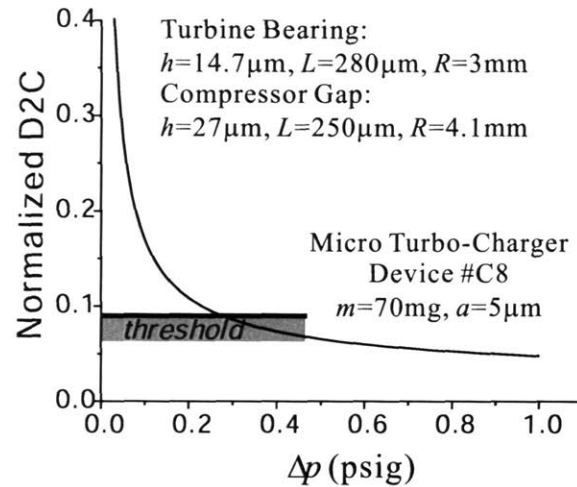


**Figure 5-10: Normalized distance to contact calculated for the micro-turbo-charger device #C8, compared with estimated threshold of 0.09.**

Therefore, with the threshold of 0.09 indicated in Figure 5-10, the highest pressure difference across the journal bearing  $\Delta p$  at which the device can be inverted is found to be 0.25psig. And this was proven by the experiments: the device was successfully inverted with a  $\Delta p$  of about 0.2psig, while it crashed at natural frequencies with high  $\Delta p$  as discussed earlier in Figure 5-6.

In fact, in the initial tests of these micro-turbo-charger devices, they were inverted at relatively high  $\Delta p$  levels, and the rotors kept crashing at natural frequencies. One of the crashes was so intense that the device (#C9) was not spinnable afterward [32]. When the models revealed that these devices can only be inverted at  $\Delta p$  levels lower than 0.25psig, the device was successfully inverted at a  $\Delta p$  of about 0.2psig.

#### **5.4 Experimental Assessment of Stability Boundary Predictions**

In Chapter 2 and 3, it was shown through first-order analytical approaches based on first principles that the two components of the destabilizing hydrodynamic force, which act in opposite directions, are of comparable magnitude due to the small  $L/D$  in the micro-bearing systems. Therefore, the whirl ratio of the ultra-short micro-isotropic journal bearing can be one order of magnitude higher than that of its large-scale conventional counterparts.

Thereafter, in Chapter 4, based on both analytical modeling and numerical simulations, hydrostatic stiffness anisotropy was found to stabilize the micro-journal-bearing system, eliminate the narrow singularity of the stability boundary in isotropic systems, and greatly increase the top speed even if the bearing clearance is off the singularity point.

In the following analyses, it will be shown that these critical concepts and mechanisms are consistent with the experimental observations.

Before beginning the comparison between the model predictions and the experimentally achieved top speeds, it is important to note the two major features of the high-speed tests. First, the crashes at high speed are destructive—the brittle silicon rotor breaks into pieces after a high-speed crash, and the experiment cannot be repeated—so, only limited experimental data was obtained for the top speeds. Secondly, the crashes can be caused by reasons other than the whirl instability of the journal-bearing system, such as structure failures, thrust bearing resonances, coupling between conical motions and radial motions, subharmonic resonances, and more. Since the crashes are abrupt and fast (with a time scale of about 0.1ms, the same as the rotation), it is almost impossible to distinguish the reason for most crashes due to the lack of on-site fast response measurement instruments. Thus, with the current limited experimental data, the model of the stability boundary cannot be fully validated.

#### 5.4.1 Stability Boundary in Isotropic Journal-Bearing Systems

As discussed in Chapter 3, the whirl ratio  $\mathfrak{R}$  is determined by the whirl number  $W$ , the ratio of hydrodynamic stiffness due to viscous drag effect to stiffness due to rotor pumping action, according to Equation (3-16).

For large conventional journal bearings, because the length is comparable to the diameter ( $L/D \sim 1$ ) and the clearance is much smaller than the length ( $h/L \ll 1$ ), the whirl number  $W = Dh/L^2$  is much smaller than 1 (the hydrodynamic force due to viscous drag effect is negligible compared to the hydrodynamic force due to rotor pumping action). For example, the large gas journal bearings investigated by Larson and Richardson in [24] had  $L=25.4\text{mm}$ ,  $R=15.9\text{mm}$ , and  $h$  from  $15\mu\text{m}$  to  $81\mu\text{m}$ . Thus, the whirl numbers  $W$  were estimated to be  $0.00075 \sim 0.004$  for these devices, according to Equation (3-15). Therefore, the whirl ratios  $\mathfrak{R}$  of these large conventional bearings were about 2 according to Equation (3-16), which is consistent with the observations by Larson and Richardson.

In fact, the widely used word “half-whirl” for conventional bearing system, which means that the natural frequency of the system is about half of the whirl stability limit (SB), has the exactly the same meaning of  $\mathfrak{R} \approx 2$  and consistent with the model.

On the contrary, high whirl ratios  $\mathfrak{R}$  (up to 30) [7] have been achieved in experiments with the micro-bearing systems.

In this high-speed spin test, the device was an isotropic micro-bearing-rig device with the bearing configuration sketched in Figure 4-20. In this test, the device was accelerated to a rotational speed of 700Krpm and decelerated back to 0 safely at a pressure difference across the journal bearing  $\Delta p$  of about 1psig. The experimental operating line is indicated by the black dots in the graph. As discussed earlier in Section 5.2.1, the sudden drop in  $\Delta p$  indicated that the natural frequency of the system was about 30krpm, which is consistent with the natural frequency predicted by the models (the red dashed line). Thus the whirl ratio for this device was higher than 29 (the black solid line). After this test, the device finally crashed at about 600Krpm in another test. The reason for the crash was hypothesized to be structure failure.

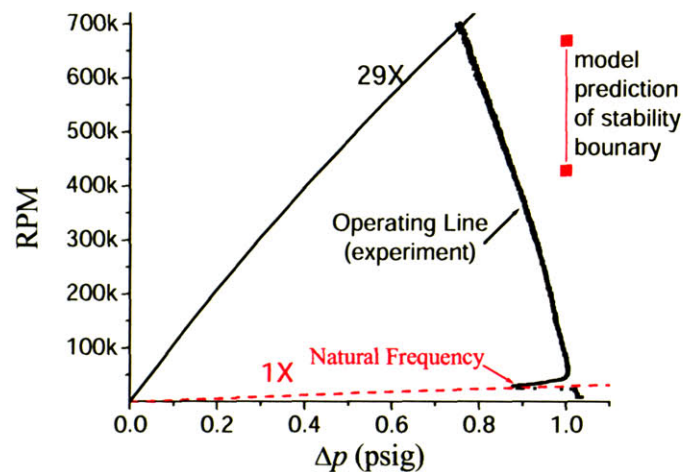


**Figure 5-11: Experimental spin test: high whirl ratio achieved in micro-bearing device [30].**

It is important to note that this whirl ratio of more than 29 is one order of magnitude higher than the ratios observed in large conventional devices, and can be explained by the mechanism of the balanced destabilizing hydrodynamic force as mentioned earlier, which is unique to the ultra-short micro-bearing system.

More specifically, the bearing had a radius of 2.1mm, due to the fabrication uncertainty, a length of  $320\mu\text{m} \pm 10\mu\text{m}$ , and a clearance of about  $18\mu\text{m}$ . With a rotor mass of

14.5mg and unbalance of  $2\mu\text{m}$ , the model-predicted stability boundary is 430Krpm (with  $L=330\mu\text{m}$ ) to 670Krpm (with  $L=310\mu\text{m}$ ) as shown in the plot, with about a 20% pressure difference between the up and down plena (Figure 4-20) observed in the experiments. Although these predicted speeds are a little lower than the experimentally achieved speed (700Krpm), they are of the same order of magnitude. The discrepancy in the model prediction can be explained by the following:

First, the fluid models established to calculate the hydrodynamic force are based on the approximation of fully developed Couette flow. As mentioned in Chapter 2, this approximation may not be precise when the flow in the journal bearing has high axial velocity and no pre-swirl before entering the bearing. In this case, the variation of the tangential flow in the vicinity of the bearing entrance can be smaller along the circumferential direction [30]. Since the hydrodynamic force is determined by this variation (no variation will yield zero hydrodynamic force), the actual hydrodynamic force will be smaller than the model prediction, though they are still of the same order of magnitude. As a result, the model assuming a fully developed flow can underestimate the system stability boundary, which is consistent with the above observations.

Second, other components in the devices, such as the turbine, can also induce hydrodynamic forces, which have not been accounted for in the models. These hydrodynamic forces from other components of the device also affect the system stability boundary and should be included in the high-order models to be developed in the future.

Moreover, each plenum (the volume) together with the bearing (the neck) forms a Helmholtz resonator. Since the up-down pair of plena have a larger volume than the left-right pair (Figure 4-20), the Helmholtz resonance frequency in the former is smaller than in the latter, and they are all on the order of 1 million rpm according to calculations [30]. Thus, as the rotor speed reaches 700krpm, which is nearer to the Helmholtz resonance frequency in the up-down pair of plena than that in the left-right pair, the pressure variation associated with the rotor oscillation in the former is larger than in the latter; this introduces hydrostatic stiffness anisotropy into the bearing system, although the pressure supplies to all the plena are the same. Thus, due to the difference in Helmholtz resonance frequencies between the two plena, the bearing system is actually anisotropic at about 700krpm, and the stability boundary can be increased by the induced anisotropy. This hypothesis is still under investigation.

As discussed in Chapter 4, the micro-turbo-charger devices were initially designed to use an isotropic journal-bearing system (sketched in Figure 4-21). The highest crash

speeds for these devices, as well as the corresponding bearing geometry, are listed in Table 5-1, according to [32].

Micro-turbo-charger Device Number		C2	C8
Turbine side	Clearance ( $\mu\text{m}$ )	15.3	14.7
	Length ( $\mu\text{m}$ )	280	280
Compressor side	Clearance ( $\mu\text{m}$ )	27	27
	Length ( $\mu\text{m}$ )	250	250
Rotor unbalance measured optically ( $\mu\text{m}$ )		5.5	5
Experimental crashes	$\Delta p$ (psig)	4.9	7
	RPM	250,000	390,000
Stability boundary predicted by models	with the above measured rotor unbalance	430,700	621,600
	with a rotor unbalance 1 $\mu\text{m}$ smaller	314,000	441,000

**Table 5-1: Crash speeds for micro-turbo-charger devices C2 and C8 (isotropic journal bearings) with the bearing geometry.**

Still, the reason for the crashes was not confirmed. It was suggested that the crashes were caused by the journal bearing stability, because the crash speeds are of the same order of magnitude and in the same trend as the system stability boundary predicted by the models. The differences between the predicted stability boundary and the real crash speeds may be also due to the reasons mentioned above and uncertainties in the bearing geometry (such as rotor unbalance and misalignment between the two disks). In fact, if the real rotor unbalances are 1  $\mu\text{m}$  smaller than the optical measurements, the predicted stability boundary will be only 50Krpm larger than the crash speeds.

Thus, the model prediction of the whirl ratio is close to the one observed by Larson and Richardson for the large-scale conventional journal-bearing systems. It also predicts a whirl ratio one order of magnitude higher for the micro-ultra-short bearing system, which is consistent with the experimental observations. Furthermore, according to Table 5-1, the stability boundary predicted by the model is of comparable magnitude and in the same trend as the experimentally achieved top speeds of the micro-bearing system.

These consistencies together suggest that the hydrodynamic force due to viscous drag becomes equally important to the hydrodynamic force due to the rotor pumping action in the micro-ultra-short bearing systems, resulting in a whirl ratio an order of magnitude higher than in the large-scale conventional counterparts, where the former is negligible compared to the latter.



### 5.4.2 Stability Boundary in Anisotropic Journal-Bearing Systems

As already shown in Chapter 4, Figure 5-12 presents a comparison of the model predictions with the experimentally achieved top speeds for anisotropic journal-bearing systems.

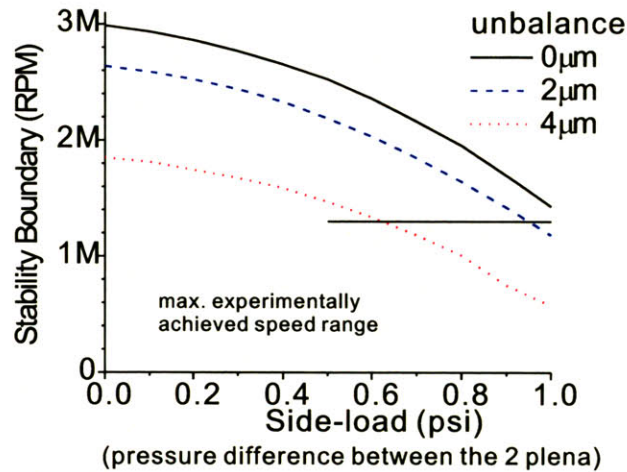


**Figure 5-12: Stability boundary predictions for the part-bearing system compared with the highest speeds achieved in micro-bearing rig builds 2 and 3.**

The experiments were done on the devices of micro bearing-rig build 2 and 3, each with bearing clearance of about  $13\mu\text{m}$  and a length of  $300\mu\text{m}$ . Fabrication research afterward showed that the rotor unbalances of these devices could be  $1\sim 3\mu\text{m}$ . With sideloads (the difference in supply pressures between the two opposite feed plena) as large as 1psi observed during the experiments, the highest speed reached by the devices was about 1.3 million rpm [8].

Then the stability boundary was calculated according to the bearing geometry described above and plotted as a function of sideload for three levels of rotor unbalance marked by the solid, dashed, and dotted lines. It can be seen that the highest speeds ever reached by these devices are comparable to the stability boundary predicted by the models with a sideload of about 1psig and an unbalance of  $1\sim 3\mu\text{m}$ . Thus, this suggests that the devices may have crashed because of journal bearing instability due to sideload.

## 5.5 Summary and Conclusions

In this chapter, the models established in previous chapters for the bearing flow, the natural frequency and the distance to contact were validated by experimental measurements. Meanwhile, an accurate and nondestructive way to measure the bearing clearance

was introduced, employing the both fluid models and static flow tests. Furthermore, the threshold of the minimum distance to contact normalized by the bearing clearance was found to be 0.09 through experiments and models, and has been successfully applied to the experiments/operating protocol.

Due to the insufficient experimental data on high-speed tests and the difficulty of finding out the causes of the high-speed crashes, the stability boundary model cannot yet be fully validated. However, comparing the whirl ratios observed in large-scale conventional bearings ( $\sim 2$ ) and the ultra-short micro-bearing system ( $>29$ , one order of magnitude higher), one can see that the micro-ultra-short bearing can have a whirl ratio one order of magnitude higher than its large conventional counterparts. This greatly increased whirl ratio in the micro-ultra-short journal-bearing system can be explained by the model established in the previous chapters. Also, the consistency between the model predictions and the experimental top speeds indicates that the hydrodynamic force due to viscous drag becomes equally important to the hydrodynamic force due to rotor pumping action in the micro-ultra-short bearing systems. As a result, the whirl ratio of the micro-ultra-short journal-bearing system is an order of magnitude higher than in the large-scale conventional systems, in which the hydrodynamic force due to viscous drag is negligible compared to the hydrodynamic force due to rotor pumping action.

Finally, the following future steps are suggested: establishing more accurate models (such as three-dimensional CFD) to calculate the hydrodynamic forces and doing more high-speed tests to find the top speeds of micro-bearing systems with variations in bearing geometry and with/without anisotropy in order to assess the models.



## Chapter 6

# Multi-Degree-of-Freedom Systems

In the previous chapters, the research focused on journal-bearing systems with radial ( $x$  and  $y$  in plane) motions of the rotating ( $\omega$ ) rotor. However, since the rotor as a rigid body has 6 degrees of freedom in the bearing cavity, it can also engage in conical ( $\alpha_x, \alpha_y$ ) and axial ( $z$ ) motions (Figure 6-1), which can couple with the radial motions and make the dynamic behavior of the system much different from that of systems with only radial motions.

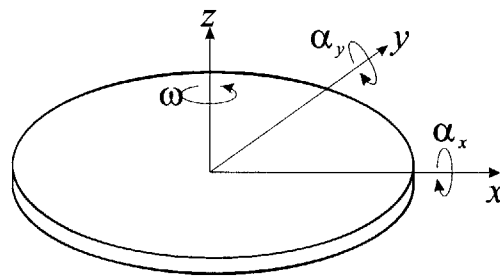


**Figure 6-1: Multiple degrees of freedom of the rotor.**

In fact, this coupling between conical motion and radial motion was observed in experiments with the micro-turbo-charger devices, and it made the devices unstable at a much lower rotor speed than the whirl instability limit of the journal-bearing system. Therefore, in this chapter, multi-degree-of-freedom models will be established to investigate the dynamic behavior of the coupled system, and a design guideline associated with this coupling effect can then be developed.

The chapter begins with a brief outline of the experimental observations as evidence of the coupling between the radial motion and the conical motion. Then, with the flow models, the coupling is found mainly from the plenum region (in the micro-turbo-charger devices (Figure 4-21)), the seal, and the thrust bearings: a radial force is induced when the rotor is tilted, and a torque is produced when the rotor moves radially. With the sources of the coupling identified and the coupling coefficients calculated by the fluid models, both a linear 4-degree-of-freedom model (the two radial motions and the two conical motions) and a nonlinear 5-degree-of-freedom numerical model (the radial, coni-

cal, and axial motions) are established to investigate the rotordynamic behavior of the system. The model's predictions agree well with the experimental observations, and the coupling between the conical and radial motions is proven to be the destabilizing factor of the multi-degree-of-freedom system. Therefore, this coupling must be reduced or eliminated in the bearing system design.

With the modeling efforts, one can find that the coupling is a strong function of the thrust bearing clearances and the rotor axial position. As a result, the stability boundary of the system can change by a factor of 2 if the rotor moves from its center position by only  $1\mu\text{m}$ . Therefore, in operation, the rotor needs to be fixed at an optimum axial position so that the system can have the highest stability boundary. Moreover, through the results of the nonlinear 5-degree-of-freedom numerical model, the amplitude of the axial oscillation is found to be negligible compared with the thrust bearing clearance. Thus, the 4-degree-of-freedom model is proven to be sufficient to investigate this multi-degree-of-freedom system.

### ***6.1 Experimental Evidence of Coupling Phenomena***

The bearing supply plenum in the micro-turbo-charger devices can generate relatively larger coupling forces and torques than in the micro-bearing-rig devices, because the radius and the area of the former are much larger than those of the latter. As a result, the coupling phenomena are mainly observed in the micro-turbo-charger devices. Of all the devices that encountered the coupling effect, some of them used the dual-bearing systems (one bearing on each of the compressor and the turbine disks), as shown in Figure 4-22. During the experiments, with fixed rotational speed and pressure settings in the thrust bearings, the flow rates through both thrust bearings started to decrease with the pressure supply to the journal-bearing system at certain points, as plotted in Figure 6-2.

During the experiments, the rotor can move axially due to the unbalanced thrust forces induced by pressure fluctuations in the device. If the rotor moves axially either up or down, the flow rate through the thrust bearing to which the rotor moves decreases, but the other one should increase because the thrust bearing clearance becomes larger due to the rotor motion. Thus, decreases in the flow rates through both thrust bearings must be induced by other rotor motions, which could be axial oscillation or conical motion according to [30]. Further investigation (presented later in this chapter) shows that the axial oscillation of the rotor is negligible. Therefore, the motion that caused both thrust bearing flow rates to decrease can only be the conical motion.

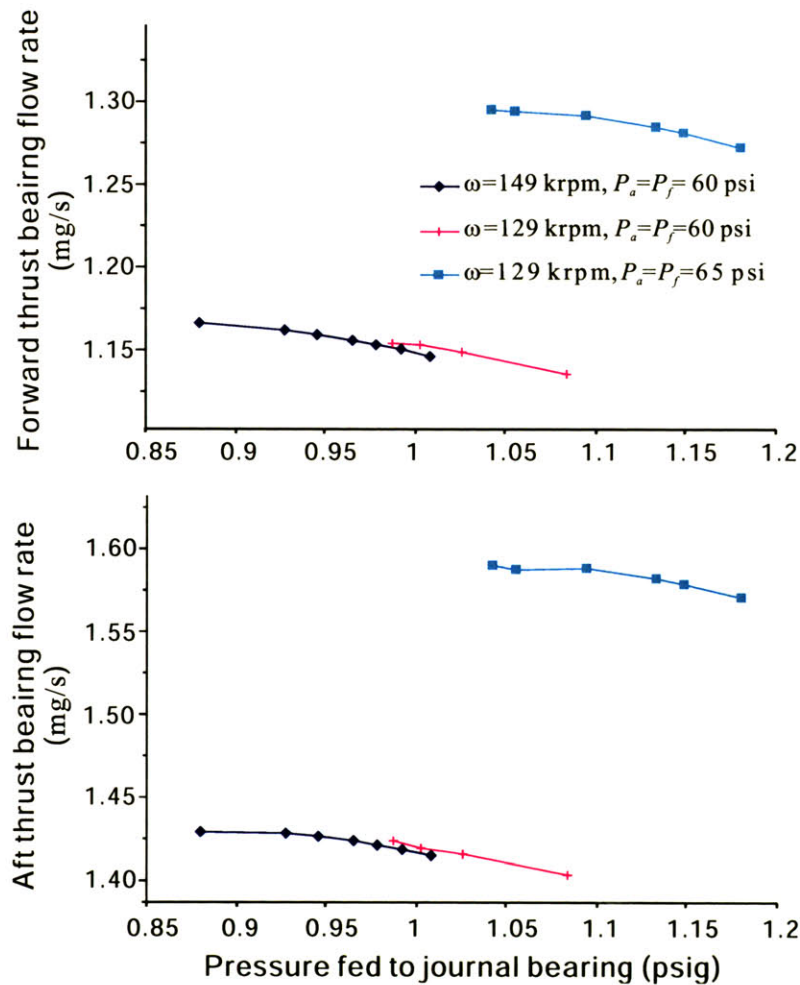


**Figure 6-2: Flow rates through both thrust bearings decreased with the pressure fed to the journal bearing, measured in the dual-bearing micro-turbo-charger device (experimental data from [31]).**

This conical motion of the rotor was picked up by the optical fiber sensor, which was acquiring the waveform of the “speed bumps” passing by (Figure 5-3). Through a spectral analysis of the waveform, the frequencies of the conical motion were obtained and are plotted in Figure 6-3.

Interestingly, these experimentally measured frequencies are not the system’s conical natural frequencies [30], indicating that the motions were not due to conical resonances. Instead, they were near the radial natural frequency of the journal-bearing system, which was calculated and also plotted in Figure 6-3. Furthermore, the frequencies of the conical motions increased with the pressure fed to journal-bearing system  $\Delta p$ , following the same trend as the natural frequencies of the journal bearing. This suggests that this ro-

tor motion, a conical motion at the radial natural frequency, is a combination of the rotor's conical motion and radial motion.

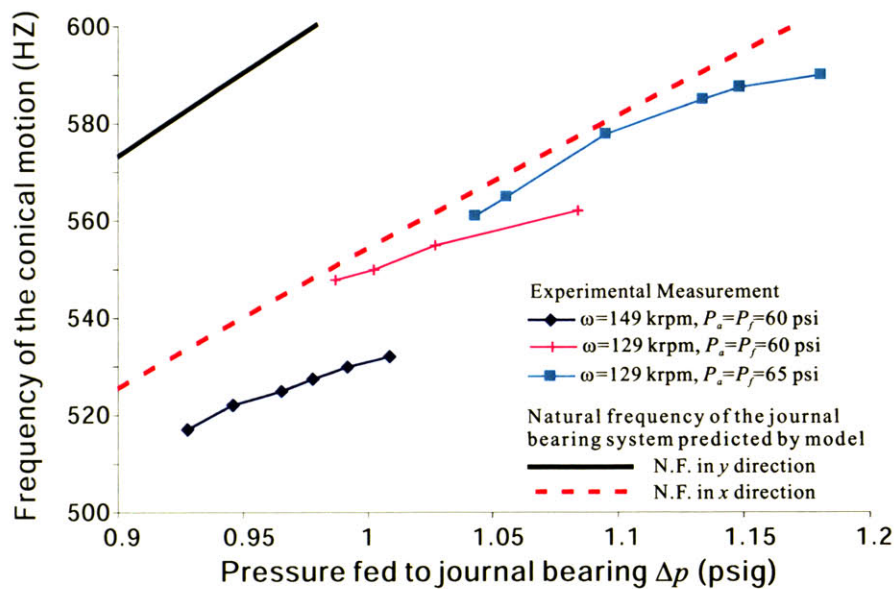


**Figure 6-3: Frequency of the conical motions as a function of  $\Delta p$  (experimental data from [31]), compared with the model prediction of the journal bearing natural frequency.**

Other devices that encountered the coupling between conical motion and radial motion were the micro-turbo-charger devices with the single-compressor-bearing configuration (Figure 6-11 with seal in the plenum to block the flow to the turbine gap). During the experiment, just before the rotors crashed, the flow rates through both thrust bearings were also decreasing. Meanwhile, the conical motions were also picked up by the optical fiber sensor, and the frequencies obtained by the spectral analysis were also close to the natural frequencies of the journal bearings. A detailed description of these observations can be found in [6].

One hypothesis to explain these conical motions at the journal bearing natural frequencies is that the rotor's conical motion and radial motion are coupled together in the system. If this is the case, the system can no longer be treated as a 2-degree-of-freedom system. Instead, 4-degree-of-freedom and 5-degree-of-freedom (with axial oscillation) models are established in the following analyses to investigate this coupled system. The agreement between the model predictions and the experimental observations shows that this hypothesis (coupling between the rotor radial and conical motions) is validated.



## 6.2 Sources of Coupling Effect

To investigate the dynamic behavior of the system with coupling and to establish the multi-degree-of-freedom models, the coupling sources must first be identified and modeled. The following analyses will show that the coupling was mainly induced by the plenum, seal, and thrust bearings.

### 6.2.1 Coupling Induced by Feed Plena

Using the fluid model established for the plenum of the micro-turbo-charger in Chapter 4, the coupling from the plenum can be modeled and computed as follows:

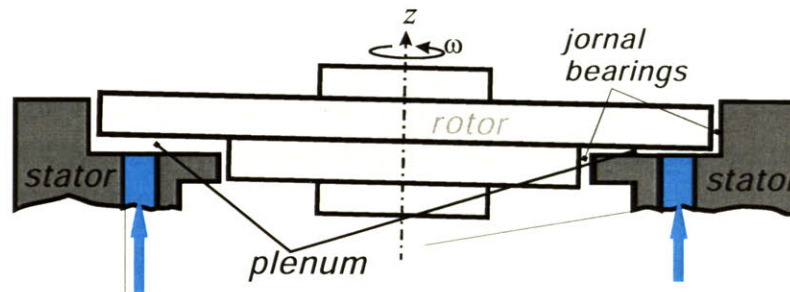


Figure 6-4: Change in plenum clearance (height) due to rotor tilt.

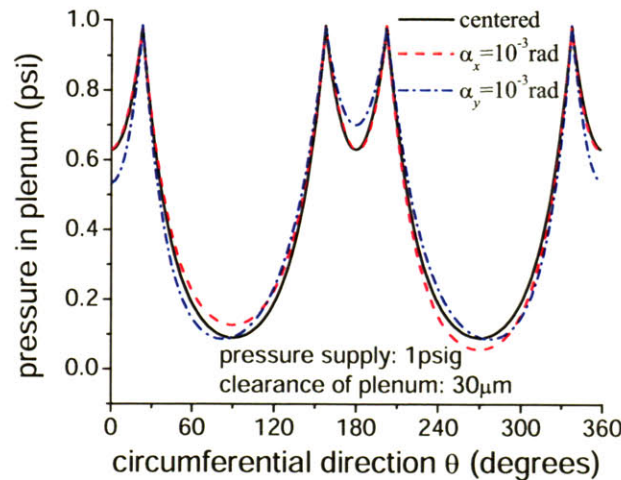
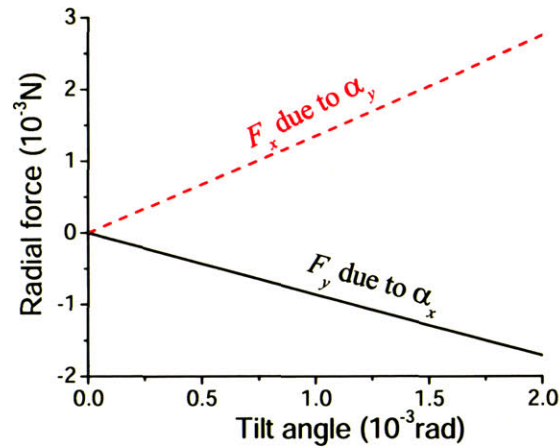


Figure 6-5: Pressure distribution in the plenum due to rotor tilt.

When the rotor tilts ( $\alpha_x$  or  $\alpha_y$  in Figure 6-1), the clearance (height) of the plenum changes accordingly (Figure 6-4), altering the flow resistance through the plenum and hence the pressure before the journal bearing entrance, as shown in Figure 6-5 (the zero of  $\theta$  is in the  $x$  direction). For example, as shown in Figure 6-4, if the rotor tilts  $\alpha_y$ , the clearance of the plenum sector on the left-hand side decreases, while the one on the other side increases. Thus the flow resistance through the former sector increases, reducing the

pressure in this sector, while it decreases in the plenum sector on the left, raising the pressure in that sector accordingly (the blue dash-dotted line in Figure 6-5).



**Figure 6-6: Radial force induced by rotor tilt.**

Thus, a radial force from the journal bearing will be produced by the tilting motions accordingly (in the negative  $y$  direction with rotor tilting angle of  $\alpha_x$  in the above example). It is important to note that, due to the symmetry of the system, the rotor tilt  $\alpha_x$  can only introduce a radial force in  $y$  direction, while the tilt  $\alpha_y$  can only introduce a radial force in  $x$  direction. These radial forces induced by the rotor tilts are calculated and plotted in Figure 6-6 as functions of tilting angles.

Meanwhile, these pressure distributions in the plenum induced by the rotor tilts will also generate torques acting on the rotor, which are calculated and plotted in Figure 6-7 as functions of tilting angles.

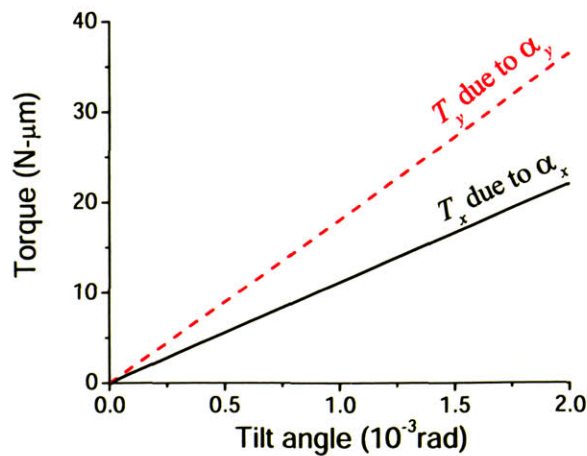


**Figure 6-7: Torques from the plenum induced by rotor tilt.**



Note that the torque induced by the rotor tilt is in the same direction as the tilt, which means that it is not restoring, but pushing the rotor even further away from the balance point. Fortunately, the restoring torque generated by the thrust bearings (90N- $\mu\text{m}$  with  $10^{-3}$  rad tilting angle [10]) is several times larger than this destabilizing torque from the plenum, keeping the system statically stable.

On the other hand, when the rotor moves in radial directions ( $x$  or  $y$  in Figure 6-1), the clearances of the journal bearings change accordingly, altering the flow rates through them. As a result, the pressure in the plenum, which is proportional to the circumferential flow rate through the plenum, also changes, as shown in Figure 6-8. For example, if the rotor moves in  $y$  direction, the flow rates through the sections of journal bearings in the  $y$  direction decrease, and they increase on the opposite side. Thus, the pressure in the plenum of the former sector increases due to the decreased pressure drop caused by the reduced flow rate through the plenum, while it decreases in the latter sector accordingly (blue dash-dotted line in Figure 6-8).

This variation of the pressure in the plenum induces a torque (in the direction of  $\alpha_x$  in the above example). Again, it is important to note that, due to the symmetry of the system, the displacement  $\delta x$  can only produce a torque in  $\alpha_y$  direction, while the displacement  $\delta y$  can only produce a torque in  $\alpha_x$  direction. These torques induced by the rotor's radial movement are calculated and plotted in Figure 6-9 as functions of rotor radial displacement.

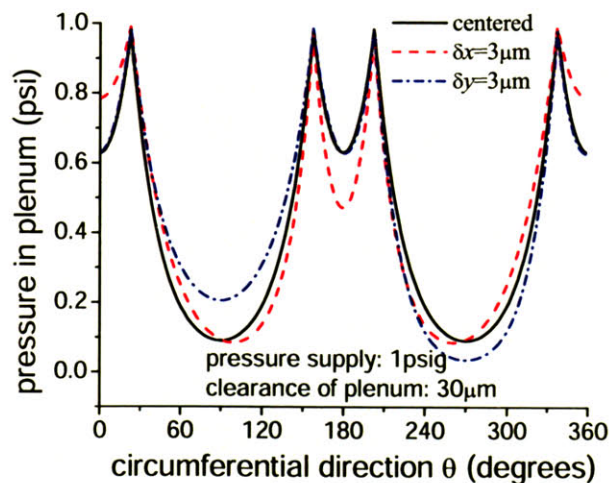


**Figure 6-8: Plenum pressure distribution due to rotor radial displacement.**

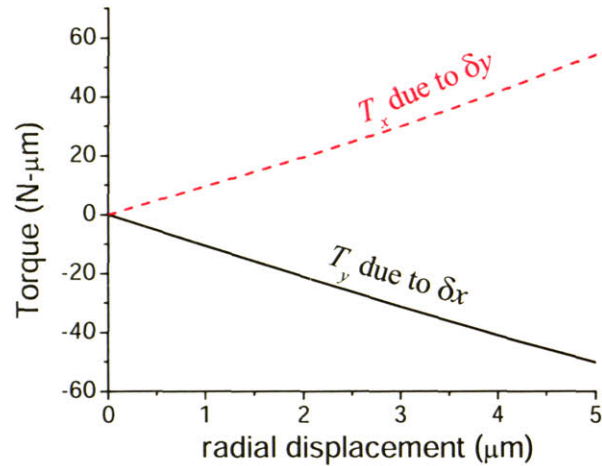


Figure 6-9: Torques induced by rotor radial displacement.

### 6.2.2 Coupling Induced by Thrust Bearings and Seals

Following the analysis below, one can find that the coupling can also be generated by the thrust bearings and the seal in the plenum, due to the non-uniform viscous stress on the rotor surface when it is tilted.

There are two thrust bearings that confine the rotor axial movement and conical motion, as shown in Figure 6-10. The upper one is denoted as the forward thrust bearing, while the lower one is denoted as the aft thrust bearing. When the rotor is axially centered without tilt, the clearances of both thrust bearings are equal and uniform— $h_0$  as shown in the sketch.

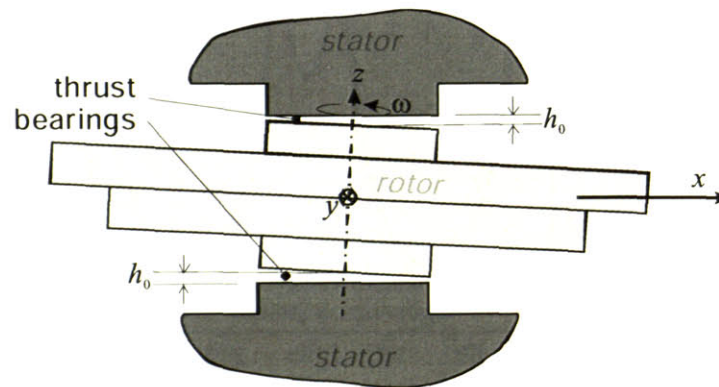


Figure 6-10: Sketch of the thrust bearings with a tilted rotor (not to scale).

If the rotor tilts  $\alpha_y$  as shown in Figure 6-10, the clearances of the thrust bearings change accordingly. For example, the clearance in the aft thrust bearing becomes  $h(r, \theta) = h_0 - r\alpha_y \cos(\theta)$ , where  $r$  and  $\theta$  are the polar coordinates in the thrust bearing pad.

Since the surface speed of the thrust bearing on the rotor side is  $v_\theta=r\omega$  and the flow in the thrust bearing gap can be approximated as Couette flow, the viscous stress on the surface of the rotor is

$$\tau_\theta = -\mu \frac{v_\theta}{h(r, \theta)} = -\mu \frac{r\omega}{h_0 - \alpha_y r \cos(\theta)}. \quad (6-1)$$

Thus, the stress is larger on the right-hand side than on the left-hand side in Figure 6-10, resulting in a net radial force in  $y$  direction

$$F_y = \int_0^{2\pi} \int_0^R \tau_\theta \cos(\theta) r dr d\theta = -\pi\mu\omega \frac{\left(h_0 - \sqrt{h_0^2 - \alpha_y^2 R^2}\right)^2}{\alpha_y^3}, \quad (6-2)$$

where  $R$  is the radius of the thrust bearing pads. The negative sign in  $F_y$  indicates that the radial force in the aft thrust bearing is in the negative  $y$  direction. Similar analysis can find  $F_y$  in the forward thrust bearing with similar expression, but in the positive  $y$  direction. Therefore, the net radial force produced by both thrust bearings due to the rotor tilt is zero when the rotor is axially centered.

However, it is important to note that when the rotor moves axially from the center position, the forces from both thrust bearings are not balanced according to equation (6-2), and thus a nonzero net radial force will be produced. For example, if the rotor moves up axially and tilts  $\alpha_y$ , the net radial force induced by the rotor tilt is not zero and acts in the positive  $y$  direction.

Besides the thrust bearings, the seal in the single-compressor-bearing configuration (Figure 6-11), which is in the plenum and used to block the flow to the gap on the turbine side, can also generate a radial force when the rotor is tilted.

Through a similar procedure and integration, the radial force induced by  $\alpha_y$  is found to be

$$F_y = -\pi\mu\omega \frac{\alpha_y^2 (R_i^2 - R_o^2) + 2h_0 \left( \sqrt{h_0^2 - \alpha_y^2 R_i^2} - \sqrt{h_0^2 - \alpha_y^2 R_o^2} \right)}{\alpha_y^3}, \quad (6-3)$$

where  $R_i$  is the inner radius of the seal and  $R_o$  is its outer radius. With the width of the seal  $L=R_o-R_i \ll R_i$ , the above equation can be simplified to

$$F_y = -2\pi\mu\omega \frac{h_0 - \sqrt{h_0^2 - \alpha_y^2 R^2}}{\alpha_y \sqrt{h_0^2 - \alpha_y^2 R^2}} RL + O\left(\left(\frac{L}{R}\right)^3\right), \quad (6-4)$$

where  $R=(R_o+R_i)/2$  is the average radius of the seal.

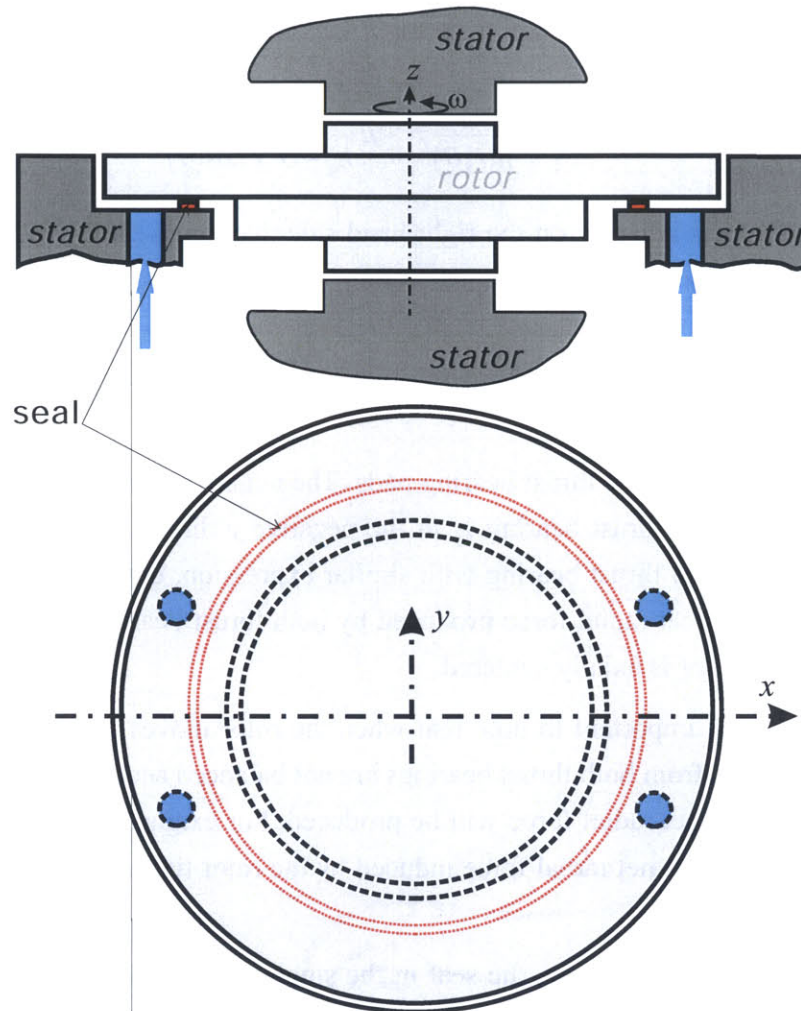


**Figure 6-11: Single-compressor bearing configuration of micro-turbo-charger device (note seal in feed plenum).**

Note that in the above analysis, the flow is approximated as Couette flow in both thrust bearing and seal gap. To assess the approximation, three-dimensional CFD calculations using 3-D Fluent were done for comparison.

Since it is difficult to generate grids and expensive to calculate the flow in the gap between tilted thrust bearing pads due to its large aspect ratio ( $D/h \sim 2000$ ), the CFD calculation (Fluent 3D) is employed to solve the flow between parallel thrust bearing pads instead, so that it can utilize the symmetry of the system (described in detail in Chapter 10). In the CFD calculations, the torque  $T_z$  due to viscous drag on the rotor surface is calculated and compared to the analytical predictions based on the approximation of Couette flow. The results are shown in Table 6-1:



Rotational speed	$\omega=1\times 10^5$ rad/s	$\omega=2\times 10^5$ rad/s
Analytical results	$4.4991\times 10^{-7}$ N·m	$8.9983\times 10^{-7}$ N·m
Fluent 3-D	$4.5630\times 10^{-7}$ N·m	$9.1248\times 10^{-7}$ N·m
Difference	1.4%	1.4%

**Table 6-1: Comparisons between torques calculated by analytical model and 3-D Fluent.**

It can be seen that the difference is as low as 1.4%. Thus, the analytical model based on the approximation of Couette flow is deemed accurate.

### 6.3 Four-Degree-of-Freedom Model with Coupling Effect

To add to the fluid force/torque models developed above and in the previous chapters, the linear 4-degree-of-freedom model is established in this section. Then, using the eigenvalue and eigenvector analyses, the dynamic behavior of the coupled system is investigated and compared to the experimental observations. The model predictions match the experimental observations, and the coupling between the conical and radial motions is found to be the destabilizing factor in the system, which should be avoided.

The rotordynamic equations that describe the radial and conical motions coupled together are:

$$\begin{cases} A\ddot{\alpha}_x + 2A\omega\alpha_y = T_x(y, \alpha_x, \dot{\alpha}_x, \alpha_y, \dot{\alpha}_y, z) + A\omega^2\phi \cos(\omega t) \\ A\ddot{\alpha}_y - 2A\omega\alpha_x = T_y(x, \alpha_x, \dot{\alpha}_x, \alpha_y, \dot{\alpha}_y, z) + A\omega^2\phi \sin(\omega t) \\ m\ddot{x} = F_x(x, \dot{x}, y, \alpha_x, \alpha_y, z) + m\omega^2 a \cos(\omega t) \\ m\ddot{y} = F_y(x, y, \dot{y}, \alpha_x, \alpha_y, z) + m\omega^2 a \sin(\omega t) \end{cases} \quad (6-5)$$

where  $A=I_x=I_y$  is the moment of inertia in  $x$  and  $y$  directions, and  $I_z=2I_x$  by approximating the rotor as a circular plane disk.  $m$  is the rotor mass, and  $a$  is the rotor static unbalance (distance from the rotor geometric center to the mass center), while  $\phi$  is the rotor dynamic unbalance (angle between the rotor geometric axis and the principal axis).  $F_x$ ,  $F_y$ ,  $T_x$ , and  $T_y$  are the fluid forces and torques.

#### 6.3.1 Linearized Equations and Coupling Coefficients

In order to find the unstable mode of motion through the eigenvalue and eigenvector analyses, Equations (6-5) need to be linearized based on the assumption of negligible unbalances  $a$  and  $\phi$ . The linearized equations of Equations (6-5) are:

$$\begin{cases} A\ddot{\alpha}_x + 2A\omega\dot{\alpha}_y = K_{xx}^T\alpha_x - k_d^T\omega\alpha_y + C_{xx}^T\dot{\alpha}_x + C_{xy}^T\dot{\alpha}_y + g_{xy}y \\ A\ddot{\alpha}_y - 2A\omega\dot{\alpha}_x = K_{yy}^T\alpha_y + k_d^T\omega\alpha_x + C_{yx}^T\dot{\alpha}_x + C_{yy}^T\dot{\alpha}_y + g_{yx}x \\ m\ddot{x} = K_{xx}^R x - k_d^R\omega y + C^R\dot{x} + f_{xy}\alpha_y + l_{xx}\omega\alpha_x \\ m\ddot{y} = K_{xx}^R y + k_d^R\omega x + C^R\dot{y} + f_{yx}\alpha_x + l_{yy}\omega\alpha_y \end{cases} \quad (6-6)$$

In the above equations,  $K_{xx}^T$  and  $K_{yy}^T$  are the system hydrostatic tilting stiffnesses generated by the thrust bearings [9], the plenum, and the seal in the plenum (in the single-bearing design);  $k_d^T$  and  $C^T$  are the intrinsic hydrodynamic tilting stiffness and the tilting damping coefficient respectively, which are produced by the thrust bearings and the seal in the plenum (in the single-bearing design).

$K_{xx}^R$  and  $K_{yy}^R$  are the system hydrostatic radial stiffnesses generated by the journal bearing(s);  $k_d^R$  and  $C^R$  are the intrinsic hydrodynamic radial stiffness and the radial damping coefficient respectively, also produced by the journal bearing(s).

The coupling coefficients  $g_{xy}$ ,  $g_{yx}$ ,  $f_{xy}$ ,  $f_{yx}$ ,  $l_{xx}$ , and  $l_{yy}$  are defined as follows:

- $g_{xy}y$  is the torque  $T_x$  introduced by the rotor radial displacement  $y$ , while  $g_{yx}x$  is the torque  $T_y$  introduced by the rotor radial displacement  $x$ . Both the torques are generated by the variation of the pressure in the plenum as discussed above (Figure 6-9).

- $f_{xy}\alpha_y$  is the radial force in  $x$  direction  $F_x$  introduced by the rotor tilting motion  $\alpha_y$ , while  $f_{yx}\alpha_x$  is the radial force  $F_y$  introduced by the rotor tilting motion  $\alpha_x$ . Both the forces are generated by the journal bearing(s) due to the variation(s) of entrance pressure(s) caused by pressure variation in the plenum (Figure 6-6).

- $l_{xx}\omega\alpha_x$  is the radial force in  $x$  direction  $F_x$  due to the rotor tilting motion  $\alpha_x$ , while  $l_{yy}\omega\alpha_y$  is the radial force  $F_y$  due to the rotor tilting motion  $\alpha_y$ . Both these two forces are produced by the thrust bearings (when the rotor is off-centered) and the seal (in the single-bearing design), according to Equations (6-2) and (6-4).

It is useful to define nondimensional variables:

$$x_1 \equiv \frac{\alpha_x}{\alpha_0}, x_2 \equiv \frac{\dot{\alpha}_x}{\omega\alpha_0}, x_3 \equiv \frac{\alpha_y}{\alpha_0}, x_4 \equiv \frac{\dot{\alpha}_y}{\omega\alpha_0}, x_5 \equiv \frac{x}{h_0}, x_6 \equiv \frac{\dot{x}}{\omega h_0}, x_7 \equiv \frac{y}{h_0}, x_8 \equiv \frac{\dot{y}}{\omega h_0}, \quad (6-7)$$

where  $h_0$  and  $\alpha_0$  are the journal bearing clearance (about 15 $\mu$ m) and the allowable tilting angle (about 0.002 rad, with which the rotor can touch the seal or the thrust bearings) respectively. Then Equation (6-6) can be rewritten as



$$\begin{cases}
\dot{x}_1 = \omega x_2 \\
\dot{x}_2 = \frac{K_{xx}^T}{A\omega} x_1 + \frac{C_{xx}^T}{A} x_2 - \frac{k_d^T}{A} x_3 + \frac{C_{xy}^T}{A} x_4 - 2x_4 + \frac{g_{xy}c}{A\alpha_0\omega} x_7 \\
\dot{x}_3 = \omega x_4 \\
\dot{x}_4 = \frac{K_{yy}^T}{A\omega} x_3 + \frac{C_{yy}^T}{A} x_4 + \frac{k_d^T}{A} x_1 + \frac{C_{yx}^T}{A} x_2 + 2x_2 + \frac{g_{yx}c}{A\alpha_0\omega} x_5 \\
\dot{x}_5 = \omega x_6 \\
\dot{x}_6 = \frac{K_{xx}^R}{m\omega} x_5 + \frac{C^R}{m} x_6 - \frac{k_d^R}{m} x_7 + \frac{f_{xy}\alpha_0}{mc\omega} x_3 + \frac{l_{xx}\alpha_0}{mc} x_1 \\
\dot{x}_7 = \omega x_8 \\
\dot{x}_8 = \frac{K_{yy}^R}{m\omega} x_7 + \frac{C^R}{m} x_8 + \frac{k_d^R}{m} x_5 + \frac{f_{yx}\alpha_0}{mc\omega} x_1 + \frac{l_{yy}\alpha_0}{mc} x_3
\end{cases} \quad (6-8)$$

Thus the characteristic matrix of equation (6-8) becomes

$$\begin{pmatrix}
0 & \omega & 0 & 0 & 0 & 0 & 0 & 0 \\
\frac{K_{xx}^T}{A\omega} & \frac{C_{xx}^T}{A} & -\frac{k_d^T}{A} & \frac{C_{xy}^T}{A} - 2 & 0 & 0 & \frac{g_{xy}c}{A\alpha_0\omega} & 0 \\
0 & 0 & 0 & \omega & 0 & 0 & 0 & 0 \\
\frac{k_d^T}{A} & \frac{C_{yx}^T}{A} + 2 & \frac{K_{yy}^T}{A\omega} & \frac{C_{yy}^T}{A} & \frac{g_{yx}c}{A\alpha_0\omega} & 0 & 0 & 0 \\
\hline
0 & 0 & 0 & 0 & 0 & \omega & 0 & 0 \\
\frac{l_{xx}\alpha_0}{mc} & 0 & \frac{f_{xy}\alpha_0}{mc\omega} & 0 & \frac{K_{xx}^R}{m\omega} & \frac{C^R}{m} & -\frac{k_d^R}{m} & 0 \\
0 & 0 & 0 & 0 & 0 & 0 & 0 & \omega \\
\frac{f_{yx}\alpha_0}{mc\omega} & 0 & \frac{l_{yy}\alpha_0}{mc} & 0 & \frac{k_d^R}{m} & 0 & \frac{K_{yy}^R}{m\omega} & \frac{C^R}{m}
\end{pmatrix} \quad (6-9)$$

Note that the elements in the top-right and bottom-left corners are the coupling coefficients. Since the above matrix is dependent on the rotating speed  $\omega$ , its eigenvalues and eigenvectors are also dependent on the rotational speed  $\omega$ . When the system is stable, the real parts of all the eigenvalues are negative. As  $\omega$  increases, the real parts of the eigenvalues of the least stable mode increase. At a threshold speed, the real parts of the eigenvalues of the least stable mode become positive, and the system is then unstable. The corresponding eigenvector indicates the unstable mode that the rotor engages in, and the

threshold speed at the onset of the instability is denoted as the stability boundary of the system.

### 6.3.2 Tilting stiffness and Damping from Thrust Bearings

Before going further to calculate the eigenvalues of Matrix (6-9), the tilting stiffness ( $K^T$ ,  $k_d^T$ ) and the tilting damping coefficient ( $C^T$ ) from the thrust bearing must be computed.

The gas in the thrust bearing is governed by the 2-D Reynolds equation [29] and can be solved by the partial-differential-equation toolbox in Matlab. When the thrust bearing pad is tilted, due to the rotor pumping action, a hydrodynamic pressure is built up. The nondimensional pressure field shown in Figure 6-12 is an example of the calculation results with thrust bearing geometry of  $h_0=3 \mu\text{m}$ ,  $R=1 \text{ mm}$ , a rotational speed of 50,000 rad/s, and the tilting angle  $\alpha_y=0.001 \text{ rad}$ . Because of the air compressibility, although the tilt is in  $\alpha_y$  direction, the pressure in the thrust bearing is a little higher on the right-hand side than on the left-hand side, causing a nonzero  $T_y$  as well as  $T_x$ .

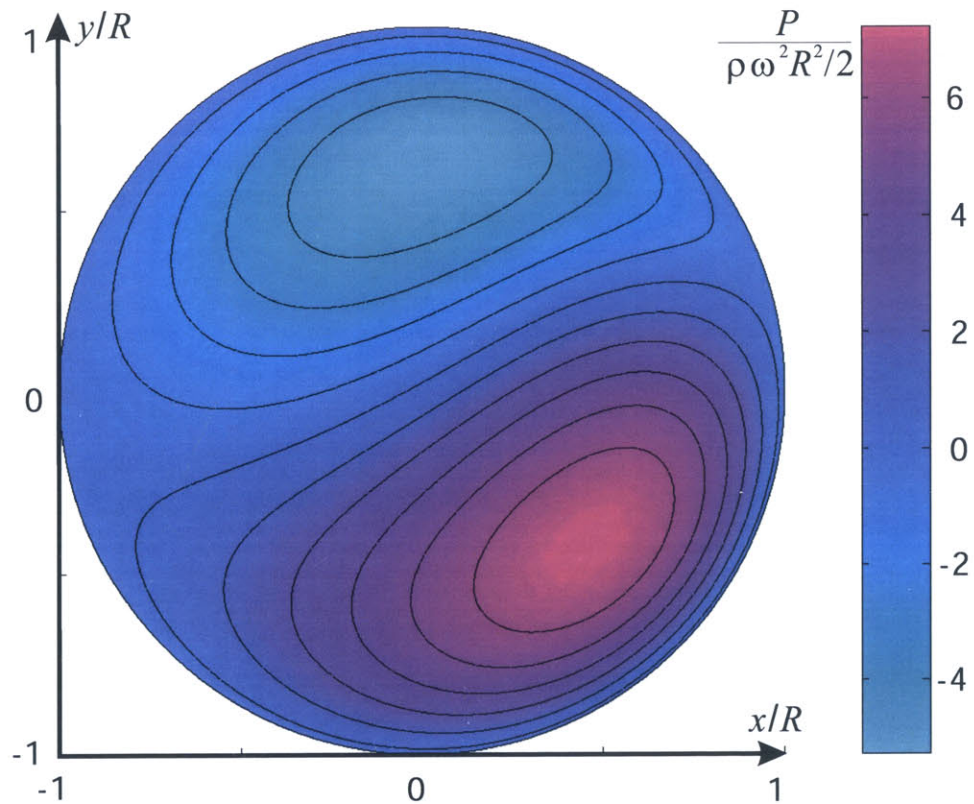


**Figure 6-12: Nondimensional Pressure distribution in the tilted thrust bearing due to rotor pumping action ( $\alpha_y=0.001\text{rad}$ ,  $\omega=50,000 \text{ rad/s}$ ,  $R=1\text{mm}$ ).**

Integration of the pressure in Figure 6-12 gives  $T_x = -5.8199 \times 10^{-6} \text{N}\cdot\text{m}$  and  $T_y = -2.6155 \times 10^{-6} \text{N}\cdot\text{m}$ . The direct-coupled tilting stiffness  $K_{xx}^T$  and the intrinsic cross-coupled stiffness  $k_d^T$  is then calculated:  $K_{xx}^T = T_y/\alpha_y = -0.0026 \text{N}\cdot\text{m}/\text{rad}$ ,  $k_d^T = (T_x/\alpha_y)/\omega = -1.1115 \times 10^{-7} \text{N}\cdot\text{m}\cdot\text{s}/\text{rad}^2$ . Using a similar method, the tilting damping coefficient can also be calculated. By repeating the procedure with different rotor speeds, a table of tilting stiffness and damping coefficients can be generated, (Table 6-2). Then, the tilting stiffness and damping coefficients at other speeds can be approximately calculated by interpolation of the data in Table 6-2. These values are then used to calculate the hydrodynamic torque and damping torque from the thrust bearing in the rotordynamic models established below.

Rotational speed (rad/s)	Cross-coupled tilting stiffness $k_d^T$	Direct tilting stiffness due to viscous pumping: $K_s^T$	Direct damping	Cross-coupled damping
1.0E+03	-1.39E-07	-1.30E-06	-2.59E-07	1.90E-09
2.0E+03	-1.39E-07	-5.22E-06	-2.59E-07	3.80E-09
5.0E+03	-1.38E-07	-3.26E-05	-2.58E-07	9.48E-09
1.0E+04	-1.38E-07	-1.29E-04	-2.57E-07	1.89E-08
2.0E+04	-1.34E-07	-5.01E-04	-2.53E-07	3.71E-08
5.0E+04	-1.16E-07	-0.0026	-2.27E-07	8.22E-08
1.0E+05	-8.30E-08	-0.0069	-1.68E-07	1.18E-07
2.0E+05	-4.4E-08	-0.0128	-8.89E-08	1.13E-07
5.0E+05	-1.39E-08	-0.0189	-2.84E-08	6.70E-08
1.0E+06	-5.40E-09	-0.0221	-1.11E-08	3.91E-08

**Table 6-2: Tilting stiffness and damping coefficients calculated by the numerical PDE solver.**

Meanwhile, the direct tilting stiffness from the thrust bearings due to the external pressure supply is calculated to be about  $0.09 \text{N}\cdot\text{m}/\text{rad}$ , with a thrust bearing supply pressure of 60psig according to [30] or Figure 10-17. This value is entered into the following models to calculate the hydrostatic torque from the thrust bearing according to the rotor tilting angle.

### 6.3.3 Predictions Using the Four-Degree-of-Freedom Model and Comparisons with Experimental Observations

Finally, all the elements in Matrix (6-9) can be computed. The next step is to investigate the dynamic behavior of the coupled system through eigenvalue/eigenvector analyses and compare them to the experimental observations.

The crash point for the device L4-2 was 460 KRPM at  $\Delta p$  of 6.2psig, with the geometry and operating conditions listed in Table 6-3 [32]. With these bearing geometry and operating conditions, the eigenvalues/eigenvectors of Matrix (6-9) can be calculated at varying rotational speeds.

<i>Compressor Bearing Device L4-2</i>	
Comp. Bearing Clearance	17.4 $\mu\text{m}$
Comp. Bearing Length	290 $\mu\text{m}$
Turb. Gap Clearance	50 $\mu\text{m}$
Turb. Gap Length	240 $\mu\text{m}$
Seal Clearance	8 $\mu\text{m}$
Seal Length	200 $\mu\text{m}$
Plenum Height	50 $\mu\text{m}$
Imbalance	0.8 $\mu\text{m}$
Crash $\Delta p$	6.2 psig
Crash Speed	460 Krpm
Seal Inner Radius:	3.29mm
Seal Outer Radius:	3.49mm
Plenum Outer Radius:	4.215mm
Turbine Radius:	3.0mm
Comp. Radius:	4.1mm

**Table 6-3: Geometry and operating conditions at the crash point for device L4-2.**

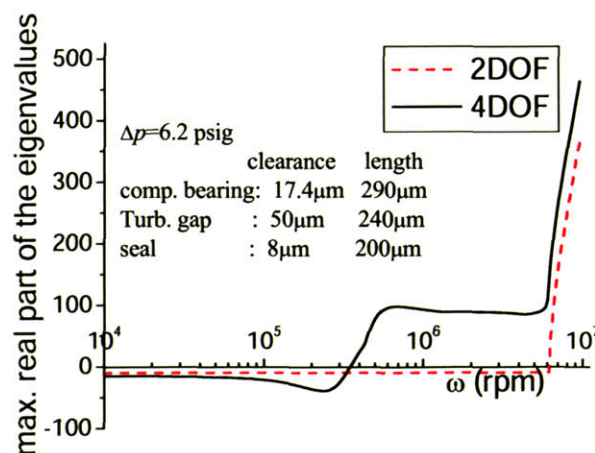


**Figure 6-13: Maximum real parts of the eigenvalues as functions of the rotational speed for the micro-turbo-charger device L4-2, using both two-degree-of-freedom and four-degree-of-freedom models.**

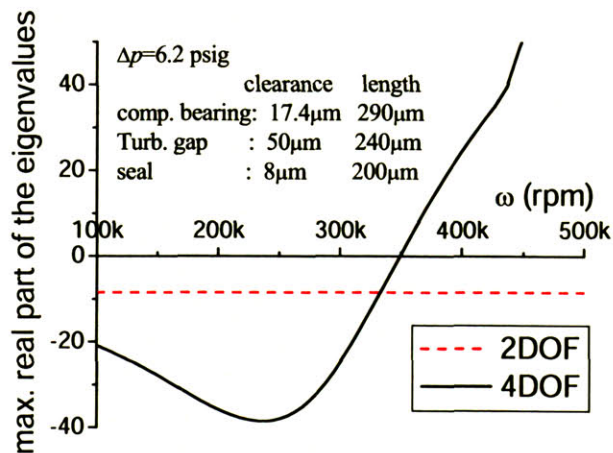


Figure 6-13 shows the maximum real parts of the eigenvalues (the least stable mode) as functions of rotating speed, calculated by both the 4-degree-of-freedom model (solid line) and the 2-degree-of-freedom model (radial modes only, dashed line). The rotational speeds at which the curves cross the horizontal axis are the stability boundary predictions from the corresponding models.

It can be seen from the plot that the maximum real part of the eigenvalues of the 4-degree-of-freedom system asymptotically approaches that of the 2-degree-of-freedom system at both low and high rotor speeds. This means that it is basically the rotor radial motion that determines the stability of the 4-degree-of-freedom system at both high and low rotor speeds. Thus, to design a 4-degree-of-freedom system, the journal bearing should first be designed to have a sufficiently high stability boundary.

Furthermore, it is important to note that the stability boundary of the 4-degree-of-freedom system is much lower than that of the 2-degree-of-freedom system, as shown in Figure 6-13, indicating that the coupling has a negative impact on the stability boundary of the system.

The zoom-in plot of Figure 6-13 is shown in Figure 6-14, and the stability boundary predicted by the 4-degree-of-freedom system is found to be about 350 KRPM, which is near the crash point of 460 KRPM in the experiment.



**Figure 6-14: Enlarged view of Figure 6-13.**

Furthermore, due to the uncertainty of the fabrication, the real seal clearance could be 1  $\mu\text{m}$  larger. If the seal clearance was actually 9  $\mu\text{m}$ , instead of 8  $\mu\text{m}$ , the stability boundary predicted by the 4-degree-of-freedom model would be about 480 KRPM (Figure 6-15), which is much nearer to the crash point. The sensitivity of the system sta-

bility boundary to the seal clearance is due to the strong dependence of the coupling coefficient on the seal clearance. This will be discussed in detail later in the chapter.

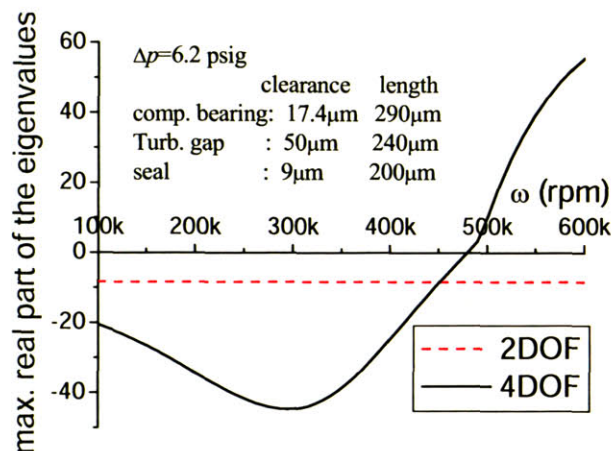


**Figure 6-15: Maximum real parts of the eigenvalues as functions of rotor speed with larger seal clearance in the device L4-2.**

With this rotational speed  $\omega=480$  KRPM, the eigenvalues of the least stable modes for the coupled system of device L4-2, which have the largest real parts, are:  $0.2852 \pm 6011.4i$ . This means that this 4-degree-of-freedom system is driven into an unstable motion at a frequency of  $6011.4 \times 60 / 2\pi = 57405$  rpm, which is near the average of the natural frequencies of the journal-bearing system: 62914 rpm and 55672 rpm in  $x$  and  $y$  directions respectively.

Meanwhile, with the corresponding least stable eigenvectors shown in Table 6-4, the unstable mode of motion is found to have large amplitude in  $\alpha_y$ .

$x_1(\alpha_x)$	$0.10921 \mp 0.34069i$
$x_2(\dot{\alpha}_x)$	$0.040745 \pm 0.013058i$
$x_3(\alpha_y)$	<b>0.74825</b>
$x_4(\dot{\alpha}_y)$	$4.2454e-006 \pm 0.089486i$
$x_5(x)$	$-0.35267 \pm 0.062334i$
$x_6(\dot{x})$	$-0.0074568 \mp 0.042177i$
$x_7(y)$	$0.13131 \pm 0.39054i$
$x_8(\dot{y})$	$-0.046706 \pm 0.015707i$

**Table 6-4: Eigenvector of the least stable mode at the onset of instability for the device L4-2.**



The above results are consistent with observations in the experiments: right before the rotor crashed, both the thrust bearing flow rates dropped due to the rotor conical motion, whose frequency was close to the radial natural frequencies of the journal bearing.

Moreover, at high rotational speed,  $\omega=9$  MRPM, the eigenvector of the least stable mode is

$x_1(\alpha_x)$	$0.00059233 \mp 0.040418i$
$x_2(\dot{\alpha}_x)$	$0.00026831 \mp 1.1583e-005i$
$x_3(\alpha_y)$	$0.031812 \mp 0.033218i$
$x_4(\dot{\alpha}_y)$	$0.00023254 \pm 0.00019825i$
$x_5(x)$	<b>0.71133</b>
$x_6(\dot{x})$	$0.00027299 \pm 0.0047181i$
$x_7(y)$	$0.55353 \pm 0.42875i$
$x_8(\dot{y})$	$-0.0026314 \pm 0.003836i$

**Table 6-5: Eigenvector of the least stable mode at a speed of 9MRPM for the device L4-2.**

Therefore, with large amplitudes in  $x$  and  $y$  directions, the unstable mode in the coupled system at high rotational speed is essentially dominated by the rotor radial motion, or the whirling motion. Thus, in order to make the coupled system stable at high speed, the journal bearing should first be designed to have a sufficiently high stability boundary.

With the geometry of the dual-bearing systems listed in Table 6-6, the unstable mode of motion can be investigated by the same analyses and compared to the experimental observations presented in Section 6.1.

<i>Dual-Bearing Devices</i>	
Comp. Bearing Clearance	14 $\mu\text{m}$
Comp. Bearing Length	330 $\mu\text{m}$
Turb. Bearing Clearance	13 $\mu\text{m}$
Turb. Bearing Length	280 $\mu\text{m}$
Plenum Height	30 $\mu\text{m}$
Plenum Outer Radius:	4.215mm
Turbine Radius:	3.0mm
Comp. Radius:	4.1mm

**Table 6-6: Geometry for dual-bearing systems in Section 6.1.**

The real part of the least stable eigenvalue of the above coupled system is calculated and plotted in Figure 6-16 along with the rotor speed, with pressure fed to the journal

bearing  $\Delta p$  of 1psig. It can be seen that the stability boundary predicted by the 4-degree-of-freedom model is about 125 KRPM, which is consistent with the observation in Figure 6-3: with a rotational speed of 129 KRPM, the conical motion started at  $\Delta p$  of about 1psig.

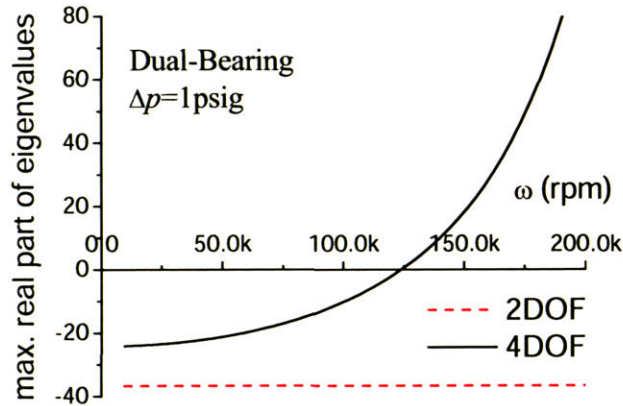


**Figure 6-16: Maximum real part of the eigenvalues as a function of the rotational speed for the dual-bearing systems of Table 6-6.**

Figure 6-16 also shows that, over 125 KRPM, the coupled 4-degree-of-freedom system is unstable, while the 2-degree-of-freedom system is still stable. This is another piece of evidence showing that the coupling has a severe negative impact on the stability of the system. Meanwhile, at a rotational speed of 129 KRPM, the eigenvalues of the least stable modes are  $2.7655 \pm 4300.5i$ , and the corresponding eigenvectors are listed in Table 6-7:

$x_1(\alpha_x)$	$0.066378 \pm 0.28552i$
$x_2(\dot{\alpha}_x)$	$-0.090879 \pm 0.02119i$
$x_3(\alpha_y)$	$-0.6129 \pm 0.060464i$
$x_4(\dot{\alpha}_y)$	$-0.019374 \mp 0.1951i$
$x_5(x)$	<b>0.65392</b>
$x_6(\dot{x})$	$0.00013387 \pm 0.20817i$
$x_7(y)$	$0.010866 \pm 0.12256i$
$x_8(\dot{y})$	$-0.039015 \pm 0.0034843i$

**Table 6-7: Eigenvector of the least stable mode at the onset of instability for the dual-bearing system of Table 6-6.**

Therefore, at 129KRPM rotational speed, the unstable mode of motion in which the rotor engaged had a large amplitude in  $x$  as well as in  $\alpha_y$ . This was the reason that the flow rates in both thrust bearings decreased at that speed.

Furthermore, through the following analyses, one can find that the stability boundary of the coupled system is affected by the pressure supply to the journal bearing as well as the pressure supply to the thrust bearing systems, which is consistent with the experimental observations shown in Figure 6-3.

If the pressure supply to the journal bearing  $\Delta p$  increases from 1psig to 1.1psig while everything else is kept the same, the coupling from the plenum in the dual-bearing systems becomes larger due to a larger pressure drop through the plenum. As a result, the stability boundary of the coupled dual-bearing systems decreases from 125KRPM to 100KRPM, as shown in Figure 6-17.

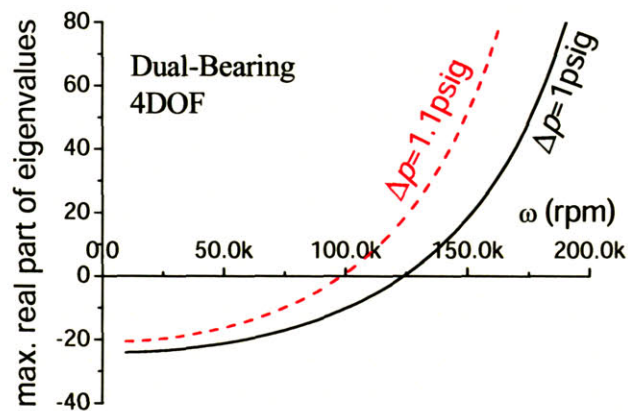


**Figure 6-17: Stability boundary of the coupled dual-bearing system decreases with  $\Delta p$ , predicted by the four-degree-of-freedom model.**

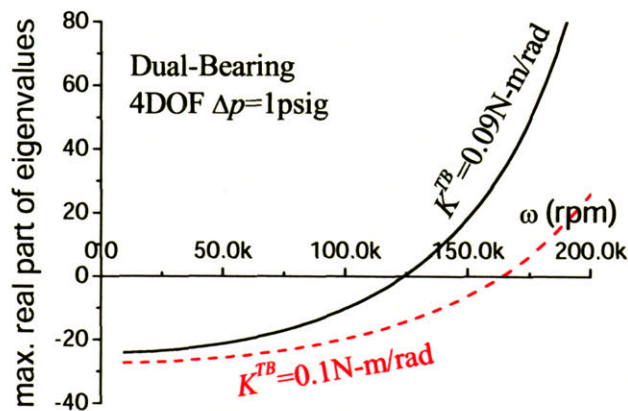


**Figure 6-18: Stability boundary of the coupled dual-bearing system increases with the static tilting stiffness.**

Furthermore, Figure 6-18 shows that if the static tilting stiffness from thrust bearings  $K^{TB}$  increases from 0.09N·m/rad to 0.1N·m/rad (by increasing the supply pressure to the

thrust bearings Figure 10-17), the stability boundary increases from 125 KRPM to about 170 KRPM.

The influences of  $\Delta p$  and thrust bearing stiffness ( $K^{TB}$ ) on the stability boundary of the dual-bearing system predicted by the 4-degree-of-freedom model are summarized in Table 6-8.

SB	$K^{TB}=0.09\text{N}\cdot\text{m}/\text{rad}$	$K^{TB}=0.10\text{N}\cdot\text{m}/\text{rad}$
$\Delta p=0.9\text{psig}$	151 KRPM <sup>1</sup>	200 KRPM
$\Delta p=1.0\text{psig}$	125 KRPM <sup>2</sup>	170 KRPM
$\Delta p=1.1\text{psig}$	100 KRPM	130 KRPM <sup>3</sup>

**Table 6-8: Stability boundary of the coupled dual-bearing system with different pressure supply to the journal bearing and static tilting stiffness, calculated by the four-degree-of-freedom model.**

Thus, with higher rotational speed and the same pressure supply to the thrust bearings (125 KRPM <sup>2</sup>  $\rightarrow$  151 KRPM <sup>1</sup> in the table), the unstable rotor conical motion occurs at a smaller pressure supply to the journal bearing  $\Delta p$  (1.0psig  $\rightarrow$  0.9 psig), which is consistent with Figure 6-3. And with higher thrust bearing pressures ( $K^{TB}=0.09$  <sup>2</sup>  $\rightarrow$   $K^{TB}=0.10$  <sup>3</sup>) and the same rotational speed ( $\sim$ 125KRPM), the unstable rotor conical motion happens at a larger  $\Delta p$  (1.0psig  $\rightarrow$  1.1psig), which is also consistent with the experimental observations shown in Figure 6-3.

Therefore, after all these comparisons with the experimental data, it is suggested that there is a strong coupling between the rotor conical and radial motions in the micro-turbo-charger devices. This coupling can destabilize the devices at speeds much lower than the whirl instability limit of the radial motions alone, and the unstable mode of motion in which the rotor engages is a conical motion with a frequency near the journal bearing natural frequencies. In the dual-bearing system, it is also found that the coupling increases with the pressure supply to the journal bearing plenum  $\Delta p$ , reducing the stability boundary even more; and this unstable conical motion can be suppressed by increasing pressure supply to the thrust bearings.

With these findings, the following design guidelines for the micro-bearing system can be established: 1) the journal bearing alone should be designed to have a sufficiently high stability boundary; 2) the coupling between the rotor conical and radial motions should be decreased as much as possible, or even eliminated (by the centrally-feed journal bearing configuration as discussed in Chapter 7); and 3) the thrust bearing system

should be designed to support the rotor with as large a tilting stiffness as possible, so that the conical motion can be suppressed.

### 6.3.4 Effects of Axial Position and Seal Clearance on Coupling and Stability Boundary

As was shown earlier for device L4-2, with a larger seal clearance, the coupling will be smaller, resulting in a higher stability boundary for the coupled system (Figure 6-15). With the following analyses, one can find that the axial position of the rotor also affects the coupling between the radial and conical motions, and hence the stability boundary of the coupled system.

From Equations (6-2) and (6-4), used to compute the coupling forces from the thrust bearing and seal respectively, the coupling coefficients  $l$  can be deduced by differentiating the forces with respect to the tilting angle  $\alpha$ . Thus the coupling coefficient  $l$  from the aft thrust bearing with clearance of  $h_0$  and radius of  $R$  is

$$l^{TB} = \left. \frac{dF_y}{d\alpha_y} \right|_{\alpha_y=0} = -\frac{\pi}{4} \mu \omega \frac{R^4}{h_0^2}. \quad (6-10)$$

The coupling coefficient from the forward thrust bearing has the same amplitude, but of the opposite sign. Furthermore, the coupling coefficient from the seal with a clearance of  $h_0$  and radial location  $R$  is

$$l^{Seal} = \left. \frac{dF_y}{d\alpha_y} \right|_{\alpha_y=0} = -\pi \mu \omega \frac{R^3 L}{h_0^2}. \quad (6-11)$$

It can be seen that the coupling coefficients are strong functions of the clearance  $h_0$ : they are inversely proportional to  $h_0^2$ . Because the clearance is already small, just several microns, a small decrease in clearance can greatly increase the coupling coefficients  $l$ . Since the radial location of the seal ( $\sim 3.4$  mm) is around 3 times larger than the radius of the thrust bearing pads ( $\sim 1$  mm), the coupling coefficients induced by the seal are comparable to those induced by the thrust bearings, even though the seal clearance ( $\sim 9$   $\mu\text{m}$ ) is larger than the clearances of the thrust bearings ( $\sim 3$   $\mu\text{m}$ ).

As discussed previously in the chapter, when the rotor is axially centered and the thrust bearings are identical, as in the micro-turbo-charger devices, the coupling contributions from both thrust bearings cancel each other. In this case, the coupling coefficient  $l$  is only from the seal in the devices with the single-bearing configuration, and it decreases



with the seal clearance  $h_0$  given by Equation (6-11), making the system more stable. This has been illustrated by the comparison between Figure 6-14 and Figure 6-15.

Furthermore, since the rotor axial movement varies the clearances of both thrust bearings and seal, strongly influencing the coupling according to Equation (6-10) and (6-11), the stability boundary of the coupled system is sensitive to the rotor axial location. For example, if the rotor of the device L4-2 (with the configurations shown in Figure 6-14) moves up by only  $0.5 \mu\text{m}$  from the axially centered position, the two thrust bearings together generate a nonzero coupling in the opposite direction of that from the seal, reducing the net coupling coefficient  $l$ . Then, the system stability boundary increases from 350 KRPM to 445 KRPM, as shown in Figure 6-19 by the red dashed line.

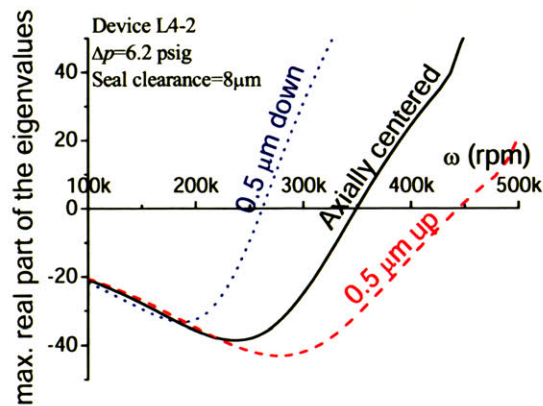


**Figure 6-19: Stability boundary of device L4-2 changes with the rotor axial position.**

Conversely, if the rotor moves down, the net coupling coefficient  $l$  is enlarged by both the contribution from the two thrust bearings and the increase from the seal, making the stability boundary even lower (blue dotted line in Figure 6-19).

Therefore, during operation, the rotor should be pushed up to an optimum axial position where the coupling coefficient  $l$  is the smallest in order to achieve a high stability boundary. In fact, during the high-speed experiment that led the device L4-2 to crash at speed of 460 KRPM, it is quite possible that the rotor was a little bit nearer to the forward thrust bearing, resulting in a crash speed a little higher than the prediction of Figure 6-14 with seal clearance of  $8 \mu\text{m}$ . Furthermore, in another high-speed test before it crashed, this device was spun at a higher speed (480 KRPM) without instability; this can also be ex-



plained by the difference in axial position, which is difficult to control in the experiments [32].

In order to reduce the coupling effect in the micro-turbo-charger devices, a new design was employed, as sketched in Figure 4-25. In this design, a larger hydrostatic stiffness anisotropy is introduced to the system (as discussed on Figure 4-27). Most importantly, the coupling coefficients are significantly reduced in this new design by increasing the seal clearance from  $8\ \mu\text{m}$  to  $20\ \mu\text{m}$ . As a result, according to the calculation results shown in Figure 6-20 using the 4-degree-of-freedom model, the stability boundary of the coupled system is much higher ( $>800\text{KRPM}$ ), even if the rotor moves  $1\ \mu\text{m}$  down.

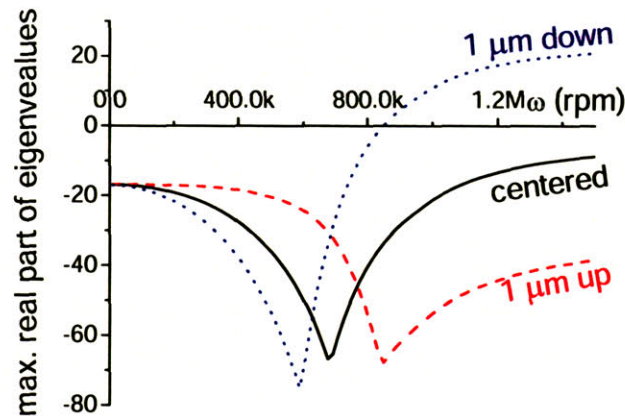


**Figure 6-20: Enhanced stability boundary of micro-turbo-charger devices due to reduced coupling effects in the new journal-bearing system design.**

The coupling between the rotor conical and radial motions is not only found in the micro-turbo-charger devices; it also exists in the micro-bearing-rig devices, where it comes from the seal (in both the blocked regions and the plenum regions (Figure 4-3)) as well as from the thrust bearings.

During the operation of the micro-bearing-rig devices, the rotors are normally axially centered, and the clearances for the two thrust bearings and the seals are all  $2\ \mu\text{m}$ . The calculations based on the 4-degree-of-freedom model show that, although the coupling reduces the system stability boundary of the micro-bearing-rig devices, the decrease is not as severe as in the micro-turbo-charger devices (Figure 6-21). This is because the overlap of the rotor and the plenum in the micro-bearing rig with the part-bearing configuration is only around  $30\ \mu\text{m}$ , much smaller than in the micro-turbo-charger ( $1\ \text{mm}$ ), resulting in much smaller coupling coefficients  $g$  in the micro-bearing-rig devices ( $\sim 0.5\ \text{N}$ ) than in the micro-turbo-charger devices ( $\sim 30\ \text{N}$  according to Figure 6-9).

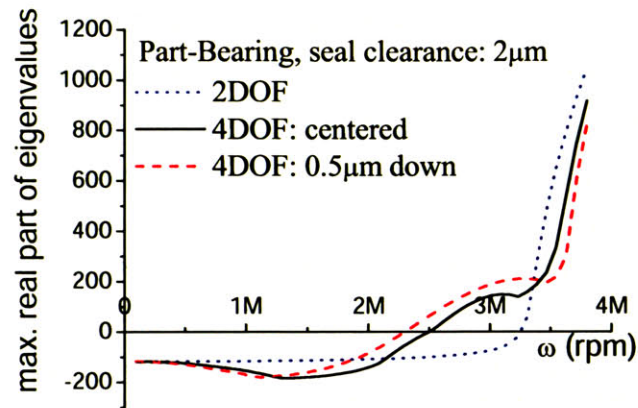


**Figure 6-21: Stability boundary in the micro-bearing-rig devices influenced by coupling with different rotor axial locations.**

However, as the rotor speed increases, the centrifugal force of the blades bonded to the rotor disk increases as a quadratic function of the rotor speed. With the bending torque induced by the centrifugal force of the blades, the rotor disk deforms into an umbrella shape. Furthermore, this “umbrella” deformation of the rotor disk becomes larger and larger as the rotor speed increases, continually reducing the seal clearance. According to [30], the axial displacement of the disk edge due to the deformation can be as large as several microns at the design speed. Thus, the rotor edge will touch the seal at the design speed (2.4 million rpm).

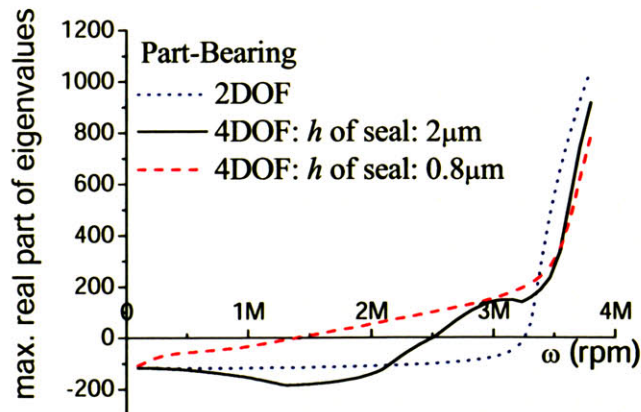


**Figure 6-22: Part-bearing system becomes unstable with smaller seal clearance due to umbrella deformation of the rotor disk.**

Moreover, according to Figure 6-22, the coupled system stability boundary ( $\sim 1.3$  MRPM with seal clearance of  $0.8\mu\text{m}$ ) can be much lower than the design speed of 2.4 MRPM due to the decrease in seal clearance caused by the disk umbrella deformation.



Therefore, even before the rotor edge touches the seal, the system becomes unstable due to the significant increase of coupling coefficient  $l$  from the seal.

To solve this problem, a new design (Figure 4-20) employing four plena with a much larger seal clearance ( $\sim 12 \mu\text{m}$ ) is proposed [7]. Even with the umbrella deformation of the disk at the design speed, the seal clearance in this design is still large enough ( $\sim 4 \mu\text{m}$ ) so that the coupling will not seriously affect the stability boundary.

### 6.4 Five-Degree-Of-Freedom Numerical Model

In the last section, it was concluded that the coupled system's dynamic behavior is sensitive to the rotor axial position. Moreover, the axial forces from the plenum in the micro-turbo-charger vary with the precessing and conical motions of the rotor (plotted in Figure 6-23), exciting the axial oscillation motion of the rotor. This rotor axial oscillation can then affect the motions of conical and radial modes, and thus all the 5 degree-of-freedom motions are coupled together.

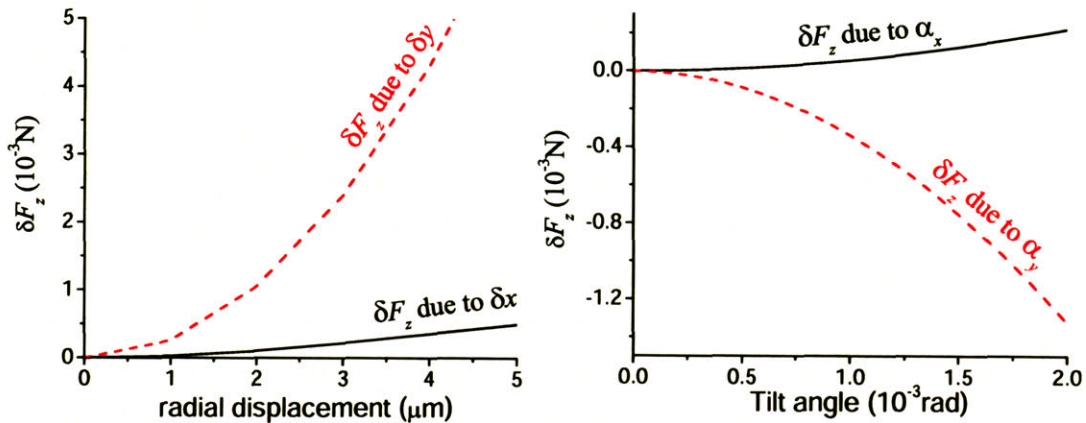


**Figure 6-23: Axial force  $\delta F_z$  from the plenum as a function of rotor radial displacement and tilting angles.**

In the following analysis, numerical simulations are employed to investigate the 5-degree-of-freedom system nonlinearly. From the simulation results, the amplitude of the rotor axial vibration excited by the coupling is found to be negligible (only several nanometers), and the above linear analyses based on the 4-degree-of-freedom model are validated.

The equations of motions for the 5-degree-of-freedom system are:

$$\begin{cases} A\ddot{\alpha}_x + 2A\omega\alpha_y = T_x(y, \alpha_x, \dot{\alpha}_x, \alpha_y, \dot{\alpha}_y, z) + A\omega^2\phi \cos(\omega t) \\ A\ddot{\alpha}_y - 2A\omega\alpha_x = T_y(x, \alpha_x, \dot{\alpha}_x, \alpha_y, \dot{\alpha}_y, z) + A\omega^2\phi \sin(\omega t) \\ m\ddot{x} = F_x(x, \dot{x}, y, \alpha_x, \alpha_y, z) + m\omega^2 a \cos(\omega t) \\ m\ddot{y} = F_y(x, y, \dot{y}, \alpha_x, \alpha_y, z) + m\omega^2 a \sin(\omega t) \\ m\ddot{z} = F_z(x, y, \alpha_x, \alpha_y, z, \dot{z}) \end{cases} \quad (6-12)$$

where  $a$  is the static unbalance of the rotor (distance from the geometric center to the mass center) and  $\phi$  is the dynamic unbalance of the rotor (angle between the geometric axis and principal axis).  $F_x, F_y, F_z, T_x$  and  $T_y$  can already be calculated by the fluid models developed in this chapter and previous chapters. From the above equations, it can be seen that motions in  $x, y, z, \alpha_x$  and  $\alpha_y$  are all coupled together. Meanwhile, the static unbalance  $a$  is the direct excitation of the rotor radial motions ( $x, y$ ), and the dynamic unbalance  $\phi$  is the direct excitation of the rotor conical motions ( $\alpha_x, \alpha_y$ ). The rotor vibration in axial direction  $z$  is excited through the dependence of  $F_z$  on its radial displacements and tilting angles (Figure 6-23).

A numerical scheme similar to the one in Chapter 4 is used to solve the equations (6-12). In every time step, the forces and torques from the journal bearing, plenum, and seal are calculated according to the rotor position and velocities, with full nonlinearity of most bearing forces and torques in the simulations. Since the computation of the torques and forces from the thrust bearing involves a 2-dimensional PDE computation, which is relatively expensive, linearized and pre-calculated ones (Table 6-2) are used instead.

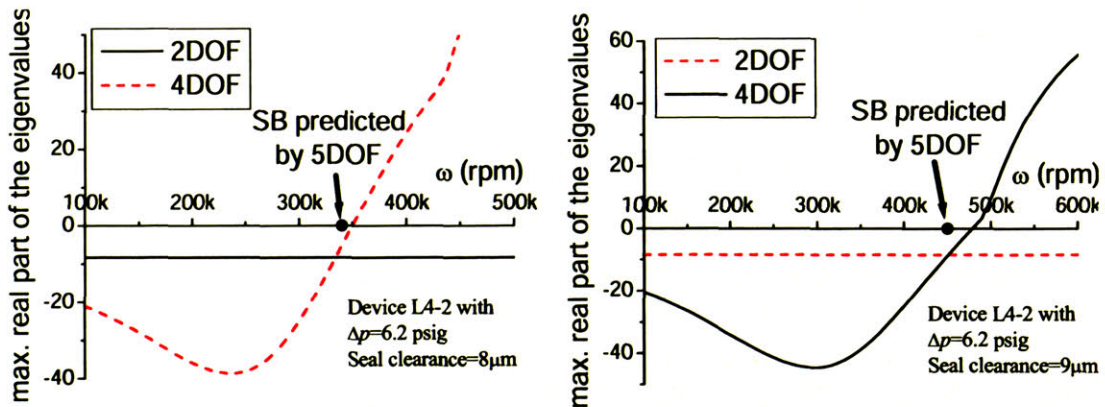


**Figure 6-24: Stability boundary of the micro-turbo-charger device L4-2 predicted by the nonlinear five-degree-of-freedom numerical simulation, compared with that predicted by the linear four-degree-of-freedom model.**

In Figure 6-24, the stability boundary in the single-compressor-bearing system (device L4-2) is calculated by this 5-degree-of-freedom numerical simulation. In the simula-



tion, the rotor is assumed to have a static unbalance of  $0.1 \mu\text{m}$  and a dynamic unbalance of  $10^{-5}$  rad, which are negligible compared with the bearing clearance ( $17.4 \mu\text{m}$ ) and allowable tilting angle ( $\sim 0.002$  rad). With these unbalances, the calculation results of the 5-degree-of-freedom numerical simulation can be used to assess the linear 4-degree-of-freedom model established above, in which negligible unbalances have been assumed. The results show that the predictions by both models are close to each other, so the linear 4-degree-of-freedom model is verified by the 5-degree-of-freedom nonlinear numerical model.

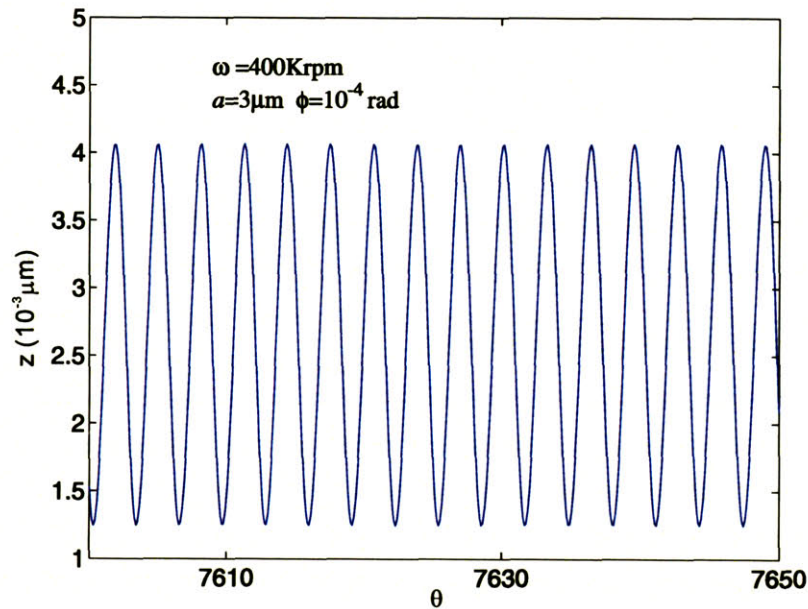


**Figure 6-25: Simulated rotor vibration in z direction with finite unbalances for micro-turbo-charger device L4-2, at rotor speed of 400KRPM.**

On the other hand, if the unbalances of the system are  $a=3 \mu\text{m}$  and  $\phi=10^{-4}$  rad, which are normal for the micro-turbo-charger devices [6], simulations show that the amplitude of rotor vibration in axial (z) direction (Figure 6-25) is very small (several nanometers) compared with the thrust bearing clearances, and is negligible. This is due to the large stiffness and damping in the thrust-bearing systems.

Then, in Figure 6-26, the simulated orbits (both radial and conical) of the rotor are plotted. In the plots, the radial displacements are normalized by the journal bearing clearance ( $h_0=17.4 \mu\text{m}$ ), while the conical tilting angles are normalized by the allowable tilting angle ( $\alpha_0=0.002\text{rad}$ ). Among the radial orbits, the inner red one is the orbit of the rotor mass center while the outer blue one is the orbit of the rotor geometric center, indicating that the rotor is spinning supercritically around its mass center at this speed (400KRPM). Among the conical orbits, the red dashed line is the orbit of the rotor principal axis, while

the blue solid line is the orbit of the rotor geometric axis. They are of comparable amplitude, indicating that the speed is near the conical natural frequency.

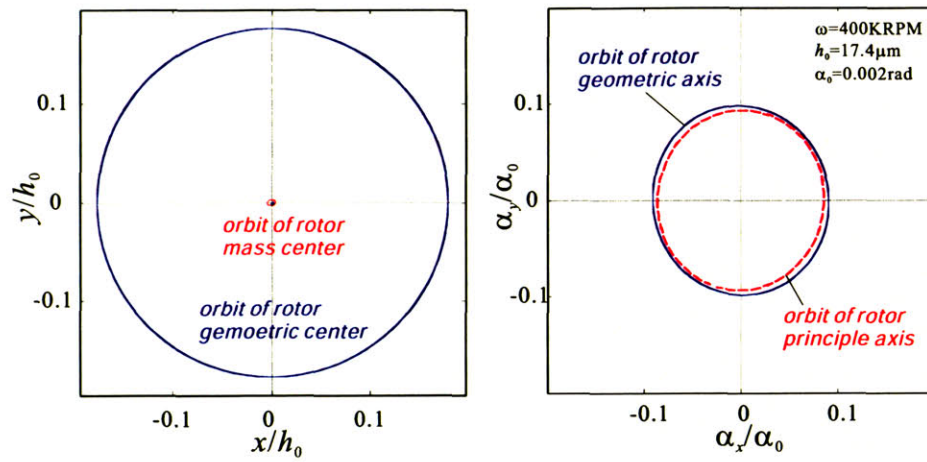


**Figure 6-26: Simulated orbits of the rotor radial (left) and conical (right) motions in micro-turbo-charger device L4-2 at rotor speed of 400KRPM.**

### 6.5 Summary and Conclusions

In this chapter, a linear 4-degree-of-freedom model was established to investigate the coupling between the radial and conical modes of motion in the micro-bearing system, and a nonlinear 5-degree-of-freedom numerical model was also established to investigate the effect of axial oscillation on the system dynamic behavior. Using an eigenvalue and eigenvector analysis, the threshold speed of the onset of instability (stability boundary) can be derived based on the linear 4-degree-of-freedom model. Through expensive numerical simulations, the stability boundary of the coupled system can also be obtained by the numerical nonlinear 5-degree-of-freedom model. The numerical simulations done using the 5-degree-of-freedom model have verified the 4-degree-of-freedom model and shown that the axial vibrations are negligible.

Coupling forces and torques from the plenum, the seal, and the thrust bearings were found to occur. The calculations show that radial forces can be induced by rotor tilting motions from the plenum, the seal, and the thrust bearings, and torques acting on the rotor can be induced by rotor radial motions from the plenum.

Most importantly, the coupling can drive the system into a conical motion with a frequency close to the natural frequency of the radial motion, destabilizing the system at a much lower speed than the whirl instability limit of the journal-bearing system alone. Furthermore, in the dual-bearing micro-turbo-charger devices, the coupling increases with the pressure supply to the journal bearing, reducing the system stability boundary;



and the static tilting stiffness generated by the thrust bearings can effectively suppress the unstable conical motion and stabilize the system. The predictions of the 4-degree-of-freedom model were consistent with the experimental observations, and hence the linear 4-degree-of-freedom model was experimentally validated.

The following design guidelines were developed based on this analysis: 1) the journal bearing alone should be designed to have a sufficiently high stability boundary; 2) the coupling between the rotor conical and radial motions should be as small as possible, or even be eliminated (by the centrally-fed journal bearing configuration discussed in Chapter 7); and 3) the thrust-bearing system should be designed to support the rotor with as large a tilting stiffness as possible, so that the conical motion can be suppressed.

Since the coupling coefficients  $l$  are strong functions of the clearances of the thrust bearings and seal, one could enlarge the seal clearances in the new design to reduce the coupling and increase the stability boundary. During the operation of the single-bearing micro-turbo-charger devices, the rotor can also be pushed axially toward the forward thrust bearing into a position where the total coupling from thrust bearings and seal is smallest, in order to enhance system stability.



## *Chapter 7*

# **Centrally-Fed Micro-Hydrostatic Gas Journal Bearings**

As was discussed in Chapter 6 on the multi-degree-of-freedom system, axially-fed micro-journal-bearing system (AFJB) designs are found to be able to introduce coupling between the rotor's radial and conical motions through the seal and plenum of the aft-side feed system, reducing the stability boundary of the coupled system.

As a possible way to eliminate this unwanted coupling, a centrally-fed configuration (as shown in Figure 1-8-*b*) is proposed for the micro-journal-bearing system. Because of the symmetry of the feed system in this configuration, no torque on the rotor can be induced by the rotor's radial movement, and no radial force can be induced by the rotor tilting movement. The coupling between the rotor's conical and radial motions can then be eliminated by this centrally-fed configuration.

Although this centrally-fed micro-journal-bearing (CFJB) system was considered for the micro-bearing system at the beginning of the MIT micro-engine project, it was found more difficult (more layers were needed) to fabricate the centrally-fed micro-journal-bearings than the axially-fed ones. Therefore, the axially-fed micro-journal bearings were chosen instead for their simpler structure, and the research has been focused on these axially-fed bearing configurations.

After observing the coupling phenomena in the experiments, this research on the application of the centrally-fed micro-journal-bearing in micro-bearing systems was motivated by the desire to eliminate the coupling. In this chapter, both fluid models and rotordynamic models for centrally-fed micro-journal-bearing systems are established. Then, based on these models, the rotordynamic behavior of the centrally-fed micro-journal-bearing system is investigated and compared to that of the axially-fed micro-journal-bearing system. The results show that, although the coupling is eliminated, the distance to contact in the centrally-fed micro-journal-bearing system is much smaller than that in the axially-fed system.

### 7.1 Centrally-Fed Micro-Journal-Bearing Configuration

In the centrally-fed micro-journal-bearing configuration sketched in Figure 7-1, the coupling between the rotor's conical and radial motions is eliminated: when the rotor moves in the radial direction, the pressure in the bearing doesn't produce any torque that may drive the rotor in a conical motion because it is acting perpendicular to the rotor surface. Thus, the coupling coefficients in the upper right corner of the characteristic matrix (6-9) are zeros. As a result, the conical motion is decoupled from the radial motion in the centrally-fed micro-journal-bearing system, eliminating the coupling that reduces the system stability boundary.

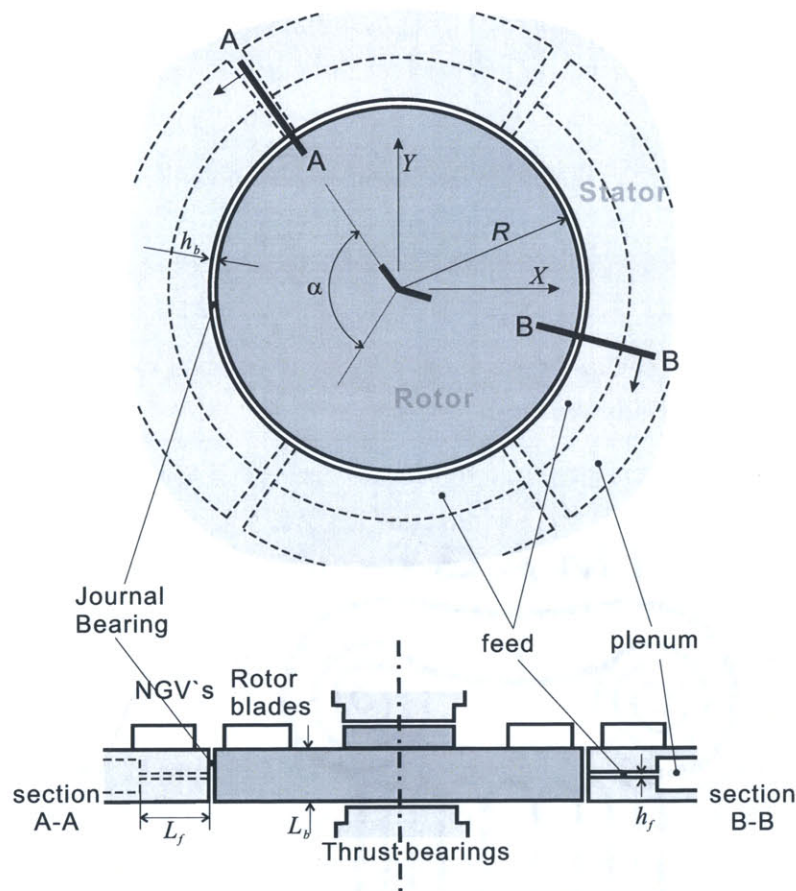


**Figure 7-1: Centrally-fed micro-journal bearing with hydrostatic stiffness anisotropy.**

In order to retain hydrostatic stiffness anisotropy in the centrally-fed micro-journal-bearing system, the four-plenum design was kept from the axially-fed micro-journal-bearing configuration shown in Figure 7-1. Thus, the feed system consists of 4 bisymmetric sections, each with its own external pressure supply and plenum. During operation of

the system, the pressure supplies to the opposite plena should be equal to avoid sideload, which reduces the stability boundary in anisotropic bearing systems as discussed in Chapter 4.

As also shown in Figure 7-1, there are two sets of clearances and lengths in the centrally-fed micro-journal-bearing system: the length of the bearing  $L_b$ , the length of feed  $L_f$ , the clearance of bearing  $h_b$ , and the clearance of the feed  $h_f$ . In this chapter, fluid models will be established to examine the influences of these parameters on the system dynamics.

## 7.2 Fluid Models for Centrally-Fed Micro-Journal Bearings

Like the fluid models developed in Chapter 2 for axially-fed micro-journal-bearing systems, the fluid models for the centrally-fed micro-journal bearings are based on the same assumptions/approximations and consist of three components: hydrostatic, hydrodynamic, and damping flow models, which are used to calculate the hydrostatic force, hydrodynamic force, and damping force respectively.

### 7.2.1 Hydrostatic Flow and Forces

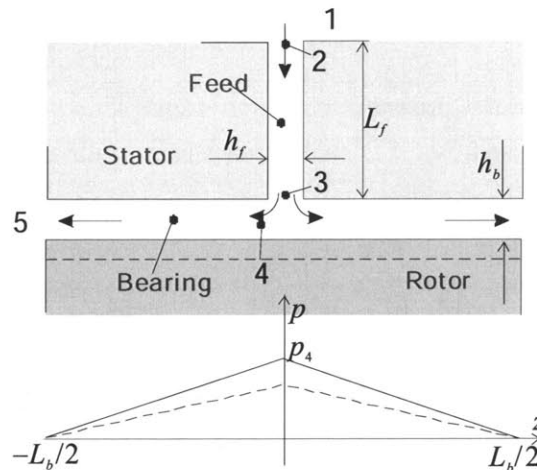


**Figure 7-2: Cross section of the centrally-fed micro-journal bearing with a sketch of the pressure distribution along the bearing.**

As shown in Figure 7-2, the air/gas is fed at point 1, with pressure of  $\Delta p$ . It goes through the feed and then enters the bearing. When the bearing clearance decreases (from the dashed line to the solid line in Figure 7-2) due to the rotor movement, the bearing flow resistance increases, reducing the flow rate in the bearing and the feed. As a result, the pressure drop through the feed decreases, raising the pressure in the bearing. On the opposite side of the centrally-fed micro-journal-bearing system, the pressure in the bear-

ing becomes lower due to the increase in bearing clearance. Therefore, a hydrostatic restoring force acting on the rotor is produced.

More specifically, similar to the analysis for axially-fed micro-journal-bearing systems in Chapter 2, the static pressure drop at the entrance of the feed is

$$p_1 - p_2 = \frac{\gamma_e}{2} \rho u_2^2 = \frac{\gamma_e}{2} \rho \frac{q^2}{h_f^2}, \quad (7-1)$$

where  $\gamma_e$  is the entrance static pressure loss coefficient, which is 1.5 according to Chapter 2;  $u$  is the average velocity in the feed; and  $q$  is the flow rate through the feed-bearing system (per unit length in the circumferential direction).

The pressure drop through the feed is

$$p_2 - p_3 = \frac{12\mu}{h_f^3} qL_f. \quad (7-2)$$

There is another pressure loss at the turning point 3-4:

$$\left( p_3 + \frac{\rho}{2} u_3^2 \right) - \left( p_4 + \frac{\rho}{2} u_4^2 \right) = \frac{\gamma_t}{2} \rho u_3^2, \quad (7-3)$$

where  $\gamma_t$  is the turning total pressure loss coefficient. This is 1.3 according to hydraulic handbooks, and is assessed by CFD calculations later in this section. Equation (7-3) can be rewritten in terms of flow rate  $q$ :

$$p_3 - p_4 = \frac{\rho}{2} \left( (\gamma_t - 1) \frac{1}{h_f^2} + \frac{1}{4h_b^2} \right) q^2. \quad (7-4)$$

Due to the symmetry, half of the flow from the feed  $q/2$  goes left through the bearing, while the other half goes right. Therefore, the pressure drop through the bearing is

$$p_4 - p_5 = \frac{6\mu}{h_b^3} qL_b. \quad (7-5)$$

Summing Equations (7-1), (7-2), (7-4), and (7-5) and noting that  $p_1 = \Delta p$  and  $p_5 = 0$  yields

$$\frac{\gamma_e}{2} \rho \frac{q^2}{h_f^2} + \frac{12\mu}{h_f^3} qL_f + \frac{\rho}{2} \left( (\gamma_t - 1) \frac{1}{h_f^2} + \frac{1}{4h_b^2} \right) q^2 + \frac{6\mu}{h_b^3} qL_b = \Delta p. \quad (7-6)$$

Therefore,



$$q(\theta) = \frac{-b(\theta) + \sqrt{b^2(\theta) + 4a(\theta) \cdot \Delta p}}{2a(\theta)}, \quad (7-7)$$

where

$$a(\theta) \equiv \frac{\gamma_e \rho}{2 h_f^2} + \frac{\rho}{2} \left( (\gamma_t - 1) \frac{1}{h_f^2} + \frac{1}{4h_b^2(\theta)} \right), \quad b(\theta) \equiv \frac{12\mu L_f}{h_f^3} + \frac{6\mu L_b}{h_b^3(\theta)},$$

and  $h_b(\theta) = h_b - \varepsilon \cos(\theta)$ ,  $\varepsilon$  is the rotor eccentricity relative to the bearing center. Integration of Equation (2-10) gives the total flow rate  $Q$  through the journal bearing

$$Q = \int_0^{2\pi} q(\theta) R d\theta. \quad (7-8)$$

Furthermore, according to Equations (7-7) and (7-5), the pressure  $p_4$  is

$$p_4(\theta) = \frac{6\mu L_b}{h_b^3(\theta)} \cdot q(\theta). \quad (7-9)$$

Integration of (7-9) with respect to  $z$  and  $\theta$  yields the hydrostatic force  $F^{hs}$ ,

$$F^{hs} = 2 \int_0^{2\pi} -R \cos(\theta) d\theta \int_0^{L_b/2} dz \left( p_4(\theta) \frac{(L_b - 2z)}{L_b} \right) = -\frac{L_b R}{2} \int_0^{2\pi} p_4(\theta) \cos(\theta) d\theta. \quad (7-10)$$

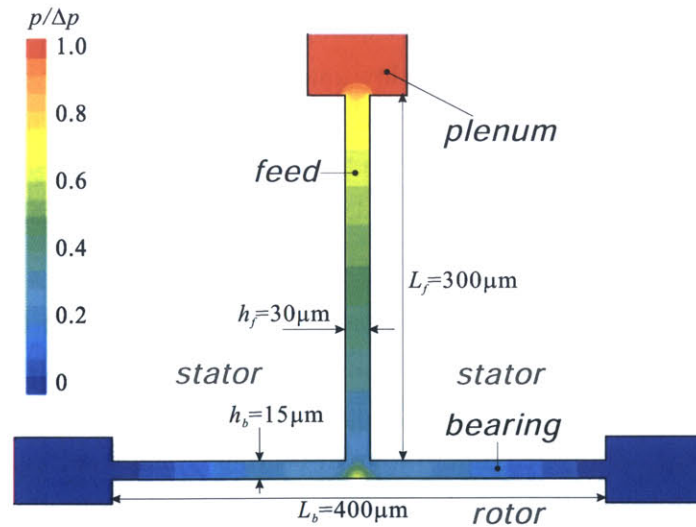


**Figure 7-3: Pressure distribution in the centrally-fed micro-journal-bearing system with  $L_b=400\mu\text{m}$ ,  $h_b=15\mu\text{m}$ ,  $L_f=300\mu\text{m}$ ,  $h_f=30\mu\text{m}$ ,  $\Delta p=5\text{psig}$ , by 2D CFD (Fluent).**

To validate the loss coefficients, 2-D CFD (Fluent 2D) calculations were done for the centrally-fed micro-journal-bearing system. From the pressure contour as shown in Figure 7-3, one can find that the distance from the entrance of the feed (bearing) to the point where the flow can be treated as fully developed is short—just on the order of the clearance of the feed (bearing). Therefore, the assumption of a fully developed flow is reasonable.

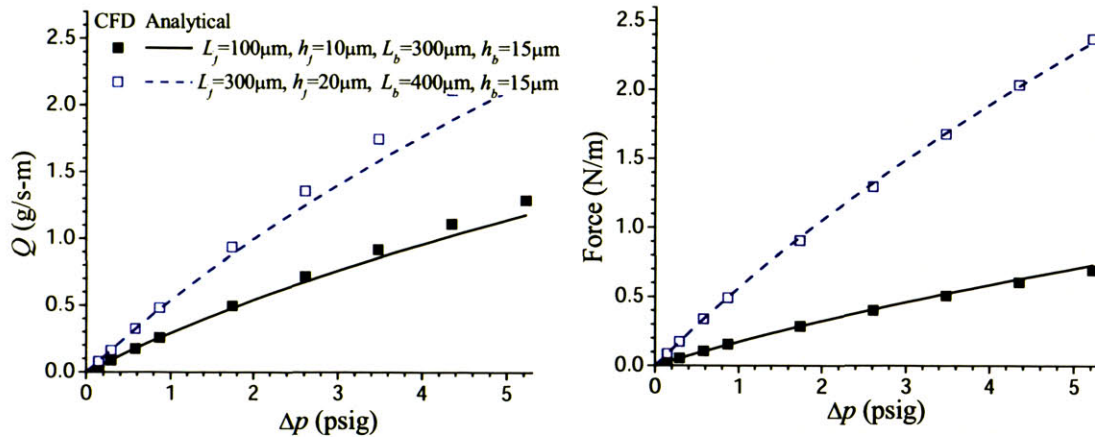


**Figure 7-4: Calculations by the model compared with CFD: flow rate (left) and force (right) for the centrally-fed micro-journal bearings.**

Changing the supply pressure  $\Delta p$  and repeating the CFD calculations, the flow rate through the bearing system and the force acting on the rotor can then be obtained as functions of  $\Delta p$ . Shown in Figure 7-4, the flow rate through the bearing system (left) and the bearing force (right) are calculated for two different centrally-fed micro-journal-bearing configurations, using the CFD and the model as comparison. The agreement between the model predictions and the CFD results indicates that the loss coefficient choices are correct for the centrally-fed micro-journal-bearing system.

Thereafter, the flow rates and the natural frequencies of the centrally-fed micro-journal-bearing system can be calculated and compared with those of the axially-fed micro-journal-bearing system (Figure 7-5). From the plot, it can be seen that as the feed clearance in the centrally-fed micro-journal-bearing system decreases from  $20\mu\text{m}$  to  $15\mu\text{m}$ , both the flow rate through the bearing system and the natural frequency decrease. This is because a decrease in feed clearance causes a larger flow resistance through the feed, reducing both the flow rate and the pressure in the bearing, which in turn reduces the hydrostatic force and hence the system natural frequency.

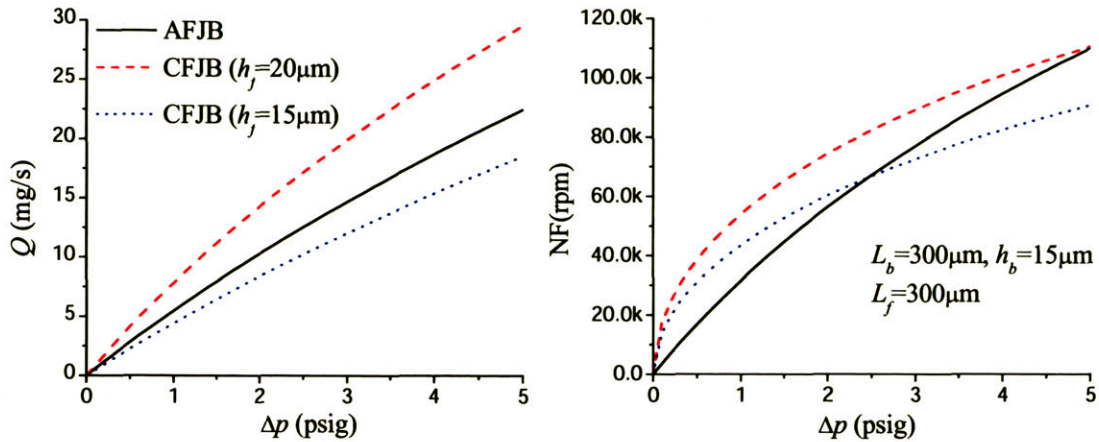


**Figure 7-5: Flow rates (left) and natural frequencies (right) of the centrally-fed micro-journal-bearing system (CFJB) compared with those of the axially-fed micro-journal-bearing system (AFJB).**

### 7.2.2 Hydrodynamic Force

As in the axially-fed micro-journal-bearing system, in the centrally-fed micro-journal-bearing system, pressure is built up in the bearing with the displaced spinning rotor due to the rotor pumping action, resulting in a hydrodynamic force. At the same time, the nonuniform viscous stress on the rotor surface due to the rotor rotation makes a further contribution to the hydrodynamic force. The following analysis will show that the hydrodynamic force due to viscous drag effect is of comparable magnitude but in the opposite direction to the hydrodynamic force due to rotor pumping action in the ultra-short centrally-fed micro-journal-bearing system.

As in the axially-fed micro-journal bearings, the pressure field due to rotor pumping action in the centrally-fed micro-journal-bearing is governed by Equation (2-18):

$$\omega \frac{\partial h_b(\theta)}{\partial \theta} = \frac{h_b^3(\theta)}{6\mu} \frac{\partial^2 p}{\partial z^2}. \quad (2-18)$$

Thus,

$$p(z, \theta) = \frac{3\mu\omega}{h_b^3(\theta)} \frac{\partial h_b(\theta)}{\partial \theta} z^2 + c_1 z + c_2, \quad (7-11)$$

where  $c_1$  and  $c_2$  are constants to be determined by the boundary conditions—Dirichlet boundary condition at the exit of the bearing:  $p(L_b/2) = 0$  and Cauchy boundary condition at the center of the bearing:  $\partial p(0)/\partial z = Kp(0)$ , where  $K$  is a constant to be determined in the

following analysis. Due to the symmetry of the system, the pressure can be solved only on the right half domain:  $z \in [0, L_b/2]$ , and the solution on the left half is identical.

Due to the presence of the feed at  $z=0$ , there is a leakage flow from the bearing to the feed  $q_f$  as shown in Figure 7-6, making function  $p(z)$  not smooth at the center of the bearing ( $z=0$ ). Thus, applying mass conservation at this joint between the feed and the bearing, and due to the symmetry of the system,  $q_f$  is  $q_f = -2q_z(0)$ . Furthermore, due to the flow resistance through the feed,  $p(0)$  is proportional to the flow rate  $q_f$ :

$$p(0) = \frac{12\mu}{h_f^3} L_f q_f = -\frac{24\mu}{h_f^3} L_f q_z(0). \quad (7-12)$$

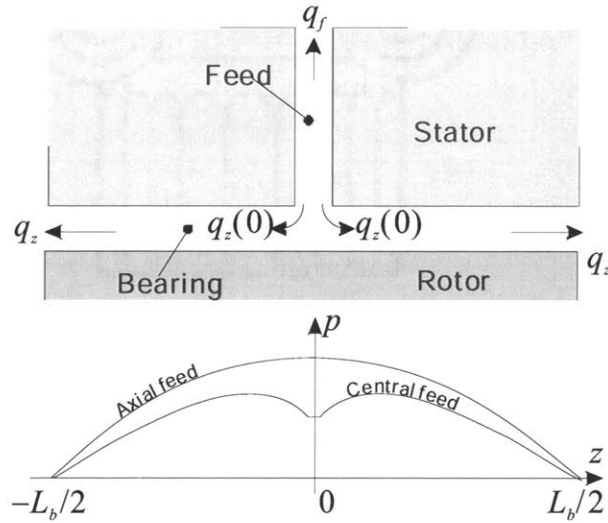


**Figure 7-6: Decrease of bearing pressure due to the leakage flow.**

Thus, according to Equation (2-15), the pressure gradient  $\partial p/\partial z$  at  $z=0$ , which is proportional to the flow rate  $q_z(0)$ , is

$$\left. \frac{\partial p}{\partial z} \right|_{z=0} = -\frac{12\mu}{h_b^3(\theta)} q_z(0) = \frac{1}{2L_f} \frac{h_f^3}{h_b^3(\theta)} p(0). \quad (7-13)$$

Substitute  $p(L_b/2)=0$  and the boundary condition (7-13) into Equation (7-11), and  $c_1$  and  $c_2$  can then be computed:

$$\begin{cases} c_1 = -\frac{\Phi}{1+\Phi/4} \frac{L_b}{8} \frac{3\mu\omega}{h_b^3(\theta)} \frac{\partial h_b(\theta)}{\partial \theta} \\ c_2 = -\frac{1}{1+\Phi/4} \frac{L_b^2}{4} \frac{3\mu\omega}{h_b^3(\theta)} \frac{\partial h_b(\theta)}{\partial \theta} \end{cases} \quad (7-14)$$



Thus, the pressure in the bearing is

$$p(z, \theta) = \frac{3\mu\omega}{h_b^3(\theta)} \frac{\partial h_b(\theta)}{\partial \theta} \left( z^2 - \frac{\Phi}{1+\Phi/4} \frac{L_b}{8} z - \frac{1}{1+\Phi/4} \frac{L_b^2}{4} \right), \quad (7-15)$$

where

$$\Phi \equiv \frac{L_b}{L_f} \frac{h_f^3}{h_b^3} \quad (7-16)$$

is the ratio of the flow resistance through the bearing to the flow resistance through the feed.

Integration of Equation (7-15) with respect to  $z$  gives the force per unit length along the circumferential direction  $f^{CF}$ ,

$$f^{CF} = 2 \int_0^{L_b/2} p(z, \theta) dz = -\frac{3\mu\omega}{h_b^3(\theta)} \frac{\partial h_b(\theta)}{\partial \theta} \frac{L_b^3}{6} \frac{1+\Phi/16}{1+\Phi/4}. \quad (7-17)$$

Thus,  $f^{CF}$  is only a function of  $\theta$ . Further integration with respect to  $\theta$  yields the hydrodynamic force due to the rotor pumping action in the centrally-fed micro-journal bearing,  $F_p^{CF}$ :

$$F_p^{CF} = - \int_0^{2\pi} f^{CF} R \sin(\theta) d\theta. \quad (7-18)$$

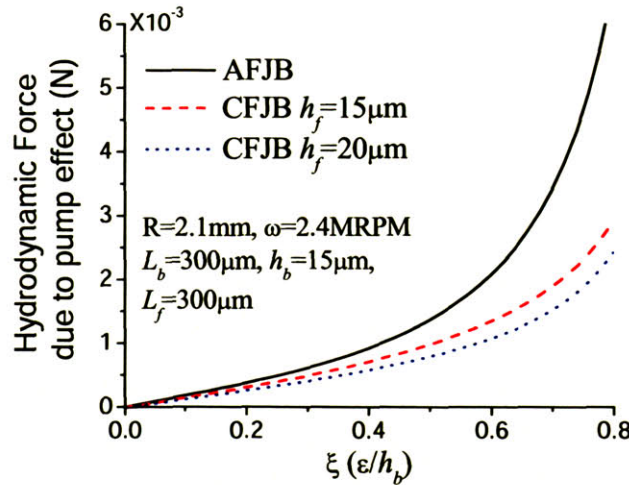


**Figure 7-7: Hydrodynamic forces due to rotor pumping action in the centrally-fed micro-journal-bearing system compared with the axially-fed micro-journal-bearing system.**

Figure 7-7 shows that the hydrodynamic force due to rotor pumping action in the centrally-fed micro-journal bearing is smaller than that in the axially-fed micro-journal bearing, due to the leakage through the feed in the former. Furthermore, the hydrodynamic force due to rotor pumping action becomes even smaller with larger feed clearance (or larger flow resistance ratio  $\Phi$ ). As is shown in the following analysis, the hydrodynamic stiffness due to rotor pumping action in the centrally-fed micro-journal-bearing system is a function of  $\Phi$ , the ratio of the flow resistance through the bearing to that through the feed. As a result, the hydrodynamic stiffness due to rotor pumping action can be adjusted by varying the feed geometry in the centrally-fed micro-journal-bearing system.

With the pressure due to rotor pumping action in the axially-fed micro-journal-bearing system given by Equation (2-19) in Chapter 3,  $f^{AF}$  is

$$f^{AF} = 2 \int_0^{L_b/2} p^{AF}(z, \theta) dz = -\frac{3\mu\omega}{h_b^3(\theta)} \frac{\partial h_b(\theta)}{\partial \theta} \frac{L_b^3}{6}. \quad (7-19)$$

Thus, the ratio of  $f^{CF}$  to  $f^{AF}$  is

$$\frac{f^{CF}}{f^{AF}} = \frac{1 + \Phi/16}{1 + \Phi/4}. \quad (7-20)$$

Since  $\partial h_b(\theta)/\partial \theta = \varepsilon \sin(\theta)$ , one can get the following equations at the centered position  $\varepsilon=0$ :

$$\left. \frac{\partial f^{CF}}{\partial \varepsilon} \right|_{\varepsilon=0} = -\frac{3\mu\omega}{h_b^3} \sin(\theta) \frac{L_b^3}{6} \frac{1 + \Phi/16}{1 + \Phi/4} \Big|_{\varepsilon=0}, \quad \text{and} \quad \left. \frac{\partial f^{AF}}{\partial \varepsilon} \right|_{\varepsilon=0} = -\frac{3\mu\omega}{h_b^3} \sin(\theta) \frac{L_b^3}{6}. \quad (7-21)$$

Therefore, when the rotor is centered, the ratio of the hydrodynamic stiffness due to rotor pumping action in the centrally-fed micro-journal bearing to the stiffness in the axially-fed micro-journal bearing is

$$\left. \frac{K_p^{CF}}{K_p^{AF}} \right|_{\varepsilon=0} = \frac{1 + \Phi/16}{1 + \Phi/4} \Big|_{\varepsilon=0}. \quad (7-22)$$

It can be seen from Figure 7-8 that as the flow resistance through the feed increases (by decreasing feed clearance or/and increasing feed length), flow resistance ratio  $\Phi$  approaches zero, resulting in the same hydrodynamic stiffness due to rotor pumping action as in the axially-fed micro-journal bearing. Conversely, if the feed has a large clearance or/and small length, the hydrodynamic stiffness due to rotor pumping action in the cen-



trally-fed micro-journal bearing becomes about one fourth of that in the axially-fed micro-journal bearing.

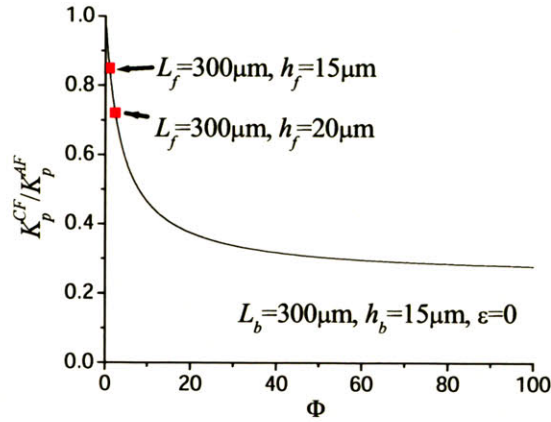


**Figure 7-8: Hydrodynamic stiffness due to rotor pumping action in the centrally-fed micro-journal bearing decreases with flow resistance ratio  $\Phi$ .**

Because the leakage flow through the feed does not affect the viscous stress in the bearing, the hydrodynamic force due to viscous drag in the centrally-fed micro-journal bearing is the same as in the axially-fed micro-journal bearing. Thus,

$$F_v^{hd,CFJB} = -2\pi\mu \frac{R^2 L_b}{h_b} \omega \frac{1 - \sqrt{1 - \xi^2}}{\xi \sqrt{1 - \xi^2}} \quad (7-23)$$

and

$$\frac{K_v^{CF}}{K_v^{AF}} = 1. \quad (7-24)$$

### 7.2.3 Damping Force

When the rotor moves, pressure in the bearing is built up due to the squeezing effect, and the flow field in the centrally-fed micro-journal bearing is also governed by Equation (2-28) of the axially-fed micro-journal bearing in Chapter 2.

$$v_r = -\frac{h_b^3(\theta)}{12\mu} \frac{\partial^2 p}{\partial z^2}, \quad (2-28)$$

where  $v_r$  is the rotor velocity in the radial direction. With exactly the same boundary conditions as the ones for the hydrodynamic flow modeled in the last section,  $p(L_b/2)=0$  and Equation (7-13), the pressure  $p$  in the bearing due to the squeezing effect caused by the rotor velocity is

$$p(z, \theta) = -\frac{6\mu}{h_b^3(\theta)} v_r \left( z^2 - \frac{\Phi}{1 + \Phi/4} \frac{L_b}{8} z - \frac{1}{1 + \Phi/4} \frac{L_b^2}{4} \right). \quad (7-25)$$

Following the same procedure as in the last section, the damping coefficient in the centrally-fed micro-journal bearing ( $C^{CF}$ ) is found to be smaller than the one in the axially-fed micro-journal bearing ( $C^{AF}$ ) due to leakage through the feed. And the ratio is

$$\left. \frac{C^{CF}}{C^{AF}} \right|_{\varepsilon=0} = \left. \frac{1 + \Phi/16}{1 + \Phi/4} \right|_{\varepsilon=0}, \quad (7-26)$$

which is exactly the same as the one for hydrodynamic stiffness due to rotor pumping action.

Furthermore, comparing the equation that governs the hydrodynamic flow (Equation (2-18)) with the one that governs the damping flow (Equation (2-28)), one can find that the former can be transferred into the latter by the substitution of  $-\omega \partial h_b(\theta) / \partial \theta$  with  $2v_r$ . As a result, the hydrodynamic pressure in the bearing (Equations (7-15)) can also be transferred into the damping pressure (Equation (7-25)) by that substitution for the centrally-fed micro-journal bearing, which is also true for the axially-fed micro-journal bearing.

Since  $\omega \partial h_b(\theta) / \partial \theta = \omega \varepsilon \sin(\theta)$ , and  $v_r = v_y \sin(\theta)$ , integrations of Equations (7-15) and (7-25) yield

$$C = -2k_p, \quad (7-27)$$

where  $C = F^{dp} / v_y$  is the damping coefficient, and  $k_p = F^{hd} / \omega \varepsilon$  is the intrinsic hydrodynamic stiffness due to rotor pumping action. As will be shown, this has a great impact on the whirl ratio of the isotropic system, which is essentially the ratio of the damping coefficient to the intrinsic hydrodynamic stiffness (the sum of the hydrodynamic stiffness due to rotor pumping action and the hydrodynamic stiffness due to viscous drag effect).

### 7.3 Dynamic Behavior of Centrally-Fed Micro-Journal-Bearing Systems

Based on the hydrostatic stiffness/force, hydrodynamic stiffness/force, and damping coefficient/force, the equations of the rotor motions in the centrally-fed micro-journal-bearing system can be established as those presented for the axially-fed micro-journal-bearing system in Chapter 3 and 4. The dynamic behavior of the centrally-fed micro-journal-bearing system can then be investigated.

### 7.3.1 Natural Frequencies

In the last section, the natural frequencies of the centrally-fed micro-journal-bearing system were calculated for two sets of bearing geometries and compared with those of the axially-fed micro-journal-bearing system (Figure 7-5). The comparison showed that a smaller feed clearance reduces the system natural frequency.

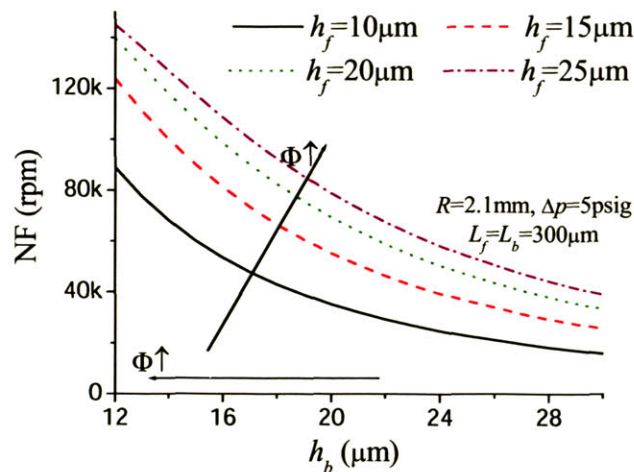


**Figure 7-9: Natural frequencies increase with flow resistance ratio  $\Phi$  in the centrally-fed micro-journal-bearing system.**

Generally, with a larger flow resistance ratio  $\Phi$ , which can be achieved by increasing feed clearance or decreasing bearing clearance, the natural frequency of the centrally-fed micro-journal-bearing system becomes larger, as shown in Figure 7-9. This is because the pressure in the bearing increases with larger  $\Phi$  due to its relatively larger flow resistance, resulting in a higher hydrostatic direct-coupled stiffness.

### 7.3.2 Distance to Contact

As discussed in Chapter 2, the distance to contact (D2C) is a crucial parameter that determines whether the rotor can be inverted: the distance to contact of the journal-bearing system should be sufficiently large for the rotor to cross the natural frequency (be inverted) safely. Then, in Chapter 5, through experiments and models, the threshold of the distance to contact normalized by the bearing clearance was determined to be 0.09. With a normalized distance to contact smaller than this threshold, the rotor may have difficulty crossing the natural frequency of the system.

The normalized distance to contact in the centrally-fed micro-journal-bearing system is calculated and plotted as a function of pressure supply to the bearing system  $\Delta p$  in Figure 7-10; the threshold is also indicated in the plot. The normalized distance to contact



in the axially-fed micro-journal-bearing system is also plotted (black solid line) for comparison.

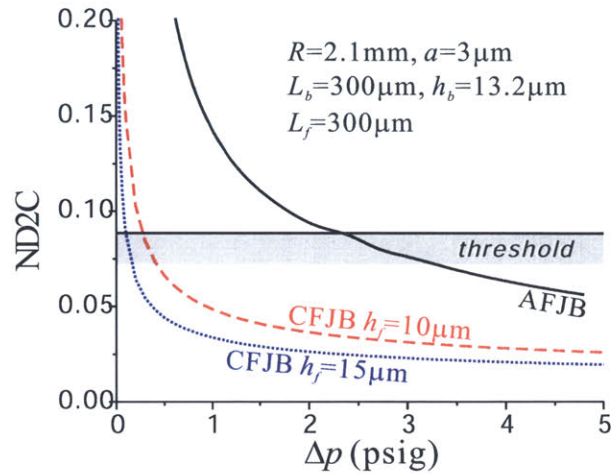


**Figure 7-10: Normalized distance to contact calculated for the centrally-fed micro-journal bearing, compared with estimated threshold.**

Thus, according to the above plot, to assure a normalized distance to contact larger than the threshold, the centrally-fed micro-journal-bearing system needs to be inverted at a bearing supply pressure  $\Delta p$  lower than 0.3 psig with a feed clearance of 10  $\mu\text{m}$  and  $\Delta p$  lower than 0.1 psig with a feed clearance of 15  $\mu\text{m}$ .

It is important to note that although the bearing dimensions of the centrally-fed micro-journal-bearing system are the same as the dimensions of the axially-fed micro-journal-bearing system in the calculations, the distances to contact in the former are much smaller than in the latter, due to the greatly reduced damping caused by the leakage through the feed in the former. With a larger feed clearance (or larger  $\Phi$ ), the damping decreases (Equation (7-25)), resulting in a even smaller normalized distance to contact and requiring an even lower bearing supply pressure  $\Delta p$  to invert the rotor.

There are two major operating concerns about the ultra-low bearing supply pressure  $\Delta p$  (about 0.1 psig in the above case) needed to invert the rotor in the centrally-fed micro-journal-bearing system. One concern is that it is difficult to precisely set that low  $\Delta p$ : with an accuracy of only 10%, the  $\Delta p$  must be controlled within a range of  $\pm 0.01$  psig, which is smaller than the error of all of the valves used in the experiments. Furthermore, there are many flows in the device, such as the turbine flow and thrust bearing flows, that can interfere with the journal bearing flow and make the actual  $\Delta p$  drift away. The other concern is that, with such small  $\Delta p$ , the operable window between the system natural fre-

quency and the system stability boundary is narrow (recall the operating protocol shown in Figure 2-21). This also adds difficulty to the smooth acceleration, through which the operating line needs to stay in that narrow window or the rotor will crash due to the instability or the large amplitude of the resonance. Thus, the centrally-fed micro-journal-bearing system may not be an acceptable design in the sense of operability due to the greatly reduced damping caused by the leakage through the feed.

To solve this problem, the length of the bearing can be increased to increase the damping. According to Equations (2-32) and (7-26), damping coefficient  $C$  increases by a factor of 8 when the bearing length doubles, and then the normalized distance to contact can be much larger, as depicted in Figure 7-11.

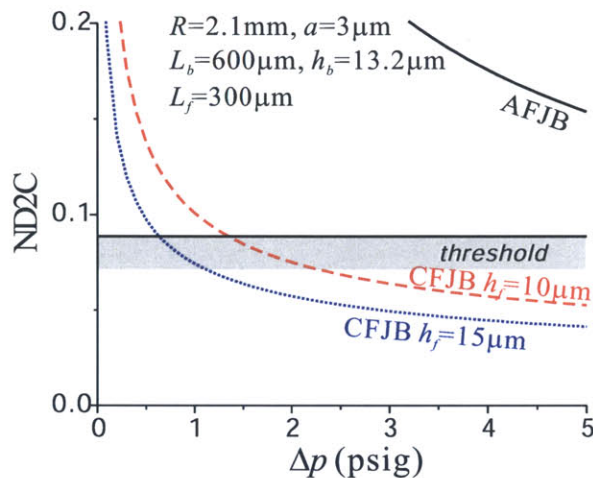


**Figure 7-11: Normalized distance to contact for the centrally-fed micro-journal-bearing system with the bearing length  $L_b=600\mu\text{m}$ .**

Therefore, due to the damping increase with the doubled bearing length, the distance to contact in the centrally-fed micro-journal-bearing system becomes much larger compared to Figure 7-10, although it is still smaller than that of the axially-fed micro-journal-bearing system. This allows the rotor to be inverted at  $\Delta p$  (pressure supply to the bearing system) of 1.3psig with a feed clearance of  $10\mu\text{m}$  and  $\Delta p$  of 0.6psig with a feed clearance of  $15\mu\text{m}$ . With these pressure settings, the devices become much easier to operate.

### 7.3.3 Stability Boundary

Based on the analyses in Chapter 3 and 4, the stability boundary of the centrally-fed micro-journal-bearing system can be calculated for both the isotropic configuration (equal pressure supplies to all four plena in Figure 7-1) and the anisotropic configuration (different pressure supplies to the left-right pair and the up-down pair of plena). The

analysis below shows that the singular peak of the whirl ratio with the isotropic configuration shifts to a smaller bearing clearance in the centrally-fed micro-journal-bearing system due to leakage through the feed. To compromise the capability to invert the rotor as discussed above, the anisotropic configuration is needed to achieve a high stability boundary with long bearings in the centrally-fed micro-journal-bearing system.

According to Equation (3-12), the whirl ratio of the isotropic centrally-fed micro-journal-bearing system ( $\mathfrak{R}^{CF}$ ) is

$$\mathfrak{R}^{CF} = \frac{\Omega_W}{\Omega_N} = \left| \frac{C^{CF}}{k_p^{CF} - k_v^{CF}} \right|, \quad (7-28)$$

where  $\Omega_W$  and  $\Omega_N$  are the stability boundary and the natural frequency of the system respectively,  $C$  is the damping coefficient, and  $k_p$  and  $k_v$  are the intrinsic hydrodynamic stiffnesses due to rotor pumping action and viscous drag respectively.

Substituting  $C$  (7-26),  $k_p$  (7-22), and  $k_v$  (7-24) into Equation (7-28) and noting Equation (7-27), equation (7-28) reduces to:

$$\mathfrak{R}^{CF} = \frac{2}{1 - W^{CF}}, \quad (7-29)$$

where the whirl number for the centrally-fed micro-journal-bearing system ( $W^{CF}$ ) is

$$W^{CF} = \frac{k_v^{CF}}{k_p^{CF}} = \frac{1 + \Phi/16}{1 + \Phi/4} \frac{2Rh_b}{L_b^2} = \frac{1 + \Phi/16}{1 + \Phi/4} W^{AF}. \quad (7-30)$$

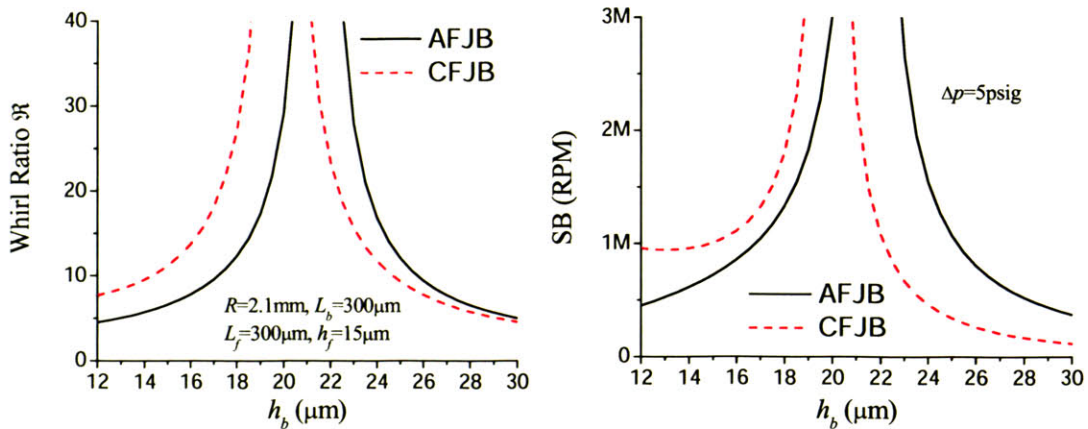


**Figure 7-12: Whirl ratio  $\mathfrak{R}$  (left) and stability boundary (right) of the isotropic centrally-fed micro-journal-bearing system.**



The whirl ratio  $\mathfrak{R}^{CF}$  and stability boundary for the isotropic centrally-fed micro-journal-bearing system are calculated and plotted with Equation (7-29) in Figure 7-12. Thus, the singularity peak shifts left due to the decrease in whirl number, according to Equation (7-30). Meanwhile, because the natural frequency of the centrally-fed micro-journal-bearing system is larger with a smaller bearing clearance (Figure 7-9), the system stability boundary, which is proportional to the system natural frequency, also increases a bit at a small bearing clearance, as shown in Figure 7-12.

According to the analysis in the last section, in order to invert the rotor in the centrally-fed micro-journal-bearing system at a relatively high supply pressure  $\Delta p$  and make the devices more operable, the bearing length should increase to about 600  $\mu\text{m}$ . However, with this large bearing length, the whirl number  $W^{CF}$  is much less than 1 according to Equation (7-30), resulting in a much lower system stability boundary (below a half-million rpm) as shown in Figure 7-13.

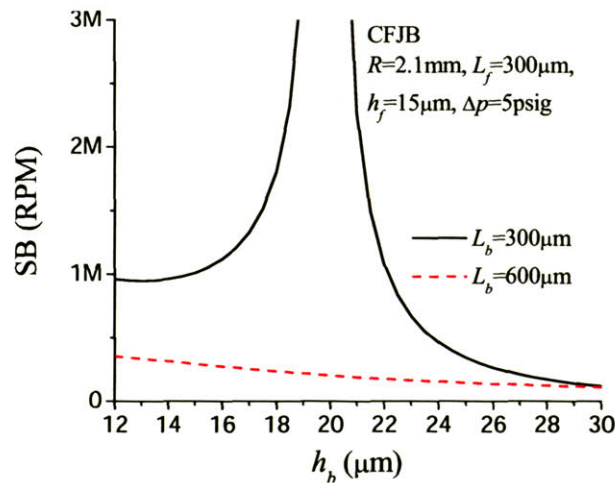


**Figure 7-13: Stability boundary with bearing length of 600 $\mu\text{m}$  is much lower than that with bearing length of 300 $\mu\text{m}$  in the centrally-fed micro-journal-bearing system (CFJB).**

To resolve the conflict between the large bearing length desired for a large distance to contact and the small bearing length required for a high stability boundary in the isotropic bearing design, an anisotropic bearing configuration is suggested instead to improve the stability boundary of the centrally-fed micro-journal-bearing system with a large bearing length.

According to Chapter 4, the stability boundary of the anisotropic bearing system is mainly determined by the ratio of the hydrostatic stiffness anisotropy to the intrinsic

cross-coupled hydrodynamic stiffness (Equation (4-11)). Thus, in the anisotropic centrally-fed micro-journal-bearing system, the stability boundary is approximately

$$\Omega_W^{CF} = \left| \frac{K_{xx}^{CF} - K_{yy}^{CF}}{2(k_p^{CF} - k_v^{CF})} \right|. \quad (7-31)$$

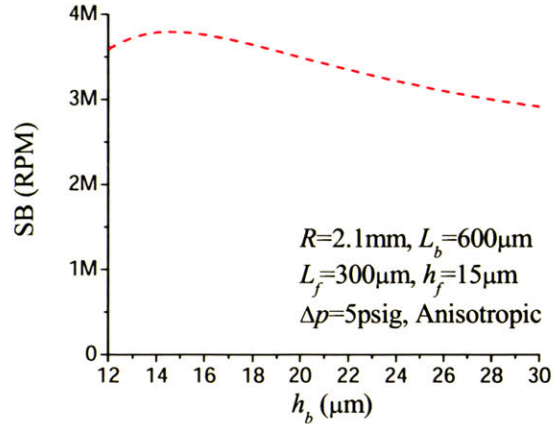


**Figure 7-14: Stability boundary of the anisotropic centrally-fed micro-journal-bearing system with bearing length of 600 $\mu\text{m}$ .**

Therefore, as shown in Figure 7-11 and Figure 7-14, with the anisotropic design and a large bearing length (600  $\mu\text{m}$ ), the centrally-fed micro-journal-bearing system has a high stability boundary and can be inverted at a relatively high supply pressure  $\Delta p$ .

### 7.3.4 Design Guidelines for Centrally-Fed Micro-Journal-Bearing Systems Used in Micro-Bearing-Rig Devices

To design an acceptable centrally-fed micro-journal-bearing system, the distance to contact should be larger than the threshold and the stability boundary of the system should be higher than the design speed. According to the analysis in the previous section, a long bearing is needed to obtain sufficient distance to contact, and the anisotropic bearing configuration is required to achieve a stability boundary higher than the design speed with the large bearing length. Furthermore, the mass flow rate through the bearing system is another concern, because the larger it is, the more power is consumed by the bearing system. Thus, the mass flow rate through the bearing system should be small as possible.

With all these requirements, it is useful to generate a design chart with overlapping contours of the distance to contact, the stability boundary, and the mass flow rate, so that an acceptable design can be chosen from the chart.



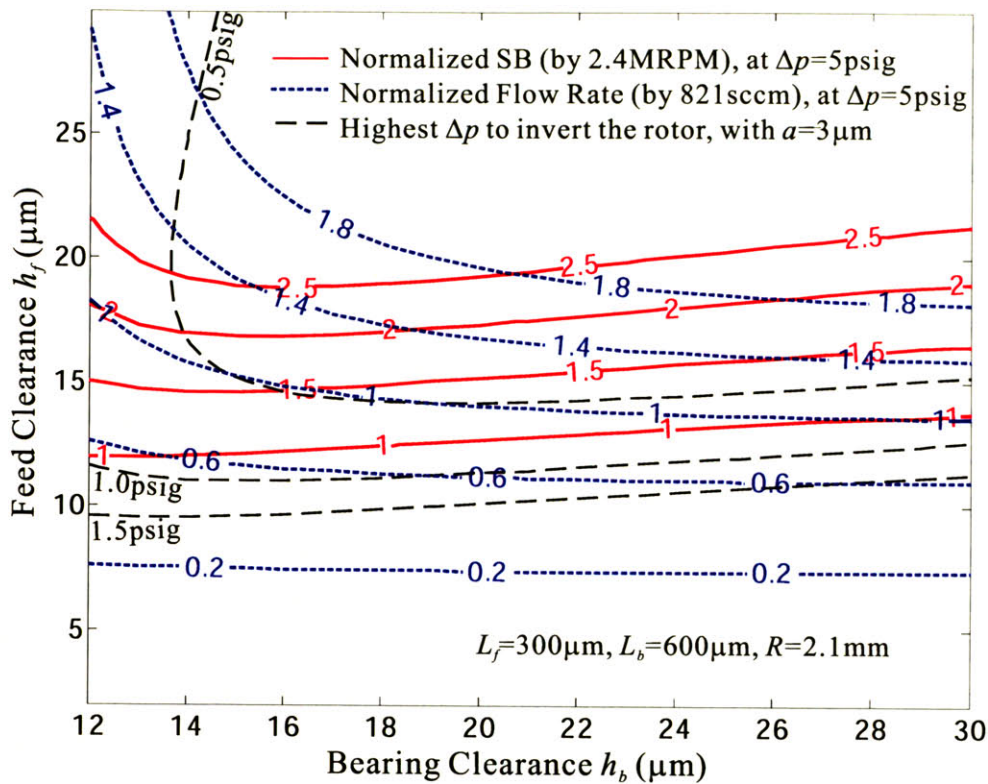


**Figure 7-15: Design chart for the anisotropic centrally-fed micro-journal-bearing system with bearing length of 600 $\mu\text{m}$ .**

Figure 7-15 is an example of the design chart generated for the centrally-fed micro-journal-bearing system used for a micro-bearing-rig device with a bearing length of 600 $\mu\text{m}$ . With the bearing clearance  $h_b$  varying from 12 $\mu\text{m}$  to 30 $\mu\text{m}$  and the feed clearance  $h_f$  varying from 2 $\mu\text{m}$  to 30 $\mu\text{m}$ , the highest  $\Delta p$  needed to invert the rotor (black dashed lines), the stability boundary (red solid lines), and the mass flow rate (blue dotted lines) are calculated and plotted as functions of  $h_b$  and  $h_f$ .

In the contour, the numbers on the red solid lines are the stability boundary normalized by the design speed of the micro-bearing rig, which is 2.4 MRPM, and the numbers on the blue dotted lines are the flow rates through the bearing system normalized by the flow rate of the device #3-4, 16.76mg/s, which is used as a benchmark. Both the flow rates and the stability boundary is calculated at a bearing supply pressure  $\Delta p$  of 5psig. Furthermore, the numbers on the black dashed lines are the highest  $\Delta p$  at which the normalized distance to contact is equal to the threshold of 0.09. The distance to contact is calculated with a rotor unbalance of 3 $\mu\text{m}$ , which is common in the micro-bearing-rig devices according to [4].

As an example, for a device with bearing clearance  $h_b=12\mu\text{m}$  and feed clearance  $h_f=15\mu\text{m}$ , the system stability boundary is about  $1.5 \times 2.4 \text{MRPM} = 3.6 \text{MRPM}$  and the flow rate is  $0.8 \times 16.76 \text{mg/s} = 13.41 \text{mg/s}$  at the bearing supply pressure  $\Delta p$  of 5psig; the highest  $\Delta p$  at which the rotor can be inverted is 0.8psig.

Although the above design seems to be a good one, the centrally-fed micro-journal-bearing design will be applied to the micro-bearing-rig devices for the following reasons: (1) According to Chapter 5, the coupling between the rotor's conical and radial motions is relatively small in the micro-bearing-rig devices and the stability boundary decrease is not as large as in the micro-turbo-charger devices. Therefore, there is no need to use the centrally-fed configuration to eliminate coupling in the micro-bearing-rig devices. (2) The bearing aspect ratio is still limited by the DRIE etching technology at this stage, so that a  $600\mu\text{m}$  long bearing with a  $15\mu\text{m}$  clearance can hardly be etched. And (3), the centrally-fed micro-journal-bearing system doesn't improve other system performance factors (stiffness, flow rate, and so on) any more than the axially-fed micro-journal-bearing system; it even greatly reduces the distance to contact.

#### **7.4 Summary and Conclusions**

The centrally-fed micro-journal-bearing system has been investigated in this chapter as an approach to eliminate coupling between the rotor's radial and conical motions. Fluid models to calculate the bearing forces in the centrally-fed micro-journal-bearing system were established, and the system's dynamic behavior, including the natural frequency, the distance to contact, and the stability boundary, were obtained. A nondimensional parameter, the ratio of the flow resistance in the bearing to that in the feed  $\Phi$ , was introduced, and the hydrodynamic force and damping force were found to decrease with it.

Due to the leakage flow from the bearing to the feed, both the damping and the hydrodynamic stiffness due to rotor pumping action in the centrally-fed micro-journal-bearing system are smaller than those in the axially-fed micro-journal-bearing system. As a result, the distance to contact is much smaller in the centrally-fed micro-journal-bearing system than in the axially-fed micro-journal-bearing system. Thus, in the centrally-fed micro-journal-bearing system, a low pressure supply to the journal-bearing system  $\Delta p$  is required to invert the rotor, and the operation window between the natural frequency and the stability boundary becomes narrow at this low  $\Delta p$ , causing a great deal of difficulty in operation.

Also because of the leakage flow from the bearing to the feed, the ratio of the whirl number in the centrally-fed micro-journal-bearing system to that in the axially-fed micro-journal-bearing system is a function of the flow resistance ratio  $\Phi$  according to Equation (7-30). As a result, the singularity peak of the stability boundary shifts in the isotropic centrally-fed micro-journal-bearing system.

To increase the distance to contact and help operate the system with the centrally-fed micro-journal bearing, the bearing length should be increased (300 $\mu\text{m}$  to 600 $\mu\text{m}$ ) for a larger damping ratio or distance to contact. But a large bearing length greatly reduces the whirl number from 1 and pushes the whirl ratio off the singularity peak, resulting in a low stability boundary in the isotropic bearing configuration. The solution to this conflict is an anisotropic centrally-fed micro-journal-bearing system with a long bearing. With the anisotropic configuration, the stability boundary can increase from about a half-million rpm (with the isotropic configuration) to over 3 million rpm, with the elimination of the narrow singular peak.

Finally, a design chart was generated for the centrally-fed micro-journal-bearing system used for micro-bearing-rig devices. Although there seem to be some acceptable designs, the centrally-fed micro-journal-bearing system is not used in the micro-bearing rigs because bearings with a high aspect ratio (600 $\mu\text{m}$  long and 15 $\mu\text{m}$  wide) cannot be etched by the current DRIE etching technology.





## Chapter 8

# Rotordynamic Effect of Journal Bearing Profile Variations

In the previous analyses, the walls of the journal bearings were assumed to be perfectly straight and parallel. However, SEM pictures reveal that the walls of most of the journal bearings fabricated were not straight and parallel, and sometimes the journal bearing profiles can be far from being so. The following SEM picture (Figure 1-10) is an example of a journal bearing that had been targeted to be fabricated straight and parallel with a clearance of  $15\mu\text{m}$ :

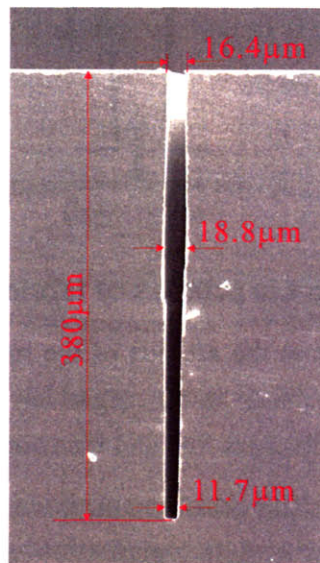


**Figure 8-1: SEM picture of a journal bearing fabricated to be straight and parallel with clearance of  $15\mu\text{m}$ .**

Since the profile of the journal bearing affects the flows through it and hence the bearing forces acting on the rotor, the real system rotordynamics will be different from the predictions based on the models established for straight-wall bearings. Therefore, to capture these and derive fabrication requirements, research on the effects of non-straight bearing profiles on the system dynamic performances is carried out in this chapter.

Through this analysis, one can find that the tapered bearings behave similarly to the straight-wall ones with the same average clearance. However, all the tapered bearings have a smaller distance to contact than the straight-wall bearings. A negatively tapered bearing with a large profile variation can even induce a positive hydrostatic direct-coupled stiffness that makes the system statically unstable at low  $\Delta p$  (pressure difference across the journal bearing). Thus, large profile variations in the journal bearings should be avoided.

### 8.1 Three Typical Journal Bearing Profiles

The SEM measurements [33] showed that there are three typical profiles of fabricated journal bearings: “positive taper,” “negative taper,” and “bow,” which are sketched in Figure 8-2.

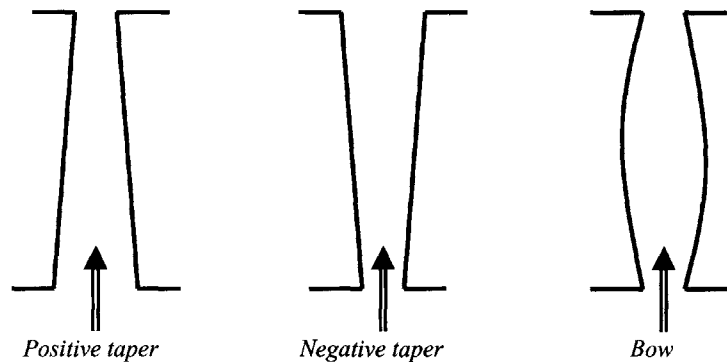


**Figure 8-2: Three typical profiles of fabricated journal bearings.**

Since the gas/air is fed from the aft side of the rotor, it contracts in the positively-tapered journal bearing but expands in the negatively-tapered one. In the bow-shaped journal bearing, the flow path diverges first and then converges.

Because other journal bearing profiles can be derived from combinations of these three, the research focuses on the three typical profiles in this chapter. Analytical fluid models are established for these basic profiles first, and then the rotordynamic behavior of the system is investigated with the bearing forces calculated by the fluid models.

### 8.2 Fluid Model for Journal Bearings with Profile Variations

As with the straight-wall journal bearings in Chapter 2, in order to obtain a physical understanding of the rotordynamic behavior of the system, the three bearing forces (hydrostatic force, hydrodynamic force, and damping force) are calculated individually for the non-straight-wall journal bearings. In the below analysis, solutions are first derived

for the general bearing profile  $h(z)$ . Then the above three typical profiles are substituted in to obtain the corresponding final solutions.

### 8.2.1 Flows in Journal Bearings of General Profile

When the profile of a journal bearing is not straight and parallel, the bearing clearance varies along the axial direction  $z$  (the direction of the hydrostatic flow), as shown in Figure 8-3. The bearing clearance as a function of  $z$  can then be written as  $h(z)=h_0+d(z)$ , where  $d(z)$  is the clearance variation relative to the entrance clearance  $h_0$ .

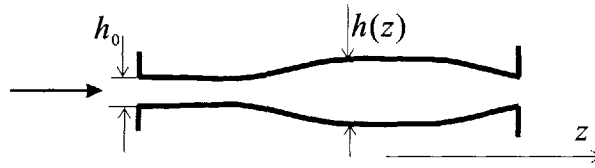


**Figure 8-3: Bearing clearance  $h$  varies along  $z$  in a non-straight-wall journal bearing (not to scale).**

Furthermore, if the rotor eccentricity relative to the bearing center is not zero, the clearance of the journal bearing is also a function of  $\theta$  (in the circumferential direction), as shown in Figure 8-4.

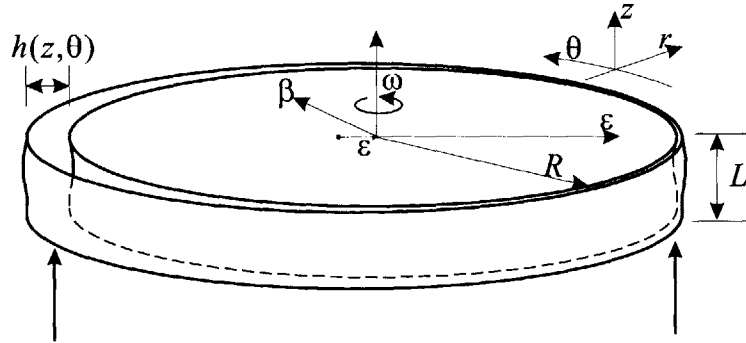


**Figure 8-4: Bearing clearance varies with both  $z$  and  $\theta$  when rotor is off-centered with non-straight-wall bearing (not to scale).**

Then one can get

$$h(z, \theta) = h_0 + d(z) - \varepsilon \cos(\theta), \quad (8-1)$$

where the circumferential direction  $\theta$  starts from the direction of the rotor displacement  $\varepsilon$ .

For the hydrostatic flow, since the flow rate  $q_z$  is constant through the bearing due to mass conservation, according to Equation (2-4) and the boundary condition  $p^{hs}(L, \theta)=0$ , the pressure in the bearing is

$$p^{hs}(z, \theta) = \left( \int_0^L \frac{12\mu}{h^3(z, \theta)} d\zeta - \int_0^z \frac{12\mu}{h^3(z, \theta)} d\zeta \right) q_z(\theta). \quad (8-2)$$

Meanwhile, as in Chapter 2, due to the entrance static pressure loss, the equation of  $q_z$  becomes

$$\Delta p = p(0, \theta) + \frac{\gamma}{2} \rho u_z^2 = \left( \int_0^L \frac{12\mu}{h^3(z, \theta)} d\zeta \right) q_z(\theta) + \frac{\gamma}{2} \rho \left( \frac{q_z(\theta)}{h_0 - \varepsilon \cos(\theta)} \right)^2. \quad (8-3)$$

Thus,  $q_z$  can be obtained by solving this parabolic equation, and hence the pressure in the bearing  $p(z, \theta)$ , according to Equation (8-2). The integration of  $p(z, \theta)$  with respect to both  $z$  and  $\theta$  yields the hydrostatic force  $F^{hs}$  (in the direction of  $\varepsilon$ )

$$F^{hs} = - \int_0^{2\pi} R \cos(\theta) d\theta \int_0^L p^{hs}(z, \theta) dz. \quad (8-4)$$

For the hydrodynamic flow, following the analysis in Chapter 2 for the straight-wall bearing, the equation that governs the pressure field induced by rotor pumping action in a non-straight-wall bearing can be derived:

$$\frac{\partial q_z}{\partial z} + \frac{\partial q_\theta}{R \partial \theta} = 0 \Rightarrow \frac{\partial}{\partial z} \left( \frac{h^3(z, \theta)}{12\mu} \frac{\partial p}{\partial z} \right) = \frac{\omega}{2} \varepsilon \sin(\theta). \quad (8-5)$$

With the boundary condition  $p^{hd}(0, \theta) = 0$ , the hydrodynamic pressure in the bearing  $p^{hd}(z, \theta)$  can be obtained from the above equation:

$$p^{hd}(z, \theta) = 6\mu\omega\varepsilon \sin(\theta) \int_0^z \frac{\zeta + c_1}{h^3(\zeta, \theta)} d\zeta, \quad (8-6)$$

where  $c_1$  is only a function of  $\theta$  and to be determined by the boundary condition of  $p^{hd}(L, \theta) = 0$ . Furthermore, the integration of  $p^{hd}$  with respect to both  $z$  and  $\theta$  yields the hydrodynamic force due to rotor pumping action  $F_p^{hd}$  (in the direction of  $\beta$ , which is perpendicular to  $\varepsilon$ ).

$$F_p^{hd} = - \int_0^{2\pi} R \sin(\theta) d\theta \int_0^L p^{hd}(z, \theta) dz. \quad (8-7)$$

It is useful to define a function  $f(\theta)$ ,

$$f(\theta) \equiv \int_0^L dz \int_0^z \frac{\zeta + c_1}{h^3(\zeta, \theta)} d\zeta = \int_0^L dz \int_0^z \frac{\zeta + c_1}{(h_0 + d(z) - \varepsilon \cos(\theta))^3} d\zeta. \quad (8-8)$$

Then Equation (8-7) can be written as

$$F_p^{hd} = -6\mu\omega\varepsilon R \int_0^{2\pi} \sin^2(\theta) f(\theta) d\theta. \quad (8-9)$$

Meanwhile, the viscous stress on the rotor surface is  $\tau(z, \theta) = \mu\omega R/h(z, \theta)$ . Thus the hydrodynamic force due to viscous drag is (also in the direction of  $\beta$ )

$$F_v^{hd} = - \int_0^{2\pi} R \cos(\theta) d\theta \int_0^L \tau(z, \theta) dz = - \int_0^{2\pi} R \cos(\theta) d\theta \int_0^L \frac{\mu\omega R}{h(z, \theta)} dz. \quad (8-10)$$

Similarly, for the damping flow, the pressure in the bearing  $p^{dp}$  is

$$p^{dp}(z, \theta) = -12\mu v_r \int_0^z \frac{\zeta + c_1}{h^3(\zeta, \theta)} d\zeta = -12\mu (v_\varepsilon \cos(\theta) + v_\beta \sin(\theta)) \int_0^z \frac{\zeta + c_1}{h^3(\zeta, \theta)} d\zeta, \quad (8-11)$$

where  $v_r$  is the rotor radial velocity  $v_r = v_\varepsilon \cos(\theta) + v_\beta \sin(\theta)$ , and  $v_\varepsilon$  and  $v_\beta$  are the components of the rotor velocity in  $\hat{\varepsilon}$  and  $\hat{\beta}$  directions respectively. Therefore, the damping force  $\vec{F}^{dp}$  can be derived by the integration of  $p^{dp}$  with respect to both  $z$  and  $\theta$ .

$$\vec{F}^{dp} = - \int_0^{2\pi} R \cos(\theta) d\theta \int_0^L p^{dp}(z, \theta) dz \hat{\varepsilon} - \int_0^{2\pi} R \sin(\theta) d\theta \int_0^L p^{dp}(z, \theta) dz \hat{\beta}. \quad (8-12)$$

Because the integrand of the following integration is skew-symmetric about  $\theta = \pi$ , one can get

$$\int_0^{2\pi} \frac{\sin(\theta) \cos(\theta)}{(a + b \cos(\theta))^3} d\theta = 0. \quad (8-13)$$

With Equation (8-8) and the above integration, Equation (8-12) becomes

$$\vec{F}^{dp} = F_\varepsilon^{dp} \hat{\varepsilon} + F_\beta^{dp} \hat{\beta} = 12\mu R \left( \int_0^{2\pi} \cos^2(\theta) f(\theta) d\theta v_\varepsilon \hat{\varepsilon} + \int_0^{2\pi} \sin^2(\theta) f(\theta) d\theta v_\beta \hat{\beta} \right). \quad (8-14)$$

Thus, all the bearing forces in the non-straight-wall journal bearing can be calculated by the equations above. The following analysis shows that there is a general relation between the intrinsic hydrodynamic stiffness due to rotor pumping action  $k^p$  and the damping coefficient  $C$  in journal bearings with any bearing profile.

According to Equation (8-8), the differential of  $f(\theta)$  with respect to the rotor eccentricity  $\varepsilon$  is

$$\frac{\partial f(\theta)}{\partial \varepsilon} = f'(\theta) \cos(\theta). \quad (8-15)$$

With this and Equations (8-9) and (8-12), the intrinsic hydrodynamic stiffness due to rotor pumping action becomes:

$$\begin{aligned} k_{xy}^p &= \frac{F_p^{hd}}{\omega \varepsilon} = -6\mu R \int_0^{2\pi} \sin^2(\theta) f(\theta) d\theta = -\frac{1}{2} \frac{F_\beta^{dp}}{v_\beta} = -\frac{1}{2} C_\beta, \\ k_{yx}^p &= \frac{dF_p^{hd}}{\omega d\varepsilon} = -6\mu R \left( \int_0^{2\pi} \sin^2(\theta) f(\theta) d\theta + \varepsilon \int_0^{2\pi} \sin^2(\theta) f'(\theta) \cos(\theta) d\theta \right) \\ &= -6\mu R \left( \int_0^{2\pi} \sin^2(\theta) f(\theta) d\theta - \int_0^{2\pi} \frac{1}{2} \sin(2\theta) d(f(\theta)) \right) \\ &= -6\mu R \left( \int_0^{2\pi} \sin^2(\theta) f(\theta) d\theta + \int_0^{2\pi} \cos(2\theta) f(\theta) d\theta \right) \\ &= -6\mu R \int_0^{2\pi} \cos^2(\theta) f(\theta) d\theta = -\frac{1}{2} \frac{F_\varepsilon^{dp}}{v_\varepsilon} \\ &= -\frac{1}{2} C_\varepsilon. \end{aligned}$$

Or,

$$C_\beta = -2k_{xy}^p, \text{ and } C_\varepsilon = -2k_{yx}^p. \quad (8-16)$$

Thus, no matter what the bearing profile is, it is always true that the damping coefficient is exactly two times the intrinsic hydrodynamic stiffness due to rotor pumping action, with the opposite sign. This relation can be used to calculate the whirl ratios of isotropic journal-bearing systems with various bearing profiles.

### 8.2.2 Bearing Flow and Bearing Forces in Journal Bearings with Tapered Profiles

The sketch in Figure 8-5 shows a typical journal bearing with a tapered bearing wall. With the air fed from the left, if the taper variation  $\Delta$  is positive, the bearing is a negatively-tapered one; if  $\Delta$  is negative, the bearing is a positively-tapered one.



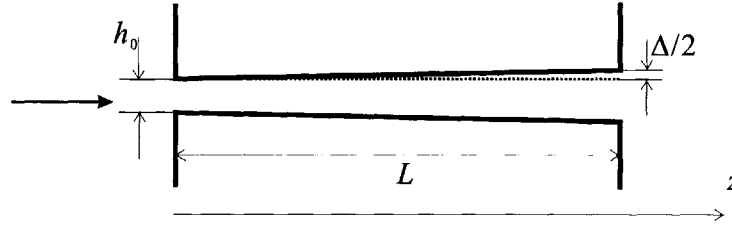


**Figure 8-5: Sketch of a tapered journal bearing (not to scale).**

Thus, the bearing clearance can be written as

$$h(z, \theta) = h_0 + \Delta \frac{z}{L} - \varepsilon \cos(\theta) = h_0 \left( 1 + \delta \frac{z}{L} - \xi \cos(\theta) \right), \quad (8-17)$$

where  $\delta = \Delta/h_0$  and  $\xi = \varepsilon/h_0$  are the profile variation and the rotor eccentricity normalized by the bearing entrance clearance  $h_0$ , respectively. Substituting Equation (8-17) into (8-2), the hydrostatic pressure  $p^{hs}$  in the tapered bearing can be obtained:

$$p^{hs}(z, \theta) = \frac{6\mu L}{\delta h_0^3} \left( \frac{1}{\left(1 + \delta \cdot z/L - \xi \cos(\theta)\right)^2} - \frac{1}{\left(1 + \delta - \xi \cos(\theta)\right)^2} \right) q_z \quad (8-18)$$

Therefore, according to Equation (8-3),  $q_z$  becomes

$$q_z(\theta) = \frac{-b(\theta) + \sqrt{b^2(\theta) + 4a(\theta)\Delta p}}{2a(\theta)}, \quad (8-19)$$

where

$$a(\theta) \equiv \frac{\gamma}{2} \rho \frac{1}{h_0^2} \frac{1}{(1 - \xi \cos(\theta))^2} \quad \text{and} \quad b(\theta) \equiv \frac{6\mu L}{\delta h_0^3} \left( \frac{1}{(1 - \xi \cos(\theta))^2} - \frac{1}{(1 + \delta - \xi \cos(\theta))^2} \right).$$

Thus, the hydrostatic flow rate through the bearing is

$$Q = \int_0^{2\pi} q_z(\theta) R d\theta. \quad (8-20)$$

At the same time, the integration of  $p^{hs}(z, \theta)$  (Equation (8-18)) with respect to  $z$  yields

$$\int_0^L p^{hs}(z, \theta) dz = 6\mu \frac{L^2}{h_0^3} \frac{q_z(\theta)}{(1 - \xi \cos(\theta))(1 + \delta - \xi \cos(\theta))^2}. \quad (8-21)$$

Then the hydrostatic force  $F^{hs}$  is

$$F^{hs} = -6\mu R \frac{L^2}{h_0^3} \int_0^{2\pi} \frac{q_z(\theta)}{(1 - \xi \cos(\theta))(1 + \delta - \xi \cos(\theta))^2} \cos(\theta) d\theta. \quad (8-22)$$

As shown in Figure 8-6, compared with straight-wall journal bearings, the negatively tapered bearing has a larger flow rate but a smaller restoring hydrostatic force, while the positively tapered bearing has a smaller flow rate but a larger restoring force. This can be explained by noting that the average clearance of the positively tapered bearing is smaller, while the clearance of the negatively tapered bearing is larger.

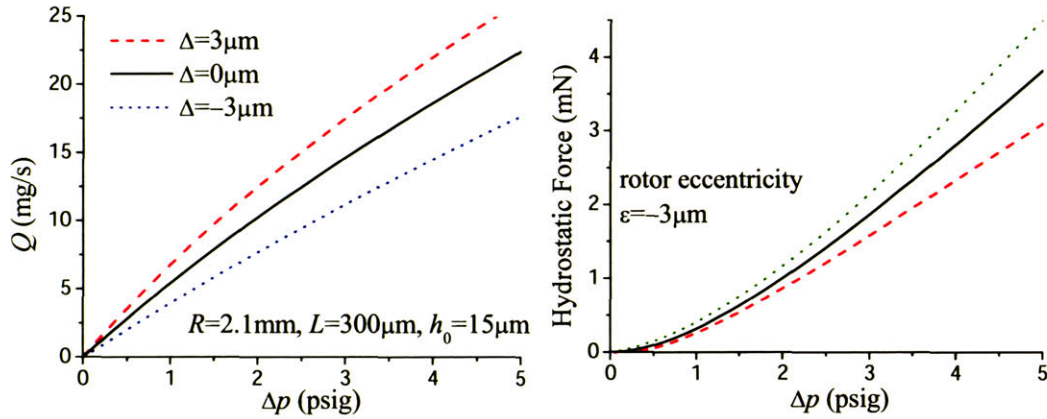


**Figure 8-6: Hydrostatic flow rate and force in tapered journal bearings with different levels of profile variation.**

Furthermore, the expression of the hydrodynamic force due to rotor pumping action  $F_p^{hd}$  can be derived by integrations:

$$F_p^{hd} = 6\pi\mu\omega \frac{L^3 R}{h_0^2} \frac{\xi}{\delta^3} \left[ \ln \left( \frac{1 + \delta + \sqrt{(1 + \delta)^2 - \xi^2}}{1 + \sqrt{1 - \xi^2}} \right) + \frac{\sqrt{1 - \xi^2} - (1 + \delta)\sqrt{(1 + \delta)^2 - \xi^2} + 2\delta\sqrt{(1 + \delta/2)^2 - \xi^2}}{\xi^2} \right] \quad (8-23)$$

Similarly, the hydrodynamic force due to viscous drag  $F_v^{hd}$  is

$$F_v^{hd} = -2\pi\mu\omega \frac{LR^2}{h_0} \frac{\sqrt{(1 + \delta)^2 - \delta} - \sqrt{1 - \xi^2}}{\delta\xi}. \quad (8-24)$$

The damping force  $F^{dp}$  in  $\hat{\varepsilon}$  direction (the direction of rotor displacement, Chapter 2) is

$$F_{\epsilon}^{dp} = -12\pi\mu v_{\epsilon} \frac{L^3 R}{h_0^3} \frac{1}{\delta^3} \left[ \ln \left( \frac{1 + \delta + \sqrt{(1 + \delta)^2 - \xi^2}}{1 + \sqrt{1 - \xi^2}} \right) + \frac{(1 + \delta)\sqrt{(1 + \delta)^2 - \xi^2} - \sqrt{1 - \xi^2} - 2\delta(1 + \delta/2)^2 / \sqrt{(1 + \delta/2)^2 - \xi^2}}{\xi^2} \right], \quad (8-25)$$

and the damping force  $F^{dp}$  in  $\hat{\beta}$  direction (the direction perpendicular to the rotor displacement, Chapter 2) is

$$F_{\beta}^{dp} = -12\pi\mu v_{\beta} \frac{L^3 R}{h_0^3} \frac{1}{\delta^3} \left[ \ln \left( \frac{1 + \delta + \sqrt{(1 + \delta)^2 - \xi^2}}{1 + \sqrt{1 - \xi^2}} \right) + \frac{\sqrt{1 - \xi^2} - (1 + \delta)\sqrt{(1 + \delta)^2 - \xi^2} + 2\delta\sqrt{(1 + \delta/2)^2 - \xi^2}}{\xi^2} \right]. \quad (8-26)$$

As the profile variation  $\delta \rightarrow 0$ , the tapered bearing reduces to the straight-wall bearing, and the hydrodynamic and damping forces in the former can be found to equal those in the latter, which were modeled in Chapter 2. Thus, the above equations of bearing forces in tapered bearings are consistent with those in straight-wall bearings.

At the centered position  $\xi=0$ , the intrinsic hydrostatic stiffness and damping coefficient in the tapered bearings are

$$k_p^{Taper} = 6\pi\mu \frac{L^2 R}{h_0^3} \frac{1}{\delta^3} \left( \ln(1 + \delta) - \frac{\delta}{1 + \delta/2} \right) = k_p^{Straight} \frac{12}{\delta^3} \left( \ln(1 + \delta) - \frac{\delta}{1 + \delta/2} \right), \quad (8-27)$$

$$k_v^{Taper} = \pi\mu \frac{LR^2}{h_0^2} \frac{1}{\delta} \left( 1 - \frac{1}{1 + \delta} \right) = k_v^{Straight} \frac{1}{\delta} \left( 1 - \frac{1}{1 + \delta} \right), \quad (8-28)$$

$$C^{Taper} = C^{Straight} \frac{12}{\delta^3} \left( \ln(1 + \delta) - \frac{\delta}{1 + \delta/2} \right). \quad (8-29)$$

Therefore, as shown in Figure 8-7, the ratios of the hydrodynamic stiffness and damping coefficient in the tapered bearing to those in the straight-wall bearing are functions of the bearing profile variation  $\delta$ . Furthermore, one can see that the hydrodynamic stiffness (both due to rotor pumping action and viscous drag effect) and damping coefficient are larger in the positively tapered bearings, while they are smaller in the negatively

tapered bearings. This is also due to the average clearance: the negatively tapered bearings have larger average clearance than the positively tapered journal bearings.

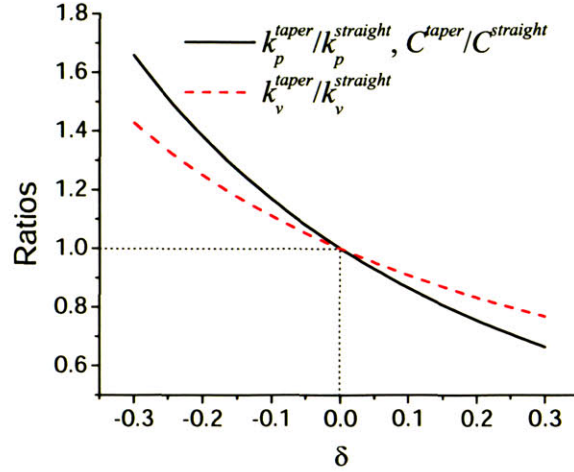


**Figure 8-7: Ratios of hydrodynamic stiffness and damping coefficient in tapered bearings to those in straight-wall bearings.**

Moreover, the average clearance of the tapered bearings is  $h_0(1+\delta/2)$ . The hydrodynamic stiffness and damping for straight-wall bearings with this clearance are

$$k_p^{Straight} \Big|_{h_0(1+\delta/2)} = \frac{\pi}{2} \mu \frac{L^3 R}{(h_0(1+\delta/2))^3} = \left(1 - \frac{3}{2} \delta + O(\delta^2)\right) k_p^{Straight} \Big|_{h_0}, \quad (8-30)$$

$$k_v^{Straight} \Big|_{h_0(1+\delta/2)} = \pi \mu \frac{LR^2}{(h_0(1+\delta/2))^2} = (1 - \delta + O(\delta^2)) k_v^{Straight} \Big|_{h_0}, \quad (8-31)$$

$$C^{Straight} \Big|_{h_0(1+\delta/2)} = \left(1 - \frac{3}{2} \delta + O(\delta^2)\right) C^{Straight} \Big|_{h_0}. \quad (8-32)$$

Then, with the Taylor expansions of Equations (8-27), (8-28), and (8-29), one can find that, by the first order approximation,

$$k_p^{Taper} \cong k_p^{Straight} \Big|_{h_0(1+\delta/2)}, \quad k_v^{Taper} \cong k_v^{Straight} \Big|_{h_0(1+\delta/2)}, \quad C^{Taper} \cong C^{Straight} \Big|_{h_0(1+\delta/2)}. \quad (8-33)$$

Thus, the hydrodynamic stiffness and damping coefficient in tapered bearings are about the same as those in straight-wall bearings with the same average clearance.

As a brief summary, the bearing forces in tapered bearings are determined by the bearing average clearance. With the same top opening, a positively tapered bearing has a smaller average clearance and hence a smaller flow rate than a negatively tapered bearing.

Furthermore, when the average bearing clearance is the same, the hydrodynamic stiffness and damping coefficient in tapered bearings are equal to those in straight-wall bearings.

### 8.2.3 Bearing Flow and Bearing Forces in Journal Bearings with Bow-Shaped Profiles

As sketched in Figure 8-8, the bow-shaped profile can be approximated by two symmetric linear segments combined together:

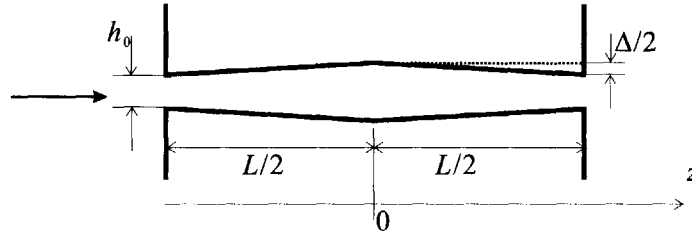


Figure 8-8: Sketch of bow-shaped journal bearing (not to scale).

Thus, the bearing clearance  $h(z, \theta)$  can be written as

$$h(z, \theta) = \begin{cases} h_0 \left( 1 + \delta \frac{L+2z}{L} - \xi \cos(\theta) \right), & z \in \left[ -\frac{L}{2}, 0 \right] \\ h_0 \left( 1 + \delta \frac{L-2z}{L} - \xi \cos(\theta) \right), & z \in \left[ 0, \frac{L}{2} \right] \end{cases} \quad (8-34)$$

Substituting Equation (8-34) into (8-2), after integration, the hydrostatic pressure in the bow-shaped bearing becomes

$$p^{hs}(z, \theta) = q_z \frac{3\mu L}{h_0^3 \delta} \cdot \begin{cases} \left( \frac{1}{(1 - \xi \cos(\theta))^2} - \frac{2}{(1 + \delta - \xi \cos(\theta))^2} + \frac{1}{(1 + \delta \cdot (L+2z)/L - \xi \cos(\theta))^2} \right), & z \in \left[ -\frac{L}{2}, 0 \right] \\ \left( \frac{1}{(1 - \xi \cos(\theta))^2} - \frac{1}{(1 + \delta \cdot (L-2z)/L - \xi \cos(\theta))^2} \right), & z \in \left[ 0, \frac{L}{2} \right] \end{cases} \quad (8-35)$$

Therefore, according to Equation (8-3),  $q_z$  in the bow-shaped bearing can be obtained:

$$q_z(\theta) = \frac{-b(\theta) + \sqrt{b^2(\theta) + 4a(\theta)\Delta p}}{2a(\theta)}, \quad (8-36)$$

where

$$a(\theta) \equiv \frac{\gamma}{2} \rho \frac{1}{h_0^2} \frac{1}{(1 - \zeta \cos(\theta))^2}, \text{ and } b(\theta) \equiv \frac{6\mu L}{\delta h_0^3} \left( \frac{1}{(1 - \xi \cos(\theta))^2} - \frac{1}{(1 + \delta - \xi \cos(\theta))^2} \right).$$

Thus, the hydrostatic flow rate through the bow-shaped bearing is

$$Q = \int_0^{2\pi} q_z(\theta) R d\theta. \quad (8-37)$$

Meanwhile, the integration of  $p^{hs}(z, \theta)$  in the bow-shaped bearing with respect to  $z$  (Equation (8-35)) yields

$$\int_0^L p^{hs}(z, \theta) dz = 6\mu \frac{L^2}{h_0^3} \frac{(1 + \delta/2 - \xi \cos(\theta)) q_z(\theta)}{(1 - \xi \cos(\theta))^2 (1 + \delta - \xi \cos(\theta))^2}. \quad (8-38)$$

Then, after integration with respect to  $\theta$ , the hydrostatic force  $F^{hs}$  in the bow-shaped bearing becomes

$$F^{hs} = -6\mu R \frac{L^2}{h_0^3} \int_0^{2\pi} \frac{(1 + \delta/2 - \xi \cos(\theta)) q_z(\theta)}{(1 - \xi \cos(\theta))^2 (1 + \delta - \xi \cos(\theta))^2} \cos(\theta) d\theta. \quad (8-39)$$

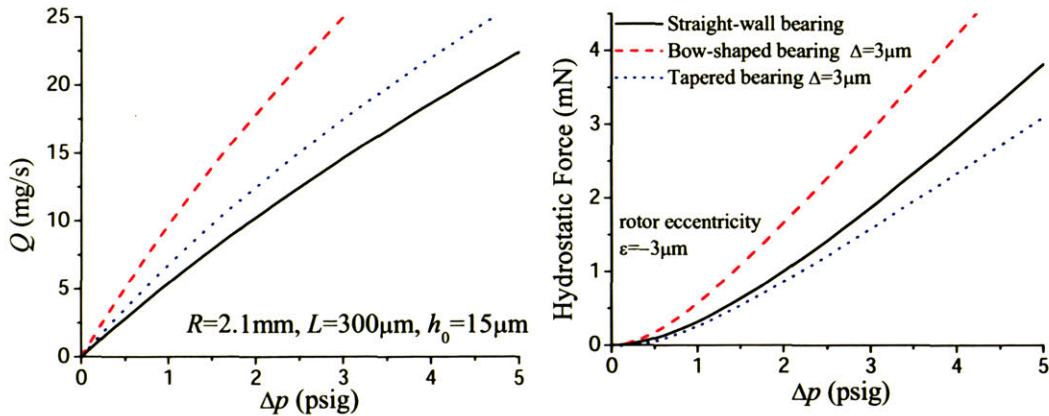


**Figure 8-9: Hydrostatic flow rate and force in bow-shaped journal bearings.**

As plotted in Figure 8-6, compared with straight-wall journal bearings, bow-shaped bearing have a larger flow rate and hydrostatic restoring force, unlike tapered bearings (also shown in the plot).

Furthermore, through integrations, the expression of the hydrodynamic force due to rotor pumping action  $F_p^{hd}$  in the bow-shaped bearing can be derived:



$$F_p^{hd} = \frac{3}{2} \pi \mu \omega \frac{L^3 R}{h_0^2} \frac{\xi}{\delta^3} \left[ \ln \left( \frac{1 + \delta + \sqrt{(1 + \delta)^2 - \xi^2}}{1 + \sqrt{1 - \xi^2}} \right) - \frac{1 + 2\delta}{\sqrt{1 - \xi^2}} \right. \\ \left. - \frac{(1 + \delta) \sqrt{(1 + \delta)^2 - \xi^2}}{\xi^2} + \frac{(1 + \delta)^2}{\xi^2 \sqrt{1 - \xi^2}} \right] \quad (8-40)$$

Similarly, the hydrodynamic force due to viscous drag  $F_v^{hd}$  is

$$F_d^r = -2\pi\mu\omega \frac{LR^2}{h_0} \frac{\sqrt{(1 + \delta)^2 - \xi^2} - \delta - \sqrt{1 - \xi^2}}{\delta\xi}. \quad (8-41)$$

The damping force  $F^{dp}$  in  $\hat{\epsilon}$  direction is

$$F_\epsilon^{dp} = -3\pi\mu\nu_\epsilon \frac{L^3 R}{h_0^2} \frac{1}{\delta^3} \left[ \ln \left( \frac{1 + \delta + \sqrt{(1 + \delta)^2 - \xi^2}}{1 + \sqrt{1 - \xi^2}} \right) - \frac{(1 + \delta)^2}{\epsilon^2 \sqrt{1 - \xi^2}} \right. \\ \left. + \frac{1}{\sqrt{1 - \xi^2}} + \frac{\delta^2}{(1 - \xi^2)^{1.5}} + \frac{(1 + \delta) \sqrt{(1 + \delta)^2 - \xi^2}}{\xi^2} \right], \quad (8-42)$$

and the damping force  $F^{dp}$  in  $\hat{\beta}$  direction is

$$F_p^{hd} = -3\pi\mu\nu_\beta \frac{L^3 R}{h_0^2} \frac{1}{\delta^3} \left[ \ln \left( \frac{1 + \delta + \sqrt{(1 + \delta)^2 - \xi^2}}{1 + \sqrt{1 - \xi^2}} \right) - \frac{1 + 2\delta}{\sqrt{1 - \xi^2}} \right. \\ \left. - \frac{(1 + \delta) \sqrt{(1 + \delta)^2 - \xi^2}}{\xi^2} + \frac{(1 + \delta)^2}{\xi^2 \sqrt{1 - \xi^2}} \right]. \quad (8-43)$$

As the profile variation  $\delta \rightarrow 0$ , the bow-shaped bearing reduces to a straight-wall bearing, and the hydrodynamic and damping forces in the former can be found to equal the ones in the latter. Thus, again, the above equations of bearing forces in bow-shaped bearings are consistent with those in straight-wall bearings.

Furthermore, at the centered position  $\xi=0$ , the intrinsic hydrostatic stiffness  $k$  and damping coefficient  $C$  in the bow-shaped bearing are

$$k_p^{Bow} = \frac{3}{2} \pi \mu \frac{L^3 R}{h_0^3} \frac{1}{\delta^3} \left( \ln(1 + \delta) - \delta + \frac{\delta^2}{2} \right) = k_p^{Straight} \frac{3}{\delta^3} \left( \ln(1 + \delta) - \delta + \frac{\delta^2}{2} \right), \quad (8-44)$$

$$k_v^{Bow} = \pi\mu \frac{L^3 R}{h_0^2} \frac{1}{\delta} \left(1 - \frac{1}{1+\delta}\right) = k_p^{Straight} \frac{1}{\delta} \left(1 - \frac{1}{1+\delta}\right), \quad (8-45)$$

$$C^{Bow} = C^{Straight} \frac{3}{\delta^3} \left( \ln(1+\delta) - \delta + \frac{\delta^2}{2} \right). \quad (8-46)$$

Again, the ratios of the hydrodynamic stiffness and damping coefficient in the bow-shaped bearing to the ones in the straight-wall bearing are functions of  $\delta$  as plotted in Figure 8-10. Furthermore, it can be seen that the hydrodynamic stiffness due to rotor pumping action and damping coefficient are larger in the bow-shaped bearing than in both the straight-wall and the negatively tapered bearings. This is because both ends of the bow-shaped bearing contract, allowing higher pressure to build up in the bow-shaped bearing than in the tapered bearing, which has a divergent end.

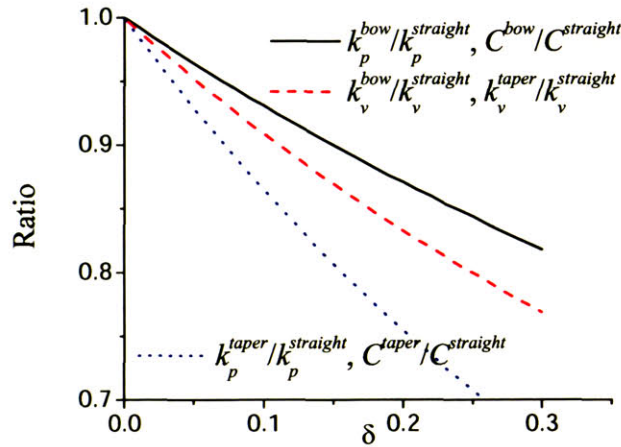


**Figure 8-10: Ratios of hydrodynamic stiffness and damping coefficient in bow-shaped bearings to those in straight-wall bearings.**

By an analysis similar to the one for the tapered bearing in Section 8.2.2, one can find that

$$k_p^{Bow} \cong k_p^{Straight} \Big|_{h_0(1+\delta/4)}, \quad k_v^{Bow} \cong k_v^{Straight} \Big|_{h_0(1+\delta/2)}, \quad C^{Bow} \cong C^{Straight} \Big|_{h_0(1+\delta/4)}. \quad (8-47)$$

Thus, the intrinsic hydrodynamic stiffness due to viscous drag effect in a bow-shaped bearing is about the same as the stiffness in a straight-wall bearing with the same average clearance. However, the intrinsic hydrodynamic stiffness due to rotor pumping action and the damping coefficient are larger than those in straight-wall bearings with the same average clearance, because both ends of the bow-shaped bearing contract and higher pressure can be built up in the bow-shaped bearing.

### 8.3 Rotordynamic Behavior in Non-Straight-Wall Journal-Bearing Systems

Using the fluid models established in the previous section, one can calculate the rotordynamic behavior of the system, such as the stability boundary and the distance to contact.

Since the hydrodynamic and damping forces in tapered bearings are equal to those in straight-wall bearings with the same average clearance, the following analysis will show that the system stability boundary of the tapered bearing behaves similarly to that of the straight-wall bearing. On the other hand, the singular peak of the system stability boundary for the bow-shaped bearing shifts to a larger bearing clearance because of its relatively larger hydrodynamic stiffness due to rotor pumping action.

Furthermore, negatively tapered journal bearings with a large profile variation  $\Delta$  are found to be able to induce positive direct-coupled hydrostatic stiffness at low  $\Delta p$  (pressure difference across the bearing), making the system statically unstable. Analyses also show that the distances to contact for all non-straight-wall journal bearings are smaller than those of straight-wall bearings, making it difficult to invert the rotor.

#### 8.3.1 Stability Boundary of Journal Bearings with Profile Variations

For bearings with the isotropic configuration, the whirl ratios can be calculated according to Equation (3-12). Thus, the whirl ratio for a tapered bearing is

$$\mathfrak{R}^{Taper} = \frac{\Omega_W}{\Omega_N} = \left| \frac{C^{Taper}}{k_p^{Taper} - k_v^{Taper}} \right| = \left| \frac{2}{1 - W^{Taper}} \right|, \quad (8-48)$$

where the whirl number for the tapered bearing  $W^{Taper}$  can be obtained from Equations (8-27) and (8-28):

$$W^{Taper} = \frac{2Rh_0}{L^2} \frac{\delta^2 (1 - 1/(1 + \delta))}{12(\ln(1 + \delta) - \delta/(1 + \delta/2))} = \frac{2Rh_0}{L^2} \left( 1 + \frac{\delta}{2} + O(\delta^2) \right). \quad (8-49)$$

Again,  $W^{Taper}$  is about the same as the whirl number for a straight-wall bearing with the same average clearance ( $h_0(1 + \delta/2)$ ). Then it is expected that the whirl ratio in the tapered bearing behaves similarly to the one in a straight-wall bearing with the same average clearance.

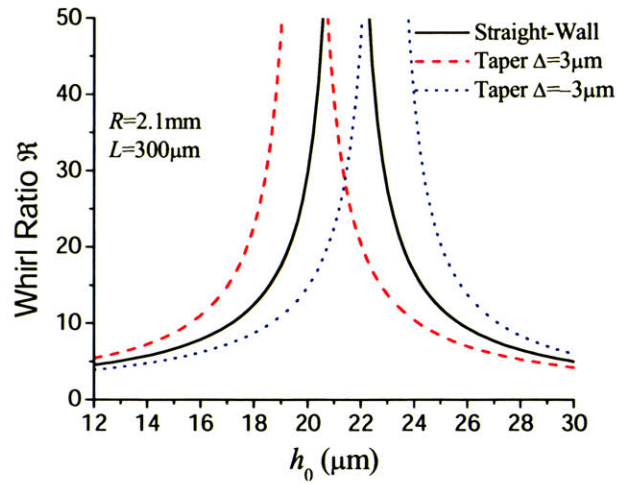


**Figure 8-11: Whirl ratios for tapered journal bearings.**

As plotted in Figure 8-11, the singular point of the negatively tapered bearing (red dashed line) is  $h_0=20\mu\text{m}$ , and the corresponding average clearance is  $21.5\mu\text{m}$ , which is the singular point in the straight-wall bearing. On the other hand, the singular point in the positively tapered bearing (blue dotted line) is  $h_0=23\mu\text{m}$ , and the corresponding average clearance is  $21.5\mu\text{m}$  again. Therefore, the tapered bearing does behave similarly to the straight-wall bearing with the same average clearance, in terms of whirl ratio.

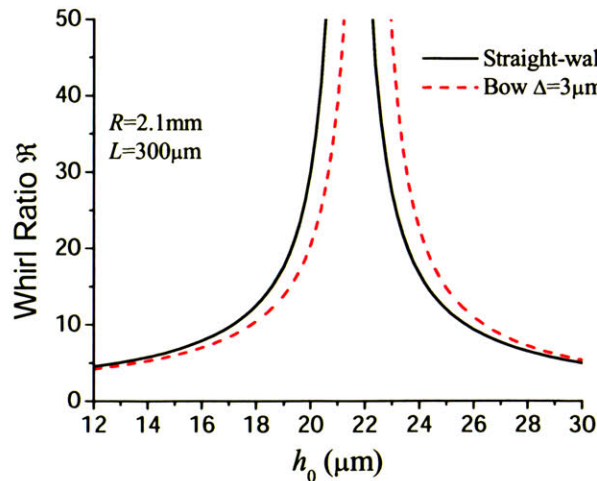


**Figure 8-12: Whirl ratio for the bow-shaped journal bearing.**

Similarly, the whirl ratio in the bow-shaped bearing is

$$\mathfrak{R}^{Bow} = \frac{\Omega_W}{\Omega_N} = \left| \frac{2}{1 - W^{Bow}} \right|, \quad (8-50)$$

where the whirl number for the bow-shaped bearing  $W^{Bow}$  is

$$W^{Bow} = \frac{2Rh_0}{L^2} \frac{\delta^2(1-1/(1+\delta))}{3(\ln(1+\delta)-\delta+\delta^2/2)} = \frac{2Rh_0}{L^2} \left(1 - \frac{\delta}{4} + O(\delta^2)\right). \quad (8-51)$$

Although the average clearance in the bow-shaped bearing is larger ( $h_0(1+\delta/2)$ ), the corresponding whirl number is about the same as the number for a straight-wall bearing with a smaller clearance ( $h_0(1-\delta/4)$ ). Then, according to Equation (8-51), the singularity point  $h_0$  in the bow-shaped bearing is a little larger than that in the straight-wall bearing, which is clearly captured in the plot of Figure 8-12.

Based on the plots in Figure 8-11 and Figure 8-12, it can be seen that with the isotropic configuration, the fabrication tolerance requirements for the bearing clearance  $h_0$  in the non-straight-wall bearings are still tight, because the singular peak is still narrow. This means that there is no acceptable isotropic design that works with all the profiles investigated above. Therefore, an anisotropic design that works with journal bearings of various bearing profiles is a positive solution to the tight fabrication tolerance requirements.

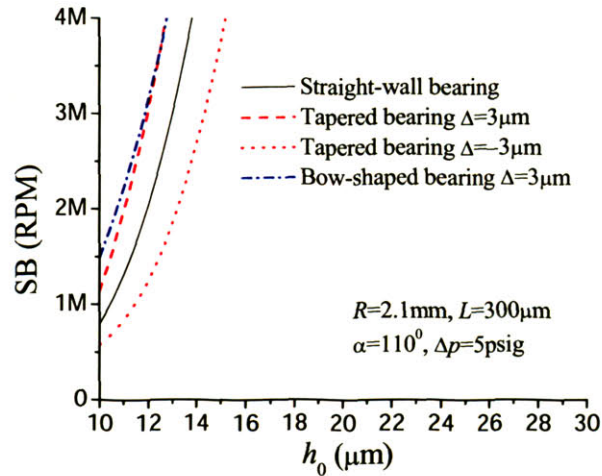


**Figure 8-13: Stability boundary in the anisotropic non-straight-wall journal-bearing system.**

In the anisotropic journal-bearing system, based on the analyses in Chapter 4, the system stability boundary is mainly determined by the ratio of the hydrostatic stiffness anisotropy to the intrinsic hydrodynamic stiffness, as described by Equation (4-11). Since these two stiffnesses in the non-straight-wall bearings are of comparable magnitude to those in the straight-wall bearings, the stability boundary of the non-straight-wall bearings is also of the same magnitude as the stability boundary in the non-straight-wall bearings (as shown in Figure 8-13).



One can see from the plots that because of larger average clearances, the stability boundary of the negatively tapered journal-bearing system (red dashed line) and the bow-shaped journal-bearing system (blue dash-dotted line) is higher than the stability boundary of the straight-wall bearing system (black solid line), while the boundary of the positively tapered journal-bearing system (red dotted line) is lower due to its smaller average clearance.

Furthermore, as with the straight-wall bearings, anisotropy in the non-straight-wall journal bearings can improve the system stability boundary, greatly releasing the fabrication tolerance requirements. According to Figure 8-13, with a bearing entrance clearance  $h_0 \geq 15 \mu\text{m}$ , the stability boundary in journal-bearing systems with all kinds of profiles can be higher than the design speed of 2.4MRPM, even if the profile variations are as large as  $3 \mu\text{m}$ .

### 8.3.2 Nonlinear and Positive Hydrostatic Stiffness with Tapered Journal Bearings

The amplitude of hydrostatic force, the restoring force, increases with eccentricity in all types of journal bearings, as shown in Figure 8-14. On the other hand, it is important to note that the hydrostatic force softens in negatively tapered bearings, while it stiffens in positively tapered bearings.

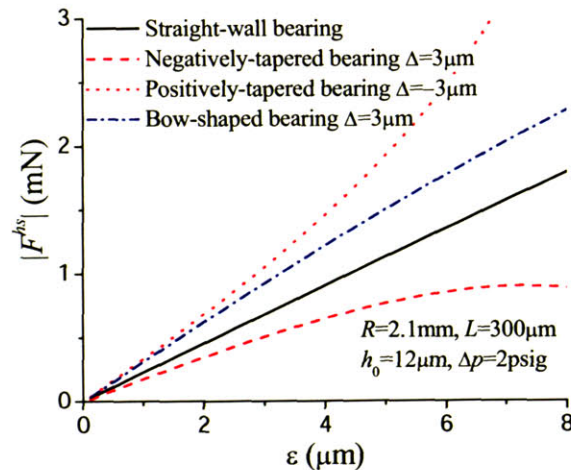


**Figure 8-14: Hydrostatic forces as functions of rotor eccentricity for journal bearings with different bearing profiles.**

The softening and stiffening hydrostatic forces are more clearly illustrated by the ratios of hydrostatic stiffness  $K^{hs}$  to  $K_0^{hs}$  as shown in Figure 8-15, where  $K_0^{hs}$  is the hydrostatic stiffness at the center position:



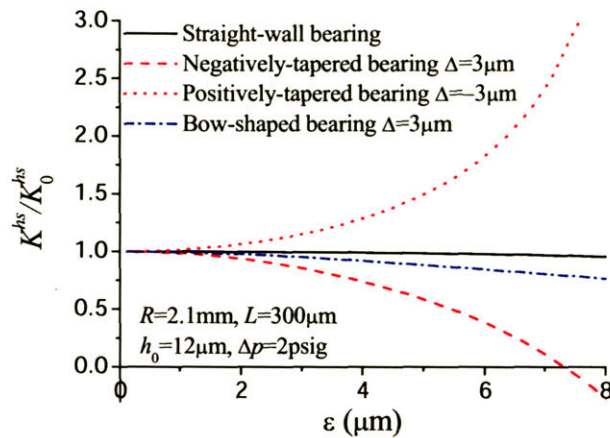


**Figure 8-15: Hydrostatic stiffness as a function of rotor eccentricity for journal bearings with different bearing profiles.**

Thus, it can be seen that the hydrostatic force/stiffness in the bow-shaped journal bearing is as linear as the hydrostatic force in the straight-wall bearing, but it is a strong nonlinear function of the rotor eccentricity in tapered bearings. This strong nonlinearity can induce nonlinear dynamic behavior in the system, such as subharmonic and superharmonic resonances, which are discussed in Chapter 9.

It is worth noticing in Figure 8-15 that the hydrostatic stiffness in the negatively tapered journal bearing (red dashed line) begins to change sign at a rotor eccentricity  $\varepsilon$  of about  $7.5\mu\text{m}$ .

Normally, the hydrostatic direct-coupled stiffness in the bearing should be negative so that additional rotor displacement can induce hydrostatic force in the opposite direction, pushing the rotor back to the original position. With the positive hydrostatic direct-coupled stiffness in the negatively tapered bearing at a large rotor eccentricity (larger than  $7.5\mu\text{m}$  in the case of Figure 8-15), additional displacement of the rotor induces an additional force in the *same* direction, pushing the rotor even further away from its original position and making the system statically unstable! Moreover, when the rotor is accelerating through the natural frequencies, the radius of its precession orbit is large (recall that the distance to contact is normally only  $1\sim 2\mu\text{m}$ ). As a result, it is quite possible for the rotor to enter this static unstable region and crash into the bearing wall.

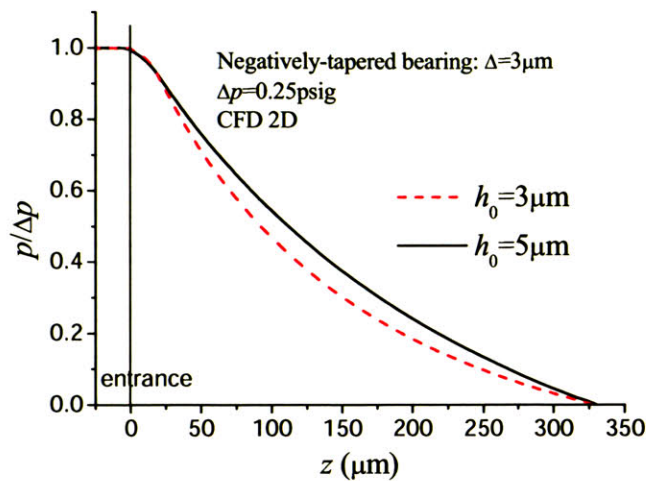


**Figure 8-16: Pressure along the negatively tapered journal bearing, calculated by CFD.**

Positive hydrostatic stiffness is caused by the decreasing flow resistance along the negatively tapered bearing. Along the flow path, the flow resistance (the slope of the pressure profile) in the negatively tapered bearing decreases, resulting in the concave pressure profile shown in Figure 8-16. This decrease in flow resistance along the bearing is faster with smaller bearing clearance  $h$ , because the resistance is inversely proportional to the cube of the bearing clearance; thus, the pressure profile along the flow path is more concave in tighter bearings. This effect is clearly captured in Figure 8-16, where the pressures along the negatively tapered journal bearing calculated by 2-D CFD (Fluent) are plotted for two different bearing clearances. It can be seen that as the bearing gap closes up (from black solid line to red dashed line), the calculated pressure profile along the negatively tapered bearing becomes more concave. As a result, the integrated force (the area below the lines) in the tighter bearing is smaller than in the bearing with larger clearance, and the net hydrostatic force pushes the rotor in the direction of the tighter bearing gap, further reducing the gap.

The positive hydrostatic stiffness in the negatively tapered journal bearing is more severe with a low pressure difference across the bearing  $\Delta p$ , large bearing profile variation  $\delta$ , or large rotor eccentricity  $\epsilon$ , as shown in Figure 8-17. Although the hydrostatic stiffness eventually becomes negative at higher  $\Delta p$ , the negatively tapered journal-bearing system is statically unstable at low  $\Delta p$  because of the positive destabilizing stiffness, even if the rotor is at the center of the bearing.



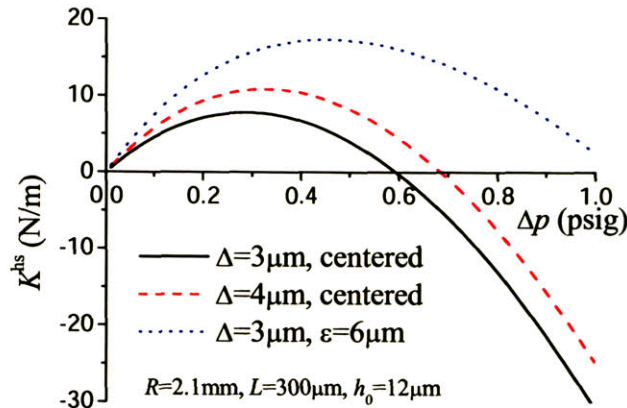


**Figure 8-17: Positive hydrostatic stiffness in the negatively tapered journal bearing changes with the pressure difference across the bearing  $\Delta p$ , the bearing profile variation  $\delta$ , and the rotor eccentricity  $\varepsilon$ .**

As has been emphasized several times before, the rotor should be inverted at a low pressure difference across the bearing  $\Delta p$  to avoid the large rotor response amplitude peak and associated small distance to contact. Furthermore, Chapter 5 shows that the relatively heavy rotors (70mg) in the micro-turbo-charger devices could not cross the natural frequency at  $\Delta p$  higher than 0.25psig with 5 $\mu\text{m}$  unbalance. Then, if the journal bearing in these devices is a negatively tapered one with a large bearing profile variation (for example, 3 $\mu\text{m}$ ), at  $\Delta p$  lower than 0.25psig, the hydrostatic stiffness is positive according to Figure 8-17, making the system statically unstable. So, the rotor can never be inverted in micro-turbo-charger devices that have negatively tapered journal bearings with large bearing profile variations. For this reason, negatively tapered journal bearings with large profile variations should be avoided in fabrication.

### 8.3.3 Distance to Contact in Non-Straight-Wall Journal-Bearing Systems

Even if the bearing profile is not a negatively tapered one with large profile variation (so that the system is statically stable), the following analysis shows that the distances to contact in non-straight-wall bearings are smaller than in straight-wall bearings and make it difficult to invert the rotor.

As discussed previously, hydrostatic force is a strong nonlinear function of rotor eccentricity. This nonlinearity skews the rotor response curves as discussed in Chapter 2, which in turn can affect the distance to contact. Furthermore, the damping coefficient and hydrodynamic stiffness in the non-straight-wall bearings are different from the ones in

the straight-wall bearings, according to Section 8.2, which can also affect the distance to contact according to Equation (2-42). These effects are accounted for in the calculations of the rotor response curve shown in Figure 8-18.

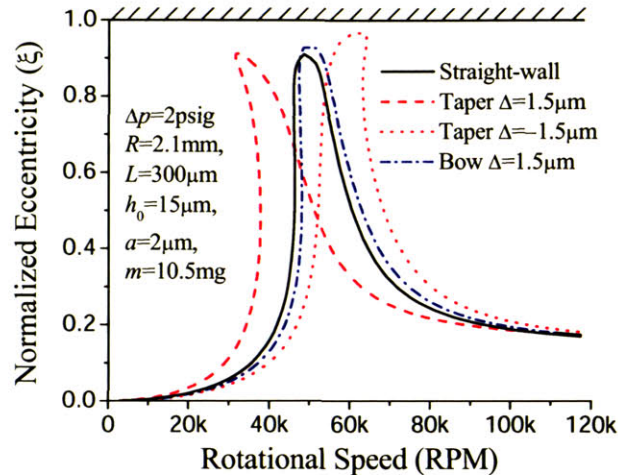


**Figure 8-18: Rotor response curves in journal bearings with various profiles.**

Moreover, numerical simulations have been run to calculate the distance to contact with different profiles and different profile variations.

$\Delta$	1 $\mu\text{m}$	1.5 $\mu\text{m}$	2 $\mu\text{m}$	3 $\mu\text{m}$
Negatively-tapered	1.6	1.7	-	-
Positively-tapered	1.5	1.3	1.1	0.6
Bow-shaped	1.7	1.5	1.4	1.1

**Table 8-1: Distance to contact for micro-turbo-pump devices with different bearing profiles and profile variations, at  $\Delta p=0.5\text{psig}$ .**

The distances to contact in Table 8-1 were calculated for the micro-turbo-pump device, in which the rotor has a relatively large mass (25.4mg) and radius (3.1mm). The length of the bearing was 300 $\mu\text{m}$ , the entrance clearance was  $h_0=15.5\mu\text{m}$ , and the pressure difference across the bearing was 0.5psig. If the bearing was a straight-wall one, the distance to contact would be 2.1 $\mu\text{m}$ . Compared with the threshold normalized distance to contact of 0.09 derived in Chapter 5, the shaded elements in Table 8-1 indicate that it is difficult to invert the rotor with the corresponding bearings. Thus, in order to invert the rotor at  $\Delta p$  of 0.5psig (with lower  $\Delta p$  the system may be static unstable, due to positive hydrostatic stiffness in the negatively tapered journal bearing), the journal bearing should be fabricated with a profile variation smaller than 1.5 $\mu\text{m}$ . In fact, simulations show that the rotor precession orbits penetrate into the region of the positive hydrostatic stiffness

and become unstable in negatively tapered journal bearings with profile variations of  $2\mu\text{m}$  and  $3\mu\text{m}$ .

### **8.4 Summary and Conclusions**

Journal bearings with various profiles were investigated, and through the analytically established fluid models, bearing forces, stiffnesses, and damping coefficients were calculated for these bearings. Then, rotordynamic behavior such as the stability boundary and distance to contact was investigated for journal bearings with the three most common profiles: positively tapered, negatively tapered and bow, which are.

According to the fluid models, it was found that the damping coefficient  $C$  is exactly twice the intrinsic hydrodynamic stiffness due to rotor pumping action  $k^p$  in all journal bearings. The hydrostatic force in bow-shaped and positively tapered journal bearings is larger than the force in straight-wall bearings, while in negatively tapered bearings it is smaller. The hydrodynamic and damping forces in tapered journal bearings are about the same (up to the first order or the rotor eccentricity) as the ones in straight-wall bearings with the same average bearing clearance.

Then, based on the fluid models, the system stability boundary in the tapered bearings was found to behave similarly to the boundary in straight-wall bearings with the same average clearance. Also, it was found that hydrostatic stiffness anisotropy can improve the system stability boundary in journal bearings with all types of profiles, so that the fabrication tolerance requirements for the bearing clearance can be greatly released.

A negatively tapered journal bearing can induce positive hydrostatic direct-coupled stiffness, which is caused by the diffuser effect and can make the system statically unstable, especially at a low pressure difference across the journal bearing  $\Delta p$ . Analysis has shown that this positive hydrostatic stiffness is more severe in negatively tapered journal bearings with a large profile variation. Thus, such negatively tapered bearings with large profile variation should be avoided in fabrication, especially for devices that need to be inverted at low  $\Delta p$ .

Furthermore, hydrostatic stiffness is found to be a strong nonlinear function of rotor eccentricity in tapered bearings, and this nonlinearity in turn skews the rotor response curves. Most importantly, numerical simulations of the rotor response curves show that the distances to contact in the non-straight-wall journal bearings, especially those with large profile variations, are smaller than the distances to contact in the straight-wall bearings. Therefore, large profile variations should be also avoided. More specifically, ac-

According to the simulation results, profile variations should be smaller than  $1.5\mu\text{m}$  for journal bearings used in the micro-turbo-pump devices so that they can be inverted at  $\Delta p$  of 0.5psig.



## Chapter 9

# Nonlinear Dynamics of Micro-Journal-Bearing Systems

As described in Chapter 5, the resonance at the natural frequency can be picked up by measuring the variation in pressure difference across the journal bearing while keeping the flow supply to the bearing constant (Figure 5-5). When a resonance occurs, the amplitude of the rotor orbit changes abruptly, altering the flow resistance through the journal bearing (Figure 2-6-a). As a result, with the constant flow rate through the journal bearing (controlled by a flow controller), the pressure difference across the journal bearing  $\Delta p$  changes, indicating the resonance. Using this method, the system natural frequencies have been successfully measured and compared well with the model predictions (Figure 5-7).

In Figure 5-5, only one peak showed in the response curve, indicating the single natural frequency of the isotropic system. However, for some devices, there were several resonances observed in the experiments.

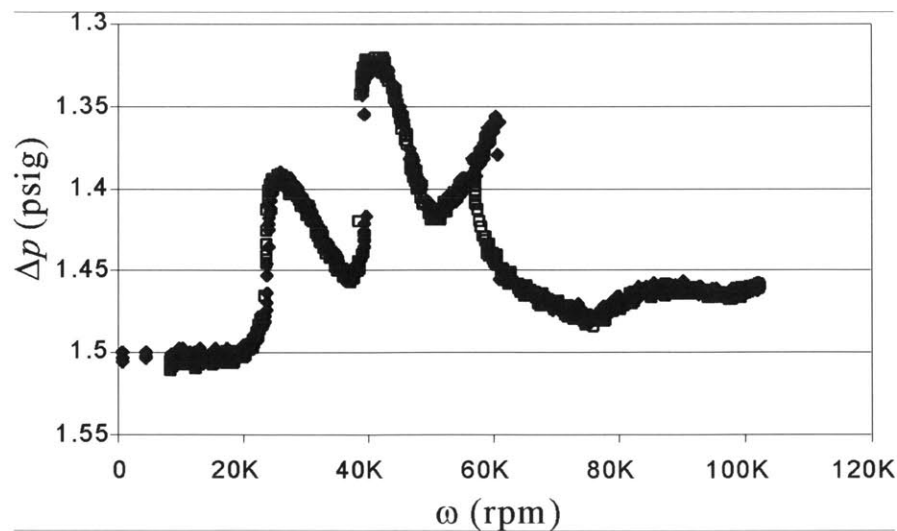


Figure 9-1: Multiple resonances observed in the experiment for the micro-bearing-rig device with part-bearing configuration [30].

For example, there were a total of 3 peaks of  $\Delta p$  variation in Figure 9-1, indicating that the rotor underwent resonances at speeds of 22krpm, 42krpm, and 60krpm. Compared with the model predictions, the first two were found to be the natural frequencies in the two principal directions respectively (the device used a part-bearing configuration). Then the question arises—what is the third resonance at the speed of 60krpm?

Through the nonlinear analysis presented in this chapter, one can find that this resonance was actually a third-order subharmonic resonance. Furthermore, because there are only odd orders of nonlinearity in the hydrostatic force due to its skew symmetry, the nonlinear resonances can only occur at the speeds that are odd times (fractions) of the natural frequency. According to the analysis based on the system with the third-order nonlinearity in hydrostatic force, the anisotropic journal-bearing system can engage in nonlinear resonances at speeds of 1) one third of the natural frequency, 2) three times the natural frequency, or 3) combinations of the natural frequencies. Through an analytical approach using the multi-scale method, the conditions under which nonlinear resonance can occur are derived and verified by the numerical simulation. Most importantly, the analysis shows that the third-order subharmonic resonance can also occur in the isotropic bearing system and its orbit is found to rotate slowly—different from the fixed orbits of the nonlinear resonances in the anisotropic system. This subharmonic resonance in the isotropic bearing system has not been observed before, according to [34]; however, it is verified by the numerical simulations presented in the chapter.

### 9.1 Nonlinearity in Hydrostatic Force

In the previous chapters, it has been shown that hydrostatic stiffness can be a strong nonlinear function of rotor eccentricity, especially in the tapered journal bearings (Figure 8-15). With this nonlinearity, the rotor response curve is skewed left or right depending on whether the stiffness is stiffening or softening (Figure 8-18). Since the nonlinearity of the hydrostatic force is the cause of the nonlinear resonances, it is useful to investigate its properties first before proceeding to analyze the nonlinear resonances.

If one follows the analyses in Chapter 2 on the hydrostatic force, the pressure at the entrance (Figure 2-3) of a straight-wall bearing is

$$p_2 = \frac{-144\mu^2 L^2 + \sqrt{(144\mu^2 L^2)^2 + 288\gamma\rho\mu^2 h^2 L^2 \Delta p}}{\gamma\rho h^2}. \quad (9-1)$$

When the rotor moves from its centered position by an infinitesimal displacement  $\varepsilon$ , the bearing clearance becomes  $h(\theta) = h_0 - \varepsilon \cos(\theta) = h_0(1 - \xi \cos(\theta))$ , where  $\xi$  is the rotor dis-

placement normalized by the bearing clearance  $h_0$ . The Taylor expansion of Equation (9-1) in  $\xi$  (which is much smaller than 1) is:

$$p_2 = a_0 + a_1 \xi \cos \theta + a_2 (\xi \cos \theta)^2 + a_3 (\xi \cos \theta)^3 + O(\xi^4), \quad (9-2)$$

where the coefficients  $a_0$ ,  $a_1$ ,  $a_2$ , and  $a_3$  are

$$a_0 = \frac{-1 + \sqrt{1 + 4\Pi}}{2} \tilde{P}, \quad a_3 = \left[ -10 + 10 \frac{1 + 2\Pi}{(1 + 4\Pi)^{3/2}} - 16 \frac{\Pi^2}{(1 + 4\Pi)^{3/2}} - 128 \frac{\Pi^3}{(1 + 4\Pi)^{5/2}} \right] \tilde{P},$$

$$a_1 = \left( \frac{2 + 4\Pi}{\sqrt{1 + 4\Pi}} - 2 \right) \tilde{P}, \quad \tilde{P} \equiv \left( \frac{L}{h_0^2} \right)^2 \frac{288\mu^2}{\gamma\rho}, \quad \text{and } \Pi \equiv \Delta p / \tilde{P}.$$

In the isotropic configuration, the integration of the pressure in the bearing yields the hydrostatic force  $F^{hs}$

$$F^{hs} = \int_0^{2\pi} -\cos(\theta) R \frac{p_2 L}{2} d\theta = K_s \xi + k_N \xi^3 + O(\xi^5), \quad (9-3)$$

where  $K_s \xi$  is the linear term ( $K_s$  denotes the direct-coupled hydrostatic stiffness) and  $k_N \xi^3$  is the nonlinear term:

$$K_s \equiv \frac{RL}{2} a_1 \int_0^{2\pi} -\cos^2(\theta) d\theta = -\frac{\pi}{2} \cdot RL a_1, \quad \text{and } k_N \equiv \frac{RL}{2} a_3 \int_0^{2\pi} -\cos^4(\theta) d\theta = -\frac{3}{8} \pi \cdot RL a_3.$$

It is important to note that the terms with the second order of  $\xi$  are integrated to be zeros because of the symmetry of the system.

On the other hand, in the part-bearing configuration (Figure 4-3), with the infinitesimal displacement  $\delta X$  in  $x$  direction and  $\delta Y$  in  $y$  direction, the bearing clearance can be expressed as  $h(\theta) = h_0(1 - \delta X \cos(\theta) - \delta Y \sin(\theta))$ . Thus the pressure at the bearing entrance  $p_2$  is

$$p_2 = a_0 + a_1 \cdot (\delta X \cos(\theta) + \delta Y \sin(\theta)) + a_2 \cdot (\delta X \cos(\theta) + \delta Y \sin(\theta))^2 + a_3 \cdot (\delta X \cos(\theta) + \delta Y \sin(\theta))^3 + O\left((\delta X \cos(\theta) + \delta Y \sin(\theta))^4\right) \quad (9-4)$$

Again, with integration, the hydrostatic forces in  $x$  and  $y$  directions become

$$F_x^{hs} = \int_{-\alpha/2}^{\alpha/2} -\cos(\theta) \frac{p_2 L}{2} R d\theta + \int_{\pi-\alpha/2}^{\pi+\alpha/2} -\cos(\theta) \frac{p_2 L}{2} R d\theta, \quad (9-5)$$

$$F_y^{hs} = \int_{-\alpha/2}^{\alpha/2} -\sin(\theta) \frac{p_2 L}{2} R d\theta + \int_{\pi-\alpha/2}^{\pi+\alpha/2} -\sin(\theta) \frac{p_2 L}{2} R d\theta. \quad (9-6)$$

Substituting Equation (9-4) into (9-5) and (9-6) yields

$$\begin{cases} F_x^{hs} = K_{xx} \delta X + k_1 \delta X^3 + k_2 \delta X \delta Y^2 + O(\delta X^5, \delta Y^5) \\ F_y^{hs} = K_{yy} \delta Y + k_3 \delta Y^3 + k_4 \delta Y \delta X^2 + O(\delta X^5, \delta Y^5) \end{cases}, \quad (9-7)$$

where

$$K_{xx} = -(\alpha/2 + \sin(\alpha)/2) RLa_1, \quad K_{yy} = -(\alpha/2 - \sin(\alpha)/2) RLa_1,$$

$$k_1 = -\frac{RLa_3}{2} \left( \int_{-\alpha/2}^{\alpha/2} \cos^4(\theta) d\theta + \int_{\pi-\alpha/2}^{\pi+\alpha/2} \cos^4(\theta) d\theta \right) = -\frac{RLa_3}{4} \left[ \frac{3\alpha}{2} + \sin(\alpha) + \frac{\sin(2\alpha)}{4} \right],$$

$$k_3 = -\frac{RLa_3}{2} \left( \int_{-\alpha/2}^{\alpha/2} \sin^4(\theta) d\theta + \int_{\pi-\alpha/2}^{\pi+\alpha/2} \sin^4(\theta) d\theta \right) = -\frac{RLa_3}{4} \left[ \frac{3\alpha}{2} - 2\sin(\alpha) + \frac{\sin(2\alpha)}{4} \right],$$

$$\begin{aligned} \text{and } k_2 = k_4 &= -\frac{3RLa_3}{2} \left( \int_{-\alpha/2}^{\alpha/2} \cos^2(\theta) \sin^2(\theta) d\theta + \int_{\pi-\alpha/2}^{\pi+\alpha/2} \cos^2(\theta) \sin^2(\theta) d\theta \right) \\ &= -\frac{3RLa_3}{16} (2\alpha - \sin(2\alpha)). \end{aligned}$$

Note that the  $k_2$  and  $k_4$  terms couple the rotor motions in the two directions, and  $k_1$ ,  $k_2$ ,  $k_3$ , and  $k_4$  all have the same sign with  $\alpha \in (0, \pi)$ .

One can find that, no matter whether the system is isotropic or anisotropic, when the rotor is centered in the bearing, there are no second-order nonlinear terms in the hydrostatic forces. As a result, the system has no second-order nonlinear resonances. In fact, because of the symmetry of the journal-bearing system when the rotor is centered, the hydrostatic force (as the restoring force) is an odd function of the rotor displacement  $\xi$ , and hence has no nonlinear terms of even orders of  $\xi$ . So, the micro-hydrostatic journal-bearing system can only engage in odd orders of nonlinear resonances.

## 9.2 Nonlinear Resonance in Isotropic Systems

With the features of the hydrostatic force nonlinearity obtained above, the nonlinear resonance can then be analyzed by the multi-scale method.

Simple one-dimensional third-order nonlinear resonances have been investigated by many researchers based on the Duffing oscillator, which can be found in textbooks on nonlinear oscillations (for example, [38]). However, the two-dimensional third-order nonlinear resonances of the micro-journal-bearing system are much more complicated than these one-dimensional resonances.

The following analyses will show that there can be a third subharmonic resonance in the isotropic journal-bearing system. Furthermore, analyses of the anisotropic journal-bearing system can be found in the next section.

Substituting the hydrodynamic and damping forces  $F_x^{hd} = -K^{hd}y$ ,  $F_y^{hd} = K^{hd}x$ ,  $F_x^{dp} = C\dot{x}$ ,  $F_y^{dp} = C\dot{y}$ , and the hydrostatic force (Equation (9-3)) into Equation (2-34) yields

$$\begin{cases} m\ddot{x} = K_s x + k_N (x^2 + y^2)x - K^{hd}y + C\dot{x} + m\omega^2 a \cos(\omega t) \\ m\ddot{y} = K_s y + k_N (x^2 + y^2)y + K^{hd}x + C\dot{y} + m\omega^2 a \sin(\omega t) \end{cases} \quad (9-8)$$

It is useful to introduce the complex displacement  $r = x + iy$ . Then the above equation reduces to

$$\ddot{r} = -\Omega_N^2 r + \frac{k_N}{m} |r|^2 r + \frac{C}{m} \dot{r} + i \frac{K^{hd}}{m} r + \omega^2 a e^{i\omega t}, \quad (9-9)$$

where  $\Omega_N$  is the natural frequency of the system. Note that the hydrodynamic stiffness  $K^{hd}$ , damping  $C$ , and nonlinear hydrostatic stiffness  $k_N$  are all small compared with  $K_s$ .

For simplicity, a general form of Equation (9-9), which can be derived by changing variables, is investigated instead:

$$\ddot{r} + (1 + k|r|^2)r + c\dot{r} + ik_d r = \omega^2 e^{i\omega t}, \quad (9-10)$$

where  $k|r|^2 r$  is the nonlinear term. The natural frequency of the system described by Equation (9-10) is 1 rad/s. Because the terms of  $k$ ,  $c$ , and  $k_d$  are all small— $O(k) \sim O(c) \sim O(k_d) \sim O(\varepsilon)$ —they can be expressed as  $k = \varepsilon K$ ,  $c = \varepsilon C$ ,  $k_d = \varepsilon K_d$ , where  $\varepsilon \ll 1$ . Then the system can be investigated using the multi-scale method, which uses two time scales (both slow and normal time) to describe the system's motion and is widely used to investigate nonlinear systems. The solution of Equation (9-10) can then be assumed to be

$$r = r_0(t, T) + \varepsilon r_1(t, T) + \varepsilon^2 r_2(t, T) + \dots, \quad (9-11)$$

where  $T = \varepsilon t$  is the large time scale that describes the slow motion of the system. Then,  $d^2/dt^2 = \partial^2/\partial t^2 + 2\varepsilon \partial^2/\partial t \partial T + \varepsilon^2 \partial^2/\partial T^2$ . Substituting the above equation into (9-10) and collecting terms according to the orders of  $\varepsilon$  yield

$$\begin{cases} \frac{\partial^2 r_0}{\partial t^2} + r_0 = \omega^2 e^{i\omega t} \\ \frac{\partial^2 r_1}{\partial t^2} + r_1 = - \left( C\dot{r}_0 + iK_d r_0 + K|r_0|^2 r_0 + 2 \frac{\partial}{\partial t} \frac{\partial}{\partial T} r_0 \right) \\ \dots \end{cases} \quad (9-12)$$

The general solution of the first equation is

$$r_0 = Ae^{it} + Be^{-it} + Fe^{i\omega t}, \quad (9-13)$$

where  $A$  and  $B$  are complex functions of  $T$  only, and  $F = \omega^2/(1-\omega^2)$ . If  $A$  or  $B$  is not zero, the rotor then engages into an asynchronous precession with the system natural frequency, resulting in a nonlinear resonance. The following analysis shows the conditions under which  $A$  or  $B$  is not zero and the system undergoes a nonlinear resonance.

Substituting Equation (9-13) into the second equation of (9-12) yields the dynamic equation of  $r_1$ :

$$\begin{aligned} \frac{\partial^2 r_1}{\partial t^2} + r_1 = & - \left[ \left( i(C + K_d)A + K(A^*A^2 + 2AB^*B + 2AF^2) + 2iA' \right) e^{it} \right. \\ & + \left( -i(C - K_d)B + K(B^*B^2 + 2BA^*A + 2BF^2) - 2iB' \right) e^{-it} \\ & + 2KA^*BF e^{i(\omega-2)t} + KA^2F e^{-i(\omega-2)t} \\ & + \left( i(C\omega + K_d) + K(2A^*A + 2B^*B + F^*F) \right) F e^{i\omega t} + 2KABF^* e^{-i\omega t} \\ & + KA^*F^2 e^{i(2\omega-1)t} + KB^*F^2 e^{i(2\omega+1)t} + 2KAB^*F e^{i(\omega+2)t} + KB^2F^* e^{-i(\omega+2)t} \\ & \left. + KA^2B^* e^{i3t} + KA^*B^2 e^{-i3t} \right]. \end{aligned}$$

When the rotor speed is near three times the natural frequency,  $\omega \approx 3$ , the oscillating terms with frequencies of 1 and -1 (or the terms with  $e^{it}$ ,  $e^{-it}$ ,  $e^{i(\omega-2)t}$  and  $e^{-i(\omega-2)t}$ ) are the secular terms (which give solutions of  $r_1$  growing with time) and should be eliminated; otherwise, the amplitude of  $r_1$  increases with  $t$  and the assumption of its being small is no longer valid. Therefore, with  $\omega = 3 + \delta\varepsilon$ , or  $\omega t = 3t + \delta T$ , the equations of  $A$  and  $B$  can be obtained:



$$\begin{cases} i(C + K_d)A + K(A^*A + 2B^*B + 2F^2)A + 2iA' + 2KA^*BF e^{i\delta T} = 0 \\ -i(C - K_d)B + K(B^*B + 2A^*A + 2F^2)B - 2iB' + KA^2F e^{-i\delta T} = 0 \end{cases} \quad (9-14)$$

With  $A$  and  $B$  in the forms  $A = ae^{i\varphi}$ ,  $B = be^{i\phi}$ , where  $a$ ,  $b$ ,  $\varphi$ , and  $\phi$  are all real, the above equations can be rewritten as

$$\begin{cases} i(C + K_d)a + K(a^2 + 2b^2 + 2f^2)a + 2i(a' + ia\varphi') + 2Kabf e^{i(\delta T - 2\varphi + \phi)} = 0 \\ -i(C - K_d)b + K(b^2 + 2a^2 + 2f^2)b - 2i(b' + ib\phi') + Ka^2f e^{-i(\delta T - 2\varphi + \phi)} = 0 \end{cases} \quad (9-15)$$

Furthermore, separating the real and imaginary parts from each other in the above equations yields

$$\begin{cases} 2a' + (C + K_d)a + 2Kabf \sin(\eta) = 0 \\ 2b' + (C - K_d)b + Ka^2f \sin(\eta) = 0 \\ -2a\varphi' + K[(a^2 + 2b^2 + 2f^2)a + 2abf \cos(\eta)] = 0 \\ 2b\phi' + K[(b^2 + 2a^2 + 2f^2)b + a^2f \cos(\eta)] = 0, \end{cases} \quad (9-16)$$

where  $\eta = \delta T - 2\varphi + \phi$ . In the steady state,  $a$  and  $b$  do not change with time, and thus  $a' = b' = 0$ .

Then, the first two equations of (9-16) become

$$\begin{cases} (C + K_d)a + 2Kabf \sin(\eta) = 0 \\ (C - K_d)b + Ka^2f \sin(\eta) = 0 \end{cases} \quad (9-17)$$

Therefore,  $a=b=0$  is the trivial solution, and the nonzero solution is

$$b = -\frac{C + K_d}{2Kf \sin(\eta)}, \quad a^2 = \frac{1}{2} \frac{C^2 - K_d^2}{(Kf \sin(\eta))^2} = 2b^2 \frac{C - K_d}{C + K_d}. \quad (9-18)$$

Note that in the steady state,  $\eta$  doesn't change with time either, and hence  $\delta + \phi' = 2\varphi'$ . Thus the last two equations of (9-16) become

$$\begin{cases} \delta + \phi' - K \left( \frac{4C}{C + K_d} b^2 + 2f^2 + 2bf \cos(\eta) \right) = 0 \\ 2\varphi' + K \left( \frac{5C - 4K_d}{C + K_d} b^2 + 2f^2 + 2 \frac{C - K_d}{C + K_d} bf \cos(\eta) \right) = 0 \end{cases} \quad (9-19)$$

The equation of  $\phi'$  can be derived by canceling the terms with  $\cos(\eta)$  in the above equations:

$$\delta + \frac{3C + K_d}{C - K_d} \phi' + K \left( \frac{C + 4K_d}{C + K_d} b^2 + \frac{4K_d}{C - K_d} f^2 \right) = 0. \quad (9-20)$$

Then the phase speed  $\phi'$  and  $\phi''$  are obtained,

$$\phi' = -\frac{C - K_d}{3C + K_d} \delta - \tilde{K} \quad \text{and} \quad \phi'' = \frac{C + K_d}{3C + K_d} \delta - \frac{\tilde{K}}{2}, \quad (9-21)$$

where  $\tilde{K} \equiv K \frac{C - K_d}{3C + K_d} \left( \frac{C + 4K_d}{C + K_d} b^2 + \frac{4K_d}{C - K_d} f^2 \right)$ .

Substituting Equation (9-21) into (9-19) yields

$$\frac{2\delta}{K} = \frac{13C - 4K_d}{C + K_d} b^2 + 6f^2 + \frac{6C + 2K_d}{C + K_d} bf \cos(\eta). \quad (9-22)$$

With the expression of  $b$  (Equation (9-18)), the right-hand side of the above equation is found to be a parabolic function of  $\cot(\eta)$ , which has a minimum value of

$$\left( 6 - \frac{(3C + K_d)^2}{(13C - 4K_d)(C + K_d)} \right) f^2 + \frac{(13C - 4K_d)(C + K_d)}{4K^2 f^2}. \quad (9-23)$$

Thus, only if

$$\frac{\delta}{K} \geq \left( 6 - \frac{(3C + K_d)^2}{(13C - 4K_d)(C + K_d)} \right) f^2 + \frac{(13C - 4K_d)(C + K_d)}{4K^2 f^2} \quad (9-24)$$

can there exist a solution of  $\eta$ , and hence a nonzero solution of  $a$  and  $b$  according to Equation (9-22). Or with  $\omega = 3 + \delta\varepsilon$ , only when  $\omega$  satisfies the following inequalities can the system engage in the subharmonic nonlinear resonance:

$$\begin{cases} \omega - 3 \geq \left( 6 - \frac{(3c + k_d)^2}{(13c - 4k_d)(c + k_d)} \right) f^2 k + \frac{(13c - 4k_d)(c + k_d)}{4kf^2}, & k > 0 \\ \omega - 3 \leq \left( 6 - \frac{(3c + k_d)^2}{(13c - 4k_d)(c + k_d)} \right) f^2 k + \frac{(13c - 4k_d)(c + k_d)}{4kf^2}, & k < 0, \end{cases} \quad (9-25)$$

The rotor response  $r_0$  can then be derived by substituting Equation (9-21) into (9-13):

$$r_0 = a \exp(it + i\phi(t)) + b \exp(-it + i\phi(t)) + f \exp(i\omega t). \quad (9-26)$$

Because

$$\begin{aligned}
 & \exp(it + i\varphi(t)) + \exp(-it + i\phi(t)) \\
 &= [\cos(t + \varphi(t)) + \cos(t - \phi(t))] + i[\sin(t + \varphi(t)) - \sin(t - \phi(t))] \\
 &= 2\cos\left(t + \frac{\varphi - \phi}{2}\right)\cos\left(\frac{\varphi + \phi}{2}\right) + 2i\cos\left(t + \frac{\varphi - \phi}{2}\right)\sin\left(\frac{\varphi + \phi}{2}\right) \\
 &= 2\exp\left(-i\frac{\varphi + \phi}{2}\right)\cos\left(t + \frac{\varphi - \phi}{2}\right),
 \end{aligned}$$

Equation (9-26) can be rewritten as

$$\begin{aligned}
 r_0 = \exp\left(i\frac{\varphi + \phi}{2}\right) & \left[ f \exp\left(i\omega t - i\frac{\varphi + \phi}{2}\right) \right. \\
 & \left. + \left( (a + b)\cos\left(t + \frac{\varphi - \phi}{2}\right) + i(a - b)\sin\left(t + \frac{\varphi - \phi}{2}\right) \right) \right]. \quad (9-27)
 \end{aligned}$$

Furthermore, since  $\eta = \delta T - 2\varphi + \phi$ , the following equations can be obtained:

$$(\omega - 3)t - 2\varphi + \phi = \eta, \text{ and } 3\left(t + \frac{\varphi - \phi}{2}\right) + \eta = \omega t - \frac{\varphi + \phi}{2}. \quad (9-28)$$

Therefore, according to Equation (9-27),  $r_0$  becomes

$$\begin{aligned}
 r_0 = \exp\left(i\frac{\varphi + \phi}{2}\right) & \left[ f \exp\left(3i\left(t + \frac{\varphi - \phi}{2}\right) + i\eta\right) \right. \\
 & \left. + \left( (a + b)\cos\left(t + \frac{\varphi - \phi}{2}\right) + i(a - b)\sin\left(t + \frac{\varphi - \phi}{2}\right) \right) \right]. \quad (9-29)
 \end{aligned}$$

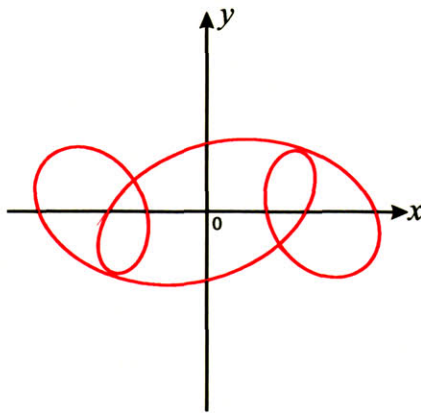


**Figure 9-2: Third-order subharmonic resonance with fixed orbit (sketch).**

The terms in the square brackets describe a third-order subharmonic motion with a fixed orbit as depicted in Figure 9-2.

Moreover, there is another phase factor outside the square brackets,  $\exp(-i(\phi+\varphi)/2)$ , and according to Equation (9-21) one can find

$$\frac{\phi+\varphi}{2} = \Omega_o t + \frac{\phi_0 + \varphi_0}{2}, \quad (9-30)$$

where  $\Omega_o \equiv \frac{k_d}{3c+k_d}(\omega-3) + k \frac{c-k_d}{3c+k_d} \left( \frac{c+4k_d}{2c+2k_d} b^2 + \frac{2k_d}{c-k_d} f^2 \right) \sim O(\varepsilon)$ .

Thus, with this phase factor, the orbit described in the square brackets is rotating with a speed of  $\Omega_o$ , which is slow (of order  $\varepsilon$ ), as sketched in Figure 9-3.

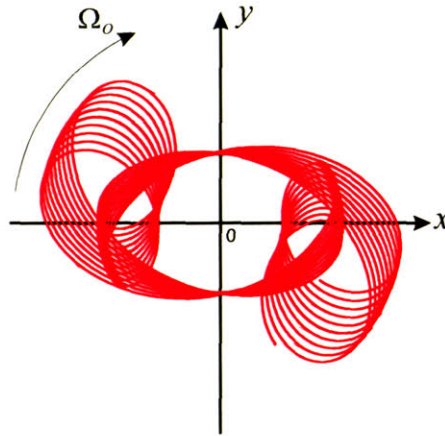


**Figure 9-3: Rotating third-order subharmonic orbit (sketch).**

Therefore, at a rotational speed near three times the natural frequency so that the condition of Equation (9-25) can be satisfied, the rotor engages in a combination of four different motions: spinning at  $\omega$ , precessing at  $\omega$  with the amplitude of the rotor unbalance, subharmonic resonance at about the system natural frequency with the amplitude given by Equation (9-18), and rotation of the orbits at a much lower frequency  $\Omega_o$ .

The above analyses can be verified by numerical simulations (ODE solvers in Matlab). The plots in Figure 9-4 are the simulated results for the system with  $k=0.08$ ,  $c=0.06$ ,  $k_d=0.02$ , and initial conditions of  $x=1.5$ ,  $y=0$ ,  $v_x=-1$ ,  $v_y=1$ , at different rotational speeds.

Therefore, when the nonlinear subharmonic resonance happens, it has a larger amplitude: the amplitude changes from 1 without the subharmonic resonance (left plot) to about 3 with the resonance. The simulations also show that the orbit of the subharmonic third-order resonance in the isotropic journal-bearing system is rotating at a much lower speed, which is of order  $\varepsilon$ .

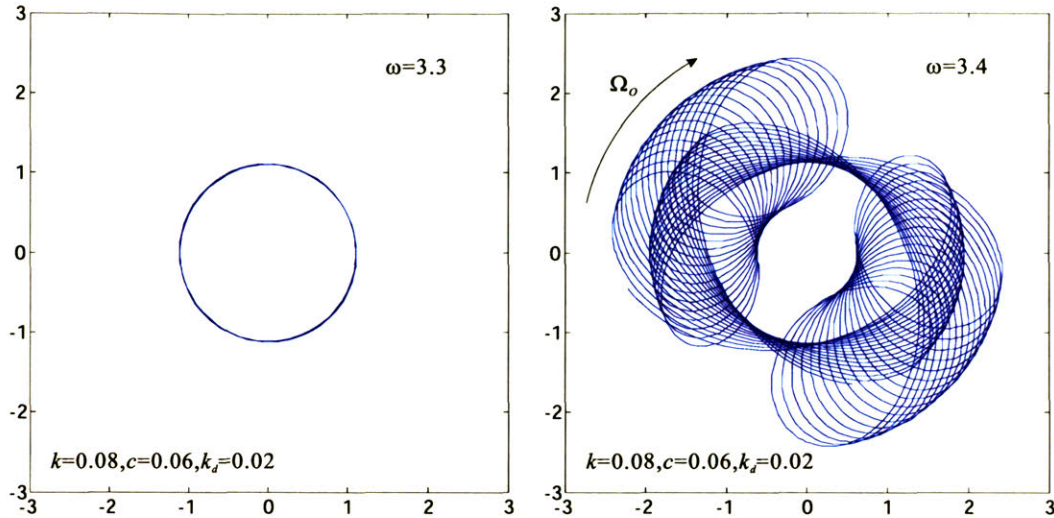


**Figure 9-4: Numerically simulated orbits for the nonlinear isotropic system (Equation (9-10)) at different rotational speeds:  $\omega=3.3$  (left) and  $\omega=3.4$  (right).**

At the same time, with the values of  $k$ ,  $c$  and  $k_d$ , the minimum rotating speed  $\omega$  to excite the subharmonic resonance can be calculated according to Equation (9-25), and it turns out to be 3.34. Thus, the system should not undergo the subharmonic resonance at the rotational speed  $\omega$  below 3.34, while it should at  $\omega$  higher than 3.34. This is validated by the simulation results in Figure 9-4.

### 9.3 Nonlinear Resonance in Anisotropic Systems

Then, by the following analysis, due to the presence of the two natural frequencies, one can find that the nonlinear resonances in the anisotropic system can be much more complicated than in the isotropic system. The secondary resonances can happen not only at speeds of 3 times the natural frequencies, but also at other combinations of the two natural frequencies in the anisotropic system.

Similar to the isotropic case, the rotordynamic Equations (2-34) can be written in terms of stiffness, damping, and nonlinearity of hydrostatic forces (Equation (9-7)):

$$\begin{cases} m\ddot{X} = K_{xx}X + k_1X^3 + k_2XY^2 + k_{xy}Y + c_x\dot{X} + m\omega^2 \cos(\omega t) \\ m\ddot{Y} = K_{yy}Y + k_3Y^3 + k_4YX^2 + k_{yx}X + c_y\dot{Y} + m\omega^2 \sin(\omega t) \end{cases} \quad (9-31)$$

The above equations have been normalized by the rotor unbalance. Again, because the nonlinear terms ( $k_1$ ,  $k_2$ ,  $k_3$ ,  $k_4$ ), the hydrodynamic terms ( $k_{xy}$ ,  $k_{yx}$ ), and the damping terms ( $c_x$ ,  $c_y$ ) are small compared to the linear terms of the hydrostatic force ( $K_{xx}$ ,  $K_{yy}$ ), the above equation can be expressed as follows:



$$\begin{cases} \ddot{X} + \Omega_x^2 X = \omega^2 \cos(\omega t) + \varepsilon (K_1 X^3 + K_2 XY^2 + K_{xy} Y + C_x \dot{X}) \\ \ddot{Y} + \Omega_y^2 Y = \omega^2 \sin(\omega t) + \varepsilon (K_3 Y^3 + K_4 YX^2 + K_{yx} X + C_y \dot{Y}) \end{cases} \quad (9-32)$$

where  $\Omega_x = \sqrt{-K_{xx}/m}$  and  $\Omega_y = \sqrt{-K_{yy}/m}$  are the natural frequencies in  $x$  and  $y$  directions respectively,  $K_1=k_1/m\varepsilon$ ,  $K_2=k_2/m\varepsilon$ ,  $K_3=k_3/m\varepsilon$ ,  $K_4=k_4/m\varepsilon$ ,  $C_x=c_x/m\varepsilon$ ,  $C_y=c_y/m\varepsilon$ , and  $\varepsilon$  is a constant of the order  $k_1/K_{xx}$ .

Again, with the multi-scale method, the solution to Equation (9-32) is assumed to be

$$\begin{cases} X = X_0(t, T) + \varepsilon X_1(t, T) + \varepsilon^2 X_2(t, T) + \dots \\ Y = Y_0(t, T) + \varepsilon Y_1(t, T) + \varepsilon^2 Y_2(t, T) + \dots \end{cases} \quad (9-33)$$

Substituting Equation (9-33) into (9-32) and collecting the terms according to the orders of  $\varepsilon$ , noting that  $d^2/dt^2 = \partial^2/\partial t^2 + 2\varepsilon \partial^2/\partial t \partial T + \varepsilon^2 \partial^2/\partial T^2$ , yields

$$\begin{cases} \left( \frac{\partial^2}{\partial t^2} + \Omega_x^2 \right) X_0 = \omega^2 \cos(\omega t) \\ \left( \frac{\partial^2}{\partial t^2} + \Omega_y^2 \right) Y_0 = \omega^2 \sin(\omega t) \end{cases} \quad (9-34)$$

These are for the 0<sup>th</sup> order of  $\varepsilon$ , and the equations of the order  $\varepsilon^1$  are

$$\begin{cases} \left( \frac{\partial^2}{\partial t^2} + \Omega_x^2 \right) X_1 = K_1 X_0^3 + K_2 X_0 Y_0^2 + K_{xy} Y_0 + C_x \frac{\partial}{\partial t} X_0 - 2 \frac{\partial^2}{\partial t \partial T} X_0 \\ \left( \frac{\partial^2}{\partial t^2} + \Omega_y^2 \right) Y_1 = K_3 Y_0^3 + K_4 Y_0 X_0^2 + K_{yx} X_0 + C_y \frac{\partial}{\partial t} Y_0 - 2 \frac{\partial^2}{\partial t \partial T} Y_0 \end{cases} \quad (9-35)$$

The general solution of  $X_0$  and  $Y_0$  to Equation (9-34) is

$$\begin{cases} X_0 = A(T) \exp(i\Omega_x t) + F \exp(i\omega t) + c.c. \\ Y_0 = B(T) \exp(i\Omega_y t) + G \exp(i\omega t) + c.c. \end{cases} \quad (9-36)$$

where  $A(T)$  and  $B(T)$  are complex functions of  $T$ , “*c.c.*” means complex conjugate terms of the terms before it,  $F=f$ , and  $G=-ig$ , with  $f$  and  $g$ :

$$f \equiv \frac{1}{2} \frac{\omega^2}{\Omega_x^2 - \omega^2}, \quad g \equiv \frac{1}{2} \frac{\omega^2}{\Omega_y^2 - \omega^2}. \quad (9-37)$$

Substituting  $X_0$  and  $Y_0$  into Equation (9-35) yields the equations of  $X_1$  and  $Y_1$ :



$$\begin{aligned}
\left(\frac{\partial^2}{\partial t^2} + \Omega_x^2\right) X_1 = & \\
& \left(3K_1(A^*A + 2F^*F)A + 2K_2(B^*B + G^*G)A + iC_x\Omega_x A - 2i\Omega_x A'\right)\exp(i\Omega_x t) \\
& + (3K_1 A^2 F)\exp(i(2\Omega_x + \omega)t) + (3K_1 A^2 F^*)\exp(i(2\Omega_x - \omega)t) \\
& + (3K_1 F^2 + K_2 G^2)A\exp(i(\Omega_x + 2\omega)t) + (3K_1 F^{*2} + K_2 G^{*2})A\exp(i(\Omega_x - 2\omega)t) \\
& + K_2 B^2 F\exp(i(2\Omega_y + \omega)t) + K_2 B^2 F^*\exp(i(2\Omega_y - \omega)t) \\
& + 2K_2 BFG\exp(i(\Omega_y + 2\omega)t) + 2K_2 BF^*G^*\exp(i(\Omega_y - 2\omega)t) \\
& + 2K_2 ABG\exp(i(\Omega_x + \Omega_y + \omega)t) + 2K_2 ABG^*\exp(i(\Omega_x + \Omega_y - \omega)t) \\
& + 2K_2 AB^*G\exp(i(\Omega_x - \Omega_y + \omega)t) + 2K_2 AB^*G^*\exp(i(\Omega_x - \Omega_y - \omega)t) \\
& + K_1 A^3\exp(i3\Omega_x t) + K_2 AB^2\exp(i(\Omega_x + 2\Omega_y)t) + K_2 AB^{*2}\exp(i(\Omega_x - 2\Omega_y)t) \\
& + \left(K_{xy}G + iC_x\omega F + 3K_1(F^*F + 2A^*A)F + K_2(2B^*BF + 2FG^*G + F^*GG)\right)\exp(i\omega t) \\
& + K_{xy}B(T)\exp(i\Omega_y t) + (K_1 F^2 + K_2 G^2)F\exp(i3\omega t) + c.c.
\end{aligned}$$

and

$$\begin{aligned}
\left(\frac{\partial^2}{\partial t^2} + \Omega_y^2\right) Y_1 = & \\
& \left(3K_3(B^*B + 2G^*G)B + 2K_4(A^*A + F^*F)B + iC_y\Omega_y B - 2i\Omega_y B'\right)\exp(i\Omega_y t) \\
& + 3K_3 B^2 G\exp(i(2\Omega_y + \omega)t) + 3K_3 B^2 G^*\exp(i(2\Omega_y - \omega)t) \\
& + (3K_3 G^2 + K_4 F^2)B\exp(i(\Omega_y + 2\omega)t) + (3K_3 G^{*2} + K_4 F^{*2})B\exp(i(\Omega_y - 2\omega)t) \\
& + K_4 A^2 G\exp(i(2\Omega_x + \omega)t) + K_4 A^2 G^*\exp(i(2\Omega_x - \omega)t) \\
& + 2K_4 AFG\exp(i(\Omega_x + 2\omega)t) + 2K_4 AF^*G^*\exp(i(\Omega_x - 2\omega)t) \\
& + 2K_4 ABF\exp(i(\Omega_x + \Omega_y + \omega)t) + 2K_4 ABF^*\exp(i(\Omega_x + \Omega_y - \omega)t) \\
& + 2K_4 AB^*F\exp(i(\Omega_x - \Omega_y + \omega)t) + 2K_4 AB^*F^*\exp(i(\Omega_x - \Omega_y - \omega)t) \\
& + K_3 B^3\exp(i3\Omega_y t) + K_4 A^2 B\exp(i(2\Omega_x + \Omega_y)t) + K_4 A^2 B^*\exp(i(2\Omega_x - \Omega_y)t) \\
& + \left(3K_3(2B^*B + G^*G)G + K_4(2A^*AG + 2F^*FG + F^2G^*) + K_{yx}F + iC_y\omega G\right)\exp(i\omega t) \\
& + K_{yx}A(T)\exp(i\Omega_x t) + (K_3 G^2 + K_4 F^2)G\exp(i3\omega t) + c.c.
\end{aligned}$$

Based on the results above, the ordinary secular terms (with the frequency of corresponding natural frequencies) in Equations (9-35) are found to be

$$\begin{cases} \left(3K_1(A^*A + 2F^*F)A + 2K_2(B^*B + G^*G)A + iC_x\Omega_x A - 2i\Omega_x A'\right)e^{i\Omega_x t} + c.c. \\ \left(3K_3(B^*B + 2G^*G)B + 2K_4(A^*A + F^*F)B + iC_y\Omega_y B - 2i\Omega_y B'\right)e^{i\Omega_y t} + c.c. \end{cases} \quad (9-38)$$

It is useful to rewrite  $A$  and  $B$  as

$$A(T) = a(T)e^{i\varphi(T)}, \quad B(T) = b(T)e^{i\phi(T)}, \quad (9-39)$$

where  $a(T)$ ,  $b(T)$ ,  $\varphi(T)$ , and  $\phi(T)$  are all real. The ordinary secular terms can then be re-written in terms of  $a$ ,  $b$ ,  $\varphi$ , and  $\phi$ :

$$\begin{cases} \left[\left(3K_1(a^2 + 2f^2) + 2K_2(b^2 + g^2) + 2\Omega_x(\theta' + iC_x)\right)a - 2i\Omega_x a'\right]e^{i\Omega_x t + i\varphi} + c.c. \\ \left[\left(3K_3(b^2 + 2g^2) + 2K_4(a^2 + f^2) + 2\Omega_y(\phi' + iC_y)\right)b - 2i\Omega_y b'\right]e^{i\Omega_y t + i\phi} + c.c. \end{cases} \quad (9-40)$$

Furthermore, in the steady state,  $a' = 0$ ,  $b' = 0$ , and the above equations reduce to

$$\begin{cases} \left[\left(3K_1(a^2 + 2f^2) + 2K_2(b^2 + g^2) + 2\Omega_x(\theta' + iC_x)\right)ae^{i\Omega_x t + i\varphi} + c.c. \right. \\ \left. \left[\left(3K_3(b^2 + 2g^2) + 2K_4(a^2 + f^2) + 2\Omega_y(\phi' + iC_y)\right)be^{i\Omega_y t + i\phi} + c.c. \right] \end{cases} \quad (9-41)$$

In addition to these ordinary secular terms, there are additional secular terms whenever the rotational speed  $\omega$  is one of the following:

1.  $\omega \cong \Omega_x/3$ ,  $\omega \cong \Omega_y/3$
2.  $\omega \cong (\Omega_x \pm \Omega_y)/2$  (assuming  $\Omega_x > \Omega_y$ )
3.  $\omega \cong 3\Omega_x$ ,  $\omega \cong 3\Omega_y$
4.  $\omega \cong 2\Omega_x \pm \Omega_y$ ,  $\omega \cong 2\Omega_y \pm \Omega_x$  (if  $2\Omega_y > \Omega_x$ )

Therefore, the secondary (nonlinear) resonances may occur at these speeds. Before continuing to the nonlinear resonances, the response of the rotor at speeds far away from these secondary resonances is calculated as follows:

Since there are no additional secular terms under this condition, the ordinary secular terms given in Equation (9-41) should vanish; otherwise,  $X_1$  and  $Y_1$  will increase with time and the assumption that they are small (of order  $\varepsilon$ ) becomes invalid. Therefore, one can find the following equations for  $a$  and  $b$ :

$$\begin{cases} \left[\left(3K_1(a^2 + 2f^2) + 2K_2(b^2 + g^2) + 2\Omega_x(\theta' + iC_x)\right)ae^{i\varphi} = 0 \right. \\ \left. \left[\left(3K_3(b^2 + 2g^2) + 2K_4(a^2 + f^2) + 2\Omega_y(\phi' + iC_y)\right)be^{i\phi} = 0 \right] \end{cases} \quad (9-42)$$

According to the above equations,  $a$  and  $b$  have to be zero, because the damping coefficients  $C_x$  and  $C_y$  are not zero. This means that besides spinning, the rotor only engages in precessing motion, according to Equation (9-36). In other words, when the rotational speed is not near the secondary resonances stated above, there is no nonlinear resonance in the system.

### 9.3.1 Secondary Resonance near $\Omega_x/3$ or $\Omega_y/3$

When the rotational speed is around one third of the natural frequency in  $x$  direction,  $3\omega = \Omega_x + \varepsilon\delta$ , there are two additional secular terms on the right-hand side of the first equation of (9-35), with the frequency of  $3\omega$ :

$$(K_1 F^2 + K_2 G^2) F \exp(i3\omega t) = (K_1 f^2 - K_2 g^2) f \exp(i\Omega_x t + i\delta T), \quad (9-43)$$

where  $T = \varepsilon t$  is the large time scale as defined above. Since all the secular terms should vanish as analyzed above, the following equations can be derived:

$$\begin{cases} \left[ 3K_1(a^2 + 2f^2) + 2K_2(b^2 + g^2) + 2\Omega_x(\theta' + iC_x) \right] a e^{i\phi} + (K_1 f^2 - K_2 g^2) f e^{i\delta T} = 0 \\ \left[ 3K_3(b^2 + 2g^2) + 2K_4(a^2 + f^2) + 2\Omega_y(\phi' + iC_y) \right] b e^{i\phi} = 0 \end{cases} \quad (9-44)$$

Judging from the second equation,  $b=0$ . Then the first one becomes

$$\left( 3K_1(a^2 + 2f^2) + 2K_2 g^2 + 2\Omega_x \theta' + iC_x \Omega_x \right) a = (K_1 f^2 - K_2 g^2) f e^{i\delta T - i\phi(T)}. \quad (9-45)$$

Since  $a$  does not change with time in the steady state, the phase on the right-hand side should not change with time either:

$$\eta \equiv \delta T - \phi(T) = \text{const}. \quad (9-46)$$

Then,  $\phi' = \delta$  or  $\phi = \delta T - \eta$ . The norm squared of (9-45) is

$$\left[ \left( 3K_1 a^2 + 6K_1 f^2 + 2K_2 g^2 + 2\Omega_x \delta \right)^2 + \left( C_x \Omega_x \right)^2 \right] a^2 = \left( K_1 f^2 - K_2 g^2 \right)^2 f^2. \quad (9-47)$$

It is a third-order polynomial equation of  $a^2$ . Furthermore, any third-order polynomial equation of the form  $x^3 + c_1 x^2 + c_2 x + c_3 = 0$  has three roots:  $x_1$ ,  $x_2$  and  $x_3$ , with  $x_1 x_2 x_3 = -c_3$ . So for the equation above, the product of the 3 roots of  $a^2$  should be

$$a_1^2 \cdot a_2^2 \cdot a_3^2 = \left( \frac{f^2}{3} - \frac{K_2}{3K_1} g^2 \right)^2 f^2 \geq 0. \quad (9-48)$$

Then, there must be a real positive root for  $a^2$ , and hence a real  $a$ , as long as the equation above is not zero. Therefore, the super-harmonic resonance around  $\Omega_x/3$  does exist, with the amplitude determined by Equation (9-47). According to Equations (9-36), the responses in  $X$  and  $Y$  directions are, with the orbit sketched in Figure 9-5,

$$\begin{cases} X_0 = 2a \cos(\Omega_x t + \varphi(T)) + 2f \cos(\omega t) = 2a \cos(3\omega t - \eta) + 2f \cos(\omega t) \\ Y_0 = 2g \sin(\omega t) \end{cases} \quad (9-49)$$

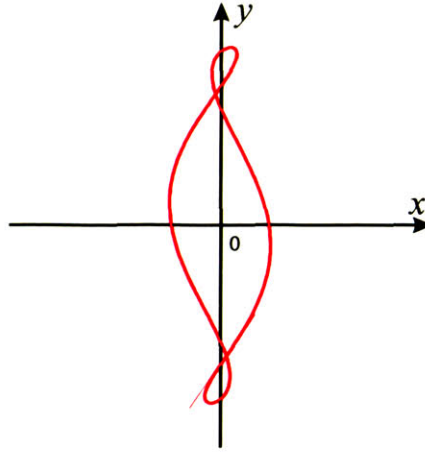


**Figure 9-5: Third-order superharmonic resonance in x direction (sketch).**

Following the same procedure, when the rotational speed is near one third of natural frequency in  $y$  direction,  $3\omega = \Omega_y + \varepsilon\delta$ , one can find that  $a=0$  and  $b$  is determined by the equation below.

$$\begin{aligned} (b^2)^3 + \left(4g^2 + \frac{4K_4}{3K_3}f^2 + \frac{4\delta}{3K_3}\Omega_y\right)(b^2)^2 \\ + \left[\left(2g^2 + \frac{2K_4}{3K_3}f^2 + \frac{2\delta}{3K_3}\Omega_y\right)^2 + \frac{C_y^2}{9K_3^2}\Omega_y^2\right]b^2 = \left(\frac{g^2}{3} - \frac{K_4}{3K_3}f^2\right)^2 g^2 \end{aligned} \quad (9-50)$$

Similarly, since

$$b_1^2 \cdot b_2^2 \cdot b_3^2 = \left(\frac{g^2}{3} - \frac{K_4}{3K_3}f^2\right)^2 g^2 \geq 0, \quad (9-51)$$

there must be a real positive root for  $b^2$ , and hence a real  $b$ , as long as the equation above is not zero. Thus the super-harmonic resonance around  $\Omega_y/3$  also exists, with the amplitude determined by Equation (9-50). The responses in  $X$  and  $Y$  directions are, with the orbit sketched in Figure 9-6,

$$\begin{cases} X_0 = 2f \cos(\omega t) \\ Y_0 = 2b \cos(3\omega t - \eta) + 2g \sin(\omega t) \end{cases} \quad (9-52)$$

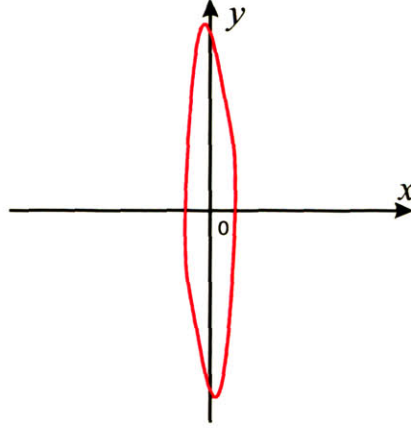


Figure 9-6: Third-order superharmonic resonance in y direction (sketch).

### 9.3.2 Secondary Resonance near $(\Omega_x - \Omega_y)/2$

When the rotational speed is near half of the difference between the two natural frequencies in  $x$  and  $y$  directions, it can be written as  $2\omega = \Omega_x - \Omega_y + \varepsilon\delta$ . Then the additional secular term on the right-hand side of the first equation of (9-35) ( $x$  component) is, with the frequency of  $\Omega_y + 2\omega$ ,

$$2K_2 BFG \exp(i(\Omega_y + 2\omega)t) = 2K_2 BFG \exp(i(\Omega_x t + \delta T)), \quad (9-53)$$

and the new secular term on the right-hand side of the second equation of (9-35) ( $y$  component) is, with the frequency of  $\Omega_x - 2\omega$ ,

$$2K_4 AF^* G^* \exp(i(\Omega_x - 2\omega)t) = 2K_4 AF^* G^* \exp(i(\Omega_y t - \delta T)). \quad (9-54)$$

By eliminating all the secular terms, one can obtain the following equations:

$$\begin{cases} \left( (3K_1(a^2 + 2f^2) + 2K_2(b^2 + g^2) + 2\Omega_x \phi' + iC_x \Omega_x) A + 2K_2 BFG e^{i\delta T} \right) = 0 \\ \left( (3K_3(b^2 + 2g^2) + 2K_4(a^2 + f^2) + 2\Omega_y \phi' + iC_y \Omega_y) B + 2K_4 AF^* G^* e^{-i\delta T} \right) = 0 \end{cases} \quad (9-55)$$

With the first equation multiplied by  $A^*$  and the second multiplied by  $B^*$ , the above equations become

$$\begin{cases} \left( (3K_1(a^2 + 2f^2) + 2K_2(b^2 + g^2) + 2\Omega_x \phi' + iC_x \Omega_x) a^2 - 2K_2 A^* BFG e^{i\delta T} \right) = 0 \\ \left( (3K_3(b^2 + 2g^2) + 2K_4(a^2 + f^2) + 2\Omega_y \phi' + iC_y \Omega_y) b^2 - 2K_4 AB^* F^* G^* e^{-i\delta T} \right) = 0 \end{cases} \quad (9-56)$$

According to Equation (9-7),  $K_2=K_4$ . Then, the complex conjugate of the second equation equals the first one in the above equations:

$$\begin{aligned} & \left(3K_1a^2 + 6K_1f^2 + 2K_2b^2 + 2K_2g^2 + 2\Omega_x\phi' + iC_x\Omega_x\right)a^2 \\ & = \left(3K_3b^2 + 6K_3g^2 + 2K_4a^2 + 2K_4f^2 + 2\Omega_y\phi' - iC_y\Omega_y\right)b^2. \end{aligned} \quad (9-57)$$

Thus, the following equations can be obtained from the imaginary parts of the above equation:

$$a^2C_x\Omega_x = -b^2C_y\Omega_y. \quad (9-58)$$

Because  $C_x\Omega_x$  and  $C_y\Omega_y$  are of the same signs,  $a^2$  and  $b^2$  can only be zeros. So there is no nonlinear resonance near  $(\Omega_x - \Omega_y)/2$ .

### 9.3.3 Secondary Resonance near $(\Omega_x + \Omega_y)/2$

When the rotational speed is near the average of the two natural frequencies in  $x$  and  $y$  directions, it can be written as  $2\omega = \Omega_x + \Omega_y + \varepsilon\delta$ . Then the additional secular term on the right-hand side of the first equation of (9-35) ( $x$  component) is, with the frequency of  $2\omega - \Omega_y$ ,

$$2K_2B^*FG \exp\left(i(-\Omega_y + 2\omega)t\right) = -2iK_2bfg \exp\left(i(\Omega_x t + \delta T - \phi)\right), \quad (9-59)$$

and the additional secular term on the right-hand side of the second equation of (9-35) ( $y$  component) is, with the frequency of  $2\omega - \Omega_x$ ,

$$2K_4A^*FG \exp\left(i(-\Omega_x + 2\omega)t\right) = -2iK_4afg \exp\left(i(\Omega_y t + \delta T - \phi)\right). \quad (9-60)$$

By eliminating all the secular terms together with the ordinary ones in (9-41), one can derive the following equations:

$$\begin{cases} \left(3K_1(a^2 + 2f^2) + 2K_2(b^2 + g^2) + 2\Omega_x\phi' + iC_x\Omega_x\right)a = 2iK_2bfg e^{i(\delta T - \phi)} \\ \left(3K_3(b^2 + 2g^2) + 2K_4(a^2 + f^2) + 2\Omega_y\phi' + iC_y\Omega_y\right)b = 2iK_4afg e^{i(\delta T - \phi)} \end{cases} \quad (9-61)$$

There is a trivial solution  $a=b=0$  to the above equations, and the following analysis shows that there are also nonzero real solutions of  $a$  and  $b$  under certain conditions.

In the steady state,  $a$  and  $b$  do not change with time. Therefore, the phase on the right-hand side of Equation (9-61) should not change with time either:

$$\eta \equiv \delta T - \phi(T) - \phi(T) = \text{const.} \quad (9-62)$$



Thus,  $\phi' + \phi' = \delta$  or  $\phi + \phi = \delta T - \eta$ . Then the first equation of (9-61) divided by  $a$  and multiplied by  $\Omega_y$ , plus the second divided by  $b$  and multiplied by  $\Omega_x$  becomes

$$\begin{aligned} & \left(3K_1(a^2 + 2f^2) + 2K_2(b^2 + g^2)\right)\Omega_y + \left(3K_3(b^2 + 2g^2) + 2K_4(a^2 + f^2)\right)\Omega_x \\ & + 2\Omega_x\Omega_y\delta + i(C_x + C_y)\Omega_x\Omega_y = 2i\left(\frac{b}{a}\Omega_x + \frac{a}{b}\Omega_y\right)K_2fge^{i(\eta)} \end{aligned} \quad (9-63)$$

Meanwhile, since the first equation of (9-61) multiplied by  $a$  equals the second one multiplied by  $b$ , the following equation can be derived from the imaginary parts:

$$a^2C_x\Omega_x = b^2C_y\Omega_y. \quad (9-64)$$

Substituting the above equation into Equation (9-63) yields

$$\begin{aligned} & i(C_x + C_y) + \left(3K_1\left(\frac{C_y\Omega_y}{C_x\Omega_x}b^2 + 2f^2\right) + 2K_2(b^2 + g^2)\right)\frac{1}{\Omega_x} + 2\delta \\ & + \left(3K_3(b^2 + 2g^2) + 2K_4\left(\frac{C_y\Omega_y}{C_x\Omega_x}b^2 + f^2\right)\right)\frac{1}{\Omega_y} = 2i\frac{(C_x + C_y)}{\sqrt{C_xC_y\Omega_x\Omega_y}}K_2fge^{i(\eta)}, \end{aligned} \quad (9-65)$$

with the norm squared of

$$\begin{aligned} & (C_x + C_y)^2 + \left[\left(3K_1\left(\frac{C_y\Omega_y}{C_x\Omega_x}b^2 + 2f^2\right) + 2K_2(b^2 + g^2)\right)\frac{1}{\Omega_x} + 2\delta\right. \\ & \left. + \left(3K_3(b^2 + 2g^2) + 2K_4\left(\frac{C_y\Omega_y}{C_x\Omega_x}b^2 + f^2\right)\right)\frac{1}{\Omega_y}\right]^2 = 4\frac{(C_x + C_y)^2}{C_xC_y\Omega_x\Omega_y}K_2^2f^2g^2 \end{aligned} \quad (9-66)$$

Therefore, with  $K_1=k_1/m\varepsilon$ ,  $K_2=k_2/m\varepsilon$ ,  $K_3=k_3/m\varepsilon$ ,  $K_4=k_4/m\varepsilon$ ,  $C_x=c_x/m\varepsilon$ ,  $C_y=c_y/m\varepsilon$ , and  $\delta=(\Omega_x + \Omega_y - 2\omega)/\varepsilon$ , the following equation of  $b^2$  can be derived from the above equation:

$$\begin{aligned} & \left[\frac{1}{\Omega_x}\left(3\frac{c_y\Omega_y}{c_x\Omega_x} + \frac{2k_2}{k_1}\right) + \frac{1}{\Omega_y}\left(\frac{2k_2}{k_1}\frac{c_y\Omega_y}{c_x\Omega_x} + \frac{3k_3}{k_1}\right)\right]b^2 \\ & = \left|\frac{c_x + c_y}{k_1}\right| \sqrt{\frac{4k_2^2f^2g^2}{c_xc_y\Omega_x\Omega_y} - 1} - \left(\frac{6}{\Omega_x} + \frac{2k_2}{\Omega_yk_1}\right)f^2 - \left(\frac{2k_2}{\Omega_xk_1} + \frac{6k_3}{\Omega_yk_1}\right)g^2 - \frac{4\omega - 2(\Omega_x + \Omega_y)}{k_1} \end{aligned} \quad (9-67)$$

Because  $k_1$ ,  $k_2$ , and  $k_3$  are all of the same sign according to Section 9.1, the coefficient of  $b^2$  is positive. Then, to have a real root of  $b$ , the right-hand side of the above equation must be real and positive:

$$\begin{cases} \frac{4k_2^2 f^2 g^2}{c_x c_y \Omega_x \Omega_y} > 1 \\ \frac{2(\Omega_x + \Omega_y) - 4\omega}{k_1} > \left( \frac{6}{\Omega_x} + \frac{2k_2}{\Omega_y k_1} \right) f^2 + \left( \frac{2k_2}{\Omega_x k_1} + \frac{6k_3}{\Omega_y k_1} \right) g^2 - \left| \frac{c_x + c_y}{k_1} \right| \sqrt{\frac{4k_2^2 f^2 g^2}{c_x c_y \Omega_x \Omega_y} - 1} \end{cases} \quad (9-68)$$

Only when the above inequalities are satisfied can there exist a real positive solution of  $b^2$ , and hence a nonzero real  $b$ . Then, the responses in  $x$  and  $y$  directions are

$$\begin{cases} X_0 = 2a \cos(\Omega_x t + \varphi) + 2f \cos(\omega t) \\ Y_0 = 2b \cos(\Omega_y t + \phi) + 2g \sin(\omega t) \end{cases} \quad (9-69)$$

To verify the above analyses and plot the resonance orbits, a numerical simulation (ODE solver in Matlab) was employed. In the simulation, the system has the two natural frequencies  $\Omega_x=1.9\text{rad/s}$  and  $\Omega_y=1\text{rad/s}$ , with damping coefficients and hydrodynamic stiffness  $c_x=c_y=-0.02$  and  $k_d=-0.01$ , and the following nonlinearity coefficient  $ks$ :  $k_1=k_2=k_3=k_4=-0.04$ . Then, according to Equations (9-68), there are secondary resonances ( $a$  and  $b$  are nonzero) only at the rotational speeds  $\omega$  between  $1.53\text{rad/s}$  and  $1.72\text{rad/s}$ . The system was simulated at speeds of  $\omega=1.5\text{rad/s}$ ,  $\omega=1.6\text{rad/s}$  and  $\omega=1.8\text{rad/s}$ , with the orbits plotted in Figure 9-7.

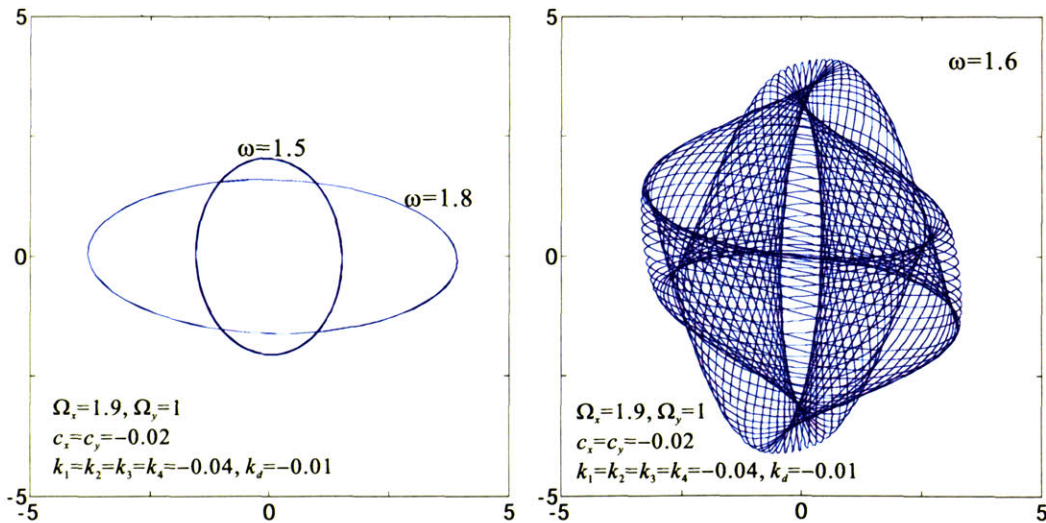


**Figure 9-7: Simulated orbits for the anisotropic system at the rotor speed near the secondary resonance  $(\Omega_x+\Omega_y)/2$ :  $\omega=1.5$  and  $1.8$  (left),  $\omega=1.6$  (right).**

It can be seen from the plots that there are no secondary resonances in the system at rotor speeds outside the range predicted by Equation (9-68) (left plots of Figure 9-7), but there are such resonances in the system at speeds within the range (the right plot). Thus,

the analytically derived conditions under which the secondary resonance  $(\Omega_x + \Omega_y)/2$  can occur are verified by the numerical simulations. Furthermore, it is important to note that the amplitude of the orbit is larger with the nonlinear resonance than without it. Thus, operation close to this nonlinear resonance should be avoided, or the rotor may crash into the bearing wall.

### 9.3.4 Secondary Resonance near $3\Omega_x$ or $3\Omega_y$

When the rotational speed is around three times the natural frequency in  $x$  direction, it can be written as  $\omega = 3\Omega_x + \varepsilon\delta$ . Then there is an additional secular term on the right-hand side of the first equation ( $x$  component) of (9-35), with the frequency of  $\omega - 2\Omega_x$ :

$$3K_1 A^* F \exp(i(\omega - 2\Omega_x)t) = 3K_1 a^2 f \exp(i\Omega_x t + i\delta T - 2i\varphi), \quad (9-70)$$

and there is no additional secular term in the  $y$  component of equation (9-35). Thus, by eliminating all the secular terms, one can obtain

$$\begin{cases} \left(3K_1(a^2 + 2f^2) + 2K_2(b^2 + g^2) + 2\Omega_x\varphi' + iC_x\Omega_x\right)ae^{i\varphi} + 3K_1a^2fe^{i\delta T - 2i\varphi} = 0 \\ \left(3K_3(b^2 + 2g^2) + 2K_4(a^2 + f^2) + 2\Omega_y\varphi' + iC_y\Omega_y\right)be^{i\phi} = 0 \end{cases} \quad (9-71)$$

Again, judging from the second equation,  $b$  should be zero. Then the first equation becomes

$$\left(3K_1(a^2 + 2f^2) + 2K_2g^2 + 2\Omega_x\varphi' + iC_x\Omega_x\right)a + 3K_1a^2fe^{i\delta T - 3i\varphi} = 0. \quad (9-72)$$

With the trivial solution  $a=0$ , nonzero  $a$  also exists under certain conditions based on the following analysis.

In the steady state,  $a$  does not change with time. As a result, the phase  $\eta = \delta T - 3\varphi$  is also constant. Therefore,

$$\varphi' = \delta/3. \quad (9-73)$$

Equation (9-72) then becomes

$$3K_1(a^2 + 2f^2) + 2K_2g^2 + 2\Omega_x\delta/3 + iC_x\Omega_x = -3K_1afe^{i\eta}. \quad (9-74)$$

The norm squared of the above equation is

$$\left(3K_1a^2 + 6K_1f^2 + 2K_2b^2 + 2K_2g^2 + 2\Omega_x\delta/3\right)^2 + (C_x\Omega_x)^2 = 9K_1^2a^2f^2, \quad (9-75)$$

which is a parabolic equation of  $a^2$ , with the roots of

$$a^2 = \frac{-p \pm \sqrt{p^2 - 4q}}{2}, \quad (9-76)$$

$$\text{where } p \equiv 3f^2 + \frac{4K_2}{3K_1}g^2 + \frac{4\delta}{9K_1}\Omega_x, \quad q \equiv \left(2f^2 + \frac{2K_2}{3K_1}g^2 + \frac{2\delta}{9K_1}\Omega_x\right)^2 + \frac{(C_x\Omega_x)^2}{9K_1^2}.$$

In order to get a positive real root of  $a^2$ , and hence a real  $a$ , the following conditions must be satisfied:

$$\begin{cases} p < 0 \Leftrightarrow -\frac{4\delta}{9K_1}\Omega_x > 3f^2 + \frac{4K_2}{3K_1}g^2 \\ p^2 \geq 4q \Leftrightarrow -\frac{8\delta}{9K_1}\Omega_x \geq 7f^2 + \frac{8K_2}{3K_1}g^2 + \frac{4(C_x\Omega_x)^2}{9K_1^2f^2} \end{cases} \quad (9-77)$$

It can be seen that the solution domain of the above first inequality is contained by that of the second inequality. So, with  $\varepsilon\delta = \omega - 3\Omega_x$ , the conditions become

$$\begin{cases} \omega \leq 3\Omega_x - \left(\frac{63k_1}{8\Omega_x}f^2 + \frac{3k_2}{\Omega_x}g^2 + \frac{c_x^2\Omega_x}{2k_1f^2}\right), & k_1 > 0 \\ \omega \geq 3\Omega_x - \left(\frac{63k_1}{8\Omega_x}f^2 + \frac{3k_2}{\Omega_x}g^2 + \frac{c_x^2\Omega_x}{2k_1f^2}\right), & k_1 < 0 \end{cases} \quad (9-78)$$

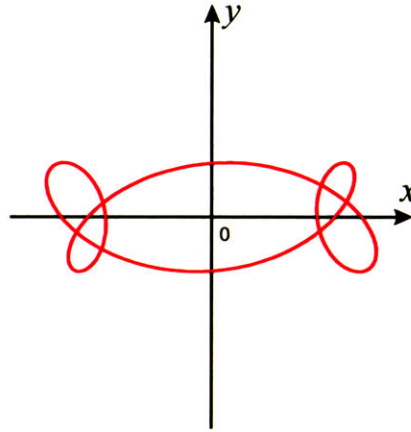


**Figure 9-8: Third-order subharmonic resonance in x direction (sketch).**

Under these conditions, the subharmonic resonance around  $3\Omega_x$  can exist with the amplitude determined by Equation (9-76). Then, according to Equations (9-36), the response in  $X$  and  $Y$  directions are, with the orbit sketched in Figure 9-8,

$$\begin{cases} X_0 = 2a \cos(\Omega_x t + \varphi(T)) + 2f \cos(\omega t) = 2a \cos\left(\frac{\omega}{3}t + \varphi_0\right) + 2f \cos(\omega t) \\ Y_0 = 2g \sin(\omega t), \end{cases} \quad (9-79)$$

where  $\varphi_0 = -\eta/3$ , derived from Equation (9-74).

On the other hand, when the rotational speed is near three times the natural frequency in  $y$  direction,  $\omega = 3\Omega_y + \varepsilon\delta$ , the following equation can be derived by following the same procedure above:

$$3K_3(b^2 + 2g^2) + 2K_2f^2 + 2\Omega_y \delta/3 + iC_y\Omega_y = 3iK_3bge^{-3i\phi_0}. \quad (9-80)$$

Therefore, only under the following conditions,

$$\begin{cases} \omega \leq 3\Omega_y - \left( \frac{63k_3}{8\Omega_y}g^2 + \frac{3k_2}{\Omega_y}f^2 + \frac{c_y^2\Omega_y}{2k_3g^2} \right), & k_3 > 0 \\ \omega \geq 3\Omega_y - \left( \frac{63k_3}{8\Omega_y}g^2 + \frac{3k_2}{\Omega_y}f^2 + \frac{c_y^2\Omega_y}{2k_3g^2} \right), & k_3 < 0 \end{cases} \quad (9-81)$$

can there exist a nonzero real solution of  $b$ , with amplitudes of

$$b^2 = \frac{-r \pm \sqrt{r^2 - 4s}}{2}, \quad (9-82)$$

$$\text{where } r \equiv 3g^2 + \frac{4K_2}{3K_3}f^2 + \frac{4\delta}{9K_3}\Omega_y, \quad s \equiv \left( 2g^2 + \frac{2K_2}{3K_3}f^2 + \frac{2\delta}{9K_3}\Omega_y \right)^2 + \frac{(C_y\Omega_y)^2}{9K_3^2}.$$

Then the nonlinear resonance orbit is, with  $\phi_0$  determined by Equation (9-80),

$$\begin{cases} X_0 = 2f \cos(\omega t) \\ Y_0 = 2b \cos\left(\frac{\omega}{3}t + \phi_0\right) + 2g \sin(\omega t) \end{cases} \quad (9-83)$$

The orbit is sketched in Figure 9-9.

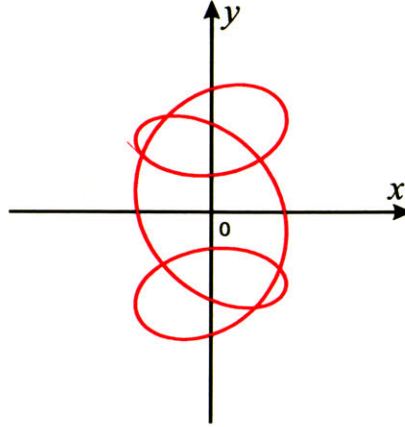


Figure 9-9: Third-order subharmonic resonance in  $y$  direction (sketch).

### 9.3.5 Secondary Resonance near $2\Omega_x - \Omega_y$ and $2\Omega_y - \Omega_x$

With the rotor speed  $\omega = 2\Omega_x - \Omega_y + \varepsilon\delta$ , there is an additional secular term in the  $x$  component of Equation (9-35),

$$2K_2 A^* B G \exp(i(\omega - \Omega_x + \Omega_y)t) = 2K_2 A^* B G \exp(i\Omega_x t + i\delta T), \quad (9-84)$$

and an additional secular term in the  $y$  component,

$$K_4 A^2 G^* \exp(i(2\Omega_x - \omega)t) = K_4 A^2 G^* \exp(i\Omega_y t - i\delta T). \quad (9-85)$$

Then, by eliminating all the secular terms, one can get

$$\begin{cases} (3K_1 a^2 + 6K_1 f^2 + 2K_2 b^2 + 2K_2 g^2 + 2\Omega_x \phi' + iC_x \Omega_x) A = -2K_2 A^* B G e^{i\delta T} \\ (3K_3 b^2 + 6K_3 g^2 + 2K_4 a^2 + 2K_4 f^2 + 2\Omega_y \phi' + iC_y \Omega_y) B = -K_4 A^2 G^* e^{-i\delta T} \end{cases} \quad (9-86)$$

It can be seen that the complex conjugate of the above second equation multiplied by  $2B^*$  equals the first one multiplied by  $A^*$ , with  $K_2 = K_4$ . Then, separating the imaginary parts from the real parts yields

$$-a^2 C_x \Omega_x = 2b^2 C_y \Omega_y. \quad (9-87)$$

Therefore,  $a$  and  $b$  can only be zeros:  $a = b = 0$ , which means that there is no secondary resonance near  $2\Omega_x - \Omega_y$ . By following the same procedure, one can find that there is no secondary resonance near  $2\Omega_y - \Omega_x$  either.



### 9.3.6 Secondary Resonance near $2\Omega_x + \Omega_y$ and $2\Omega_y + \Omega_x$

With the rotor speed  $\omega = 2\Omega_x + \Omega_y + \varepsilon\delta$ , there is an additional secular term in the  $x$  component of Equation (9-35),

$$2K_2 A^* B^* G \exp\left(i(\omega - \Omega_x - \Omega_y)t\right) = -2iK_2 abg \exp\left(i\Omega_x t + i\delta T - i\varphi - i\phi\right), \quad (9-88)$$

and an additional secular term in the  $y$  component,

$$K_4 A^{*2} G \exp\left(i(\omega - 2\Omega_x)t\right) = -iK_4 a^2 g \exp\left(i\Omega_y t + i\delta T - 2i\phi\right). \quad (9-89)$$

Therefore, eliminating all the secular terms yields

$$\begin{cases} \left(3K_1 a^2 + 6K_1 f^2 + 2K_2 b^2 + 2K_2 g^2 + 2\Omega_x \phi' + iC_x \Omega_x\right) a = 2iK_2 abg e^{i\delta T - 2i\varphi - i\phi} \\ \left(3K_3 b^2 + 6K_3 g^2 + 2K_4 a^2 + 2K_4 f^2 + 2\Omega_y \phi' + iC_y \Omega_y\right) b = iK_4 a^2 g e^{i\delta T - 2i\varphi - i\phi} \end{cases} \quad (9-90)$$

Besides the trivial solution  $a=b=0$ , the following analysis shows that there can also exist nonzero real solutions of  $a$  and  $b$  under certain conditions.

In the steady state,  $a$  and  $b$  do not change with time. Therefore, the phase on the right-hand sides of Equations (9-90) should not change with time either:

$$\eta \equiv \delta T - 2\varphi(T) - \phi(T) = \text{const}. \quad (9-91)$$

Thus,  $2\varphi' + \phi' = \delta$  or  $2\varphi + \phi = \delta T - \eta$ . Then the first equation of (9-90) divided by  $a$  and multiplied by  $2\Omega_y$  plus the second divided by  $b$  and multiplied by  $\Omega_x$  becomes

$$\begin{aligned} & 2\Omega_y \left(3K_1 (a^2 + f^2) + 2K_2 (b^2 + g^2)\right) + \Omega_x \left(3K_3 (b^2 + g^2) + 2K_4 (a^2 + f^2)\right) \\ & + 2\Omega_x \Omega_y \delta + i(2C_x + C_y) \Omega_x \Omega_y = \left(4b\Omega_y + \frac{a^2}{b} \Omega_x\right) K_2 g e^{i\eta}. \end{aligned} \quad (9-92)$$

Meanwhile, the first equation of (9-90) multiplied by  $a$  equals the second one multiplied by  $2b$ . Then, one can obtain the following equation from the imaginary parts:

$$a^2 C_x \Omega_x = 2b^2 C_y \Omega_y. \quad (9-93)$$

Substituting the above equation into (9-92) yields

$$\begin{aligned} & i(2C_x + C_y) + \left(3K_1 \left(\frac{2C_y \Omega_y}{C_x \Omega_x} b^2 + 2f^2\right) + 2K_2 (b^2 + g^2)\right) \frac{2}{\Omega_x} + 2\delta \\ & + \left(3K_3 (b^2 + 2g^2) + 2K_4 \left(\frac{2C_y \Omega_y}{C_x \Omega_x} b^2 + f^2\right)\right) \frac{1}{\Omega_y} = 2i \left(\frac{2}{\Omega_x} + \frac{C_y}{C_x \Omega_x}\right) K_2 b g e^{i\eta} \end{aligned} \quad (9-94)$$

The norm squared of the above equation is

$$\begin{aligned} & \left(2C_x + C_y\right)^2 + \left[ \left( 3K_1 \left( \frac{2C_y\Omega_y}{C_x\Omega_x} b^2 + 2f^2 \right) + 2K_2(b^2 + g^2) \right) \frac{2}{\Omega_x} + 2\delta \right. \\ & \left. + \left( 3K_3(b^2 + 2g^2) + 2K_4 \left( \frac{2C_y\Omega_y}{C_x\Omega_x} b^2 + f^2 \right) \right) \frac{1}{\Omega_y} \right]^2 = 4 \left( \frac{2}{\Omega_x} + \frac{C_y}{C_x\Omega_x} \right)^2 K_2^2 b^2 g^2, \end{aligned} \quad (9-95)$$

which is a parabolic equation of  $b^2$ . With  $K_1=k_1/m\varepsilon$ ,  $K_2=k_2/m\varepsilon$ ,  $K_3=k_3/m\varepsilon$ ,  $K_4=k_4/m\varepsilon$ ,  $C_x=c_x/m\varepsilon$ ,  $C_y=c_y/m\varepsilon$ , and  $\delta=(\Omega_x+\Omega_y-2\omega)/\varepsilon$ , it is useful to define

$$\begin{aligned} a_1 & \equiv \left( \frac{12}{\Omega_x} + \frac{4}{\Omega_y} \frac{k_2}{k_1} \right) \frac{C_y\Omega_y}{C_x\Omega_x} + \frac{4}{\Omega_x} \frac{k_2}{k_1} + \frac{3}{\Omega_y} \frac{k_3}{k_1} > 0, \quad a_3 \equiv \left( \frac{2}{\Omega_x} + \frac{c_y}{c_x\Omega_x} \right)^2 \left( \frac{k_2}{k_1} \right)^2 g^2 > 0 \\ a_2 & \equiv \left( \frac{12}{\Omega_x} + \frac{2}{\Omega_y} \frac{k_2}{k_1} \right) f^2 + \left( \frac{4}{\Omega_x} \frac{k_2}{k_1} + \frac{6}{\Omega_y} \frac{k_3}{k_1} \right) g^2, \quad \text{and} \quad a_4 \equiv a_2 + 2 \frac{\omega - 2\Omega_x - \Omega_y}{k_1}. \end{aligned}$$

Then, the following equation of  $b^2$  can be derived:

$$a_1^2 b^4 + (2a_1 a_4 - 4a_3) b^2 + a_4^2 + (2c_x + c_y)^2 / k_1^2 = 0. \quad (9-96)$$

In order to get a real positive  $b^2$ , and hence a nonzero real  $b$ , the following conditions must be satisfied:

$$\begin{cases} (2a_1 a_4 - 4a_3) < 0 \Leftrightarrow 2a_3 > a_1 a_4 \\ 4a_3 (a_3 - a_1 a_4) \geq a_1^2 (2c_x + c_y)^2 / k_1^2 \Leftrightarrow a_4 \leq \frac{a_3}{a_1} - \frac{a_1}{4a_3} \left( \frac{2c_x + c_y}{k_1} \right)^2 \end{cases} \quad (9-97)$$

Since the solution domain of the above first inequality is contained by that of the second inequality, the final condition becomes

$$\begin{cases} \omega \leq 2\Omega_x + \Omega_y + \frac{k_1 a_3}{2a_1} - \frac{k_1 a_1}{8a_3} \left( \frac{2c_x + c_y}{k_1} \right)^2 - \frac{k_1 a_2}{2}, & k_1 > 0 \\ \omega \geq 2\Omega_x + \Omega_y + \frac{k_1 a_3}{2a_1} - \frac{k_1 a_1}{8a_3} \left( \frac{2c_x + c_y}{k_1} \right)^2 - \frac{k_1 a_2}{2}, & k_1 < 0 \end{cases}. \quad (9-98)$$

Thus, there can be a secondary resonance at the speed around  $2\Omega_x + \Omega_y$ , as long as the above condition is satisfied. Take the system in Section 9.3.3 on the secondary resonance of  $(\Omega_x + \Omega_y)/2$ , for example ( $\Omega_x=1.9$ ,  $\Omega_y=1$ ,  $k_1=k_2=k_3=k_4=-0.04$ ,  $c_x=c_y=-0.02$ ,  $k_d=-0.01$ ): according to the Equations (9-98), there are resonances only at the rotational speed

$\omega > 5.06$ . Then the orbits of the system at  $\omega = 5.0$  and  $\omega = 5.1$  are simulated and shown in Figure 9-10. The numerical simulations show that there is no resonance at rotational speed  $\omega = 5.0$ , but there is a nonlinear resonance at  $\omega = 5.1$ . Thus the analytically derived conditions under which the secondary resonance  $2\Omega_x + \Omega_y$  can occur are verified by the numerical simulations.

Furthermore, it is important to note that the secondary resonance has a much larger amplitude ( $1 \rightarrow$  about 7), which may cause the rotor to crash into the bearing wall. Thus, operation close to this nonlinear resonance should be avoided.

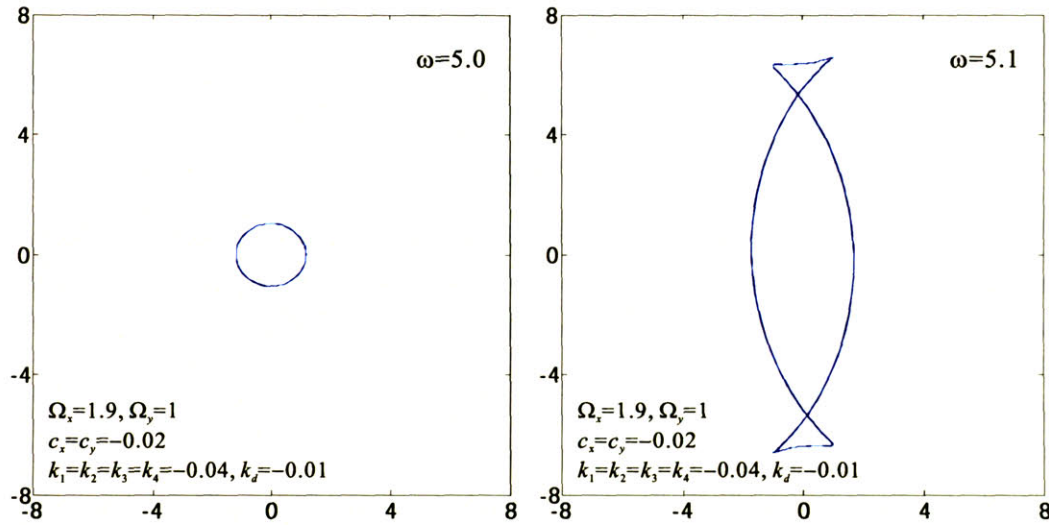


**Figure 9-10: Simulated orbits for the anisotropic system at speeds near the secondary resonance  $2\Omega_x + \Omega_y$ :  $\omega = 5.0$  (left) and  $\omega = 5.1$  (right).**

On the other hand, when the speed  $\omega = \Omega_x + 2\Omega_y + \varepsilon\delta$ , the secular terms to be eliminated are

$$\begin{cases} (3K_1 a^2 + 6K_1 f^2 + 2K_2 b^2 + 2K_2 g^2 + 2\Omega_x \phi' + iC_x \Omega_x) a = -K_2 b^2 f e^{i\eta} \\ (3K_3 b^2 + 6K_3 g^2 + 2K_4 a^2 + 2K_4 f^2 + 2\Omega_y \phi' + iC_y \Omega_y) b = -2K_4 a b f e^{i\eta} \end{cases} \quad (9-99)$$

where  $\eta = \delta T - \phi - 2\phi$ , and  $\phi' + 2\phi' = \delta$ . Following the same procedure as the above yields this equation of  $a^2$ ,

$$c_1^2 a^4 + (2c_1 c_4 - 4c_3) a^2 + c_4^2 + (c_x + 2c_y)^2 / k_3^2 = 0, \quad (9-100)$$

where

$$c_1 \equiv \left( \frac{12}{\Omega_y} + \frac{4 k_2}{\Omega_x k_3} \right) \frac{C_x \Omega_x}{C_y \Omega_y} + \frac{4 k_2}{\Omega_y k_3} + \frac{3 k_1}{\Omega_x k_3} > 0, \quad c_3 \equiv \left( \frac{2}{\Omega_y} + \frac{c_x}{c_y \Omega_y} \right)^2 \left( \frac{k_2}{k_3} \right)^2 f^2 > 0$$

$$c_2 \equiv \left( \frac{12}{\Omega_y} + \frac{2 k_2}{\Omega_x k_3} \right) g^2 + \left( \frac{4 k_2}{\Omega_y k_3} + \frac{6 k_1}{\Omega_x k_3} \right) f^2, \quad \text{and} \quad c_4 \equiv c_2 + 2 \frac{\omega - \Omega_x - 2\Omega_y}{k_3}.$$

Therefore, to obtain a real positive root of  $a^2$ , and hence a nonzero real  $a$ , the following conditions must be satisfied:

$$\begin{cases} \omega \leq \Omega_x + 2\Omega_y + \frac{k_3 c_3}{2c_1} - \frac{k_3 c_1}{8c_3} \left( \frac{c_x + 2c_y}{k_3} \right)^2 - \frac{k_3 c_2}{2}, & k_3 > 0 \\ \omega \geq \Omega_x + 2\Omega_y + \frac{k_3 c_3}{2c_1} - \frac{k_3 c_1}{8c_3} \left( \frac{c_x + 2c_y}{k_3} \right)^2 - \frac{k_3 c_2}{2}, & k_3 < 0 \end{cases} \quad (9-101)$$

Using the same system as in Section 9.3.3, one can calculate that the secondary resonance can only exist at a rotational speed  $\omega > 4.15$ . The orbits of the rotor at  $\omega = 4.1$  and  $\omega = 4.2$  are simulated and shown in Figure 9-11.

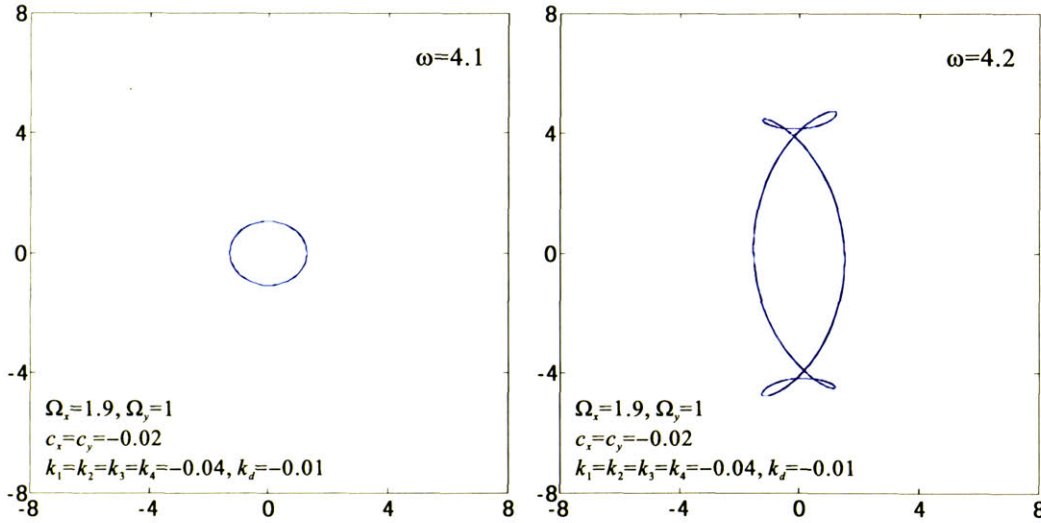


**Figure 9-11: Simulated orbits for the anisotropic system at speeds near the secondary resonance  $\Omega_x + 2\Omega_y$ :  $\omega = 4.1$  (left) and  $\omega = 4.2$  (right).**

Again, the analytically derived conditions under which the secondary resonance  $\Omega_x + 2\Omega_y$  can occur are verified by the numerical simulations. Also, the secondary resonance has a much larger amplitude (1  $\rightarrow$  about 5) and hence should be avoided in operation.

### 9.3.7 Experimental Observations of Nonlinear Resonances

Coming back to the experimental observation of Figure 9-1, with the analyses above, it can be seen that the nonlinear resonance indicated by the pressure peak at about 60krpm was actually the subharmonic resonance of  $3\Omega_y$ . For clarity, Figure 9-1 is replotted below, with the peaks labeled with the corresponding types of the resonances:  $\Omega_x$  and  $\Omega_y$  in black, indicating the resonances due to the two natural frequencies, and  $3\Omega_y$  in red, indicating the nonlinear subharmonic resonance that happens at speeds of three times the natural frequency in y direction  $3\Omega_y$ .

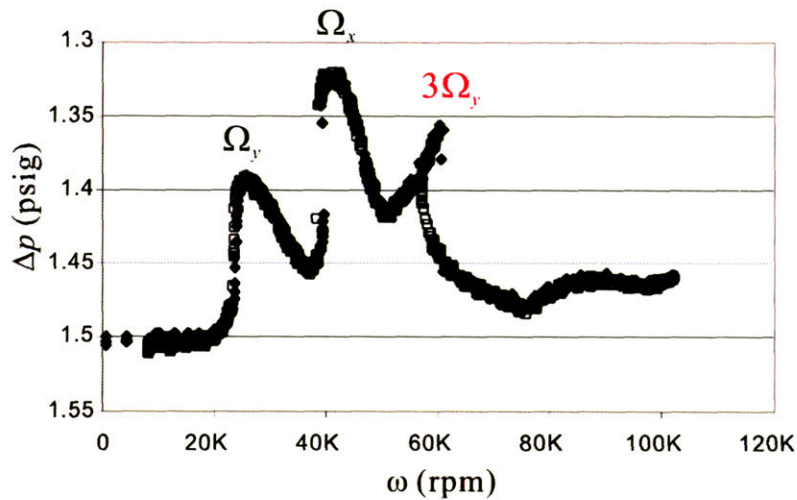


Figure 9-12: Experimental data showing the secondary resonance at speed of  $3\Omega_y$  [30].

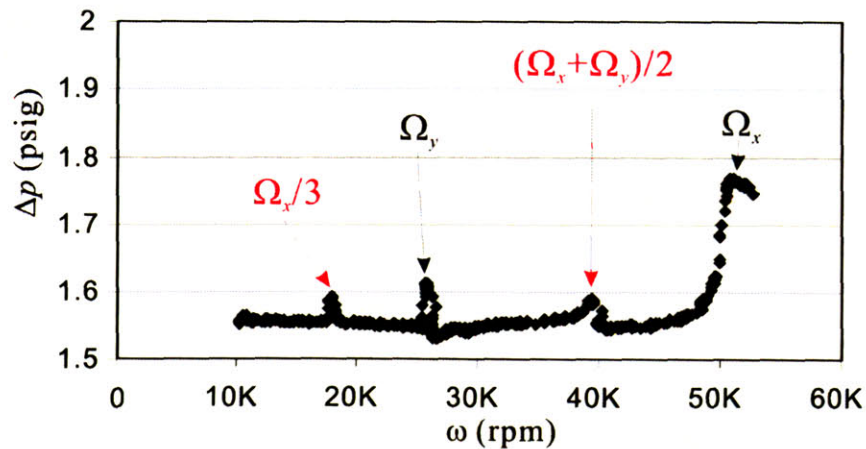


Figure 9-13: Experimental data showing the secondary resonances of  $(\Omega_x + \Omega_y)/2$  and  $\Omega_x/3$  [30].

Besides the subharmonic resonance, other types of nonlinear resonances have also been observed in the experiments, as shown in Figure 9-13. With the fixed flow rate supply to the journal bearing, the device was accelerated from the speed of 10krpm, which was far below the natural frequency in  $y$  direction, to about 50krpm, the natural frequency in  $x$  direction. First of all, the pressure peaks at  $\sim 26$ krpm and  $\sim 52$ krpm were due to the natural frequencies of the system, which were consistent with the model predictions. Then, the small pressure peak at about 39krpm, which was between the two naturals, implied that the system had engaged in a secondary resonance of  $(\Omega_x + \Omega_y)/2$ . There was another secondary resonance, the third-order superharmonic resonance of  $\Omega_x/3$ , indicated by the small pressure peak at the rotor speed near 18krpm.

### ***9.4 Summary and Conclusions***

The nonlinear dynamics and third-order secondary resonances in the journal-bearing system have been investigated by the multi-scale method.

In the isotropic system, it is found that the subharmonic resonance can happen at speeds near three times the natural frequency ( $3\Omega_N$ ). Furthermore, the orbit of the subharmonic resonance in the isotopic journal-bearing system is found to rotate at a speed much slower than the rotor speed, which is different from the fixed nonlinear resonance in the anisotropic system.

In the anisotropic system, the secondary resonances that may occur include superharmonic resonances at one third of the natural frequencies in both directions ( $\Omega_x/3, \Omega_y/3$ ), subharmonic resonances at three times the natural frequencies in both directions ( $3\Omega_x, 3\Omega_y$ ), and the resonance at the combinations of the two naturals:  $(\Omega_x + \Omega_y)/2, 2\Omega_x + \Omega_y$  and  $\Omega_x + 2\Omega_y$ . The conditions under which these nonlinear resonances happen were derived in the analyses, and these analytically derived conditions were verified by numerical simulations. The model predictions agreed with the experimental observations; thus, the model was validated.

Since these secondary nonlinear resonances normally have large amplitudes that may cause the rotor to crash, they should be avoided during normal operation, especially the subharmonic ones. Also, according to Chapter 8, tapered bearings are found to induce strong nonlinearity of the hydrostatic force, which causes the nonlinear resonances during operation. Therefore, again, tapered bearings with large profile variations should be avoided in fabrication.



It is important to note that this is only a preliminary investigation on the nonlinear dynamics of micro-journal-bearing systems. Besides the third-order nonlinear terms, there exist higher odd-order ones in hydrostatic force, which in turn may cause higher-order nonlinear resonances. According to the numerical simulations based on the bilinear stiffness system done by Ehrich [34], these higher-order resonances have even larger amplitudes. Furthermore, several devices have crashed at speeds of high odd multiples ( $7\times$  or even  $9\times$ ) of the natural frequency in the experiments [30]. Also according to Ehrich [34], there is even some chaotic behavior at certain rotor speeds due to the nonlinear bearing forces, making the system much more complicated. Besides the nonlinearity of hydrostatic force, the nonlinearities of hydrodynamic and damping forces may also affect the system's dynamic behavior. Although it is important to do deeper investigation on the nonlinear dynamics of micro-journal-bearing systems, they are not within the scope of this thesis work and may form another research project.



## *Chapter 10*

# **Hydrostatic Thrust-Bearing Systems**

As mentioned earlier in the thesis, besides the journal bearing, thrust bearings are also needed in the micro-rotating devices to support the rotor. They are important to the micro-rotating devices because they not only generate axial stiffness in the device confining the rotor axial movement, but also produce tilting stiffness confining the rotor conical movement; the latter is crucial to the stability of the multi-degree-of-freedom system discussed in Chapter 6. The micro-thrust bearings are located above and below the rotor, as sketched in Figure 1-5 to Figure 1-7. The one located above the rotor is called the forward thrust bearing (FTB), while the one below the rotor is called the aft thrust bearing (ATB).

Both the hydrostatic and the hydrodynamic thrust-bearing systems used in the micro-engine devices were thoroughly and successfully investigated by Teo [9][10]. The results showed that hydrostatic systems with high pressure supplies (60~70psig) can generate relatively higher stiffness, and hence should be used for the micro-devices. Furthermore, the stiffness produced by the hydrodynamic thrust bearing depends on the rotor speed and is zero when the rotor is not spinning. Therefore, the hydrodynamic thrust bearing cannot support the rotor at all when the rotor speed is low. So, if the device uses hydrodynamic thrust bearings to support the rotor, hydrostatic bearings are still needed to avoid contact during the start-up, making the thrust-bearing system essentially a hybrid system.

The method Teo used to investigate the hydrostatic thrust bearing and then to compute the axial stiffness and tilting stiffness was the Green's Function Method. This method can give accurate results, but is expensive to implement because it involves a numerical computation for a 2-dimensional PDE. In this chapter, a different and faster approach, the Image Method, is introduced as a complementary way to compute these two stiffnesses. Furthermore, this method is evaluated by 3-D CFD (Fluent 3D) calculations as well as the experimental data.

Two types of hydrostatic thrust bearings are used in the micro-engine devices: the circular thrust bearing (Figure 1-5 and Figure 1-6) and the annular thrust bearing (Figure

1-7). The former is used in the micro-bearing-rig and micro-turbo-charger devices, while the latter is used in the micro-turbo-pump devices. These two types of bearings are both covered in the following analysis.

### 10.1 Circular Hydrostatic Thrust Bearings

The circular thrust bearings are located at the center of the device, as shown in Figure 1-5 and Figure 1-6. Figure 10-1 shows the structure of a typical circular thrust bearing used in the micro-bearing-rig devices (the sketch in the left bottom corner is a cut-out from Figure 1-6).

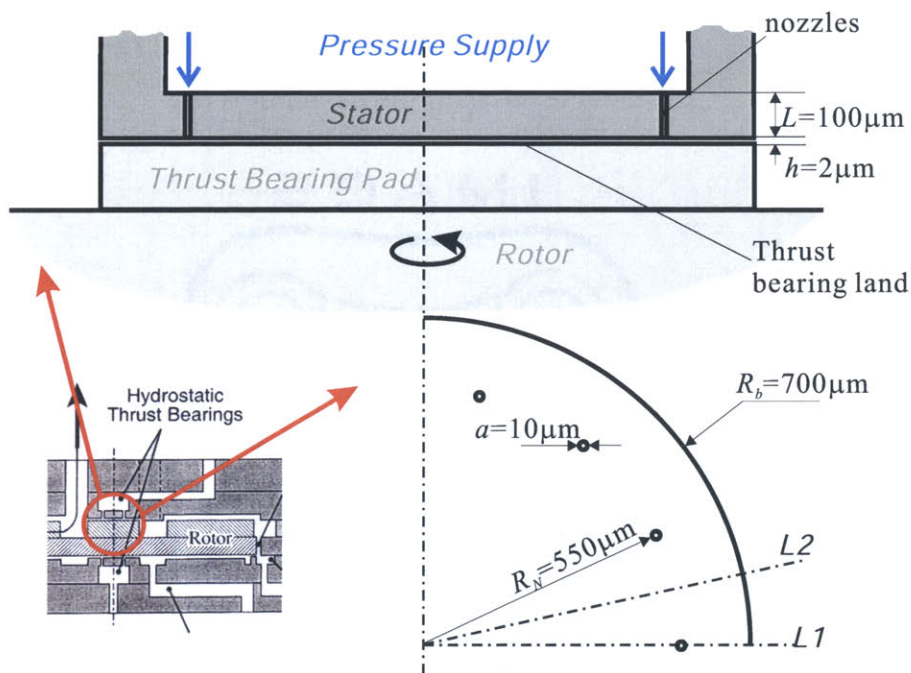


**Figure 10-1: Sketch and dimensions of the structure of a typical thrust bearing used in a micro-bearing rig (not to scale).**

In the hydrostatic thrust bearing, the pressurized air is fed through 14 to over 70 discrete nozzles, which are evenly distributed along the circumferential direction with a length of  $100\mu\text{m}$  and diameter of  $10\mu\text{m}$ . Then the air flows through the thrust bearing gap with a clearance of  $2\sim 3\mu\text{m}$ . The radius of the thrust bearing pad is normally from  $0.7\text{mm}$  to  $0.9\text{mm}$ .

#### 10.1.1 Flow Field in Hydrostatic Thrust Bearings

Because the air pressure fed to the thrust bearing is about 4 atmospheric pressures, and the exit pressure is the atmospheric pressure, the flow in the thrust bearing is com-

pressible. The flow in the thrust bearing can be assumed to be a fully developed Poiseuille-type flow combined with Couette-type flow due to the small clearance ( $\sim 2\mu\text{m}$ ) and low Reynolds number ( $\sim 30$ ). The flow rates in the radial ( $r$ ) and tangential ( $\theta$ ) directions in the thrust bearing gap are then

$$\begin{cases} Q_r = -\frac{h^3}{12\mu} \frac{\partial P}{\partial r} \\ Q_\theta = -\frac{h^3}{12\mu} \frac{\partial P}{r \partial \theta} + \frac{\omega r h}{2} \end{cases} \quad (10-1)$$

where  $P$  is the pressure in the bearing,  $\mu$  is the viscosity of the air, and  $\omega$  is the rotational speed of the rotor. Applying mass conservation in the thrust bearing gap, one can get

$$\frac{1}{r} \frac{\partial}{\partial r} (r \rho Q_r) + \frac{1}{r} \frac{\partial}{\partial \theta} (\rho Q_\theta) = s(r, \theta), \quad (10-2)$$

where  $\rho$  is the density of the air and  $s(r, \theta)$  is the flow source. With the typical dimensions of the micro-thrust bearing, the nozzles have a much smaller diameter ( $10\mu\text{m}$ ) than that of the thrust bearing pad ( $1400\mu\text{m}$ ), and thus they can be treated as point sources in the bearing. Then  $s(r, \theta)$  for each nozzle is  $\dot{m}_i \delta(\vec{r} - \vec{r}_i)$ , where  $\dot{m}_i$  and  $\vec{r}_i$  are the mass flow rate and the position of the nozzle  $i$  respectively, and  $\delta(\vec{r})$  is the 2-dimensional Dirac delta function.

Since the flow through the thrust bearing gap is fully developed as assumed above, the air in the thrust bearing can be treated as isothermal, because the Prandtl number ( $Pr$ ) of air is around 1 and silicon is a good heat conductor. Then the density of air, as an ideal and isothermal gas, is proportional to its pressure. The combination of Equations (10-1) and (10-2) then yields

$$\sum_i \dot{m}_i \delta(\vec{r} - \vec{r}_i) = \frac{1}{r} \frac{\partial}{\partial r} \left( r \frac{\rho_0}{P_0} P \cdot \left( -\frac{h^3}{12\mu} \frac{\partial P}{\partial r} \right) \right) + \frac{1}{r} \frac{\partial}{\partial \theta} \left( \frac{\rho_0}{P_0} P \cdot \left( -\frac{h^3}{12\mu} \frac{\partial P}{r \partial \theta} + \frac{\omega r h}{2} \right) \right), \quad (10-3)$$

where  $P_a$  is the atmospheric pressure and  $\rho_a$  is the air density at  $P_a$ . The right-hand side of the above equation is exactly the same as the Reynolds equation for the film flow.

When the rotor is not tilted, bearing clearance  $h$  is uniform in the thrust bearing. Assuming the rotor is not rotating (the rotation effect is investigated later in the chapter), the above equation then reduces to

$$\Delta P^2 = -\frac{24\mu P_a}{h^3 \rho_a} \sum_i \dot{m}_i \delta(\vec{r} - \vec{r}_i), \quad (10-4)$$

which is a Poisson equation of  $P^2$ , with the boundary condition  $P=P_a$  at  $r=R_b$ , the exhaust of the bearing. This equation can be solved by various methods. Among them, the Image Method is a fast and accurate analytical approach.

Since the electrostatic field is also governed by the Poisson equation, the Image Method can be briefly described using the electrostatic field as an example (detailed descriptions of this method can be found in textbooks on electrostatic fields).

As shown in Figure 10-2, the electrostatic potential field generated by a positive point charge above a grounded plate is governed by the Poisson equation, with the boundary condition that the electrostatic potential on the plate is constant and zero. If the plate is replaced by a negative charge with the same intensity at the image position of the positive one, the potential at the virtual surface of the original plate is also zero and constant. According to Green's theorem, the Poisson equations with the same boundary conditions have exactly the same solution. Thus, the electrostatic potentials in the upper half space of both settings are equal. As a result, the original complicated problem can be solved with an equivalent simpler one.

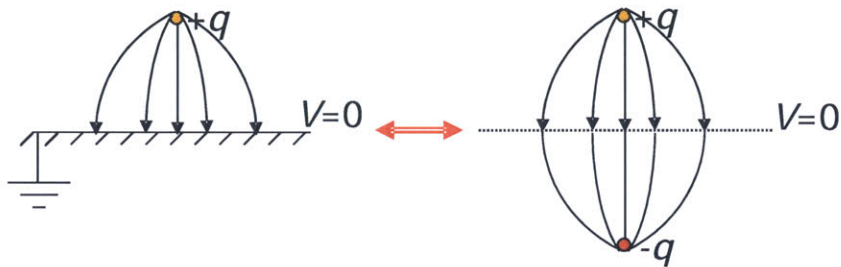


**Figure 10-2: Image Method for the electrostatic field.**

This technique can then be used to solve the pressure fields in thrust bearing gaps, and the image setting for the circular thrust bearings can be found in Appendix B.

### 10.1.2 Model Assessment

To evaluate the assumptions of isothermal Poiseuille-type flow and Couette-type flow, 3-D compressible CFD (Fluent) calculations were run as described below.

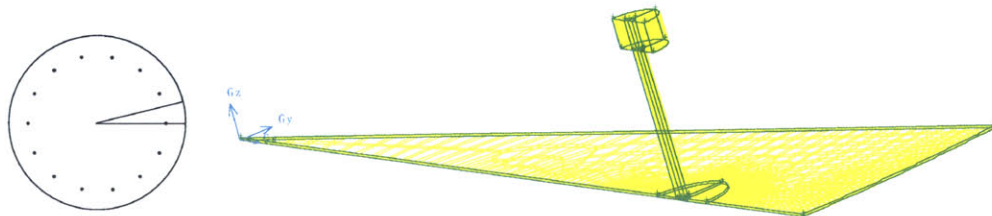
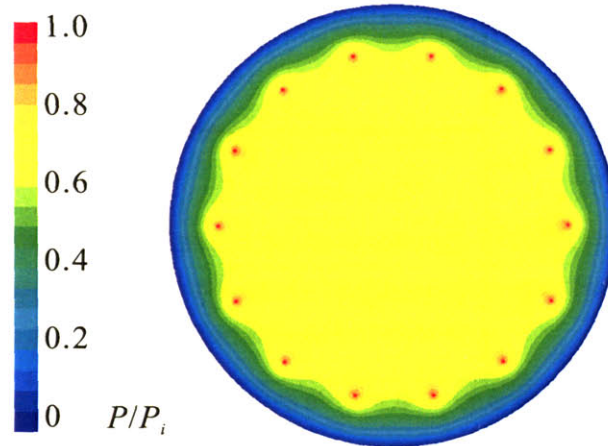


**Figure 10-3: The thrust bearing grids used in 3-D Fluent calculations.**



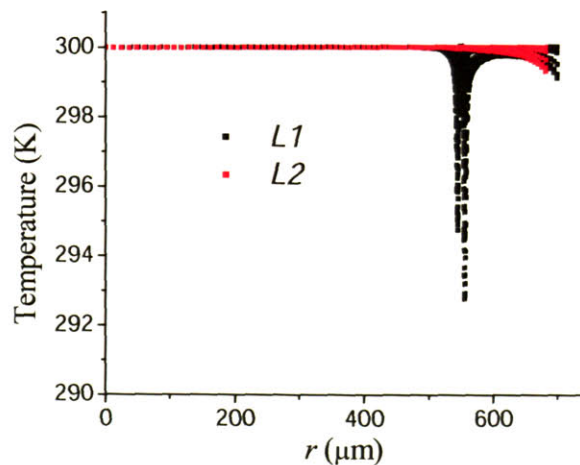
It is worth noting that there are two symmetric lines in the thrust bearing:  $L1$  and  $L2$ , as shown in Figure 10-1. The CFD configuration can take advantage of this, and instead only a slice of the bearing was calculated as depicted in Figure 10-3.

Figure 10-4 shows the pressure distribution in the bearing calculated by the CFD model with the mass flow rate through each nozzle of  $0.02\text{mg/s}$ . In the calculation, the wall temperature was set constant at  $300\text{K}$ , due to the high conductivity of silicon.



**Figure 10-4: Pressure distribution normalized by the inlet pressure in the thrust bearing with the mass flow rate of  $0.02\text{mg/s}$  per nozzle, calculated by 3-D Fluent.**

It can be seen that the pressure at the center of the thrust bearing is essentially constant – the nozzles act as a “fence” for the pressure “reservoir” in the center.



**Figure 10-5: Temperatures in the thrust bearing gap with bearing wall temperature of  $300\text{K}$ , by 3-D Fluent.**

Temperatures in the thrust bearing gap along the  $L1$  and  $L2$  lines calculated by the CFD are shown in Figure 10-5. One can see that the temperature variation in the thrust bearing gap is no more than 8 Kelvin, and hence the isothermal approximation is validated.

Furthermore, the pressure distributions calculated by the Image Method are compared with the CFD results, shown in Figure 10-6.

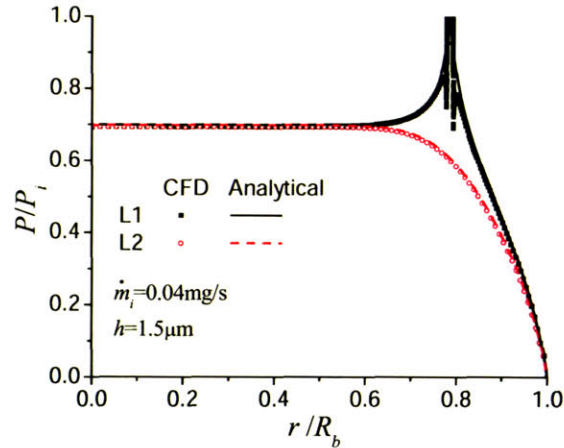


**Figure 10-6: Pressure normalized by the inlet pressure along L1 and L2, calculated by the Image Method and 3-D Fluent.**

Integrating the pressure in the thrust bearing yields the thrust force, which is plotted in Figure 10-7.

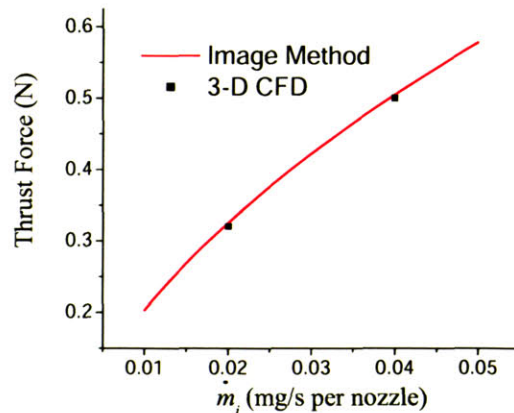


**Figure 10-7: Thrust force as a function of the mass flow rate per nozzle, calculated by the Image Method and 3-D Fluent.**

These comparisons show that the results of the Image Method match the 3-D compressible Fluent results well with the given flow rates, and thus the assumptions of iso-

thermal Poiseuille-type flow and Couette-type flow in the thrust bearing are validated. The Image Method is also proven to be accurate to model the flow in the micro-hydrostatic circular thrust bearing. Furthermore, the results also agree with [9].

The next step is to calculate the mass flow rate through each nozzle, and hence the thrust force with a given pressure supply. To do this, pressure losses through the nozzle, the inlet, and the corner need to be calculated for a given mass flow rate.

With the assumption of isothermal Poiseuille flow, the pressure drop through the nozzle is

$$P_1^2 - P_2^2 = \frac{256\mu L}{\pi a^4} \frac{P_a}{\rho_a} \dot{m}, \tag{10-5}$$

where  $P_1$  is the pressure at the entrance of the nozzle,  $P_2$  is the pressure at the exit of the nozzle, and  $a$  and  $L$  are the radius and length of the nozzle respectively. The entrance loss is still determined by the empirical formula  $\Delta P_e = 1.5\rho v^2/2$ .

Furthermore, the pressure loss at the corner can be derived empirically by curve-fitting the CFD results with the formula below:

$$\Delta P_c = K_1 \left( \frac{A_1}{A_2} \right)^{K_2} \rho v^2 \tag{10-6}$$

where  $A_1$  is the flow area before the corner, which is the area of the nozzle cross section:  $\pi a^2/4$ ;  $A_2$  is the flow area after the corner, which is  $\pi ah$ ; and  $K_1$  and  $K_2$  are the coefficients to be determined by the curve-fitting.

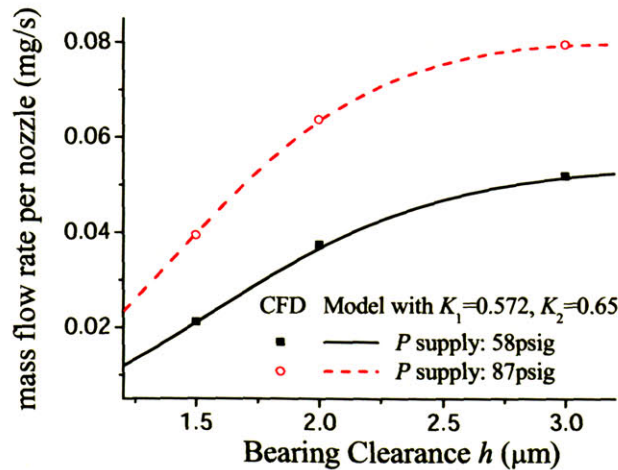
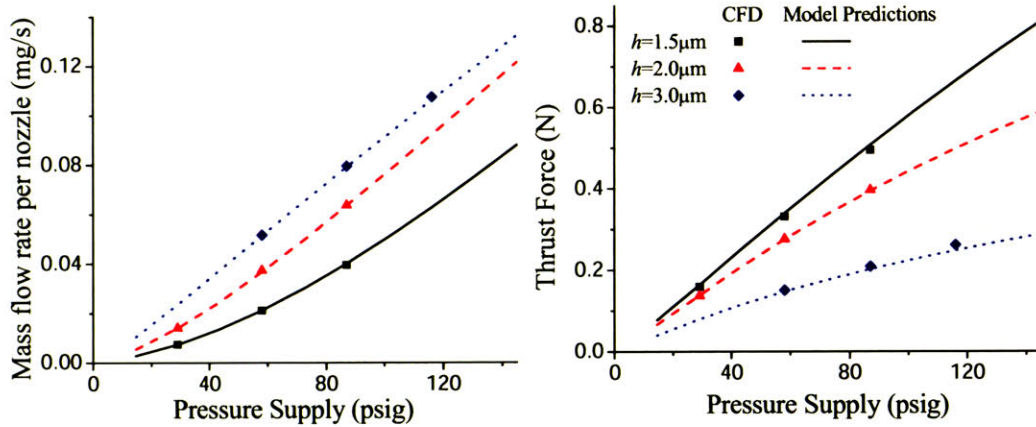


Figure 10-8: Curve-fitting to find the loss coefficients at the corner.



Thus, with the curve fitting shown in Figure 10-8,  $K_1$  and  $K_2$  are found to be 0.572 and 0.65 respectively. Note that the curves of the mass flow rate start to be flat at a bearing clearance of about  $3\mu\text{m}$ , indicating that the flow starts to choke in the nozzle, causing the mass flow rate to be independent of the bearing clearance. This choking phenomenon has been excessively discussed by Teo in [9] and found to be the cause of instability in the thrust-bearing system.



**Figure 10-9: Model predictions with different supply pressures and bearing clearances, compared with 3-D Fluent results: the mass flow rate (left) and the thrust force (right).**

To further assess the accuracy of the loss coefficients, several more CFD (3-D Fluent) calculations with different bearing clearances and supply pressures were done and compared with the model predictions. Figure 10-9 shows that this empirical model of the losses works well with the Image Method for the micro-thrust-bearing system.

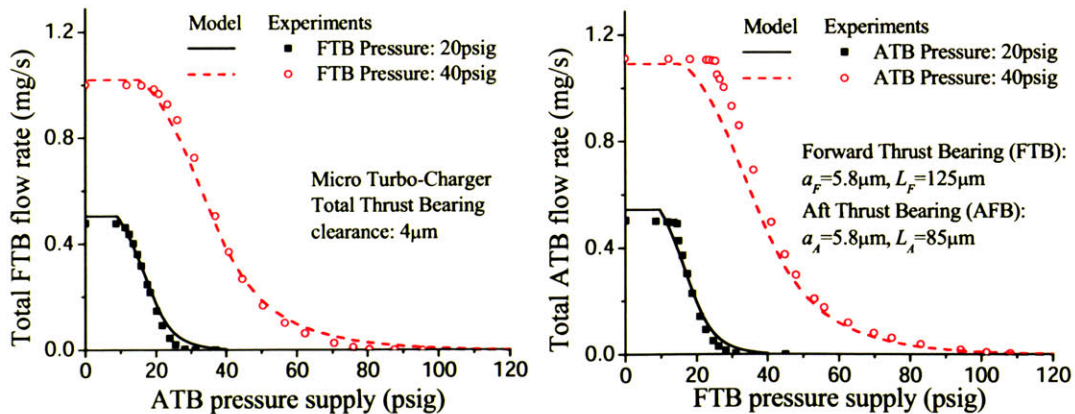


**Figure 10-10: Static flow tests (experimental data from [6]) in the thrust bearings, compared with the model predictions.**

To validate the model experimentally, a static flow test can be done by keeping the pressure supply to one of the thrust bearings constant and varying the supply pressure to the other at the same time. Since both bearing clearances change as the rotor moves axially with the varying pressure, the flow rate through the former bearing changes as shown in Figure 10-11, although its pressure supply is fixed all the time.

The comparison shows that the model predictions agree well with the experimental data, in both trend and magnitude, and thus the Image Method is also validated by the experimental data.

With this Image Method, the natural frequency of the thrust-bearing system can then be calculated, and the results are plotted in Figure 10-11.

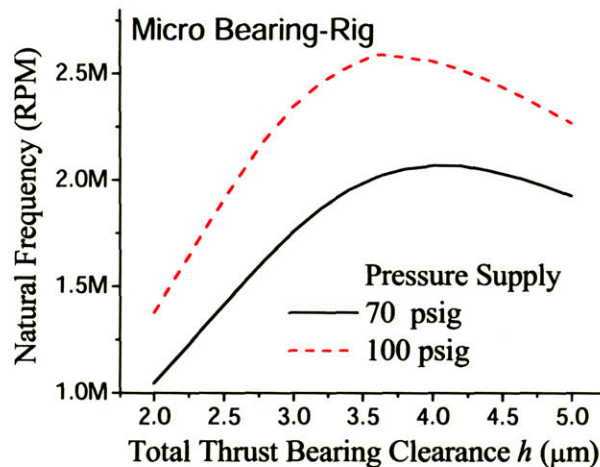


**Figure 10-11: Natural frequency prediction by the model for the hydrostatic thrust bearing used in the micro-bearing-rig devices.**

Thus, to get a maximum thrust bearing natural frequency (higher than the design speed of 2.4 million rpm), the total bearing clearance (the sum of the forward thrust bearing and the aft thrust bearing clearances) should be about  $4\mu\text{m}$ .

### 10.1.3 Effect of Rotor Rotation

When the rotor is rotating, the air in the bearing is dragged with the rotor disk in the tangential direction. The centrifugal body force induced by this tangential flow can reduce the pressure and hence the thrust force in the bearing. The following analysis using both the analytical approach and 3-D Fluent show that this pressure decrease is negligible compared with the external pressure supply to the bearing. As a result, the rotation effect

on the thrust force in the bearing is also negligible compared to the thrust force produced by the external static pressure.

The steady Navier-Stokes equation ( $r$  component) in polar coordinates ( $r$  and  $\theta$ ) becomes

$$\rho \left( u_r \frac{\partial u_r}{\partial r} + \frac{u_\theta}{r} \frac{\partial u_r}{\partial \theta} - \frac{u_\theta^2}{r} + u_z \frac{\partial u_r}{\partial z} \right) = -\frac{\partial P}{\partial r} + \mu \left( \frac{1}{r} \frac{\partial}{\partial r} \left( r \frac{\partial u_r}{\partial r} \right) - \frac{u_r}{r^2} + \frac{1}{r^2} \frac{\partial^2 u_r}{\partial \theta^2} - \frac{2}{r^2} \frac{\partial u_\theta}{\partial \theta} + \frac{\partial^2 u_r}{\partial z^2} \right) \quad (10-7)$$

To simplify the above question and focus on the centrifugal force induced by the tangential flow, the pressure supply and hence the mass flow rate through the nozzles can be assumed to be zero, so that the system becomes axisymmetric. Then all the  $\partial/\partial\theta$  terms in the above equation can be dropped. Furthermore, with the similar scaling analysis in Chapter 2 for journal bearing flow, all the viscous terms except the last one can be negligible and the above equation becomes

$$\rho \left( u_r \frac{\partial u_r}{\partial r} - \frac{u_\theta^2}{r} + u_z \frac{\partial u_r}{\partial z} \right) = -\frac{\partial P}{\partial r} + \mu \left( \frac{\partial^2 u_r}{\partial z^2} \right). \quad (10-8)$$

With the mass conservation equation

$$\frac{1}{r} \frac{\partial}{\partial r} (r \rho u_r) + \frac{1}{r} \frac{\partial}{\partial \theta} (\rho u_\theta) + \frac{\partial}{\partial z} (\rho u_z) = 0, \quad (10-9)$$

one can find that  $u_\theta R \sim u_z/h$ , or  $u_z \ll u_\theta$ . Therefore,  $u_z \partial u_r / \partial z$  is negligible compared with  $u_\theta^2/r$  in Equation (10-8). Furthermore, since the ratio of  $\rho u_r \partial u_r / \partial r$  to  $\mu \partial^2 u_r / \partial z^2$  is on the order of 0.04, much smaller than 1, the former is negligible as well. Equation (10-8) then reduces to

$$\frac{\partial P}{\partial r} - \rho \frac{u_\theta^2}{r} = \mu \frac{\partial^2 u_r}{\partial z^2}. \quad (10-10)$$

The second term on the left-hand side of the above equation is the centrifugal force induced by the tangential flow. Assuming no flows through the nozzles, the flow in the thrust bearing is fully developed and hence the tangential flow is the Couette-type flow

$$u_\theta = \omega r z/h. \quad (10-11)$$

Substituting the above equation into (10-10), and with the non-slip boundary conditions  $u_r(0)=u_r(h)=0$ ,  $u_r(z)$  can be obtained:



$$u_r(z) = -\frac{\rho}{12\mu}\omega^2 r \frac{z(z^3 - h^3)}{h^2} + \frac{1}{2\mu} \frac{\partial P}{\partial r} z(z-h). \quad (10-12)$$

Integration with respect to  $z$  yields the flow rate in the radial direction  $Q_r$ :

$$Q_r = 2\pi r \left( -\frac{\rho}{12\mu}\omega^2 r \left( -\frac{3}{10}h^3 \right) + \frac{1}{2\mu} \frac{\partial P}{\partial r} \left( -\frac{1}{6}h^3 \right) \right) \quad (10-13)$$

Because of mass conservation and symmetry,  $Q_r$  should be equal to 0. Then, the pressure gradient can be derived from the above equation:

$$\frac{\partial P}{\partial r} = \frac{3}{10} \rho \omega^2 r. \quad (10-14)$$

Again, the air can be assumed to be isothermal. The integration of the above equation yields the pressure in the thrust bearing  $P$

$$P(r) = P_a \left[ \exp \left( \frac{3}{20} \frac{\rho_a}{P_a} \omega^2 (r^2 - R^2) \right) - 1 \right]. \quad (10-15)$$

Since the exponent ( $\sim 0.06$ ) is much smaller than 1 with the design speed ( $\omega=2.4$  MRPM) and thrust bearing radius ( $R=0.7$ mm), the expression above can be approximated as

$$P(r) = \frac{3}{20} \rho_a \omega^2 (r^2 - R^2). \quad (10-16)$$

Then, with the integration, one can find that the thrust force due to the centrifugal force caused by the rotor rotation  $F$  is

$$F = -\frac{3\pi}{40} \rho_a \omega^2 R^4. \quad (10-17)$$

The thrust force is independent of the bearing clearance  $h$ , indicating that the centrifugal force induced by the rotor rotation doesn't affect the axial stiffness. Furthermore, the above analysis is validated by the 3-D Fluent calculation, as shown in Figure 10-12.

It can also be seen that the thrust force due to centrifugal force is so small ( $\sim 0.003$ N) that it is negligible compared with the thrust force due to external static pressure ( $\sim 0.3$ N according to Figure 10-9). Furthermore, the corresponding pressure decrease ( $\sim 0.13$ psi) is also negligible compared with the pressure supply through the nozzles ( $\sim 60$ psi).

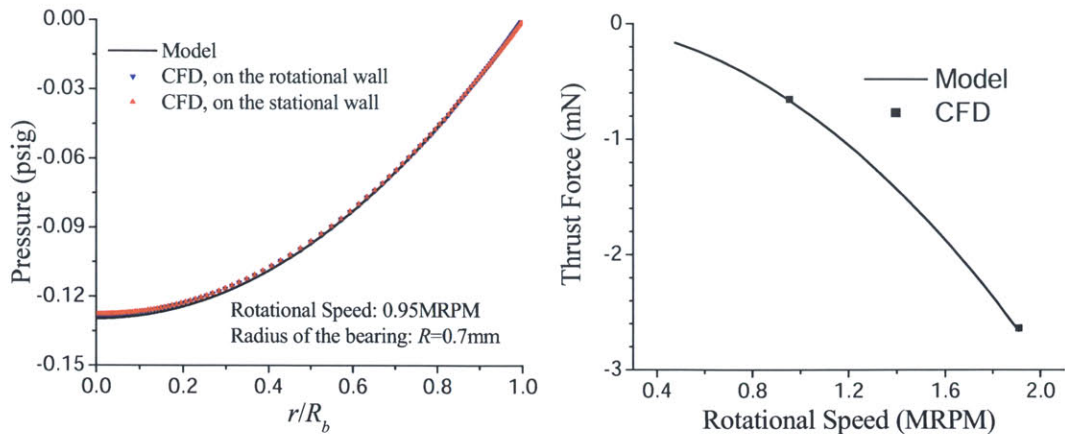


**Figure 10-12: Pressure distribution in the thrust bearing (left) and the thrust force (right) due to the centrifugal force, without flows through the nozzles, calculated by both the model and 3-D Fluent.**

Note that the above analysis assumes there are no flows through the nozzles. The following CFD results show that even with the flows through the nozzles, which can couple with the tangential flow induced by the rotor rotation, the thrust force decrease is still negligible.

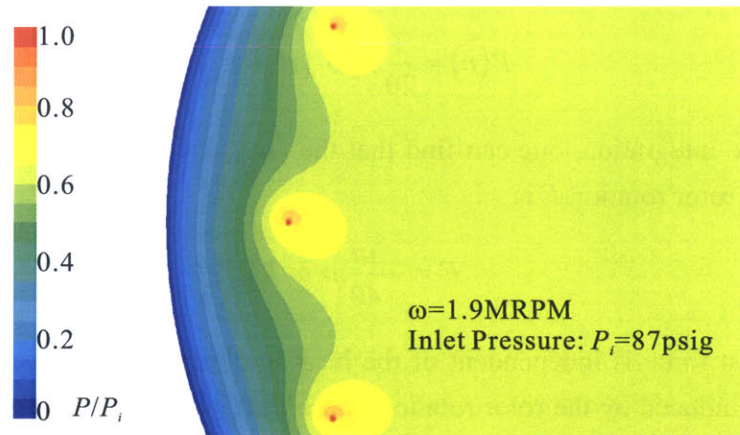


**Figure 10-13: Pressure distribution in the thrust bearing with rotor speed of 1.9 MRPM and supply pressure of 87 psig, calculated by 3-D Fluent.**

Since an analytical solution is impossible for this complicated problem because of the strong nonlinearity of Equation (10-3) with rotation, the 3-D CFD is employed to investigate the effect of the rotor rotation together with the flows through the nozzles on the thrust forces. Figure 10-13 shows the pressure distribution in the thrust bearing with both the pressure supply to the nozzles (87 psig) and the rotor rotation (1.9 MRPM) calculated by the 3-D Fluent. Compared with Figure 10-4, it can be seen that the pressure fields in

the vicinity of the nozzles are distorted by the rotor rotation. But this difference is only distinguishable in that small region. Therefore, the thrust force as the integration of the whole pressure field is not much affected by the rotor rotation, which is verified by the comparison between the CFD (3-D Fluent) results and model predictions listed in Table 10-1. The comparison shows that the rotor rotation coupled with nozzle flows can only induce a thrust force decrease of 2% to 4%, which is negligible.

	CFD results			Model
	0	0.95	1.9	
Rotational speed (MRPM)	0	0.95	1.9	-
Flow rate per nozzle (mg/s)	0.0396	0.0390	0.0386	0.0400
Pressure at the center (psig)	55.98	55.65	54.10	57.14
Thrust force (N)	0.495	0.495	0.486	0.5056

**Table 10-1: The flow rates, pressures, and thrust forces in the thrust bearing calculated by 3-D Fluent and the Image Method, with rotor rotation and supply pressure of 87psig.**

## 10.2 Annular Hydrostatic Thrust Bearing

Unlike the other micro-rotating devices, the micro-turbo-pump used an annular thrust-bearing configuration (Figure 1-7). Besides supporting the rotor axially, the forward annular thrust bearing used in this device also functioned as a seal which prevented the high-pressure liquid in the pump region (located at the center) from leaking to the turbine region (located in the outer space of the rotor). That was the major reason why annular thrust bearings were chosen instead of circular ones. How the forward annular thrust bearing acts as a seal is discussed by Teo in [9] and is not covered here. This section only focuses on using the Image Method to calculate the thrust force.

The sketch in Figure 10-14 shows the structure of the annular thrust bearings used in the micro-turbo-pump devices with the dimensions and the typical pressure distribution in the bearing calculated by 3-dimensional CFD (3-D Fluent).

The gas in the annular thrust bearing is governed by the same equation as the circular one—the Poisson equation (10-4)—but with different boundary conditions: the pressure at the outer boundary is the atmospheric pressure,  $P(R_O)=P_a$ , and the pressure at the inner boundary is the pump pressure,  $P(R_I)=P_{pump}$ . In order to use the Image Method, a series of image points are needed to mimic the boundary conditions (details can be found in Appendix C). The comparison in Figure 10-15 between the pressures calculated by the Image Method and 3-D Fluent shows that the Image Method also works well for the micro-hydrostatic annular thrust bearings.

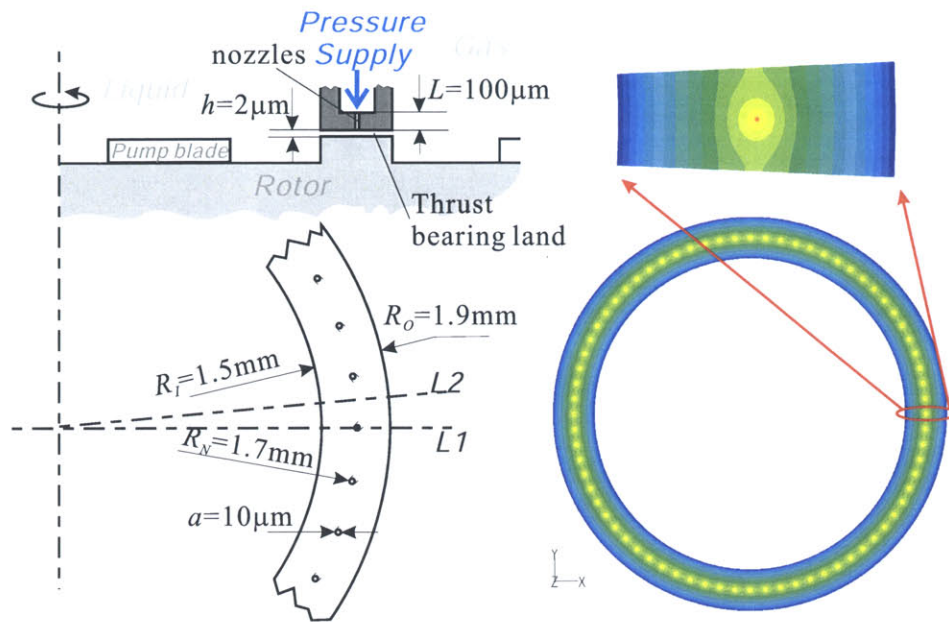


**Figure 10-14: Structural sketch (left, not to scale) of the micro-hydrostatic annular thrust bearing and the pressure distribution in the bearing calculated by 3-D Fluent.**

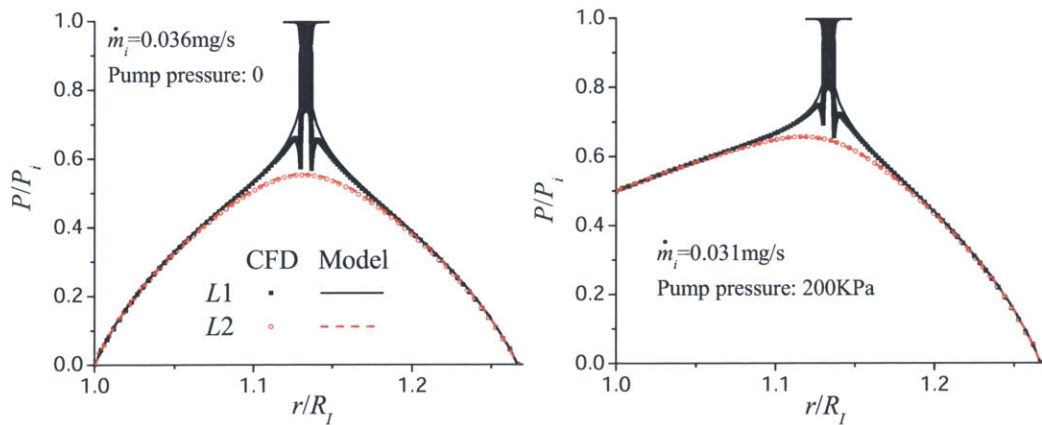


**Figure 10-15: Pressure distributions normalized by the inlet pressure along symmetry lines L1 and L2 in the micro-hydrostatic annular thrust bearing with pump pressures 0 (left) and 29 psig (right), compared with the CFD results.**

Using the same loss models derived in the last section for the circular thrust bearings, the mass flow rates through the nozzles in the annular thrust bearings can be calculated with given pressure supplies. Then, the pressure field in the annular thrust bearing and hence the thrust force are obtained as functions of the pressure supply to the bearing.

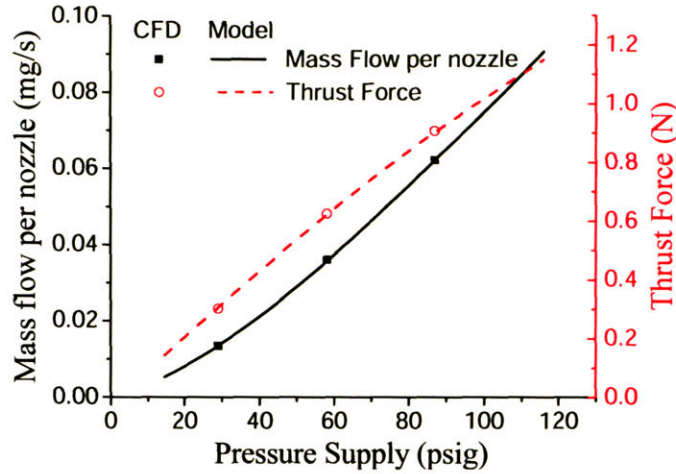


**Figure 10-16: Mass flow rate per nozzle and thrust force calculated by the model for the annular thrust bearing, compared with the CFD results.**

Figure 10-16 shows that the Image Method together with the loss model also matches the CFD results and hence works well in the annular thrust bearing.

### 10.3 Tilting stiffness

Besides the axial stiffness, the tilting stiffness provided by the circular thrust bearing is also important to the micro-rotating devices, as discussed in Chapter 6. The tilting stiffness can be calculated by the Green's Function [10]. The following analysis shows that it can also be calculated by the Image Method with perturbation.

When the rotor is tilted by a infinitesimal angle  $\alpha$ , the clearance of the thrust bearing is  $h(r, \theta) = h_0 + \alpha r \cos(\theta) = h_0(1 + \varepsilon \cos(\theta)/R_b)$ , where  $\varepsilon \equiv \alpha R_b/h_0 \ll 1$ . Substituting this into Equation (10-3) and assuming the rotational speed is zero again, the expansion of Equation (10-3) to the first order of  $\varepsilon$  can be obtained:

$$\begin{aligned} \frac{1}{r} \frac{\partial}{\partial r} \left( r \left( 1 + 3\varepsilon \frac{r}{R} \cos(\theta) \right) \frac{\partial P^2}{\partial r} \right) + \frac{1}{r^2} \frac{\partial}{\partial \theta} \left( \left( 1 + 3\varepsilon \frac{r}{R} \cos(\theta) \right) \frac{\partial P^2}{\partial \theta} \right) + O(\varepsilon^2) \\ = -\frac{24\mu}{h_0^3} \frac{P_a}{\rho_a} \sum_i \dot{m}_i \delta(\vec{r} - \vec{r}_i). \end{aligned} \quad (10-18)$$

The solution of  $P^2$  with the perturbation of the tilt can be written as

$$P^2 = P_0^2 + \varepsilon P_1^2 + O(\varepsilon^2). \quad (10-19)$$

Substituting the above equation into (10-18) and then collecting the terms of order  $\varepsilon^0$  yields



$$\Delta P_0^2 = -\frac{24\mu P_a}{h_0^3 \rho_a} \sum_i \dot{m}_i \delta(\bar{r} - \bar{r}_i). \quad (10-20)$$

The above equation of  $P_0$  is exactly the same as Equation (10-4), and thus has the solution shown in Figure 10-4. Furthermore, the equation of  $P_1$  can be derived by collecting the terms of order  $\varepsilon^1$ :

$$\begin{aligned} \Delta P_1^2 &= -3 \left[ \frac{1}{r} \frac{\partial}{\partial r} \left( r \frac{r}{R_b} \cos(\theta) \frac{\partial P_0^2}{\partial r} \right) + \frac{1}{r^2} \frac{\partial}{\partial \theta} \left( \frac{r}{R_b} \cos(\theta) \frac{\partial P_0^2}{\partial \theta} \right) \right] \\ &= -3 \left[ \cos(\theta) \frac{r}{R_b} \Delta P_0^2 + \frac{\cos(\theta)}{R_b} \frac{\partial P_0^2}{\partial r} - \frac{\sin(\theta)}{r R_b} \frac{\partial P_0^2}{\partial \theta} \right]. \end{aligned} \quad (10-21)$$

The first term on the right-hand side of the above equation is given by Equation (10-20), and the last term is around zero and symmetric about the symmetry lines  $L1$  and  $L2$  according to Figure 10-4, so its contribution to  $P_1$  is negligible. Then the above equation can be solved with the approximation of the second term on the right-hand side as shown in the analysis below.

The mass flow rate in the radial direction induced by  $P_0$  is

$$\dot{m}_{r,0} = -\frac{h_0^3 \rho_a}{24\mu P_a} \frac{\partial P_0^2}{\partial r}. \quad (10-22)$$

Due to the symmetry of the system and mass conservation, the above equation can be approximated as

$$\dot{m}_{r,0} \cong \Theta(r - R_N) \sum \dot{m}_i / 2\pi r, \quad (10-23)$$

where  $\sum \dot{m}_i$  is the total mass flow rate through all the nozzles,  $\Theta(x)$  is the step function with a value of 1 when  $x \geq 0$  and 0 when  $x < 0$ , and  $R_N$  is the radial location of the nozzles. Then Equation (10-21) becomes

$$\Delta P_1^2 \cong \frac{72\mu P_a}{h_0^3 \rho_a} \cos(\theta) \left[ \frac{r}{R_b} \sum_i \dot{m}_i \delta(\bar{r} - \bar{r}_i) + \frac{\Theta(r - R_N)}{2\pi r R_b} \sum_i \dot{m}_i \right]. \quad (10-24)$$

Furthermore, the second term in the square brackets of the above equation is an area flow source distributed between  $R_N$  and  $R_b$ . This source can be divided into slices of the same number of nozzles. As an approximation, each slice can then shrink to the position of the corresponding nozzle, and hence becomes a point source with an intensity of



$$\int_{R_N}^{R_b} \frac{\dot{m}_i}{2\pi r} dr = \dot{m}_i \cdot (R_b - R_N). \quad (10-25)$$

Thus Equation (10-21) can be approximated as

$$\begin{aligned} \Delta P_1^2 &\cong \frac{72\mu}{h_0^3} \frac{P_a}{\rho_a} \cos(\theta) \left[ \frac{r}{R_b} \sum_i \dot{m}_i \delta(\bar{r} - \bar{r}_i) + \frac{R_b - R_N}{R_b} \sum_i \dot{m}_i \delta(\bar{r} - \bar{r}_i) \right] \\ &= \frac{72\mu}{h_0^3} \frac{P_a}{\rho_a} \cos(\theta) \sum_i \dot{m}_i \delta(\bar{r} - \bar{r}_i) \end{aligned} \quad (10-26)$$

Combining Equations (10-20) and (10-26) yields the equation of the total pressure  $P$  in the thrust bearing, according to Equation (10-19):

$$\Delta P^2 \cong \Delta(P_0^2 + \varepsilon P_1^2) \cong -\frac{24\mu}{h_0^3} \frac{P_a}{\rho_a} \sum_i (1 - 3\varepsilon \cos(\theta_i)) \dot{m}_i \delta(\bar{r} - \bar{r}_i). \quad (10-27)$$

Thus the original problem (non-uniform bearing clearance with the tilted thrust pad) can be approximated to a simpler one, in which the clearance is kept uniform while the mass flow rate through each nozzle is modulated according to the equation above. The tilting torque can then be approximately calculated by the Image Method, and hence the tilting stiffness can be determined. The calculated results for the thrust bearings used in the micro-turbo-charger device are shown in Figure 10-17.

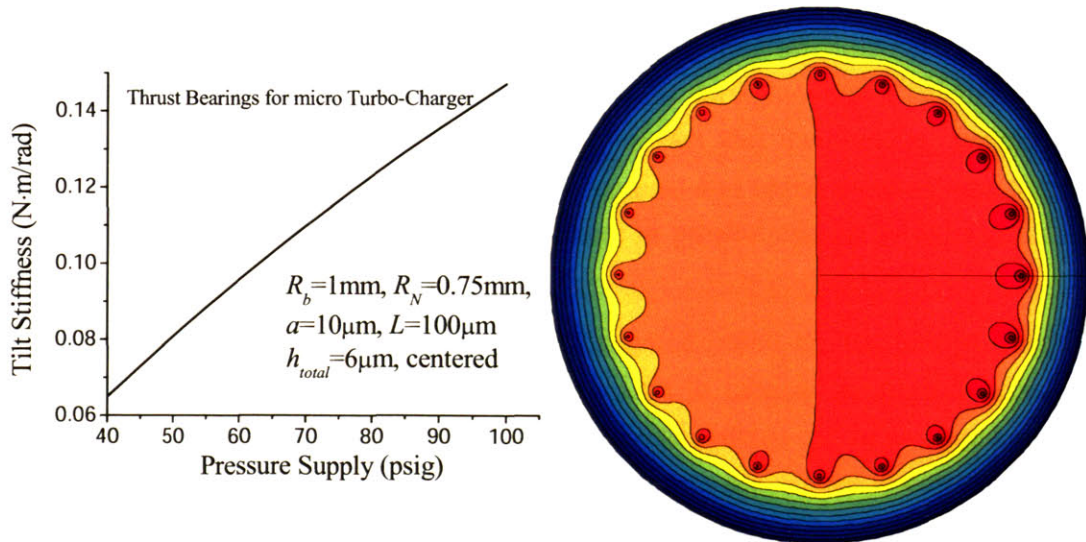


**Figure 10-17: Tilting stiffness (left) and pressure field (right, 70 psig supply and  $2 \times 10^{-4}$  rad tilting angle) in the thrust bearings of the micro-turbo-charger device by the Image Method.**

### ***10.4 Summary and Conclusions***

The Image Method has been used to investigate the hydrostatic thrust bearings in the micro-devices. With this approach, the pressure field in the thrust bearing and hence the thrust force can be calculated for both circular and annular thrust bearings, and the results are validated by both the CFD calculations and the experimental data. Furthermore, the tilting stiffness in circular thrust bearing can also be calculated by this method with perturbation.

The effect of rotor rotation on the pressure in the thrust bearing was also investigated using both the analytical approach and 3-dimensional CFD (Fluent). The results show that the decrease in pressure and thrust force due to centrifugal body force caused by the tangential flow in the bearing induced by rotor rotation is negligible compared to that induced by the high external static pressure supply.

Since the Image Method doesn't involve numerical calculation of the two-dimensional Reynolds equation, it is much faster than the Green's Function method. Thus, it is the recommended method for fast evaluation of the thrust bearing axial and tilting stiffness. However, since it cannot solve the original Reynolds equation in which the rotor rotation and the non-uniformity of the bearing clearance are coupled together, the Image Method cannot be used to solve the hydrodynamic pressure in the thrust bearing induced by rotor pumping action. Thus, in order to calculate the hydrodynamic torque in the thrust bearing due to the rotor pumping effect when the rotor is tilted, a numerical scheme is still needed.

## *Chapter 11*

# **Journal-Bearing System Design for Self-Sustained Micro-Engine**

The self-sustained micro-engine (SSME) currently under development at MIT GTL is a prototype micro-engine that can self-sustain and output power, with the major challenge of closing the system thermodynamic cycle. The goal of this project is to design and fabricate this self-sustained micro-engine system with all the components (micro-turbine, micro-compressor, micro-bearing, and micro-combustor) integrated and to demonstrate the break-even operation experimentally.

Based on the models and knowledge of journal-bearing systems obtained in the previous chapters, journal-bearing systems for the self-sustained micro-engine devices are investigated and designed in this chapter. The micro-bearing design for the self-sustained micro-engine is challenging for several reasons: 1) the relatively heavy rotor (over 700mg, compared with 10mg in the micro-bearing rig); 2) a low damping ratio due to the limited bearing length (less than 450 $\mu\text{m}$ ) and the heavy rotor, resulting in a small distance to contact; 3) variation of the bearing clearance (over 10 $\mu\text{m}$ ) during operation due to the thermal and centrifugal expansion of the rotor; 4) the fact that dual-bearing systems are needed to eliminate coupling between the rotor conical and radial motions; and 5) misalignment between the two micro-journal bearings in parallel caused by fabrication imperfections.

Meanwhile, dual-bearing systems are investigated based on the journal bearings used in the self-sustained micro-engine devices. Due to fabrication imperfections, the misalignment between the two journal bearings in these systems can be as large as 6  $\mu\text{m}$ . In these misaligned dual-bearing systems, four parameters are needed to describe the rotor imperfection instead of the single unbalance used in the single-bearing system. According to the numerical simulation results, the rotor camming motion due to the misalignment is found to reduce both the distance to contact and the stability boundary of the dual-bearing systems.

Last, several designs are suggested for self-sustained micro-engine devices with misalignment of  $6\ \mu\text{m}$  and without any misalignment.

### 11.1 Design Requirements for Micro-Journal-Bearing Systems Used in Self-Sustained Micro-Engines

According to Sirakov [35], the design speed of the self-sustained micro-engine is 600Krpm and the rotor will be made of several silicon layers, as shown in Figure 11-1.

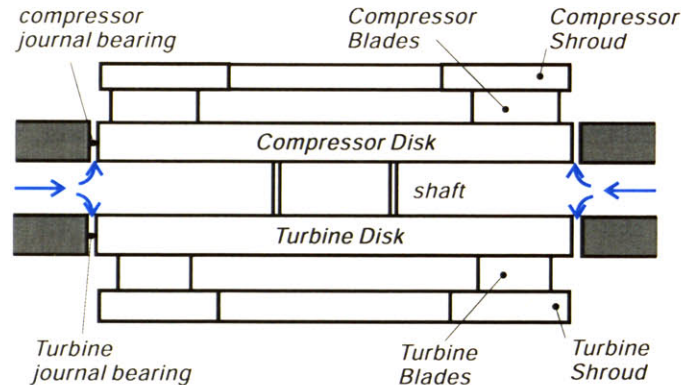


**Figure 11-1: Sketch of the self-sustained micro-engine rotor (thrust bearing pads are not shown and the sketch is not to scale).**

Both the turbine and the compressor disks have a radius of 8mm and a thickness of  $450\ \mu\text{m}$ . The generator is integrated in the compressor shroud. Due to the high rotor speed and tall blades ( $800\ \mu\text{m}$ – $990\ \mu\text{m}$ ), the centrifugal force on the blades can bend the two disks; thus, both shrouds are also designed to reduce the bending moment and hence the disk deformation. The mass of the whole rotor is 733mg, with a rotor unbalance of about  $1\ \mu\text{m}$  according to [4] and [31]. Compared with the rotor mass in the previously discussed micro-rotating devices (10mg for the micro-bearing rig, 25mg for the micro-turbo-pump, and 70mg for the micro-turbo-charger), the rotor mass of the self-sustained micro-engine is one order of magnitude higher.

According to Chapter 5, coupling between the rotor radial and conical motions can destabilize the system and should be avoided. Therefore, with the rotor structure depicted in Figure 11-1, the journal bearings should be located at the circumferential peripheries of both the compressor and the turbine disks, with the air fed from between the two disks, so that the coupling can be eliminated.

Furthermore, in order to implement the hydrostatic stiffness anisotropy, the turbine shroud needs to be replaced by a compensation ring, as shown in the sketch of Figure



11-2. The compensation ring has two functions in the self-sustained micro-engine devices: to balance the bending momentum induced by the centrifugal force on the turbine blades and to seal the flow between the feeding plena.

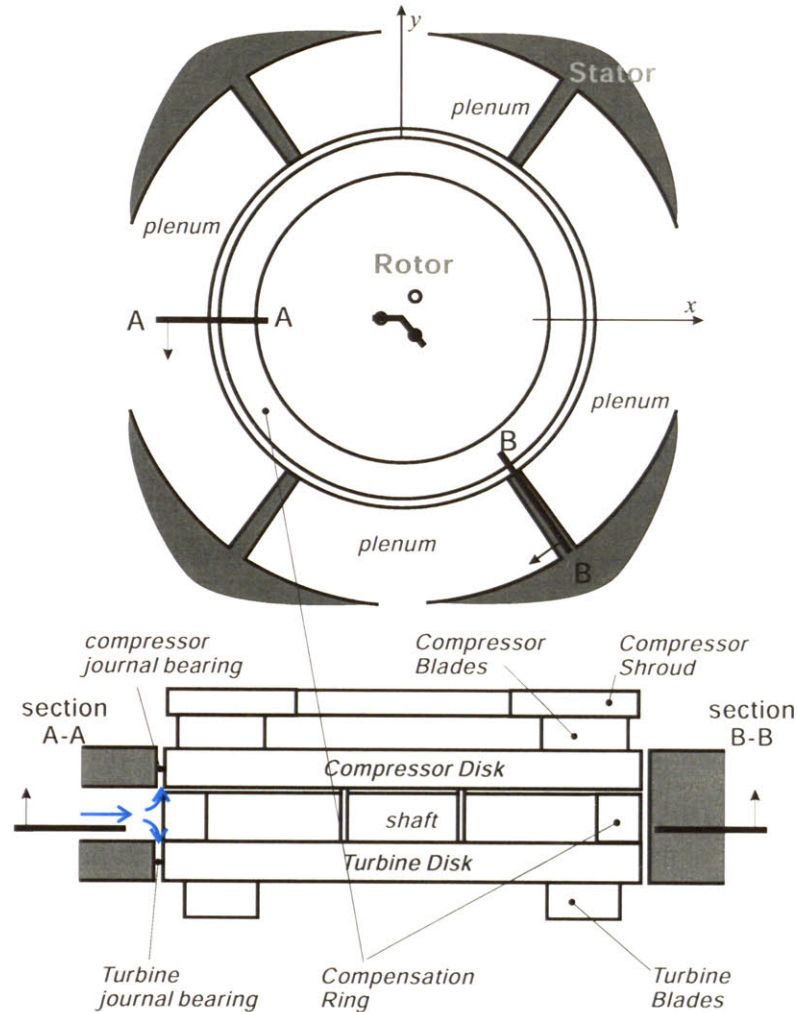


**Figure 11-2: Implementation of the anisotropic journal bearings in the self-sustained micro-engine devices (not to scale).**

Under the operating condition, the hot exhaust air (over 1000 Kelvin) from the combustor can heat both the static structure and the rotor. According to [35], the temperature of the static structure is about 688K, and the turbine disk temperature is 891K. To prevent heat transfer from the turbine disk to the compressor disk, which can impair the compressor's performance, thermal isolation shafts are used, as shown in the sketch. As a result, the temperature of the compressor disk is about 475K. The temperature differences between the static structure and the rotor can change both the journal bearing clearances under operating conditions due to thermal expansion. With the linear thermal expansion

coefficient of silicon (which is  $\sim 4 \times 10^{-6} \text{K}^{-1}$  in this temperature range), the clearance of the compressor journal bearing can increase by  $6.8 \mu\text{m}$ , while the clearance of the turbine journal bearing can decrease by  $6.5 \mu\text{m}$ . Furthermore, the centrifugal force of the disks due to the high rotating speed can also expand the rotor and hence reduce both journal bearing clearances by  $3 \sim 5 \mu\text{m}$  at the design speed according to [36].

As the start protocol, the rotor is inverted at a low pressure difference across the journal bearings  $\Delta p$  without ignition. Spinning supercritically, it is accelerated to the design speed cold at high  $\Delta p$ , and the combustor is then ignited. After ignition, the rotor spins at the design speed and eventually reaches the temperatures stated above.

	Crossing the natural frequency, cold	Accelerated to the design speed before the ignition of combustor	At the design speed and normal operating conditions
Clearance of the turbine journal bearing	$h_t$	$h_t - 5 \mu\text{m}$	$h_t - 11.5 \mu\text{m}$
Clearance of the compressor journal bearing	$h_c$	$h_c - 3 \mu\text{m}$	$h_c + 3.8 \mu\text{m}$

**Table 11-1: Clearances of the turbine and the compressor journal bearings under different operating conditions.**

During this start procedure, the clearances of the journal bearings vary according to the operating conditions as summarized in Table 11-1, assuming the fabricated clearances of the turbine journal bearing and the compressor journal bearing are  $h_t$  and  $h_c$  respectively. Note that, as the rotor accelerates across the system's natural frequency, the rotational speed is low; hence, the centrifugal force is small, and at this speed, the combustor is not ignited yet. Therefore, under these conditions, the bearing clearances are essentially unchanged from the fabricated ones. However, they can vary as much as  $11.5 \mu\text{m}$  during the whole start procedure. This is one of the major challenges to designing a successful journal-bearing system for the self-sustained micro-engine devices.

Although it is easier to invert the rotor at a lower pressure difference across the journal bearings  $\Delta p$ , the lowest reliable and feasible  $\Delta p$  that could be used experimentally to invert the rotor is about 0.2psig according to [31]. Therefore, when designing the journal bearing systems used for the self-sustained micro-engine devices, the following requirements should be satisfied:

1. The rotor has sufficient distance to contact (larger than the threshold normalized distance to contact obtained in Chapter 5) at  $\Delta p$  of 0.2psig to be inverted.



2. The rotor can be accelerated to high speed when the system is cold; i.e., the stability boundary of the journal-bearing system with the centrifugal expansion but without the thermal expansion should be higher than the design speed of 600Krpm.
3. The rotor can spin stably under operating conditions; i.e., the stability boundary of the journal-bearing system with both the centrifugal and the thermal expansion should be higher than the design speed.

### ***11.2 Dual-Bearing System without Wafer Misalignment***

As shown in Figure 11-2, in order to eliminate the coupling between the rotor radial and conical motions, a dual-bearing configuration is used in the self-sustained micro-engine devices.

If the two bearings are etched at the same time after the two disks are bonded together (or “single cut” according to [4]), they can be perfectly aligned.

Generally, if the second bearing is identical to the first one, the system stiffness and damping coefficient are twice as large as the ones in the original systems. Then, the natural frequency of the dual-bearing system is  $\sqrt{2}$  of the natural frequency of the original single-bearing counterpart. According to the analyses in Chapter 2 (Equation (2-40)), the peak amplitude of the rotor response curve is smaller in the new system, resulting in a larger distance to contact, because the unbalances are same in both systems. Meanwhile, since the stability boundary of the anisotropic journal-bearing system is mainly determined by the ratio of the hydrostatic stiffness anisotropy to the intrinsic hydrodynamic stiffness, it does not change in the new system. So, adding the second identical bearing can improve the system dynamics by increasing the distance to contact and stiffness while maintaining the stability boundary.

However, since the variations of the two bearing clearances are different during operation (Table 11-1), it is not necessarily the optimal design to make the two bearings identical. To find the optimal design with different bearing clearances, Figure 11-3 of the distance to contact and stability boundary contours are generated by the numerical simulations. The horizontal axis is the compressor journal bearing clearance  $h_c$  in microns, while the vertical one is the turbine journal bearing clearance  $h_t$  in microns. Both the clearance values on the axes indicate the original clearances (without the thermal and centrifugal expansion of the rotor), or the bearing clearances just after fabrication.

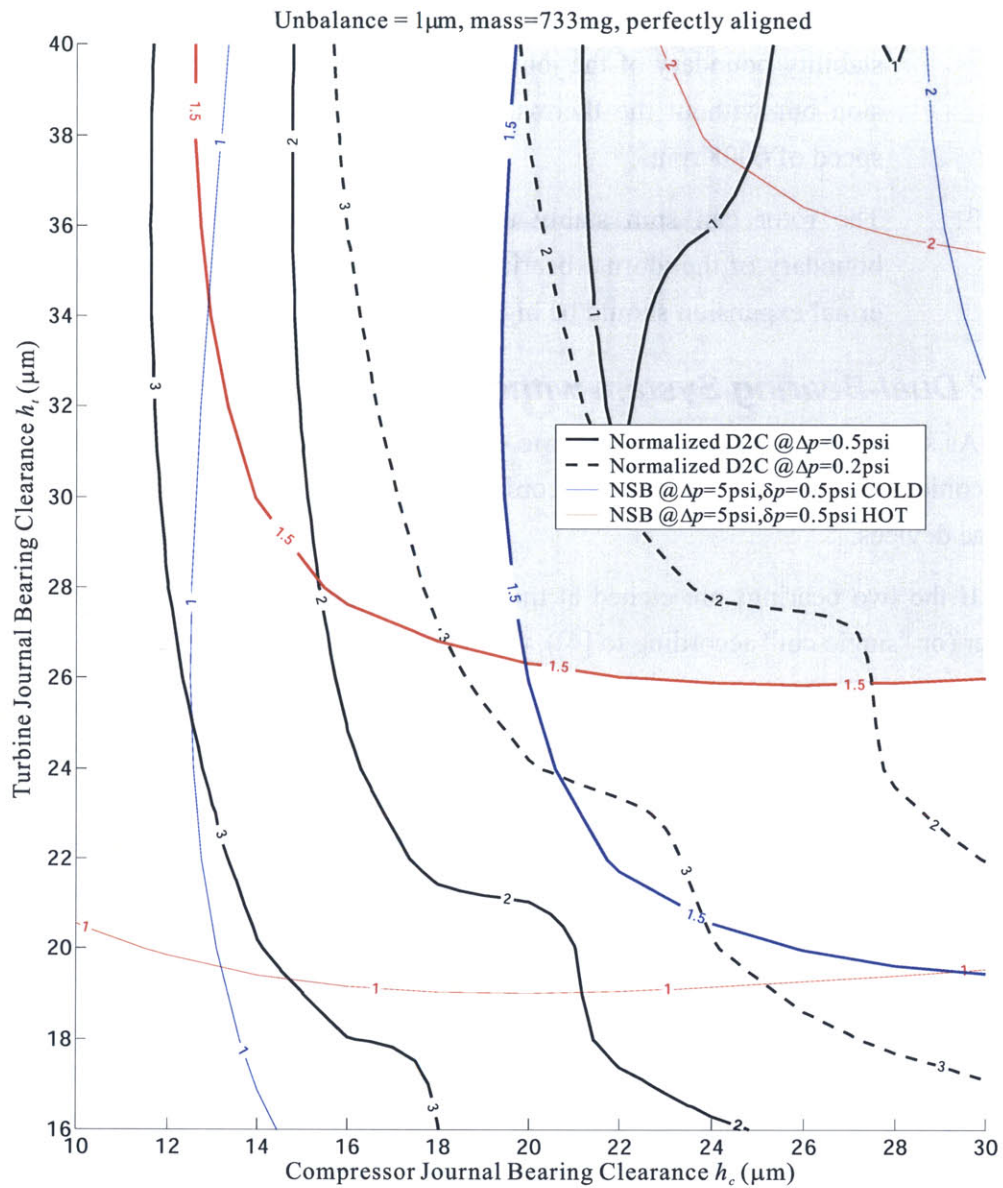


**Figure 11-3: Distance to contact and stability boundary as functions of bearing clearances for perfectly aligned dual-bearing systems.**

The numbers on the black solid lines are the normalized distance to contact with a given set of clearances at a pressure difference across the journal bearings  $\Delta p$  of 0.5psig. By “normalized,” it means the ratio of the smallest distance to contact normalized by the corresponding bearing clearance in the two journal bearings to the threshold, which is 0.09, derived in Chapter 5. Therefore, if the number is larger than 1, the rotor can be inverted at  $\Delta p$  of 0.5psig with the given set of bearing clearances. The numbers on the black dotted lines are the normalized distance to contact with the given set of bearing

clearances at  $\Delta p$  of 0.2psig. Obviously, with smaller  $\Delta p$ , the distance to contact is larger and it is easier for the rotor to be inverted.

The numbers on the blue solid lines are the normalized stability boundary with a given set of bearing clearances when the system is cold, at pressure difference across the journal bearings  $\Delta p$  of 5psig and with the sideload  $\delta p$  of 0.5psi (the pressure difference between the pairs of plena in opposite directions, which is common according to the previous experiments [30]). Here, by “normalized,” it means the ratio of the stability boundary to the design speed (600Krpm). Therefore, if the number is larger than 1, the stability boundary of the system is higher than the design speed with the given bearing clearances. For example, on the lines numbered 1.5, the stability boundary is  $1.5 \times 600\text{Krpm}$  (=900Krpm).

It is important to note that since the rotor expands at high speed, both bearing clearances decrease as the speed increases. Thus, in the simulations to calculate the above system stability boundary, the decreased bearing clearances are computed according to the equation below and accounted for, assuming both the turbine and the compressor disks are plain cylindrical disks:

$$\Delta h = -2.524 \times 10^{-9} R^3 \omega^2. \quad (11-1)$$

Therefore, the clearances with which the stability boundary is calculated are actually smaller than the fabricated ones. For example, on the blue lines of 1.5, the actual bearing clearances of both the journal bearings at the threshold speed of onset of instability (900Krpm) are  $11.5\mu\text{m}$  smaller than the original/fabricated ones. This is a large decrease compared with the bearing clearances themselves (about  $20\mu\text{m}$ ).

The numbers on the red solid lines are the normalized stability boundary with a given set of bearing clearances when the self-sustained micro-engine is hot and under normal operating conditions after ignition, at the pressure difference across the journal bearing  $\Delta p$  of 5psig and with the sideload  $\delta p$  of 0.5psi. Due to the thermal expansion of both the static structure and the rotor, the bearing clearances are further changed from the ones with the centrifugal force effect. According to the analysis in the last section, the clearance of the turbine journal bearing can further decrease by  $6.5\mu\text{m}$  from the cold system at the same speed, while the clearance of the compressor journal bearing can increase by  $6.8\mu\text{m}$ . Therefore, as a example, on the red lines marked 1.5 (speed of 900Krpm and hot), the turbine journal bearing clearance is a total of  $18\mu\text{m}$  smaller than the original/fabricated one, while the compressor journal bearing clearance is a total of  $4.7\mu\text{m}$  smaller.

Thus, based on the contours and design requirements described at the beginning of this chapter, the acceptable designs lie in the space below the black dotted line numbered 1, above the red line, and right to the blue solid lines numbered 1. However, with 50% safety margins for the stability boundary, the acceptable design space then shrinks to the up right corner (the shaded area in Figure 11-3).

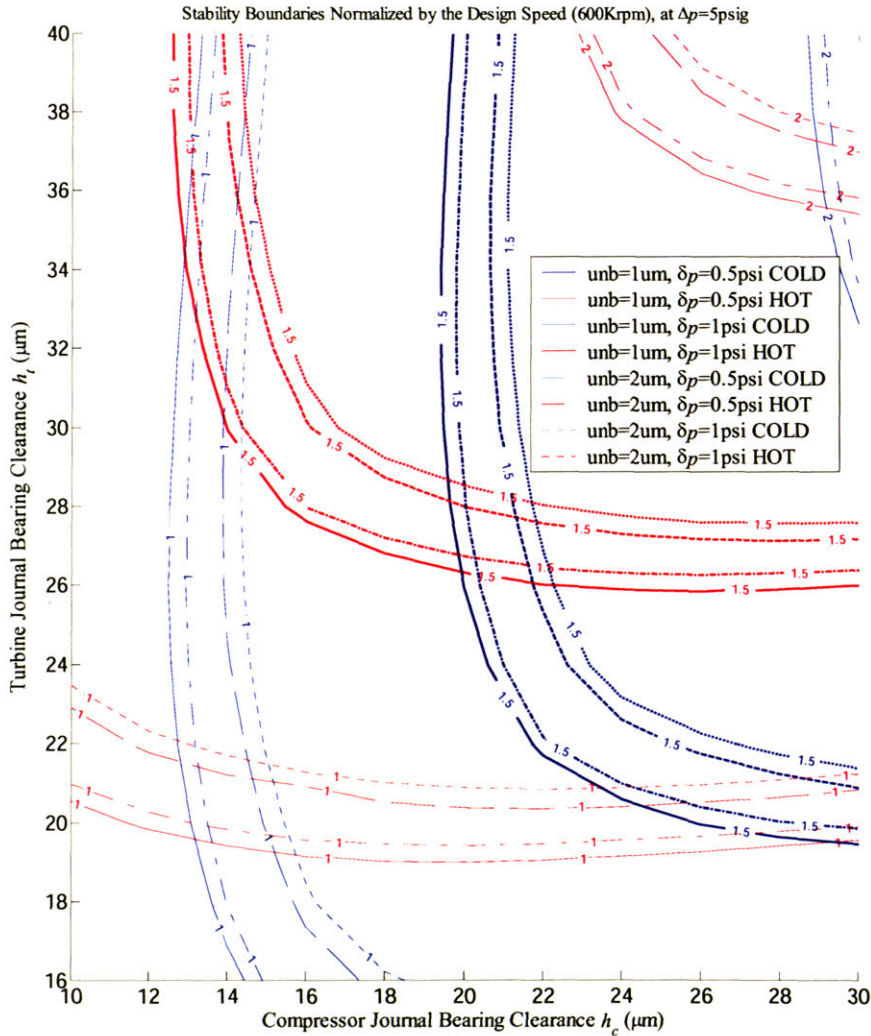


**Figure 11-4: Rotor unbalance and bearing side load  $\delta p$  reduce the stability boundary.**

In order to further investigate the sensitivity of the stability boundary to the rotor unbalance and the bearing side load, the contours in Figure 11-4 are generated. It can be seen that the side load has a larger negative influence on the stability boundary than the rotor unbalance does. Furthermore, the 50% safety margin is enough to compensate for the decreases in the stability boundary due to these two effects.

In the above calculations as well as the ones following, to calculate the bearing forces in the simulations, the flow is assumed to be a fully developed quasi-steady flow, as in Chapter 2. Furthermore, because the length-to-diameter ratio and the gap (distance between the two bearings)-to-diameter ratio of the micro-bearing systems in the self-sustained micro-engine are on the order of 0.03, the rotor can be approximated as a thin disk.

### 11.3 Dual Bearing System with Wafer Misalignment

The above contours are for the dual-bearing system without misalignment between the two bearings, which can be achieved by the “single cut”—etching the two bearings in a line after the two disks are bonded together. However, this technology is far from feasible yet, because the bearing to be etched in the “single cut” is longer than 1mm, making its aspect ratio out of the range that can be etched based on today’s technology.

So, it is more realistic to etch the two journal bearings at the turbine disk and the compressor disk separately before bonding. With this method, there is always a certain wafer misalignment between the two disks due to the imperfections of machines and the fabrication processes. The analyses below show that this misalignment can have a great impact on the dynamic behavior of the system.

#### 11.3.1 Rotor Camming Motion Due to Wafer Misalignment

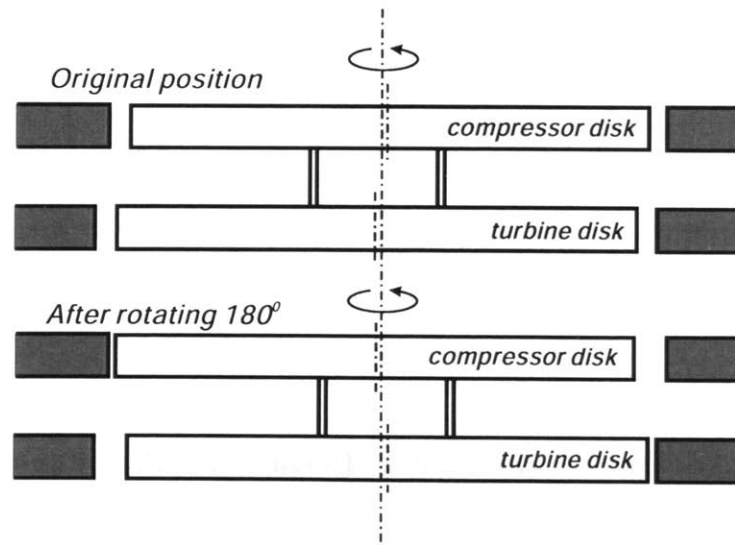


Figure 11-5: Rotor camming motion due to misalignment between the two journal bearings in a dual-bearing system.

As shown in Figure 11-5, when there is a misalignment between the two bearings/disks, the rotor engages in a camming motion when it spins.

With the fabricated/original position, both disks are sitting at the centers of their corresponding bearings, and hence the bearing clearances around them are uniform. However, when the rotor rotates around a certain axis by 180 degrees, the clearances are no longer uniform. Moreover, if the misalignment is large enough (compared with the bearing clearance), the rotor can touch the bearing wall, and then it can no longer rotate.

Even if the misalignment is small, one can see that both clearances keep changing and are functions of time as the rotor rotates. Thus, the rotor camming motion makes the system time-dependent. With this nonlinear effect, the system dynamics can only be investigated by numerical simulations.

### 11.3.2 Parametric Description of Rotor Imperfection

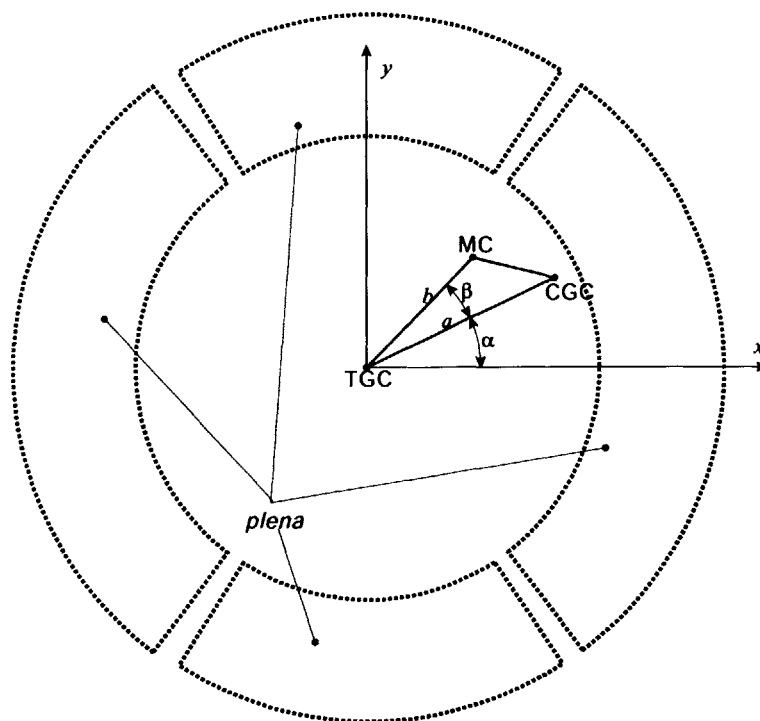


**Figure 11-6: Four parameters required to describe the rotor imperfection in dual-bearing systems with wafer misalignment.**

In the single-bearing system, only one parameter is needed to describe the imperfection of the rotor: the unbalance that represents the distance from the mass center to the geometric center of the rotor. However, in the dual-bearing system with wafer misalignment, one parameter is not enough because there are three centers on the rotor, as shown



in Figure 11-6: the compressor geometric center (CGC), the turbine geometric center (TGC), and the mass center of the whole rotor (MC).

Since the three centers do not coincide with the wafer misalignment, they form a triangle and thus three parameters are needed to describe the locations relative to each other: the misalignment  $a$  (distance from TGC to CGC), the distance from the MC to the TGC  $b$ , and the angle between segments TGC-CGC and TGC-MC  $\beta$ . Moreover, to describe the direction of the wafer misalignment relative to the static structure (or the anisotropy), another parameter is needed: the angle  $\alpha$  between TGC-CGC and the  $x$  axis.

According to [4], the wafer misalignment between the compressor and turbine disks  $a$  can be as large as  $6\mu\text{m}$  (the worst case), with the most possible value about  $4\mu\text{m}$ . This misalignment can be in any direction, so that  $\alpha$  varies from 0 to  $2\pi$ .

Besides the wafer misalignment between the two disks/bearings, there are other misalignments in the multi-layer rotor. They are the misalignments of each layer relative to the next one due to the photo-resist pattern misalignments. These misalignments are typically  $2\mu\text{m}$  according to [4], and also occur in random directions. With this information and the mass of each layer, it can be derived that the mass center (MC) of the whole rotor lies in the shaded circle shown in the sketch of Figure 11-7.

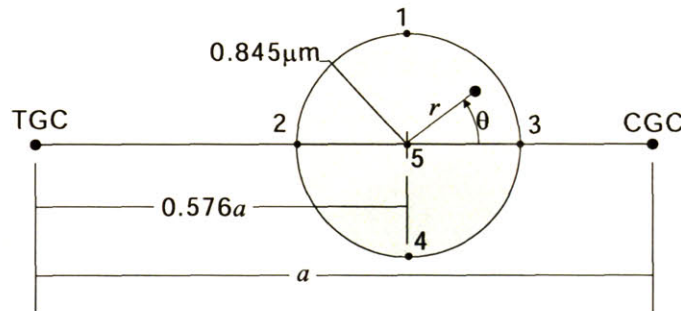


**Figure 11-7: Mass center of the rotor lies in a circle located between the geometric centers of the turbine and compressor disks.**

The center of the circle (point 5) is located on the segment TGC-CGC and  $0.576a$  from the TGC. The radius of the circle is  $0.845\mu\text{m}$ . Therefore, the parameters  $b$  and  $\beta$ , which describe the relative location of the mass center, can be determined. It is convenient to replace them with another two parameters: the distance from the mass center to the center of that circle  $r$ , and the direction of the mass center relative to the segment TGC-CGC  $\theta$ . Then,  $r$  is smaller than  $0.845\mu\text{m}$ , and  $\theta$  can vary from 0 to  $2\pi$ .

To successfully design a dual-bearing system with all the imperfections in the rotor, the designed system should be able to be inverted (cross the natural frequency) and accel-

erated to the design speed with all possible combinations of  $a$ ,  $\alpha$ ,  $r$  and  $\theta$  from normal fabrication. In other words, given a pair of bearing clearances  $h_t$  and  $h_c$ , systems with all possible combinations of  $a$ ,  $\alpha$ ,  $r$ , and  $\theta$  must be simulated to see whether all the possible systems can reach the design criteria with this pair of clearances  $h_t$  and  $h_c$ . Because there are infinite possible combinations, it is not feasible to do simulations with all the combinations. Therefore, several representative values are chosen for each of these four parameters to check whether the possible systems with these limited combinations of the four parameters can satisfy the design requirements.

Since the angles  $\alpha$  and  $\theta$  are evenly distributed from 0 to  $2\pi$ , their representative values should also be evenly distributed from 0 to  $2\pi$ . Thus, the representative mass center angles  $\theta$  are chosen as  $0^\circ$ ,  $90^\circ$ ,  $180^\circ$ , and  $270^\circ$ , or the points 1, 2, 3, and 4 in Figure 11-7. The misalignment angles  $\alpha$  can be chosen as  $0^\circ$ ,  $30^\circ$ ,  $60^\circ$  and  $90^\circ$  due to the symmetry of the system as shown in Figure 11-6.

### 11.3.3 Design Guidelines for Dual-Bearing Systems with Most-Likely Imperfection

According to [4], the most possible wafer misalignment between the two disks  $a$  is  $4\mu\text{m}$ . Thus  $4\mu\text{m}$  is chosen as the representative value of the wafer misalignment  $a$ . Furthermore, using the Monte Carlo method, the distribution pattern of the mass center in the rotor frame can be derived as shown in Figure 11-8.

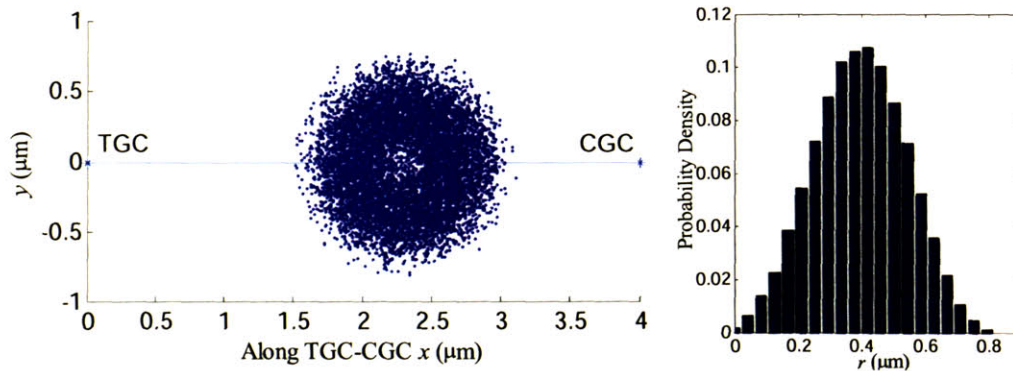


**Figure 11-8: Mass center distribution in the rotor frame.**

The plot on the left-hand side shows simulation results with 10,000 samples. It can be seen that the mass center is located in the circle with a radius of  $0.8454\mu\text{m}$ . The plot on the right-hand side in Figure 11-8 shows the probability density of  $r$ . Since the density function peaks at about  $0.45\mu\text{m}$ ,  $r=0.5\mu\text{m}$  is chosen as the representative value in the most possible case. Thus, with these two representative values of  $a$  and  $r$ , combined with



the representative values of  $\alpha$  and  $\theta$ , the systems with all 16 possible combinations of these four parameters are simulated for each set of  $h_t$  and  $h_c$  in the design space.

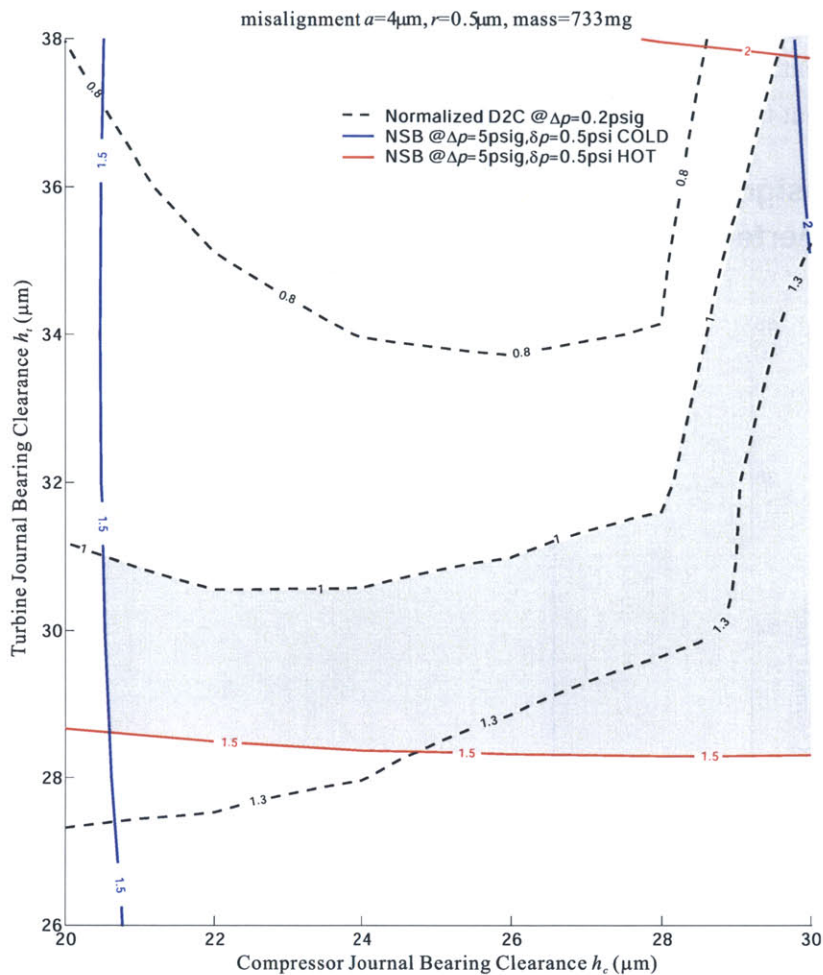


**Figure 11-9: Distance to contact and stability boundary as functions of bearing clearances for dual-bearing systems with a wafer misalignment of  $4\mu\text{m}$  and  $r=0.5\mu\text{m}$ .**

For example, with bearing clearances  $h_t=30\mu\text{m}$  and  $h_c=22\mu\text{m}$ , 16 possible systems with various combinations of those four parameters are simulated to calculate the distance to contact. After these simulations, 16 distances to contact are obtained, and the smallest one is chosen/plotted for the design contours with  $h_t=30\mu\text{m}$  and  $h_c=22\mu\text{m}$ . Following the same procedure for other bearing clearances, the whole contour of the distance to contact can then be generated. Following the same procedure for the stability boundary (when the systems are cold and hot), the stability boundary contours can also be generated. The distance to contact and stability boundary contours for these most possible cases are plotted in Figure 11-9.

Therefore, there are acceptable design points in the space below the black dotted line numbered 1, above the red solid line numbered 1.5, and to the right of the blue solid line numbered 1.5 (the shaded area in Figure 11-9). It is important to note that with the wafer misalignment, both the stability boundary and the distance to contact are much lower than those without the wafer misalignment (Figure 11-3) because of the rotor camming motion.

### 11.3.4 Design Guidelines for Dual-Bearing Systems with Worst-Case Imperfection

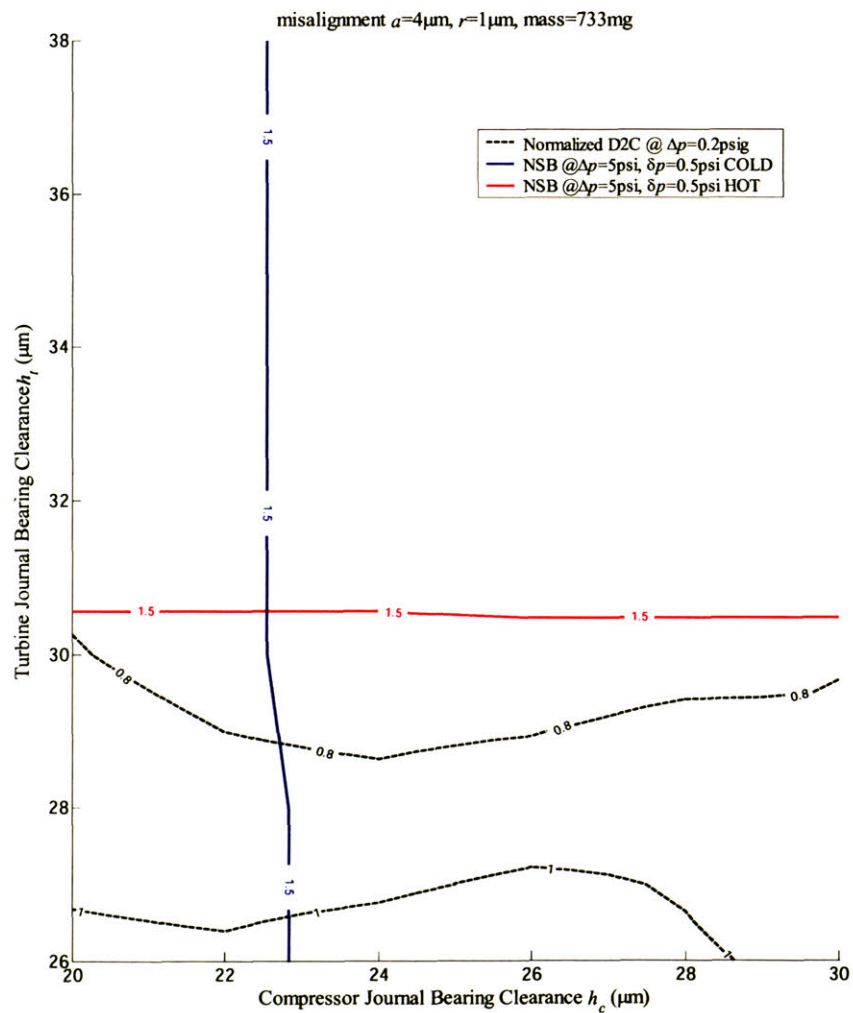


**Figure 11-10: Distance to contact (at  $\Delta p$  of 0.2 psig) and stability boundary as functions of bearing clearances for dual-bearing systems with a wafer misalignment of  $4\mu\text{m}$  and  $r=1\mu\text{m}$ .**

In the worst case, the wafer misalignment  $a$  can be as large as  $6\mu\text{m}$ , and  $r$  can be as large as  $1\mu\text{m}$ . However, even if the wafer misalignment is still  $4\mu\text{m}$ , with  $r=1\mu\text{m}$ , there is no feasible design point as shown in the contours of Figure 11-10, because the distances to contact are all smaller than the threshold distance to contact at the pressure difference across the journal bearings  $\Delta p$  of 0.2psig. Therefore, to work with the worst case of  $6\mu\text{m}$  wafer misalignment, the rotor needs to be inverted at an even lower  $\Delta p$ , 0.1psig, as shown in the contours of Figure 11-11.

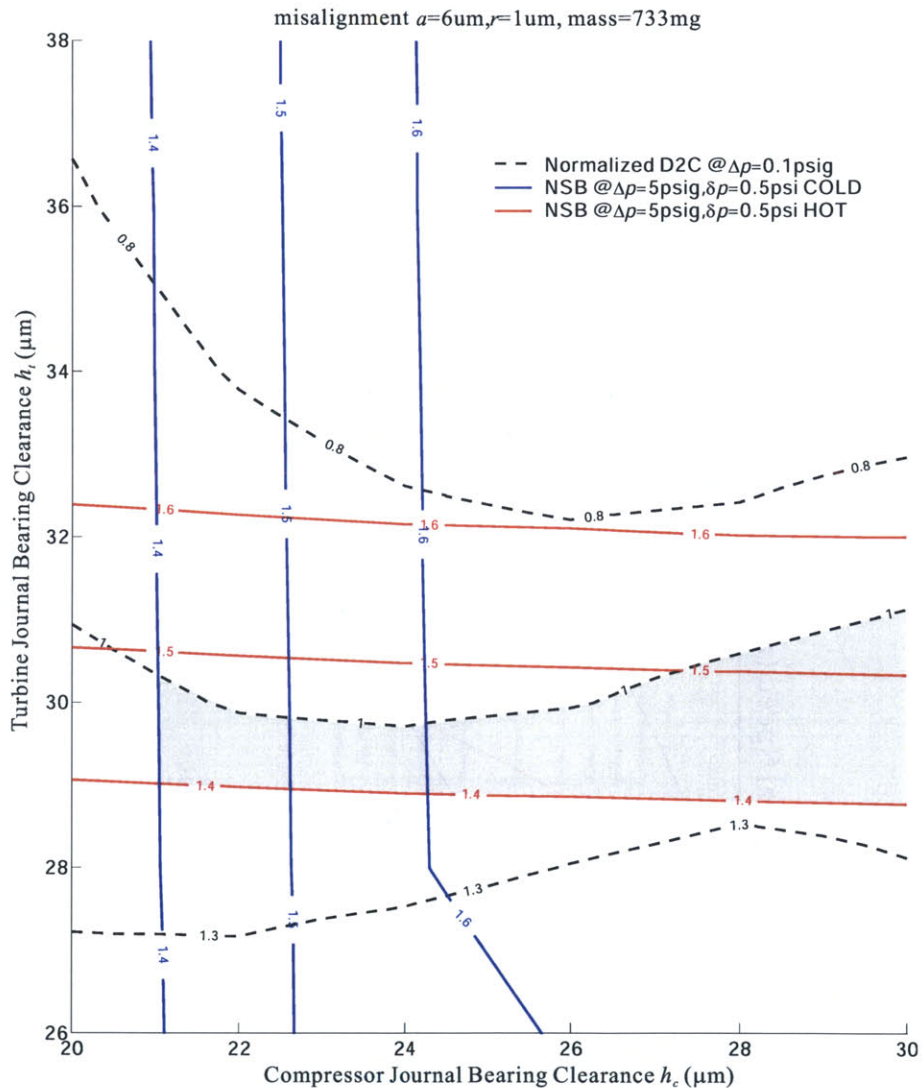


**Figure 11-11: Distance to contact (at  $\Delta p$  of 0.1 psig) and stability boundary as functions of bearing clearances for dual-bearing systems with a wafer misalignment of  $6\mu\text{m}$  and  $r=1\mu\text{m}$ .**



Therefore, according to Figure 11-11, if the safety margin of the stability boundary is reduced to 40%, and if it is feasible to invert the rotor at a pressure difference across the journal bearings  $\Delta p$  of 0.1psig, there can be acceptable design points in the space below the black dotted line numbered 1, above the red solid line numbered 1.4, and to the right of the blue solid line numbered by 1.4 (the shaded area in Figure 11-11). However, if it is not feasible to get the  $\Delta p$  of 0.1psig when the rotor is inverted, it seems that there is no acceptable design.

However, there is a way to invert the rotor at  $\Delta p$  of 0.2psig in this worst case: inverting the rotor on a single compressor bearing by blocking the turbine side bearing. Using this method, the rotor is then supported only by the single compressor bearing and the system natural frequency decreases from 35Krpm to 21Krpm at a  $\Delta p$  of 0.2psig, resulting in a larger distance to contact according to Chapter 2. After inverting the rotor by this single bearing configuration, the rotor speed can be safely increased to a speed higher than the natural frequency of the dual-bearing systems (35Krpm), while still below the stability boundary of the single-bearing system (58Krpm). Then the turbine area can be unblocked, turning on the turbine journal bearing without changing the rotor speed. At this point, the rotor speed is already in the supercritical region of the dual-bearing system, and the rotor has been inverted.

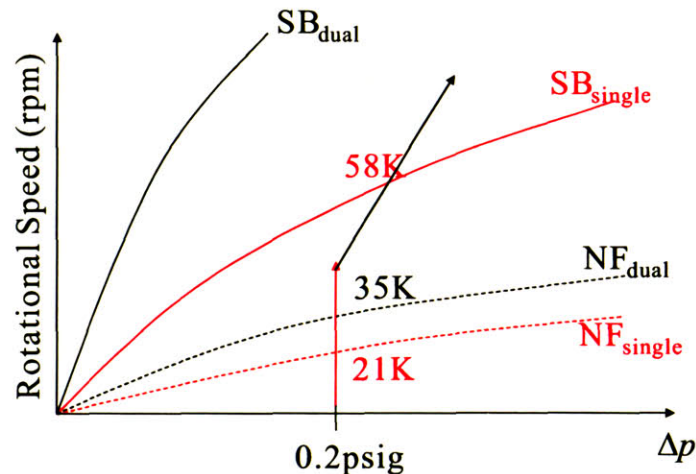


**Figure 11-12: Inverting the rotor with the single-compressor bearing at a pressure difference across the journal bearings  $\Delta p$  of 0.2 psig.**

Using this method, the acceptable designs of dual-bearing systems with  $6\mu\text{m}$  wafer misalignment are not limited by the distance to contact of the dual-bearing, but by that of the single-compressor bearing, as shown in Figure 11-13.



However, it can be seen that the safety margin of the stability boundary still needs to be reduced to 40% to get acceptable designs. Thus, the design points lie in the space to the left of the black solid line numbered 1, above the red solid line numbered 1.4, and to the right of the blue solid line numbered 1.4 (the shaded area in Figure 11-13).

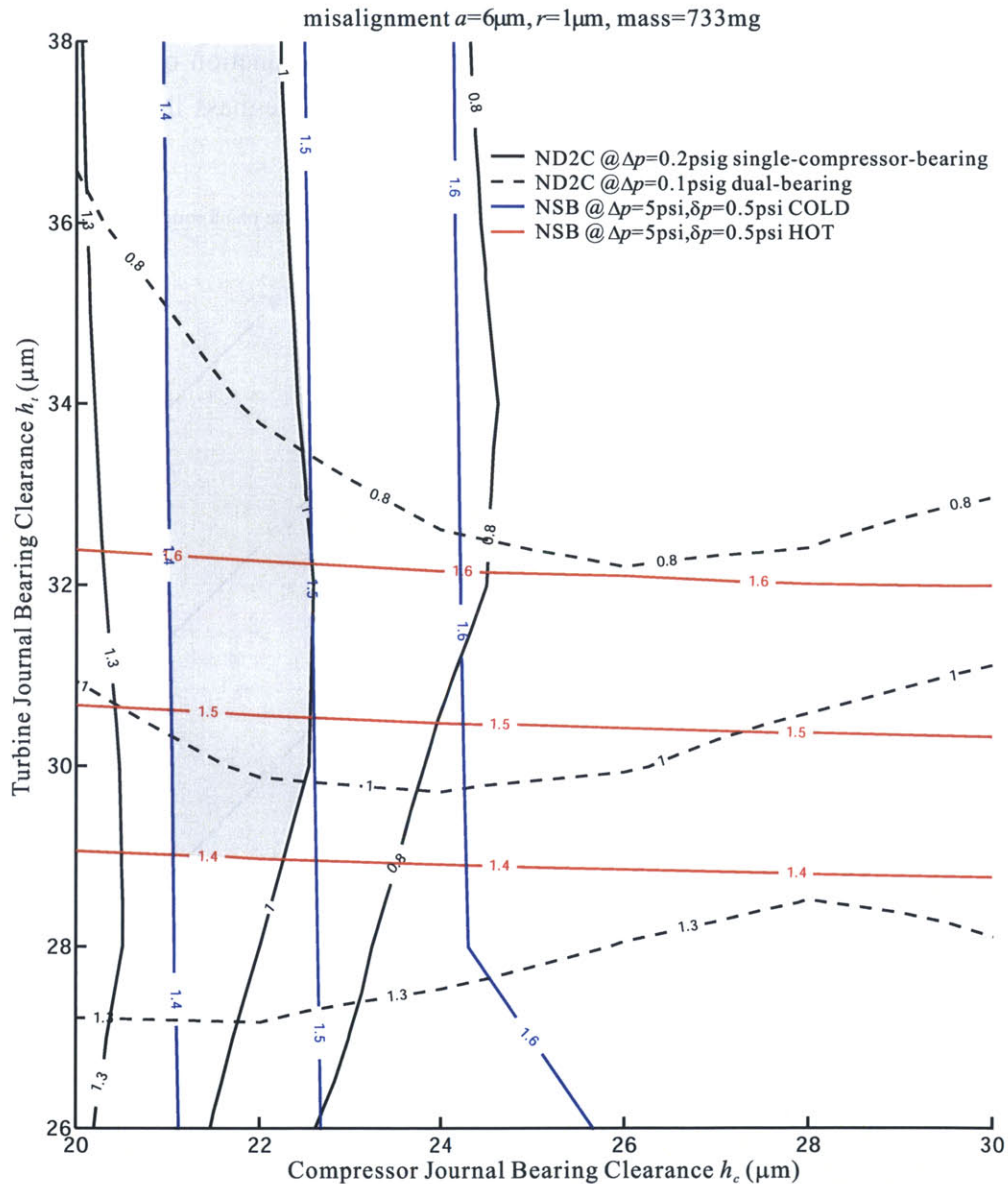


**Figure 11-13: Distance to contact (at  $\Delta p$  of 0.2 psig with the single-compressor-bearing, and at  $\Delta p$  of 0.1 psig with the dual-bearing) and stability boundary as functions of bearing clearances for the dual-bearing systems with a wafer misalignment of  $6\mu\text{m}$  and  $r=1\mu\text{m}$ .**

### 11.4 Suggested Designs and Conclusions

Using the design contours generated for dual-bearing systems with and without wafer misalignment, the acceptable designs can be chosen. Meanwhile, it is important to note that the flows through the journal bearings come from the device itself under normal operating conditions. Thus, the journal bearings must consume as little flow as possible to save power. On the other hand, the mass flow rate is a function of the bearing clearances, which is shown in Figure 11-14 and normalized by the mass flow rate through the turbine.

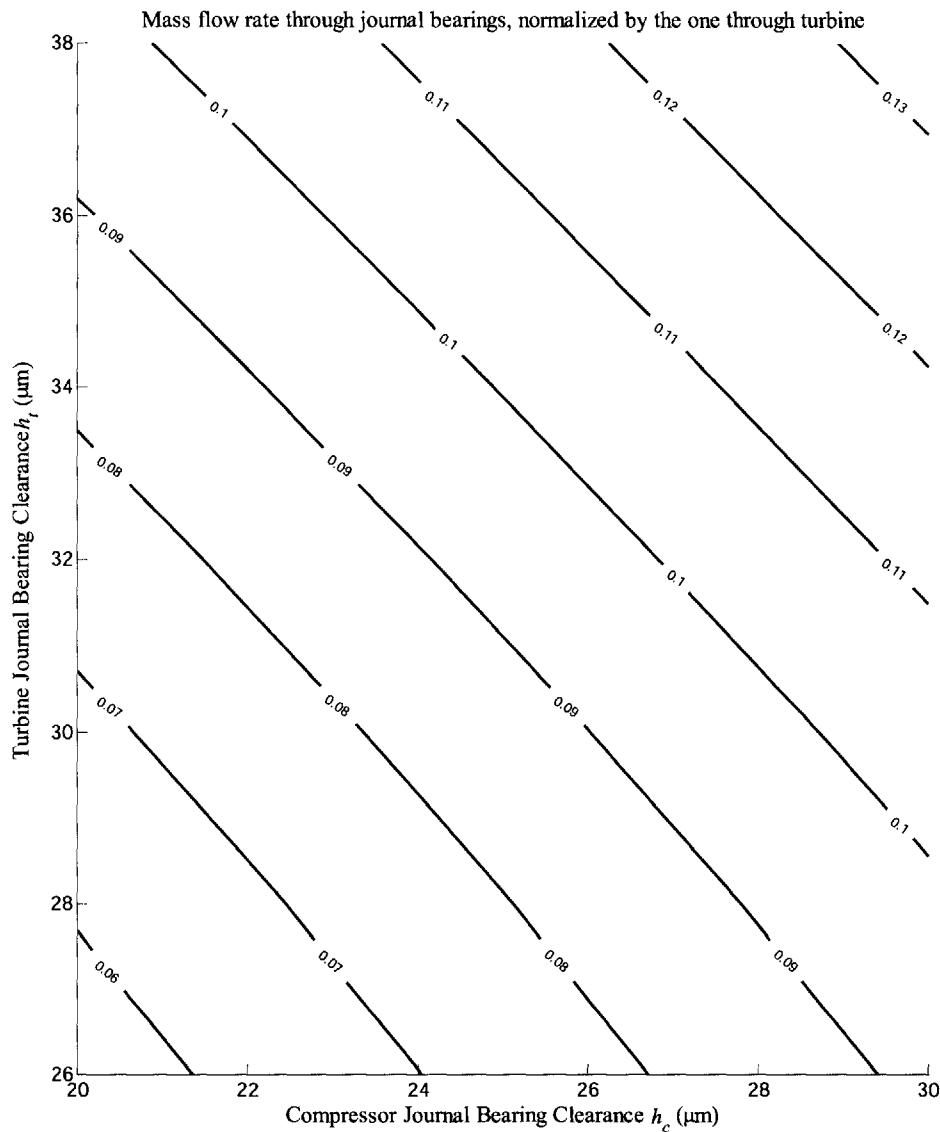


**Figure 11-14: Mass flow rate through the bearing system under normal operating conditions, normalized by the mass flow rate through the turbine.**

Thus, to design journal bearing systems that work with the self-sustained micro-engine, the clearances should be as small as possible to reduce the mass flow through the journal bearings. Based on this knowledge, the following designs are suggested:

1. For dual-bearing systems without wafer misalignment (which can be obtained by future “single-cut” technology), if the clearances of the journal bearings on the turbine disk and the compressor disk must be identical, then both clearances should be  $26\mu\text{m}$  (Figure 11-3). The journal bearings consume 7.7% of the mass flow through the turbine.
2. For dual-bearing systems without wafer misalignment, if the bearing clearances can be different, then  $h_c=20\mu\text{m}$  with  $h_t=26.5\mu\text{m}$  is the optimal journal bearing design (Figure 11-3), consuming 5.6% of the mass flow rate through the turbine.
3. For dual-bearing systems with wafer misalignment as large as  $6\mu\text{m}$ ,  $h_c=21\mu\text{m}$  with  $h_t=29\mu\text{m}$  is the optimal journal-bearing design (Figure 11-12). The mass flow rate through the journal bearings is 6.8% of the flow rate through the turbine. In this case, the rotor may need to be inverted, either at a pressure difference across the bearings  $\Delta p$  of 0.1psig with the dual bearing or at a  $\Delta p$  of 0.2psig with the single-compressor bearing.

In this chapter, dual-bearing systems were investigated based on the journal-bearing designs for the self-sustained micro-engine devices. Four parameters were found necessary to describe the imperfections of the rotor in the dual-bearing system with wafer misalignment between the two bearings. It was found that the rotor camming motion driven by the wafer misalignment can greatly reduce both the system stability boundary and the distance to contact in the dual-bearing system.

In the above calculations, the fluid models are essentially the same as the models established in Chapter 2. Thus, the flow in the bearing has been assumed to be quasi-steady and fully developed. As was discussed in Chapters 2 and 5, when the rotor speed and the flow axial velocity are high, the model prediction can be not accurate. As a result, the stability boundary can be higher than the model predictions, because the destabilizing hydrodynamic force is lower with an undeveloped bearing flow.

Because the length-to-diameter ratio and the gap (distance between the two bearings)-to-diameter ratio of the bearings are on the order of 0.03, the rotor is approximated as a thin disk. If the shafts are made longer to get better thermal isolation performance, this approximation may be invalid. In this case, the rotor conical motion under the torque

produced by the dual-journal-bearing system and the thrust bearings must be accounted for in the simulations.

## *Chapter 12*

# **Summary, Conclusions, and Suggestions for Future Work**

In this chapter the entire thesis is summarized and several suggestions are made for future research work.

### ***12.1 Summary and Conclusions***

In this research work, micro-hydrostatic gas-bearing (both journal-bearing and thrust-bearing) systems were investigated.

#### **12.1.1 Basic Fluid and Rotordynamic Models**

First of all, a fluid model and a basic rotordynamic model were established analytically in Chapter 2, based on first principles and assumptions/approximations of fully developed quasi-steady flow in the journal-bearing system. The models are capable of dealing with all the elements of (1) micro-devices, (2) dynamic response characteristics of axial-flow hydrostatic bearings, (3) evaluation of stiffness, natural frequency, and damping, and (4) evaluation of instability boundary.

The fluid forces were analytically modeled component by component. The hydrostatic direct-coupled force, induced by the Lomakin effect, is found to increase with the pressure difference across the bearing  $\Delta p$ , and hence causes the natural frequency of the system to also increase with  $\Delta p$ . Furthermore, the hydrostatic force is a nonlinear function of the rotor eccentricity, making the rotor response curve either lean right with stiffening hydrostatic stiffness or lean left with softening hydrostatic stiffness. This skewness of the rotor response curve is accompanied by a hysteresis phenomenon.

Because of the relatively small  $L/D$  ( $<0.075$ ) in the micro-bearing system, the hydrodynamic force has two components of comparable magnitude: the one due to viscous drag and the one due to rotor pumping action. Since they act in opposite directions, it is possible that the two hydrodynamic force components cancel each other and the net hydrodynamic force vanishes.

The damping force is generated by the squeezing effect caused by the rotor translational motion, and is found to strongly depend on length over clearance of the bearing. Both the hydrodynamic stiffness and the damping coefficient are strong nonlinear functions of the rotor eccentricity—they quickly increase as the rotor approaches the bearing wall. As a result, the rotor response curve becomes wide and flat.

According to the modeling, the distance to contact is large with large bearing length and radius, small bearing clearance and natural frequency, and small rotor mass and unbalance. The distance to contact should be large (larger than the normalized distance to contact threshold of 0.09) for the rotor to be inverted, which requires a low pressure difference across the journal bearing  $\Delta p$  because the damping ratio is inversely proportional to the square root of  $\Delta p$  according to the scaling laws [37]. On the other hand, the stability boundary must be high for the system to reach the high design speed, which requires high  $\Delta p$  for a high natural frequency for a given whirl ratio, determined by the bearing geometry. As a result, an operating protocol was developed to achieve controlled acceleration to high speed.

The predictions of the mass flow rate through the bearing, the natural frequencies, and the distance to contact agreed well with the experimental observations, and thus the models were validated. An important feature of the flow model is that it can reversely calculate the bearing clearance according to a static flow test; thus, the flow model provides an accurate and nondestructive method to measure the bearing clearance. Furthermore, through experiments and modeling, the threshold of the distance to contact normalized by the bearing clearance is found to be 0.09 for a safe transition through the resonance at the natural frequency. With a distance to contact larger than this threshold, the rotor can be inverted; otherwise, it will have difficulty crossing the natural frequency. This threshold has been successfully applied to the operating protocol.

### **12.1.2 Stability Boundary of the Micro-Hydrostatic Gas Journal-Bearing System**

Then, based on first-principle analysis, a singular behavior that has not been observed in large-scale conventional journal bearings was found in the stability boundary for the isotropic micro-journal-bearing system. The underlying physical mechanism of this unique singularity is that the two components of the cross-coupled hydrodynamic force due to rotor pumping action and viscous drag effect, which act in opposite directions, are of comparable magnitude and capable of canceling each other, because the hy-



hydrodynamic force due to viscous drag effect becomes dominant at  $L/D \ll 1$  in the ultra-short micro-bearing system.

Furthermore, the hydrodynamic force, as the destabilizing factor in the system, was shown to drive the rotor into a whirling motion. A simple criterion of the whirl instability was established based on first-principle analysis. It suggests that at the onset of instability, the rotor tends to whirl forward if the hydrodynamic force due to rotor pumping action is larger than the hydrodynamic force due to viscous drag, and it tends to whirl backward if the former is smaller than the latter.

With the definition of the whirl number  $W=2Rh/L^2$ , which is only a function of bearing geometry, the whirl ratio is  $\mathfrak{R}=2/(1-W)$  in the isotropic micro-journal-bearing system. The highest possible whirl ratio  $\mathfrak{R}$  (over 20) is desired, which means that the whirl number  $W$  needs to be close to 1, so that the destabilizing hydrodynamic force is small and the singularity of the stability boundary can be utilized to achieve a high stability boundary. In other words, the length-to-diameter ratio should equal the clearance-to-length ratio,  $L/D=h/L$ , in order to obtain the high whirl ratio. This means that for a small  $h/L$ , governed by the damping ratio requirements, the bearing length-to-diameter ratio  $L/D$  should be small and about  $h/L$ . Thus the high whirl instability limit requirement demands a small  $L/D$ : an ultra-short hydrostatic gas bearing with an  $L/D$  one order of magnitude smaller than that of a conventional hydrostatic gas bearing yields a whirl ratio  $\mathfrak{R}$  one order of magnitude larger than that of a conventional gas bearing. Or, put another way, ultra-high-speed devices that require high whirl ratios demand ultra-short (small  $L/D$ ) bearings.

Then, with both the analytical linear approach and the numerical full nonlinear simulations, the micro journal bearing systems with hydrostatic stiffness anisotropy are investigated. It is shown that, by breaking symmetry in hydrostatic stiffness, the novel bearing design increases bearing top speed and can eliminate the narrow singularity peak of stability boundary in the isotropic system, greatly relieving fabrication tolerance requirements.

With the knowledge obtained from the micro-gas-bearing theory and the experimental results, the following bearing design implications can be established:

1. In order to improve the dynamic behavior and to increase the whirl ratio, the difference in hydrostatic stiffness in the two orthogonal directions (anisotropy) should be maximized. This can be achieved (while maintaining adequate levels of average stiffness) by supplying hydrostatic feed air at different pressures over parts of the journal circumference.

2. In addition, the hydrodynamic stiffness of the journal bearing should be minimized. For a given bearing  $L/D$ , this can be done using the criteria established for isotropic bearing configurations by adjusting the bearing geometry according to  $W = 2Rh/L^2 = 1$ .
3. The mechanical design of the bearing air supply system and piping should be kept bisymmetric, and the pressure losses in the opposite feed systems should be matched to avoid any rotor sideload.
4. The rotor unbalance should be kept low. However, anisotropic bearing designs enable a relief in fabrication tolerance requirements and a relaxation in rotor balancing constraints compared to their isotropic counterparts.

Due to insufficient experimental data and the difficulty of determining the real cause of the high-speed crashes, the models of stability boundary have not yet been fully validated. However, through the whirl ratios observed in large-scale conventional bearings ( $\sim 2$ ) and the one reached by the ultra-short micro-bearing system ( $> 29$ , one order of magnitude higher), one can see that the ultra-short micro-bearings can reach a whirl ratio one order of magnitude higher than the large-scale conventional journal bearings. This is consistent with the model predictions.

### 12.1.3 Barriers to High Speeds

Although the micro-journal bearings can be designed to have high stability boundary, the devices can fail due to reasons other than bearing instability, such as structural failure, thrust-bearing resonances, and nonlinear resonances.

One such cause can be the coupling effect between the rotor conical and radial motions. To investigate the unstable mode of motion, a linear 4-degree-of-freedom model was established to investigate the coupling between the radial and conical modes of motion in the micro-bearing system, and a nonlinear 5-degree-of-freedom numerical model was also established to investigate the effect of axial oscillation on the system's dynamic behavior. Using the fluid-force models, coupling force and torque were found to be generated by the plenum, the seal, and the thrust bearings. The calculations showed that radial forces can be induced by rotor tilting motions from the plenum, seal, and thrust bearings, and torques acting on the rotor can be induced by rotor radial motions from the plenum.

Results of the 5-degree-of-freedom numerical simulations agreed with those of the 4-degree-of-freedom linear model and showed that the axial vibrations are negligible be-

cause of the large axial damping from the thrust-bearing system. Most importantly, the models proved that the coupling can drive the system into a conical motion with a frequency close to the natural frequency of the radial motion, making the system unstable at a much lower speed than the whirl instability limit of the journal-bearing system alone. This is consistent with the experimental observations. Thus, the bearing system should be designed with as small a coupling as possible between the rotor conical and radial motions.

Since the coupling coefficients are strong functions of the clearances of the thrust bearings and seal, it is suggested to increase the seal clearances in the new design to reduce the coupling so that the stability boundary can be higher. On the other hand, during the operation of the single-bearing micro-turbo-charger devices, the rotor can be pushed axially toward the forward thrust bearing into an optimum position where the total coupling from thrust bearings and seal is smallest, to make the stability boundary of the system higher.

The centrally-fed journal-bearing system was then modeled as another approach to eliminate the coupling. A nondimensional parameter of the ratio of the flow resistance in the bearing to that in the feed  $\Phi$  was introduced, and the bearing forces and hence the system dynamics were found to be strongly affected by it.

Due to leakage flow from the bearing to the feed, both the damping and the hydrodynamic stiffness due to rotor pumping action in the centrally-fed journal-bearing are smaller than those in the axially-fed counterpart. As a result, the distance to contact is much smaller in centrally-fed journal-bearings than in axially-fed journal-bearings. Thus, in the centrally-fed journal-bearing system, a much lower pressure supply  $\Delta p$  is required to invert the rotor, and the operation window between the natural frequency and the stability boundary becomes narrow at this low  $\Delta p$ , causing a great deal of difficulty in operation.

Through the investigation of micro-journal-bearing systems with three typical profile variations—negative taper, positive taper, and bow—bearing profile variation was also found to have negative effects on the rotordynamic behavior of the system.

Although the system stability boundary in the tapered bearings behaves similarly to the boundary in straight-wall journal bearings with the same average clearance, negatively tapered journal bearings can induce a positive hydrostatic direct-coupled stiffness, making the system statically unstable at a low bearing pressure difference across the journal bearing  $\Delta p$ . The analysis shows that the positive hydrostatic stiffness is more severe

in negatively tapered journal bearings with large profile variations. Thus, negatively tapered bearings with large profile variations should be avoided in fabrication, especially for the devices that need to be inverted at low  $\Delta p$ .

Furthermore, hydrostatic stiffness was found to be a strong nonlinear function of rotor eccentricity in tapered bearings, and this nonlinearity in turn skewed the rotor response curves. Most importantly, numerical simulations showed that the distances to contact in journal bearings with profile variations are smaller than those in straight-wall journal-bearings, and the distance to contact is even smaller with larger profile variations. Therefore, large profile variations should be avoided. More specifically, according to the simulation results, the profile variation should be smaller than  $1.5\mu\text{m}$  for journal bearings used in the micro-turbo-pump devices, so that they can be inverted at  $\Delta p$  of 0.5psig.

Then, with the nonlinear resonance models established using the multi-scale method, the nonlinearity of the hydrostatic force was found to be able to induce nonlinear resonances in the micro-bearing systems. As a result, subharmonic resonance can occur at speeds near three times the natural frequency ( $3\Omega_N$ ) in the isotropic journal-bearing system, with a slowly rotating orbit. In the anisotropic system, several secondary resonances may occur: superharmonic resonances at one third of the natural frequencies in both directions ( $\Omega_x/3$ ,  $\Omega_y/3$ ), subharmonic resonances at three times the natural frequencies in both directions ( $3\Omega_x$ ,  $3\Omega_y$ ), and resonances at the combination of the two naturals:  $(\Omega_x+\Omega_y)/2$ ,  $2\Omega_x+\Omega_y$ , and  $\Omega_x+2\Omega_y$ .

Since these secondary nonlinear resonances normally have large amplitudes, which may cause the rotor to crash, they should be avoided during normal operation, especially the ones that happen at high rotor speeds. Also, according to Chapter 8 on the bearing profile effect, tapered bearings are found to induce strong nonlinearity of the hydrostatic force, which causes the nonlinear resonances during operation. Therefore, again, tapered bearings with large profile variations should be avoided in fabrication.

Finally, dual-bearing systems were investigated based on bearing designs for the self-sustained micro-engine devices. Four parameters were found necessary to describe the imperfections of the rotor in the dual-bearing system with wafer misalignment between the two bearings. Furthermore, this wafer misalignment between the two bearings can greatly reduce both the system stability boundary and the distance to contact in the dual-bearing systems, because of the rotor camming motion. For example, with  $4\mu\text{m}$  of misalignment, the stability boundary can decrease by about 20%, and the distance to con-

tact can decrease by a factor of 3. Thus, in fabrication, the misalignment between the two disks should be as small as possible.

#### 12.1.4 Hydrostatic Gas Thrust Bearings: Axial and Tilting stiffness

It was shown in the research that the axial and tilting stiffness in the hydrostatic gas thrust bearings (both circular and annular) can be calculated using the Image Method. The results were validated by both CFD calculations and experimental data.

The effect of rotor rotation on the pressure distribution in the thrust bearing was also investigated via the analytical approach and 3-dimensional CFD calculations by Fluent. The results showed that the decrease in pressure and thrust force due to centrifugal body force caused by the tangential flow in the bearing induced by rotor rotation is negligible compared to that induced by the high external static pressure supply.

Since the Image Method doesn't involve numerical calculation of the 2-dimensional Reynolds equation, it is much faster than the Green's Function method. Thus, it is the recommended method for fast evaluation of the thrust bearing axial and tilting stiffness.

#### 12.1.5 Design Recommendations for the Journal-Bearing Systems Used in the Self-Sustained Micro-Engine

Thus, based on the knowledge obtained from the research and modeling, the following bearing designs are suggested for the self-sustained micro-engine:

1. For dual-bearing systems without wafer misalignment (which can be obtained by future "single-cut" technology), if the clearances of the journal bearings on the turbine and compressor disks must be identical, then both clearances should be  $26\mu\text{m}$ . The journal bearings consume 7.7% of the mass flow through the turbine.
2. For dual-bearing systems without wafer misalignment, if the two bearing clearances can be different, then  $h_c=20\mu\text{m}$  with  $h_r=26.5\mu\text{m}$  is the optimal bearing design, consuming 5.6% of the mass flow rate through the turbine.
3. For dual-bearing systems with a wafer misalignment as large as  $6\mu\text{m}$ ,  $h_c=21\mu\text{m}$  with  $h_r=29\mu\text{m}$  is the optimal design. The mass flow rate through the journal bearings is 6.8% of the flow rate through the turbine. In this case, the rotor may need to be inverted, either at the pressure difference across the bearings  $\Delta p$  of 0.1psig with the dual bearing, or at  $\Delta p$  of 0.2psig with the single-compressor bearing.

## ***12.2 Suggested Future Research Work***

“Rome wasn’t built in a day,” and neither can the models for the micro-hydrostatic journal-bearing system be. In this research work, in order to find the analytical solutions to the research questions while capturing the underlying physics of the system, the bearing flow has been assumed to be steady and fully developed.

Recent research has shown that the flow in the vicinity of the bearing entrance may not be a fully developed Couette flow, if the flow has a high axial velocity and no pre-swirl before entering the bearing. Since the hydrodynamic force is induced by the flow variation around the bearing, its two components—hydrodynamic force due to viscous drag effect and hydrodynamic force due to rotor pumping action—will be smaller than the model predictions, in which developed flow is assumed. As a result, the whirl ratio, which is inversely proportional to the hydrodynamic stiffness as shown in the research, can be larger than the model prediction. Furthermore, because the balance point of the two decreased components is not necessarily the same as the model prediction, the singularity point of the stability boundary in the isotropic journal-bearing system can be shifted.

Thus, to obtain a more accurate prediction of the whirl ratio as well as the stability boundary of the system, the fluid models to be established in the future should include the effects of undeveloped flow. Moreover, other components in the micro-devices, such as the thrust bearings, can also introduce hydrodynamic stiffness due to viscous drag into the system; these should also be considered in future models.

As the rotor speed increases to millions of rpm, the fluid particle flow through time can be comparable to the time scale of the rotor movement, and the approximation of a quasi-steady flow may not be valid in this case. Determining how the unsteady flow affects the rotordynamics and is affected by the rotor movement at ultra-high speeds requires an unsteady model, in which the flow and the rotor movement should be coupled together. Furthermore, since the Helmholtz resonance frequency of the plenum (the volume) and bearing (the neck) system in the current bearing design is just about 1 million rpm, the Helmholtz resonance can also affect the system rotordynamic behavior by changing the pressure in the plenum when the rotor speed is near that resonance frequency. In the future, it is suggested to investigate this Helmholtz resonance effect or to redesign the plenum so that the resonance frequency can be out of the operation region.

The nonlinear resonance needs deep investigation, because it was observed to cause crashes in the experiments. It is important to note that the research on the nonlinear resonance presented in this thesis is only a preliminary analysis. Besides the third-order



nonlinear terms, there exist higher odd-order ones in hydrostatic force, which in turn may cause higher-order nonlinear resonances. According to the numerical simulations based on the bilinear stiffness system done by Ehrich [34], these higher-order resonances have even larger amplitudes. Furthermore, several devices have crashed at speeds of high odd multiples ( $7\times$  or even  $9\times$ ) of the natural frequency in the experiments [30]; this needs attention.

Also according to Ehrich [34], chaotic behavior occurs at certain rotor speeds due to the nonlinear bearing forces, making the system much more complicated. Besides the nonlinearity of hydrostatic force, the nonlinearities of hydrodynamic and damping forces may also affect the system's dynamic behavior. To investigate nonlinear resonance and chaotic behavior in the micro-bearing system, a much more complicated model together with numerical simulation is required.

### ***12.3 Contributions of Thesis***

Fluid models have been established that are capable of solving the hydrostatic, hydrodynamic, and damping forces analytically and individually in the micro-ultra-short hydrostatic gas journal bearings. With these fluid models, the bearing clearance can be reversely calculated according to the static flow test, which essentially becomes an accurate and non-destructive measuring tool. Both the natural frequency and the distance to contact predicted by the models agree well with the experimental measurements; an operating protocol was established accordingly and was successfully applied in the experiments.

Singular behavior of the stability boundary was found in the ultra-short micro-journal bearings with isotropic configuration. The underlying physical mechanism of this unique and important feature is that the hydrodynamic force due to viscous drag becomes dominant with  $L/D \ll 1$  and acts in the opposite direction of the hydrodynamic force due to rotor pumping action, so that the net destabilizing hydrodynamic force can vanish with certain bearing geometry. Thus the ultra-short bearing is suggested as a suitable design which enables a large DN number and a high whirl ratio; a whirl ratio over 30 has been demonstrated in experiments with this ultra-short bearing design, one order of magnitude higher than the whirl ratios in large-scale journal bearings.

Using both analytical and numerical models, the anisotropy of hydrostatic stiffness was found to improve system stability. The underlying physical mechanism is that the destabilizing hydrodynamic force can be balanced by the hydrostatic anisotropy. With the anisotropic configuration, the fabrication tolerance requirements can be released because

the hydrostatic anisotropy can eliminate the narrow singular peak in the stability boundary. However, sideload was found to reduce the stability boundary in the anisotropic micro-journal-bearing systems and hence should be avoided during operation.

Some other factors in the bearing system that can impair the system top speed were identified: 1) the coupling between the rotor conical and radial motions induced by the plenum, seal, and thrust bearings; 2) large bearing profile variations, especially in the negatively tapered bearing where a positive stiffness is induced and the system becomes statically unstable; 3) misalignment in dual-bearing systems. All these factors should be noted in the design and fabrication process.

The third-order nonlinear resonances were captured by both analytical models and numerical simulations. Most importantly, the model predicted a subharmonic resonance in the isotropic journal-bearing system, with a slow rotating noncircular orbit such that the symmetry of the system is broken by itself in the nonlinear resonance. This phenomenon has not been observed before; but, this subharmonic resonance in isotropic bearing systems was verified by the numerical simulation. Furthermore, the anisotropic journal-bearing system was found to be able to engage in multi-type nonlinear resonances: superharmonic resonances at one third of the natural frequencies, subharmonic resonances at three times the natural frequencies, and combinations (such as the average) of the two natural frequencies. The conditions under which these resonances can occur were derived analytically and then verified by numerical simulation.

# Appendix A

## Stability Boundary for Anisotropic Micro-Journal-Bearing Systems with Hydrodynamic Stiffness of the Same Sign

Equation (4-9) in Chapter 4 shows the stability boundary for the anisotropic micro-journal-bearing system when the two hydrodynamic stiffnesses  $K_{xy}$  and  $K_{yx}$  are of opposite signs. With certain journal bearing geometry and the blockage of the axial flow in the bridge region, the intrinsic hydrodynamic stiffnesses  $k_{xy}$  and  $k_{yx}$  can be of the same sign, resulting in a negative  $C_x C_y / k_{xy} k_{yx}$ . This in turn causes  $\Omega_W$  in Equation (4-9) to have no real root, and it seems that the system can always be stable. However, the following analysis shows that in this case, the system can still be unstable due to the positive stiffness caused by high hydrodynamic stiffness at high speed.

When the intrinsic hydrodynamic stiffnesses  $k_{xy}$  and  $k_{yx}$  can be of the same sign, there is a trivial solution to Equation (4-6):  $\Omega=0$  and

$$\Omega_W = \sqrt{\frac{K_{xx} K_{yy}}{k_{xy} k_{yx}}}, \quad (\text{A-1})$$

where  $\Omega_W$  is the stability boundary when  $k_{xy} k_{yx} > 0$ . Since  $K_{xy} = k_{xy} \omega$  and  $K_{yx} = k_{yx} \omega$ , according to Equation (A-1), when  $K_{xy} K_{yx} > K_{xx} K_{yy}$  (or  $k_{xy} k_{yx} \omega^2 > K_{xx} K_{yy}$ ), the system can be driven into an unstable mode with  $\Omega$  of 0, different from the whirl one.

To understand the underlying physics of this destabilizing mechanism, the stiffness of the system can be analyzed with the stiffness matrix below:

$$\begin{pmatrix} K_{xx} & K_{xy} \\ K_{yx} & K_{yy} \end{pmatrix}. \quad (\text{A-2})$$

This stiffness matrix has the characteristic equation of

$$\lambda^2 - (K_{xx} + K_{yy})\lambda + (K_{xx} K_{yy} - K_{xy} K_{yx}) = 0, \quad (\text{A-3})$$

which has two roots (eigenvalues of matrix of (A-2)):

$$\lambda = \frac{(K_{xx} + K_{yy}) \pm \sqrt{(K_{xx} + K_{yy})^2 - 4(K_{xx}K_{yy} - K_{xy}K_{yx})}}{2}. \quad (\text{A-4})$$

Under normal conditions, the hydrostatic force is a restoring one, and hence the hydrostatic stiffnesses  $K_{xx}$  and  $K_{yy}$  are negative. Then with  $(K_{xx}+K_{yy})<0$ , Equation (A-3) can be found to have a positive real root if  $K_{xy}K_{yx}>K_{xx}K_{yy}$ . This means that the stiffness is positive in a certain direction. With this positive stiffness, if the rotor is displaced in this direction due to perturbations, the additional force acting on the rotor is in the same direction as the rotor displacement, pushing the rotor even further away from its original position. Thus, in this case, the system is statically unstable.

Furthermore, according to Chapter 2, the ratio of hydrostatic stiffness to intrinsic hydrodynamic stiffness is always large (on the order of magnitude of  $10^6$ ) for ultra-short gas micro-bearings. Therefore, when the intrinsic hydrodynamic stiffnesses  $k_{xy}$  and  $k_{yx}$  are of the same sign, the stability boundary given by (A-1) is already much higher than the design speed.

# Appendix B

## Image Method for Circular Thrust Bearings

The following shows how to use the Image Method to solve the Poisson equation for the circular thrust bearings. First, the case that the point source is placed at the origin of an infinite 2-dimensional plane with a mass flow rate of  $\dot{m}$  is considered, as follows. The pressure field  $P$  is then governed by the Poisson equation, as below:

$$\Delta P^2 = -\frac{24\mu P_a}{h^3 \rho_a} \dot{m} \delta(\vec{r}). \quad (\text{B-1})$$

Because of the axis-symmetry and mass conservation, the flow rates in both the radial ( $r$ ) and tangential ( $\theta$ ) directions are

$$\begin{cases} Q_r = -\frac{h^3}{12\mu} \frac{\partial P}{\partial r} = \frac{\dot{m}}{2\pi r \rho} = \frac{\dot{m} P_a}{2\pi r P \rho_a} \\ Q_\theta = -\frac{h^3}{12\mu} \frac{\partial P}{r \partial \theta} = 0. \end{cases} \quad (\text{B-2})$$

Then, from the first Equation (B-2), the gradient of  $P^2$  can be derived:

$$-\frac{h^3}{24\mu} \frac{\partial P^2}{\partial r} = \frac{\dot{m} P_a}{2\pi r \rho_a} \Rightarrow \frac{\partial P^2}{\partial r} = -\frac{12\mu P_a \dot{m}}{\pi h^3 \rho_a} \frac{1}{r}. \quad (\text{B-3})$$

After integration with respect to  $r$ ,  $P^2$  is found to be

$$P^2 = -\frac{12\mu P_a \dot{m}}{\pi h^3 \rho_a} \ln(r) + c, \quad (\text{B-4})$$

where  $c$  is a constant to be determined by the boundary condition.

Furthermore, if the point source is not at the origin, but at  $r_0$ , the Poisson equation becomes

$$\Delta P^2 = -\frac{24\mu P_a}{h^3 \rho_a} \dot{m} \delta(\vec{r} - \vec{r}_0). \quad (\text{B-5})$$

In this case, by transformation of coordinates,  $P^2$  becomes

$$P^2 = -\frac{12\mu P_a \dot{m}}{\pi h^3 \rho_a} \ln |\vec{r} - \vec{r}_0| + c. \quad (\text{B-6})$$

Therefore, the solution for the Poisson equation with the point source positioned anywhere in the infinite 2-dimensional plane has been derived. Next, the boundary condition is applied. For this particular problem of the thrust bearing, the boundary condition is that the pressure at the exhaust of the bearing ( $r=R_b$ ) is atmospheric pressure  $P_a$  (Figure B-1).

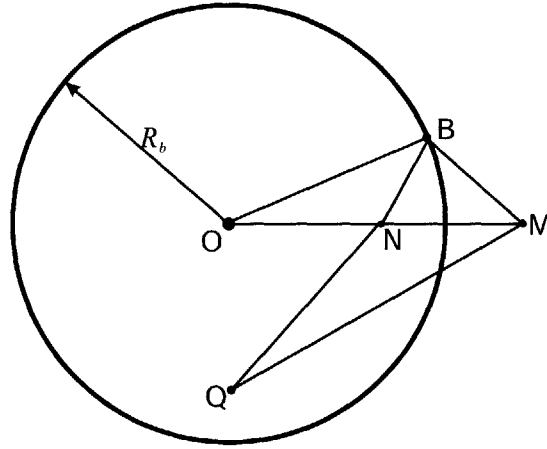


**Figure B-1: Circular boundary condition can be simulated by an image point sink.**

If the boundary condition is replaced by a point sink M with the same intensity as the point source N, then the pressure fields  $P^2$  at point B, which is an arbitrary point on the original boundary circle, generated by N and M are

$$P^2|_N^B = -\frac{12\mu P_a \dot{m}}{\pi h^3 \rho_a} \ln NB + c, \quad (\text{B-7})$$

$$P^2|_M^B = \frac{12\mu P_a \dot{m}}{\pi h^3 \rho_a} \ln MB + c', \quad (\text{B-8})$$

where NB is the distance from N to B and MB is the distance from M to B. Because the Poisson equation is linear in  $P^2$ , the final pressure  $P^2$  at B is the superimposition of the solutions of (B-7) and (B-8):

$$P^2|_{M\&N}^B = \frac{12\mu P_a \dot{m}}{\pi h^3 \rho_a} \ln \frac{MB}{NB} + c''. \quad (\text{B-9})$$



If  $OM \cdot ON = R_b^2$ , the triangles  $\triangle OBN$  and  $\triangle OMB$  are similar triangles. Then one can find that  $NB/MB=ON/OB$  and Equation (B-9) becomes

$$P^2 \Big|_{M\&N}^B = \frac{12\mu P_a \dot{m}}{\pi h^3 \rho_a} \ln \frac{OB}{ON} + c'' . \quad (B-10)$$

Because  $OB=R_b$  and  $ON$  are constant,  $P^2$  at B introduced by both the source and the image sink are also constant. This constant can be simply set equal to  $P_a^2$  by adjusting  $c''$  to simulate the original boundary condition. Furthermore, because B is an arbitrary point on the circle, the pressure on the whole circle is constant and equal to  $P_a$ . So the boundary condition of the original problem is simulated by the image sink M. Then  $P^2$  at an arbitrary point Q in the bearing region is

$$P^2 \Big|_{M\&N}^Q = \frac{12\mu P_a \dot{m}}{\pi h^3 \rho_a} \ln \frac{MQ}{NQ} + c'' = \frac{12\mu P_a \dot{m}}{\pi h^3 \rho_a} \ln \frac{MQ \cdot ON}{NQ \cdot R_b} + P_a^2 . \quad (B-11)$$

According to Green's theorem, the Poisson equation has a unique solution with the same boundary conditions. Since the solution described by Equation (B-11) satisfies the boundary condition that  $P^2(R_b)=P_a^2$ , it is the unique solution.

When more than one point source exists, as there are several nozzles in the thrust bearing, image sinks can be introduced corresponding to each point source and the boundary condition can still be simulated. Then the solution of  $P^2$  in the thrust bearing is

$$P^2 \Big|_{M_i}^Q = \frac{12\mu P_a}{\pi h^3 \rho_a} \sum_i \dot{m}_i \ln \frac{M_i Q \cdot ON_i}{N_i Q \cdot R_b} + P_a^2 , \quad (B-12)$$

where  $N_i$  is the position of the  $i$ th point source,  $\dot{m}_i$  is its mass flow rate, and  $M_i$  is the corresponding image sink position, given by  $OM_i \cdot ON_i = R_b^2$ .



# Appendix C

## Image Method for Annular Thrust Bearings

The last appendix showed how to use the Image Method to calculate the pressure distribution in the circular thrust bearings. The following will describe how to use the Image Method to solve the pressure distribution in the annular thrust bearings.

Since there are two boundary conditions in the annular bearings, the pressures at both the inner boundary and the outer boundary should be constant; one image sink for each point source cannot work here. Instead, a series of point sources and sinks are needed to mimic the boundary conditions as shown in Figure C-1.

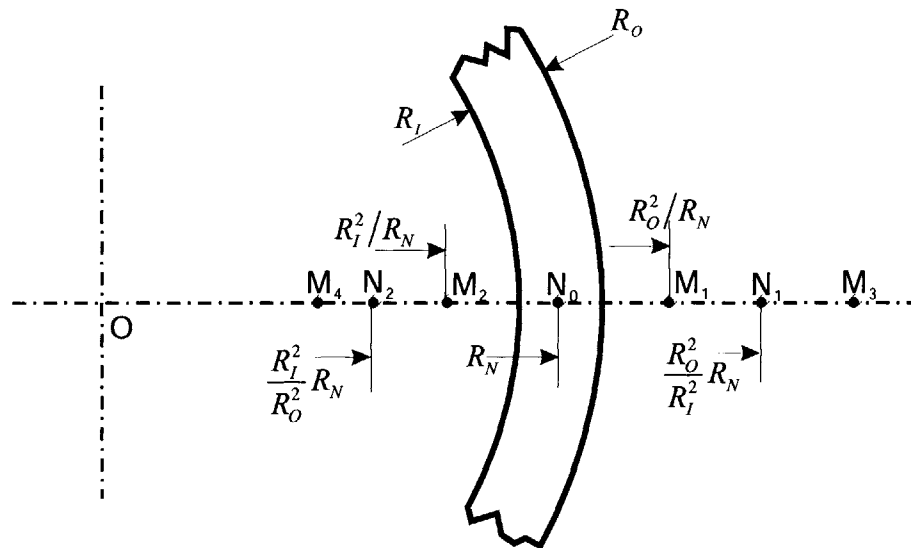


**Figure C-1: Arrangement of the series of image points.**

First, to make the pressure constant at the outer circle, a point sink needs to be placed at point  $M_1$  to balance the pressure variation induced by the point source at point  $N_0$ . Then, both a point sink and a point source should be placed at points  $M_2$  and  $N_2$  respectively, to make the pressure constant at the inner circle by balancing the pressure variation induced by the point source and the point sink at  $N_0$  and  $M_1$ . Now the pressure at the inner circle is constant, but the pressure at the outer circle is no longer constant because of the additional image source and sink. Therefore, an additional point source and

sink should be placed at points  $N_1$  and  $M_3$  respectively to balance the sink and source just placed at  $M_2$  and  $N_2$ , and so on and so forth...

It can be seen that infinite sinks and sources inside as well as outside the annuli are needed to ensure that the pressures at the inner and outer boundary circles remain constant. The outside sinks/sources become farther and farther away from the annuli, while the inside sinks/sources trend to the center of the annuli. Because the sinks/sources placed both far away from the annuli and at the center of the annuli can only generate constant pressures at the inner circle and outer circle, only a finite series of sources and sinks are needed in the calculations.

The above efforts can successfully make the pressures at the inner and outer circles constant. However, the inner circle pressure can be different from the outer circle pressure in the thrust bearings used in the micro-turbo-pump devices, due to the high pressure in the pump region. This difference can be created in the model by placing a source/sink right at the center of the annuli with suitable intension, without destroying the constancy of the pressures at either the inner or the outer circle.

## Reference

- [1] Epstein, A. H., Senturia, Anathasuresh, Ayon, Breuer, Chen, Ehrich, Exteve, Gauba, Ghodssi, Groshenry, Lang, Lin, Mehra, Mur, Miranda, Nagle, Orr, Piekos, Schmidt, Shirley, Spearing, Tan, Tzeng, and Waitz, "Power MEMS and Micro-engines," *presented at IEEE Conference on Solid State Sensors and Actuators*, Chicago, IL, June 1997.
- [2] Epstein A., 2004. "Micro-Engines – Scholar Lecture". *ASME J. of Turbomachinney*, vol. 5, 2 pp. 204-211.
- [3] Epstein, A.H., and Senturia, S.D., 1997, "Macro Power from Micro Machinery", *Science*, 276, p. 1211.
- [4] Li, H., personal communications.
- [5] Main, J. 2003. Exo-Skeleton Developments. Presentation by John Main, DARPA, to the Committee on Soldier Power/Energy Systems. Washington, D.C. June 19.
- [6] Savoulides, N., 2004. *Development of a MEMS Turbocharger and Gas Turbine Engine*. Ph.D. thesis, Department of Aeronautics and Astronautics, MIT.
- [7] Teo, C. J., 2005, Ph.D. thesis in preparation, Department of Aeronautics and Astronautics, MIT.
- [8] Wang, C. W., 2004. *Design, Fabrication, Experimentation and Analysis of High-Speed Microscale Gas Bearings*. M.S. thesis, Department of Mechanical Engineering, MIT
- [9] Teo, C. J., Spakovszky, Z., "Modeling and Experimental Investigation of Micro-Hydrostatic Gas Thrust Bearings for Micro-Turbomachines", *Proceedings of ASME Turbo Expo, International Gas Turbine and Aeroengine Congress and Exhibition*, Reno, June 2005.
- [10] Teo, C. J., Spakovszky, Z., "Analysis of Tilting Effects and Geometric Non-Uniformities in Micro-Hydrostatic Gas Thrust Bearings", *Proceedings of ASME Turbo Expo, International Gas Turbine and Aeroengine Congress and Exhibition*, Reno, June 2005.
- [11] Paduano, J., 2002., Aug. Personal communication, MIT Gas Turbine Laboratory.
- [12] Steyn, L., 2005. *A Microfabricated ElectroQuasiStatic Induction Turbine-Generator*. Ph.D. thesis, Department of Aeronautics and Astronautics, MIT.
- [13] Jamonet, L., 2002. *Testing of a microrocket engine turbopump*. M.S. thesis, Depart-

- ment of Aeronautics and Astronautics, MIT.
- [14] H.C. Rothe, 1959. "Air bearings for guidance components of ballistic missiles and their production aspects". In *First Int. Symp. Gas-Lubricated Bearings*, P. 68, Washington, DC.
- [15] "A large tank of liquid helium for nuclear experiments". *New Scientist*, (325):277, 1963
- [16] G.L. Agrawal, 1997. "Foil air/gas bearing technology – an overview". *ASME 97-GT-347, International Gas Turbine & Aeroengine Congress & Exhibition*, Orlando, FL.
- [17] Piekos, E., Orr, D., Jacobson, S., Ehrich, F., and Breuer, K., 1997. "Design and Analysis of Microfabricated High Speed Gas Journal Bearings". In 28<sup>th</sup> AIAA Fluid Dynamics Conference, Snowmass Village, Colorado, AIAA Paper 97-1966.
- [18] Piekos, E., and Breuer, K., 1999. "Pseudospectral Orbit Simulation of Nonideal Gas-Lubricated Journal Bearings for Microfabricated Turbomachines". *ASME J. of Tribology*, 121 [May], pp. 604-609.
- [19] Piekos, E., 2000. *Numerical Simulation of Gas-Lubricated Journal Bearings for Microfabricated Machines*. Ph.D. thesis, Department of Aeronautics and Astronautics, MIT.
- [20] Fuller D., 1969. "A Review of the State-of-the-Art for the Design of Self-Acting Gas-Lubricated Bearings". *Journal of Lubrication Technology*, vol. 91(1) pp. 1-16.
- [21] Garner D., Lee C., and Martin F., 1980. "Stability of Profile Bore Bearings: Influence of Bearing Type Selection". *Tribology International*, vol. 13(5) pp. 204-210.
- [22] Samoson A., Tuhern T. and Past J., 2001. "Ramped-Speed Cross Polarization MAS NMR". *J. Magnetic Resonance*, 149, pp. 264-267.
- [23] Ehrich F. and Jacobson S., 2001. "Development of High-Speed Gas Bearings for High-Power-Density Micro-Devices". In *ASME Turbo Expo*, New Orleans, LA. Paper 2001-GT-478.
- [24] Larson, R., and Richardson, H., 1962. "A Preliminary Study of Whirl Instability for Pressurized Gas Bearings". *ASME J. of Basic Engineering* [Dec.], pp. 511-520
- [25] Lomakin A., 1958. "Calculation of Critical Number of Revolutions and the Conditions Necessary for Dynamic Stability of Rotors in High-Pressure Hydraulic Machines when Taking into Account Forces Originating in Sealings." In *Power and Mechanical Engineering (in Russian)*.
- [26] Gong, Y., personal communications.
- [27] Smith D., 1933. "Motion of a Rotor Carried by a Flexible Shaft in Flexible Bearings." In *Proceedings of the Royal Society*, vol. 142 n.864A. (pp. 92–118).



- 
- [28] Ehrich F., 1989. "The Role of Bearing Support Stiffness Anisotropy in Suppression of Rotordynamic Instability." In *ASME DTC – 12th Biennial Conference on Mechanical Vibration and Noise*, Montreal, Canada.
- [29] Childs, D.W., 1993. *Turbomachinery rotordynamics: phenomena, modeling, and analysis*. Wiley-Interscience, New York.
- [30] Teo, C.J., personal communications.
- [31] Jacobson, S., personal communications.
- [32] Savoulides, N., personal communications.
- [33] Miki, N., personal communications.
- [34] Ehrich, F., personal communications.
- [35] Sirakov, B.T., 2005. *Characterization and Design of Non-Adiabatic Micro-Compressor Impeller and Preliminary Design of Self-Sustained Micro-Engine System*. Ph.D. thesis, Department of Aeronautics and Astronautics, MIT.
- [36] Chandrasekaran, V., personal communications.
- [37] Spakovszky Z. and Liu L., 2003. "Scaling Laws For Ultra-Short Hydrostatic Gas Journal Bearings." In *ASME Design Engineering Technical Conference*, Chicago, IL. Paper DETC2003/VIB-48468.
- [38] Hagedorn, Peter. 1981. *Non-Linear Oscillations*. Oxford, New York.